THREE-DIMENSIONAL GEOMETRY CHARACTERIZATION USING STRUCTURED LIGHT FIELDS

Paulo José da Silva Tavares

FACULDADE DE ENGENHARIA DA UNIVERSIDADE DO PORTO

Departamento de Engenharia Mecânica e Gestão Industrial

Submetida em cumprimento parcial dos requisitos para a obtenção do grau de Doutor em Engenharia Mecânica

Orientador: Prof. Mário A. P. Vaz

December 2008

This page intentionally left blank.

À família e aos amigos...
As duas melhores coisas da vida.

This page intentionally left blank.

Abstract

This essay doesn't correspond to a thesis in the usual sense, i.e., the preposition of a hypothesis about a certain issue, followed by a thorough study and a development that may or may not confirm the initial supposition. It is rather a dissertation about an ongoing work which embraced a large subset of the 3D image acquisition methods, the Phase Measurement Fringe Projection techniques. These are but a fraction of the active imaging contactless techniques available today, but nevertheless a very important one, when high resolution, robust all-round methods are sought.

Still, the approach taken in this work, which came to require the development of just about every tool deemed necessary along the way, inevitably led to posing and dwelling with theses about different subjects, from profilometre calibration to resolution increase or fringe correction. These theses were all developed and led to publications, some of which can be found at the end of this document. But they led further to the small advances that were necessary at each step. Camera calibration algorithms, profilometre calibration, image processing, filtering or transforming are just a few examples of the tools that had to be developed from scratch to attain the desired goals.

The objectives of the work described here below have been satisfactorily achieved with the implementation of three different methods which can cope with most of the situations commonly found in laboratory work: Fourier Transform Fringe Analysis, Spatial Carrier Phase Shifting and Temporal Phase Unwrapping.

The calibration method was devised for phase methods in general and can thus be applied to all three techniques. It is a two step method that starts with camera calibration and which establishes a relation between phase and height or surface profile based on two positions of the calibration target. The camera calibration method itself was developed on the basis of a method for feature detection on the calibration target with sub-pixel resolution, which relies on the properties of the Hilbert Transform and of a centroid detection algorithm.

During the implementation of the Fourier Transform Fringe Analysis method, a method for the elimination of the central dc frequency and the enlargement of the filter window for carrier removal was devised and implemented. An appreciable increase in frequency resolution was thus obtained at the expense of using two frames with fringe projection at right angles, instead of a single one. Although the method looses the ability to deal with dynamical situations, the improvements obtained in static situations are certainly worth the extra effort.

A simple method for correction of the projector limitations, which distort the si-

nusoidal fringes necessary for phase calculation, has also been developed and implemented. The method uses a Modulation Transfer Function analysis to calculate the synthetic patterns that become sinusoidal when sent through the projection system.

One of the most stimulating projects that stemmed from the present work was the development of a coherent fringe projection system to allow the use of the profilometre under all lighting conditions, either inside a controlled lighting environment, such as a laboratory, or in outdoor applications. This is really an ongoing project which will keep on being improved as experience dictates. It is now on its 2nd version, improved over the 1st one in several respects, such as beam quality or mechanical stability, but still has to endure field tests and some improvements to the light fields are already apparent, such as beam shaping or condenser control.

Although the laboratory has been endowed with a set of tools for 3D surface acquisition under diverse conditions, both in static and dynamic situations, it is no less true that a long way lies ahead, which may continue fuelling interesting developments in this fascinating research field. Several functionalities remain to be explored and other methods may prove more efficient, where the ones described and implemented during the present work behave less adequately.

Resumo

Este ensaio não corresponde a uma tese no sentido habitual do termo, i.e., a preposição de uma hipótese acerca de uma determinada questão, seguida de um estudo bastante completo e um desenvolvimento que pode confirmar, ou não, a suposição inicial. Trata-se, sim, de uma dissertação acerca de um trabalho contínuo que abraçou um vasto subconjunto dos métodos de aquisição de imagens tridimensionais, as técnicas de projecção de franjas com medição de fase. Estas são apenas uma pequena fracção das técnicas de imagem activas sem contacto disponíveis nos dias de hoje, mas uma muito importante quando se pesquisam métodos robustos, flexíveis e de elevada resolução.

Apesar disso, a abordagem adoptada neste trabalho, que veio a exigir a desenvolvimento de praticamente todas as ferramentas necessárias ao longo do caminho, conduziu inevitavelmente à proposta e resolução de teses sobre assuntos diferentes, desde a calibração do perfilómetro até à melhorada resolução ou à correcção das franjas projectadas. Essas teses foram todos desenvolvidos e levaram a publicações, algumas dos quais podem ser encontrados no final deste documento. Mas levaram, mais ainda, aos pequenos avanços necessários a cada passo. Algoritmos de calibração de câmara, calibração do próprio perfilómetro, processamento de imagens, filtragem ou transformação, são apenas alguns exemplos das ferramentas que tiveram de ser desenvolvidas a partir do zero para atingir os objectivos desejados.

Os objectivos do trabalho descrito abaixo, foram alcançados satisfatoriamente com a implementação de três métodos diferentes que endereçam a maioria das situações comummente encontradas no trabalho de laboratório: Análise de Franjas por Transformada de Fourier, Desmodulação de Fase com Portadora Espacial e Desmodulação Temporal de Fase.

O método de calibração foi concebido para métodos de fase em geral e pode assim ser aplicado a qualquer uma das técnicas. É um método em dois passos que começa com a calibração da câmara que estabelece, em seguida, uma relação entre fase e altura ou perfil de superfície a partir de duas posições do alvo de calibração. O próprio método de calibração da câmara assenta num método de detecção de padrões do alvo de calibração com resolução subpixel baseado nas propriedades da Transformada de Hilbert e num algoritmo de detecção de centróides.

Durante o desenvolvimento do método de Análise de Franjas por Transformada de Fourier, foi concebida e implementada uma técnica para a eliminação do pico central de frequência e o alargamento da janela do filtro para remoção da portadora. Um aumento apreciável de resolução em frequência foi assim obtido à custa da utilização

de dois padrões com franjas ortogonais, em vez de um único. Embora o método perca a capacidade para lidar com situações dinâmicas, as melhorias obtidas nas situações estáticas são valem certamente o esforço suplementar.

Um método simples para a correcção das limitações do projector que levam à distorção das franjas sinusoidais, característica necessária para o cálculo de fase, foi ainda desenvolvido. O método utiliza uma análise da Função de Transferência de Modulação para calcular os padrões sintéticos que se tornam sinusoidais quando enviados através do sistema de projecção.

Um dos mais estimulantes projectos que nasceram do presente trabalho foi o desenvolvimento de um sistema coerente de projecção de franjas para permitir a utilização do perfilómetro em todas as condições de iluminação, quer num ambiente de iluminação controlado, como um laboratório, ou em aplicações de exterior. Este é, na verdade, um projecto que se mantém em curso e que continuará a ser melhorados conforme a experiência dite. Está agora na sua 2^a versão, melhorada significativamente em relação à 1^a em vários aspectos tais como a qualidade do feixe ou a estabilidade mecânica. O actual projector deverá ainda suportar testes no terreno e algumas melhorias já detectadas tais como a controlo da forma da frente de onda são ou o controlo do próprio grupo óptico de condensação.

Embora o laboratório tenha sido dotado de um conjunto de ferramentas para aquisição de superfície 3D sob diversas condições, em situações estáticas e dinâmicas, não é menos verdade que resta um longo caminho por percorrer que pode continuar a alimentar desenvolvimentos interessantes nesta área de investigação fascinante. Diversas funcionalidades continuam a ser exploradas e outros métodos poderão revelar-se mais eficientes, onde as técnicas descritas e implementadas durante o presente trabalho se comportam de forma menos adequada.

Resumé

Cet essai ne correspond pas à une thèse au sens habituel du terme, c'est-à-dire, la préposition d'une hypothèse sur une certaine question, suivie d'une étude approfondie et un développement qui peut se confirmer ou non sur l'hypothèse initiale. Il s'agit plutôt d'une thèse sur un travail continu qui englobe une grande partie des méthodes d'acquisition d'image en 3D, les techniques de mesure de phase par projection des franges. Il ne s'agit que d'une fraction des techniques d'imagerie actives sans contact disponibles aujourd'hui, mais une qu'est néanmoins très importante, quand on cherche les méthodes robustes d'haute résolution très flexibles.

Dans tous cas, l'approche adoptée dans ce travail, qui fini par exiger le développement d'à peu près tous les outils jugés nécessaires au fur et à mesure du développent, mena inévitablement à poser des thèses sur différents sujets, de la calibration du profilomètre à l'amélioration de la résolution ou la correction des franges. Ces thèses ont conduit à des publications, dont certaines peuvent être trouvés à la fin de ce document. Mais surtout, elles ont conduit aux brefs progrès nécessaires à chaque étape. Algorithmes de calibration de camera, calibration du profilomètre, traitement d'images, filtrages ou transformations ne sont que quelques exemples des outils qui a fallu développer à partir de zéro pour atteindre les objectifs souhaités.

Les objectifs des travaux décrits ci-dessous ont été réalisés de façon satisfaisante avec l'implémentation de trois méthodes différentes qui peuvent faire face à la plupart des situations communément trouvée dans les travaux de laboratoire: analyse des franges par Transformé de Fourier, Démodulation de Phase avec Porteuse Spatiale et Démodulation Temporale de Phase.

La méthode de calibration a été élaborée pour les méthodes de phase, en général, et peut donc être appliquée à tous les trois techniques. Il s'agit d'une méthode en deux étapes qui commence par calibration de la caméra et qui établit ensuite une relation entre la phase et l'hauteur ou profil de la surface à partir de deux positions de la cible de calibrage. La méthode de calibration de la caméra a elle-même été développée sur une méthode de détection de caractères dan la cible de calibration avec résolution sous-pixel, qui s'appuie sur les propriétés de la Transformée de Hilbert et un algorithme de détection de centroïdes ou barycentres.

Au cours de l'implémentation de la méthode d'analyse des franges par Transformé de Fourier, une technique pour l'élimination de la fréquence centrale et l'élargissement de la fenêtre du filtre de suppression de la porteuse a été conçue et mis en œuvre. Une augmentation appréciable de la résolution en fréquence a donc été obtenue au détriment de l'utilisation de deux cadres avec frange de projection orthogonales, au

lieu d'un seul. Bien que la méthode perde la capacité de faire face à des situations dynamiques, les améliorations obtenues dans les situations statiques méritent certainement l'effort supplémentaire.

Une méthode simple pour la correction des limitations du projecteur, qui déforment les franges sinusoïdales, nécessaires au calcul de la phase, a également été développée et implémenté. La méthode utilise une analyse de la fonction de transfert de modulation pour calculer les franges synthétiques qui deviennent sinusoïdales lorsque envoyés par le système de projection.

Un des projets les plus stimulants qui découle du présent travail a été le développement d'un système de projection de franges cohérente afin de permettre l'utilisation du profilomètre sous toutes les conditions d'illumination, soit dans un environnement contrôlé, comme un laboratoire, ou dans les applications d'extérieur. C'est vraiment un projet en cours qui continue d'être amélioré tant que l'expérience l'exige. Il est maintenant sur sa 2ème version, améliorée vers la 1ère à plusieurs égards, tels que la qualité du faisceau ou la stabilité mécanique, mais il doit encore subir des essais et quelques améliorations sont déjà évidents, comme le contrôle de la forme du faisceau ou du groupe condenseur il-même.

Bien que le laboratoire a été doté d'un ensemble d'outils pour l'acquisition de surface 3D dans des conditions diverses, tant en situations statiques et dynamiques, il n'est pas moins vrai qu'un long chemin reste à faire, qui peut continuer à sustenter des développements intéressants dans ce domaine de recherche fascinant. Plusieurs fonctionnalités restent à explorer et d'autres méthodes peuvent se révéler plus efficaces, où celles qui sont décrites et mises en œuvre au cours du présent travail se comportent de façon moins adéquate.

Acknowledgements

Thanks are in order to a number of people who have had contributed, either directly or indirectly, to the present work.

First and foremost, a very special thank you to Professor Mário Vaz, my advisor and a person I look up to in so many regards. Always with a comforting word or an appraisal, he has been all through the years a true friend more than an advisor, in many respects. His outstanding moral character and open mindedness is an example to the entire laboratory which he leads by example, more than words.

Thanks are also due to the entire department whose people conveyed a feeling of belonging that will hardly be forgotten. In particular, to Professor Silva Gomes whose availability and affirmative response, on several occasions, was much appreciated and to the department secretary, Fernanda Fonseca, who was never too busy to help whenever necessary, always with a smile on her face.

A very special thank you is also due to all the colleagues at LOME, who have indeed been very supportive. In particular to Jaime Monteiro, Jorge Reis and Nuno Ramos, who had to endure the long stake outs and sleepless nights in so many occasions and made so many valuable contributions to this work. But also to Fernando Ferreira, Hernani Lopes or João Martins, who have helped in different ways, and to all who weren't directly involved but had to withstand my enthusiasm and doubts anyway, whenever some calculation went wrong or every time some new technique or algorithm was being explored, such as, Teresa Azevedo, Daniela Sousa, João Ribeiro, Cláudia Simão, Arcelina Marques, Pedro Magalhães, Raquel or Rodolfo.

Throughout this project there were many occasions when help has been requested to extraordinary people out there and kindly given. Amongst them were Prof. Mitsuo Takeda, University of Electro-Communications, Dept. of Information and Communication Engineering, Tokyo, Prof. Chris Dainty, National University of Ireland, Galway, Prof. Karl Stetson, Karl Stetson Associates, Coventry, Dr. Roger Mohr, directeur de l'ENSIMAG, Grenoble, Dr Vyacheslav Volkov, Brookhaven National Laboratory, Upton, NY, and Prof. Katherine Creath, Research Professor of Optical Sciences, University of Arizona.

Thanks are also due to the wonderful team at Norcam, who have always been very supportive, and in particular to Marco Gomes and Vitor Martins.

Special thanks are also due to the people at the Faculty of Dental Medicine, and the Sports Faculty, University of Porto, in particular to Sara Oliveira who graciously tolerated the long sessions for full-body 3D acquisition with the new swimwear, so hard to endure.

Last, but in no way least important, my family, always behind me and so supportive. Teresa, Francisca, João and Paulo, all had to endure their share, and it wasn't a minor one. Absent nights, missed weekends and events, lack of attention, they have bravely taken all of that and much more. Simply put, this work wouldn't have been possible without their courageous attitude and incentive.

Table of Contents

Appendices

This page intentionally left blank.

List of Figures

This page intentionally left blank.

List of Tables

This page intentionally left blank.

List of Symbols and Abbreviations

$<>$	Time average or average over one cycle for periodic phenomena;
§	Section number indicator;
λ	Wavelength;
π	The number *pi*. Approximately 3.1415927;
Π	The rectangular or *boxcar* function;
ω	Angular frequency;

2D	Two-dimensional;
3D	Three-dimensional;
ac	Alternating Current;
A.D.	*Anno Domini* - Latin abbreviation for Christian Era;
AM	Amplitude Modulation;
AND	Boolean *and* operation;
BS	Beam Splitter;
CAD	Computer-Aided Design;
CCD	Charge-Coupled Device;
CAT	Computerized Axial Tomography;
CG	Conjugate Gradient;
CMM	Coordinate Measurement Machine;
CT	Computed Tomography;
CWS	Collaborative Work Systems;
DFT	Discrete Fourier Transform;
DIC	Digital Image Correlation;
DLP	Digital Light Processor;
DSP	Digital Speckle Photography;
DSPI	Digital Speckle Pattern Interferometry;
DPM	Diode Pumped Microchip;
DPSS	Diode Pumped Solid State ; Direct Phase Measurement module;
e.g.	*exempli gratia* - Latin abbreviation for *for example*;
ESPI	Electronic Speckle Pattern Interferometry;
f; F	Focal distance;
FFT	Fast Fourier Transform;

FEA	Finite Element Analysis;
GLARE	GLAss-REinforced fibre metal laminate;
FM	Frequency Modulation;
FTP	Fourier Transform Profilometry;
GCM	Gray Code Method;
GRIN	Gradient index;
HWP	Half-Wave Plate;
HCP	High-Cycle Fatigue;
He-Ne	Helium-Neon;
i.e.	*id est* - Latin abbreviation for *that is to say*;
IST	Information Society Technologies;
KTP	Potassium Titanyl Phosphate;
LASER	Light Amplification by Stimulated Emission of Radiation;
LCD	Liquid Crystal Display;
LED	Light Emitting Diode;
LSI	Linear Shift Invariant;
LOME	Optics and Experimental Mechanics Laboratory;
MRI	Magnetic Resonance Imaging;
MST	Minimum Spanning Tree;
MTF	Modulation Transfer Function;
NDT	Non Destructive Testing;
PCG	Preconditioned Conjugate Gradient;
OCT	Optical Coherence Tomograpphy;
OPD	Optical Path Difference;
OR	Boolean *or* operation;

OTF	Optical Transfer Function;
OWT	Orthogonal Wavelet Transform;
PET	Positron Emission Tomography;
PLL	Phase-Locked Loop;
PMP	Phase Measurement Profilometry;
ppb	Parts per billion;
ppm	Parts per million;
PSF	Point Spread Function;
PET	Positron Emission Tomography;
QWP	Quarter-Wave Plate;
RAC	Radial Alignment Constraint;
RE	Reverse engineering;
RPM	Rotations per Minute;
SPM	Spatial Phase Measurement;
SEE	Spectrally Encoded Endoscopy;
SESAR	Single European Sky ATM Research Programme;
SVD	singular value decomposition;
TPM	Temporal Phase Measurement;
TPU	Temporal phase unwrapping;
TOF	Time-of-Flight;
UIPE	Undistorted Image Plane Error;
VCO	Voltage Controlled Oscillator;
WFT	Windowed Fourier Transform;
XOR	Boolean *exclusive OR* operation;

Chapter 1

Introduction

Begin the beguine...
Cole Porter

The dissertation presented herein describes the study of several aspects of three-dimensional geometry characterization using structured light fields. Thus stated, this work has been restricted to a small domain of active image processing, wherefore some sort of interaction occurs between the acquisition apparatus and the scene itself. This interaction, usually in the form of an energy exchange - such as can be done by shedding light onto the surface under study and collecting it with an imaging device - marks the departure of these methods from the more popular passive imaging ones, which make up for the absence of such interaction with the use of two or more imaging devices. Still, and even if these are very different methodologies, there are a number of similarities and contact areas between the two domains. Such is the case with calibration, for instance, which runs along the same lines whatever the chosen image processing method may be.

When choosing the most appropriate method to face a certain situation, several factors must be carefully weighted, such as whether it is a static or quasi-static situation, if there's a controlled lighting environment such as can be found in a laboratory or if it's a simple or a rather complex geometry. It is not uncommon to find the development of active image processing methods in connection to other imaging techniques in experimental mechanics research groups. There is a motif - the need to complement bi-dimensional stress and strain measurements with surface geometry - there are usually enough means - imaging and projecting devices, as well as a strong supportive experience in the field - and there are plenty of opportunities, as anyone connected to optical metrology and experimental mechanics would promptly corroborate. The present work was born from such motifs and opportunities and having

been developed entirely on an optics and experimental mechanics laboratory, benefited from the available dedicated means.

Actually, this work has been devised in such a way as to bridge the gap between the non destructive testing techniques, which constitute the core of the laboratory work, and surface measurement and characterization, which now becomes available in the sequence of this research. A complete software platform, integrated with a commercially available frame grabbing hardware environment, has been developed during the course of this thesis to support the current research. This software, described in one of the appendices, is responsible for frame grabber control, camera focus and calibration and all the image processing tasks deemed necessary during the present work, such as image masking, filtering and arithmetic, spatial and temporal differentiation, direct and reverse Fourier transforming and spectrum manipulation, phase-shifting calculations, phase unwrapping, image feature detection and height to phase calibration, amongst other. A considerable amount of time and energy has been put into all the details of this task. Even the most undemanding image manipulation or numerical calculation algorithms, either entirely developed here or adopted from other sources, have been carefully scrutinized for errors and deviations and therefore, some algorithmic redundancy subsisted, when different applications of the same principle required different approaches. It is expected that this work will be pursued in the years to come, as it's been developed in an open and flexible environment, but the insights gained from such reasoning have clearly been the major reward and already paid for most of the hard effort put into this task, as several research topics benefited naturally from them.

Other contributions worth mentioning from this work were:

- A method for increasing the resolution of Fourier Transform phase analysis at the expense of acquiring one further image, whenever this can be indulged. The second image is acquired with the grating projected at a right angle to the first one, in order to fully eliminate the central dc frequency in reciprocal space and increase the filter width twice;

- A novel approach to phase-to-height calibration, which uses just two images, significantly reducing the usual image acquisition and processing burden for this absolutely indispensable calibration step.

- A sub-pixel corner detection algorithm for camera calibration. Separation of the intrinsic and extrinsic calibration parameters detection was also implemented in a very flexible way, to facilitate camera repositioning;

- A coherent light projection system was further developed and tested under

broad day light. This seems to be a very promising technique, which enables the use of active image processing outside of carefully controlled lighting environments. At the time of this writing, the projection unit is still being improved with the addition of a commercial laser unit and other important modifications.

1.1 3D Image Acquisition - an historical perspective

Figure 1.1 - Moai sculptures in Easter island, Chile.

Unlike most every research topic at the forefront of scientific knowledge, when it comes to 3D, one can go back in time to the very origin of human consciousness searching for mankind's first attempts to create familiar representations in three dimensions. Such fine examples as the Moai in Easter Island, from A.D. 1100 – 1000., or the Cycladic idols from A.D. 3000 to 2000., which seem to have marked the beginning of sculpture in Greece and were a brilliant legacy from the Cycladic civilization of the Aegean sea, illustrate this point.

Figure 1.2 - Cycladic art.

Further back in the upper Palaeolithic, the Venus of Willendorf, carved in oolitic limestone between A.D. 24,000 - 22,000, was apparently an idealization instead of a representation of the female figure, with all fertility traits clearly pronounced. After the discovery of this sculpture, several similar statuettes have been found, collectively referred to as Venus figurines. Two much older representations are the Venus of Berekhat Ram, found on the Golan Heights and dating to between A.D. 800,000 and 233,000, and the Venus of Tan-Tan, discovered in Morocco which dates to between A.D. 500,000 and 300,000, the Middle Acheulean period.

Figure 1.3 - The Venus of Willendorf.

Throughout the history, Man never ceased this apparently fundamental activity of representing feats, deities or himself, as we so well know from the wealth of sculpture heritage of all times. Yet, it was not until the 19th century that the fundamentals of Man's three-dimensional perception mechanism were questioned and the endeavour for the development and use of artificial systems for 3D replication begun.

It seems to have been in fact the well known English physicist Sir Charles Wheatstone in 1833, who first reported the stereoscopic phenomenon in a lecture to the Royal Society of London, later to be published on the Philosophical Transactions under the name *Contributions to the Physiology of Vision.—Part the First. On some remarkable, and hitherto unobserved, Phenomena of Binocular Vision*. Wheatstone built a stereoscope to demonstrate his ideas of binocular vision wherefore two images of the same object taken from different points are so combined as to make the object stand out with a solid aspect. It was Sir David Brewster with an improvement to the Wheatstone stereoscope by dispensing with mirrors that brought it into its existing form with lenses in 1949 - the first true stereo camera with two lenses.

The chief applications of stereoscopy were essentially entertainment and photogrammetry, for the rest of the 19th century and a good part of the 20th century. Sev-

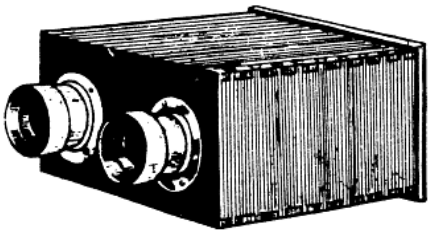

Figure 1.4 - The first stereo camera with two lenses.

eral stereo cameras were built, such as the Vérascope, the Heidoscope or the Rolleidoscope for recording stereo pairs, and numerous other models came into existence after the adoption of 35mm film which had been introduced by William Dickson and Thomas Edison in 1892.

Figure 1.5 - Stereos cameras from the 20th century.

Stereoscopy for entertainment is still very popular in our days, mainly due to the introduction of the ViewMaster viewers and films in 1939 by William Gruber, which lasted till today. Viewmaster films are circular cardboard disks with 14 slides, i.e., 7 stereoscopic images. The depth sensation achieved through stereoscopy is based on the reinforcement of the physiological cues of binocular parallax and convergence. A stereoscopic viewing system forces the eyes to see two images taken from different viewpoints at the same time. Modern stereoscopes range from relatively inexpensive pocket models that use only convex lenses, to more complex models that use mirrors, prisms and convex lenses.

Photogrammetry, the determination of geometrical properties of objects from photographic images, being used mainly for aerial survey, had to wait for the development of reliable aircrafts in World War I. The experiments during the war clearly demonstrated the advantages of aerial survey as a military tool, and this was to be one fundamental drive of the technology during most of the 20th century.

Analogue Photogrammetry was developed during the first half of the 20th century by people such as Edouard Deville, with the invention of the first stereoscopic-plotting instrument called the Stereo-Planigraph, Dr. Carl Pulfrich, with the first

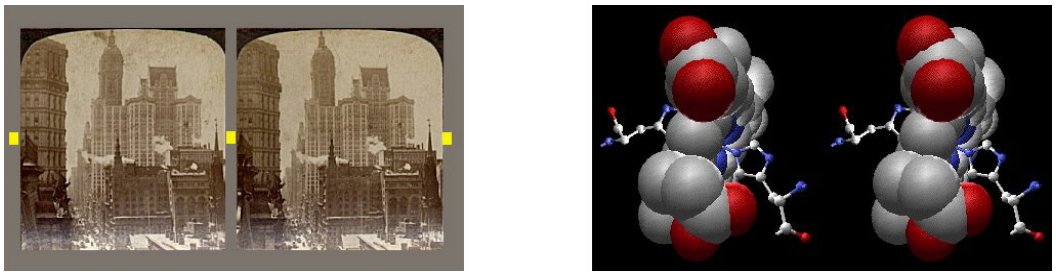

Figure 1.6 - Analogue and digitally synthesized stereo pairs.

stereo-comparator and the Pulfrich Effect, which describes the illusion of depth on transverse moving objects when part of the trajectory is illuminated differently, due to the slow response of the eye-brain in low light levels. Rittel Von Orel developed the first stereo-autograph to be built by Zeiss Works. Professor Reinhard Hugershoff developed several photogrammetric instruments, such as the first analogue plotter, the Autocartograph, an aerial camera, used to obtain oblique photography by hand or attached to the side of an aircraft, a universal phototheodolite with several innovations to achieve reasonable accuracy in spite of the rugged construction, amongst many others. Otto Von Gruber developed the fundamental tools of Analytical Photogrammetry to come: the projective equations and their differentials. Sherman Fairchild with the Fairchild Aerial Camera Corporation and camera aerial models such as the K-3, and some years later with the monoplanes built at his Fairchild Airplane Manufacturing Corporation had a decisive contribution, as had Heinrich Wild with his Wild Heerbrugg company manufacturing accurate surveying and mapping instruments from 1921 to 1989 which, after acquiring the Swiss Kern of Aarau, another surveying company, and Cambridge Instruments, became the widely known Leica group.

Figure 1.7 - Fairchild F-71 stereoscope.

Figure 1.8 - The Fairchild FC2W2 monoplane for aerial survey.

Analytical photogrammetry, developed after 1950, was essentially propelled by the growth of computing power. Amid the contributors to this development cycle are names such as Dr. Hellmut Schmid, responsible for the development of multi station photogrammetry with matrix notation, Duane Brown who, while working at the RCA Missile Test Project, developed new approaches to camera calibration including the formulation of the bundle adjustment or Houssam Mahmoud Karara and Abdel-Aziz who developed in 1971 the Direct Linear Transformation method, to express the projective transformation of 3D object points into 2D image points in homogeneous coordinates. Even if computer systems are used for aerial triangulation, measuring map data, editing and output with pen plotter, in analytical photogrammetry a stereo pair of analogue films are set up in a stereo plotter and the operator will manually read terrain features through a stereo photogrammetric or analytical plotter.

In Digital Photogrammetry, developed in the 1980's and onwards, aerial films are converted into digital image data with high resolution. A digital elevation model is automatically generated with stereo matching using a digital photogrammetric workstation.

Close-range photogrammetric methods are also used in passive image processing 3D image acquisition techniques, such as those currently in use with robot or machine vision.

Active image processing methodologies are latecomers to the 3D image acquisition arena, having given its first steps with the exploration of Moiré back in the 1960's.

In Optics, the expression Moiré relates to the beat pattern resulting from the superposition of two gratings of approximately the same frequency. This is probably

the most well known effect in optics, though most persons don't quite realize it. It can be seen on folding curtains, overlapping window blinds or even looking at stripe or square pattern shirts on television. This effect was first reported by Lord Rayleigh in 1874 when observing two identical diffraction gratings placed in nearly parallel superposition. He appreciated the fact that this phenomenon could immediately detect imperfections in gratings.

Figure 1.9 - Moiré pattern from crossed blindfolds.

The first significant works with Moiré fringes, though a few had been reported at the end of the 19th and first half of the 20th centuries, seem to have been impelled by the works of Ligtenberg (Ligtenberg, 1954) and Guild (Guild, 1956) who first published rigorous treatments of stress analysis with slope contours and displacement measurements. A plethora of works has been published on the subject during the decade of 1960 and onwards until our days. Initial applications of Moiré techniques were essentially on stress analysis, even if there have been publications on other research topics such as the work by Nishijima and Oster on refractive index determination (Nishijima and Oster, 1964). Rowe and Welford seem to have first reported the projection of interference fringes for object contouring in 1967 (Rowe and Welford, 1967) while the work by Brooks and Heflinger on projection Moiré for out-of-plane deformation measurement in 1969, marks the start of fringe projection methodologies for deformation measurements (Brooks and Heflinger, 1969). Basically, it consisted on recording the contour maps of an object illuminated with an interference pattern, developing the photographic plate and replacing it on the camera. Any change on the

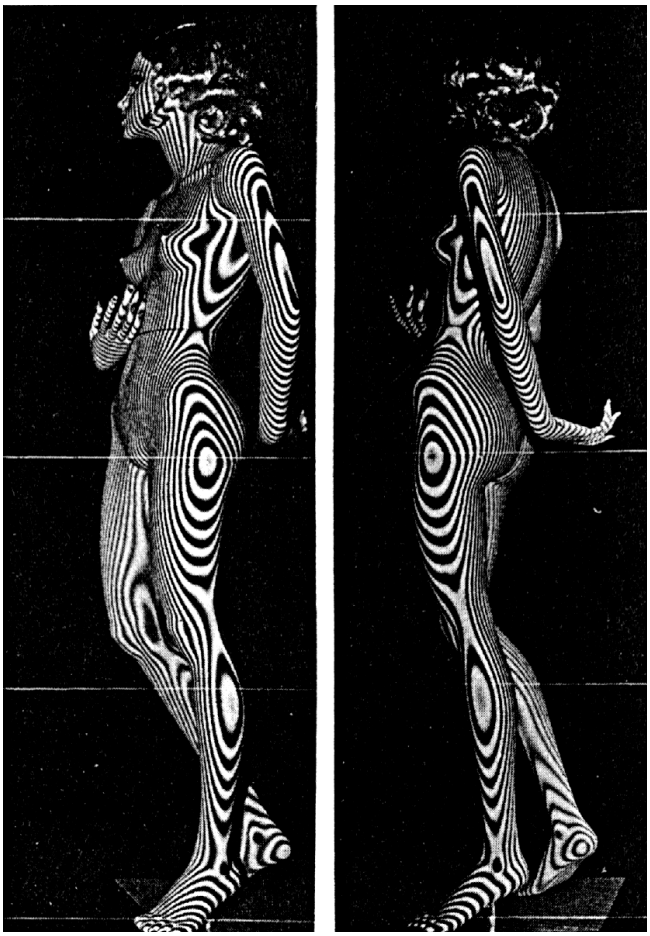

Figure 1.10 - Full body Shadow Moiré contouring (Takasaki, 1970).

object topography by either straining or heating it, was readily observed as a Moiré beat. This type of Moiré was to be known as Projection Moiré. Shadow Moiré, wherefore only one grating is used and the projected fringes are observed through it, was developed independently by Meadows and Takasaki in 1970 (Meadows et al., 1970; Takasaki, 1970).

The evolution of computing power, alongside the development of efficient light sources, imaging devices and real time sub-pixel digital peak detection algorithms in the decades to come, had an impressive effect on the progress of active sensing. A wealth of concepts and devices were proposed, developed and commercialized. A peek at present day commercial panorama is by no means representative of the evolution of methods and devices, as many excellent developments were simply not successful at that level. A taxonomy of present day panorama is presented in next section and a brief report on the current status of this research area is presented in

Chapter 2.

1.2 A simple taxonomy

Over the years, there have been several attempts at systematizing the optical techniques related to 3D surface acquisition, and eventually they all fail. It will thus come as no surprise the fact the attempt presented herein is also bound to fail sooner or later. This is a rapidly changing field of knowledge and new methods are constantly being suggested and implemented. One may legitimately ask therefore, what is the point of the exercise? If none other, the classification of the available methods at one moment in time puts the metrology work in a different perspective, allowing the rapid identification of the most suitable technique for a particular task. Taking the point somewhat farther, J. M. Burch from the NPL advocated the use of a table he put forward to help bridge the gap between the Laboratory's customers and the metrologist (Burch, 1975). The table included all the optical metrology methods available in NPL at the time, and was built in such a way as to facilitate the election of a particular method according to the problem's characteristics such as the surface dimension or finish.

The classification presented in Fig. 1.11 broadens the taxonomy implied in this proposal by including some methods not in use at the time, but is, on the other hand, restricted to surface acquisition techniques. A clear separation of the active and passive image processing is amply justified by the totally different approaches from both methods, as is the separation of the contactless methods into reflective and transmissive. It should be noted that phase methods appear on a class of its own, even if they are used in other classes, such as fringe projection or holography. In fact, if it weren't for the phase methods development, resolutions of $\lambda/100$ would be totally out of the question for some of these classes. The optical methods referred to in this classification will be covered in Chapter 2.

1.3 3D surface acquisition in experimental mechanics

The bulk of any experimental mechanics laboratory work is centred around vibration, strain and stress analysis. The shape information of a study specimen is a valuable part of most analysis work both to (i) complete the subject study and (ii) predict and model 3D behaviour of the specimen under selected influences. Finite Element Analysis (FEM) is a numerical analysis tool totally dependent on shape information. Whether it is modelled from scratch, or based on 3D surface acquisition, is a decision the Mechanical Engineer has to take at an early stage of the analysis workflow.

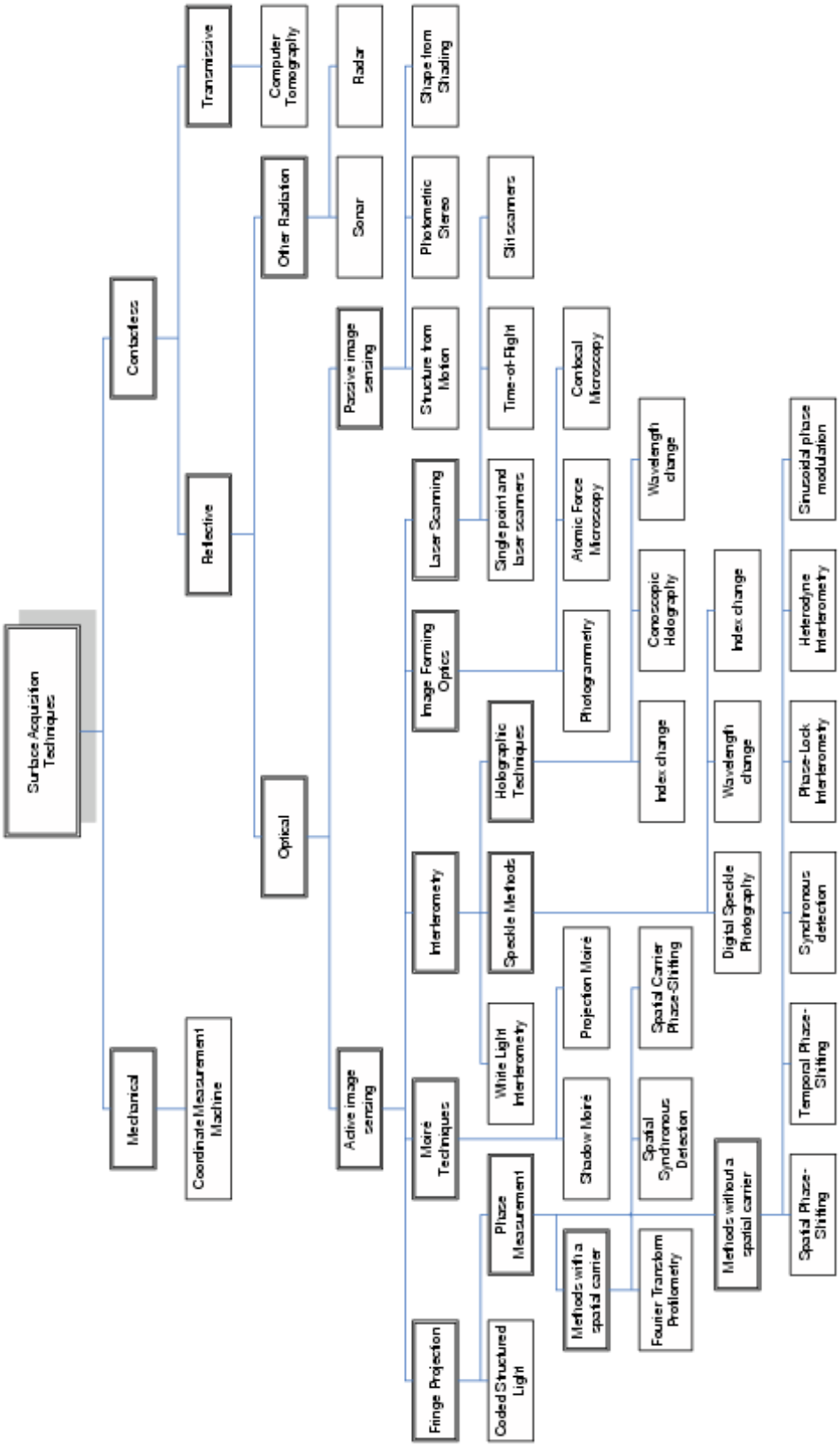

Figure 1.11 - A taxonomy proposal for 3D surface acquisition.

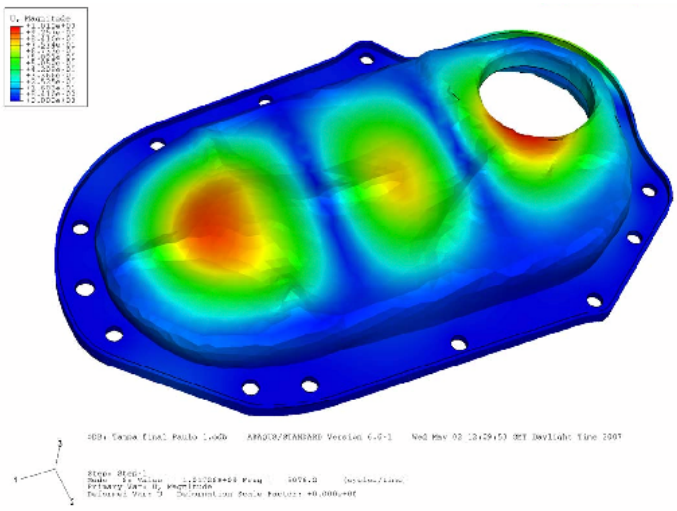

Figure 1.12 - FEM analyses based on acquired 3D shapes - LOME.

Many FEM analyses can be built on scratchpad models, owing to the fact that mechanical behaviour can be approximated to an acceptable level with a simple to moderately complex design and a rational mass distribution, even if they take a long time to develop. Yet, complex surfaces such as a helix blade or a human mandible are very difficult to model on such simple grounds. Surface acquisition is an indispensable tool when such cases arise, providing the analyst with the necessary starting information. Furthermore, this is done at a fraction of the time, and the cost, it would take to draw the specimen in three-dimensions, and to a much better approximation degree. One example of a FEM analysis based on 3D acquired shape at LOME can be seen in Fig. 1.12, which will be further discussed in Chapter 5.

1.4 Applications

The range of 3D sensing acquisition applications is confined by human imagination alone. The optical non-contact methods have been steadily gaining acceptance in most of these applications. Some important examples are given below, notwithstanding the vast wealth of applications beyond these few ones.

Industrial inspection

The past two decades have seen a rapid advance in industrial 3D measurement systems. The demand for higher accuracy and efficiency from the aerospace, automotive or most every industry, together with very strong competition amongst commercial

providers of systems and services, has been driving the rapid deployment of techniques and methodologies. Most importantly, the trend towards total automation of the measurement set up and acquisition processes, user-directed real time measurements, and provision for direct input of 3D coordinates into CAD models, has brought plentiful laboratory developments into the daylight, in the form of successful University spin-off's in such areas as digital image correlation or interferometry.

As a consequence, the precision and reliability of the acquired data are steadily improving, due to both better system designs and increased computer processing capabilities. A large number of such systems are now seen by the users as standard, *off-the-shelf*, tools to produce the desired results in their applications, already at a stage of development where semi-skilled operators can successfully conduct accurate and reliable measurements with minimal training.

Although the initial acceptance of optical systems based was very slow, such systems are now seen as viable 3D measurement techniques which compete with the more traditional mechanical ones, such as coordinate measuring machines (CMM) with the immense advantages of being contactless and faster. Their range is also far less limited than it is in contact methods. A number of other reasons for the broad acceptance of optical methods could be cited, such as the continuous improvement of these systems, which has been fuelled by the demands of industry, or the fact the commercial suppliers have been eager to provide measurement solutions which were not seen as specialized systems to be operated only by experts, in order to improve their competitiveness against established techniques. Certainly as important are the development of niche markets and specific applications of different systems, and the necessity for large aerospace and manufacturing organizations to have a range of reliable measurement systems readily available.

A thorough study of over 200 products by Tim Clarke of the Optical Metrology Centre in the UK, exposes the benefits and disadvantages of the most common optical methods in industrial inspection (Clarke and Williams, 1999). An insight into the diversity of applications can be gained by looking at Table 1.1 from Clarke's study.

Reverse engineering

Reverse engineering (RE) is the determination of the operation principles of a device or system through the analysis of its structure, function and operation. As far as shape is concerned, the RE process involves measuring an object and reconstructing it as a functional 3D model. Shape acquisition techniques are thus central to this discipline, to provide the required data for analysis.

The purpose of RE can be either to provide digital support for subsequent life

Single point triangulation	Laser stripe	Photogrammetry
Tire treads	Logs	Aerospace
Archaeological artefacts	Road surfaces	metrology
Printed circuit boards	Human body	Automobile
Road surfaces	Industrial components	manufacture
Paper roughness	Rare objects	Shipbuilding
Solder paste thickness	Joint tracking	Mapping
Connector pin warp	Seam tracking	Architectural models
Silicon wafer thickness	Welding	Building facades
CD pickup travel	Object presence	Archaeology
Industrial plant scanning	Part positioning	Human body scans
Turbine blades	Web presentations	Gait analysis
Building facades	Virtual reality environments	Missile or plane tracking
	Steel production inspection	Virtual reality Entertainment

Ultrasound	Time of Flight	Laser trackers
Liquid level measurement	Civil Engineering surveying	Robot tracking calibration, and testing
Counting objects on production lines	Profiling rock faces in quarries	Shipbuilding
Thread or wire break detection	Tunnel profiling	Aircraft manufacturing
Robotic sensing for navigation	Hydrographic survey of buoys, barges and oil rigs	Verification of jig design
Vehicle obstacle detection		Inspection and alignment
Wall-to-wall distance measurement	Range and bearing information	Surfaces
Camera focusing	Aerial surveys	

Table 1.1 - Typical objects measured by each measuring system

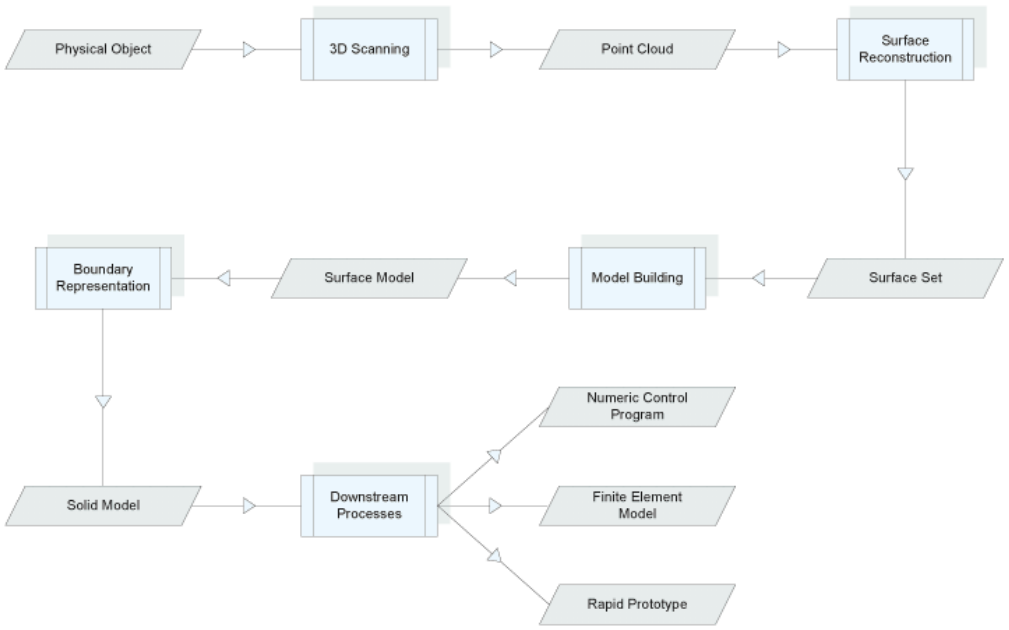

Figure 1.13 - A typical Reverse Engineering workflow.

cycle stages of a product for which no computer-aided design (CAD) model is available, or to support the redesign of an existing product. To actually offer this support, it is necessary that the 3D scanning of the object results in a very dense and accurate point set. From the digitized points the dimensions or the shape of the product can then be obtained, as illustrated in the workflow in Fig. 1.13

This task is typically hard to automate, although recent trends in RE already include automatic or semi-automatic edge detection and shape feature recognition in an attempt to address that issue.

Collaborative Work Systems

Computer-supported Collaborative Work Systems (CWS) are an example of emergent or reborn disciplines owing to 3D sensing advances. These are systems developed with remote geographic collaboration in mind, to achieve higher levels of participation, productivity, and creativity.

Visualization is one of the most natural and intuitive ways to exchange information between humans, and it has so become the principal medium used in cooperative and multi-user situations. Up until recently, the state of the art of collaborative

real-time audiovisual systems relied on 2D environments to share information, but for many professional applications, there's only so much interest in these systems as the exchange of physical 3D information of common interest becomes possible. These applications include, but are not limited to, clinical discussions among teams of medical specialists, multi-disciplinary scientific debate or design reviews between original equipment manufacturers and suppliers using CAD. The object under discussion may be anatomical, molecular or a product model, and since these are typically very complex 3D objects, providing collaborative environments able to process, transmit and display 3D data in ways that match human perceptual abilities is therefore critically important.

The Coherent project is a recent EU initiative from the Sixth Framework Program, FP6, within the Information Society Technologies (IST) priority, to pursue this objective by building a new networked holographic audio-visual platform to support real-time collaborative 3D interaction between geographically distributed teams. A display component based on innovative holographic techniques, can present, at natural human interaction scale, realistic animated 3D images to an unlimited number of freely moving simultaneous viewers. The design of the basic networked audiovisual components is driven by two innovative demanding applications - a collaborative medical visualization system and a collaborative design review system for the automotive industry.

Even though the accent is set on the display rather than the acquisition procedure, the requirements of CWS on high quality rendered models pose ever increasing constraints on 3D sensing techniques.

Cultural heritage preservation

The 2001 destruction of the three standing Buddha statues near Bamiyan, Afghanistan, left few people undisturbed all over the world. This region, one of the major Buddhist centres from the second century AD up to the time when Islam entered the area in the ninth century, was included in the UNESCO World Heritage List in 2003 and still has one of the greatest concentrations of Buddhist art (Gruen et al., 2004).

This incident is a token of the motivations that spurred the development of cultural heritage preservation policies and the funding of research in the subject. The EU framework programs have already funded several projects in this research topic as part of the IST program.

There are many research groups actively involved in cultural heritage preservation in Europe. Common goals for these projects are:

- the advance of 3D sensing technologies for digital recording of cultural heritage,

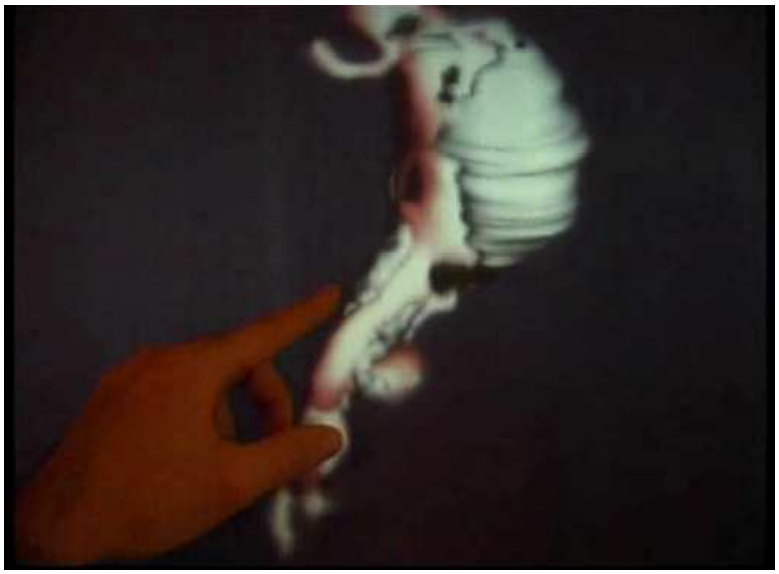

Figure 1.14 - Interactive discussion over holographic visualization of an Abdominal Aortic Aneurysm model on the Collaborative Medical Diagnostic Application. Courtesy, HOL – Holografika e.c.

with a special emphasis on automation procedures;

- the development of data processing methodologies, which involve the modelling of the digitized object through the unification of partial scans, geometric and texture data processing, and texture mapping;
- the development of data archiving, management and dissemination tools, to support the virtual reality environments necessary to implement virtual museums.

Research in this area faces several difficulties, such as the varying size of objects,

Figure 1.15 - The Bamyian Buddha sites. Courtesy, Prof. Armin Gruen, Institute of Geodesy and Photogrammetry, ETH Zurich.

Figure 1.16 - The Digital Michelangelo Project. Digitalization of the statue of St. Matthew: Acquisition of range data and colour data and the rendered surface. Courtesy, Mark Levoy, Stanford.

from small artefacts to large statues such as the 5m tall Michelangelo's David from the Digital Michelangelo Project in Stanford, digitized with two billion polygons. The diversity of materials such as translucent marble or reflective canvas oil, and the necessary detail to assemble a useful digital model, impose difficult restrictions as well: the chisel marks in statuary determine the level of envisaged detail for digitalization, since these are often meant as a finishing detail, but to assist in detection of surface defects such as cracks, the required resolution may be much larger.

The advantages and disadvantages of the 3D sensing methods in artwork conservation have been described in detail (Pieraccini et al., 2001). Special scanning instruments are often deemed necessary due to the dimensions and geometry of the objects (Fontana et al., 2002).

Forensic analysis

Three-dimensional data acquisition of crime scenes for subsequent reconstruction and analysis in criminal investigation is a relatively new application. The advantages of a contact free method can't be underestimated, as it provides a solution to avoid tampering with the scene and reliably reconstructing it later without the accidental introduction of artefacts. There are several advantages to this technique still under exploration, such as:

- contactless measurement of the scene;
- adaptation of the measurement resolution to the dimension of the details of interest for afterwards investigations, such as the victim or the lesions;
- elaboration of the raw data sets to create the topological description of the scenarios, by means of suitable triangle meshes;

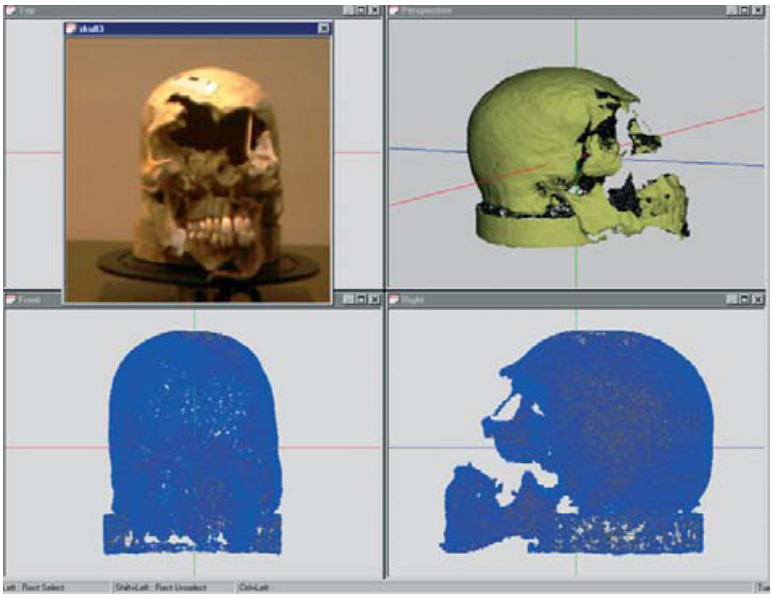

Figure 1.17 - Forensic evidence digital recording and measurement.

- accurate measurement of distances, areas and volumes;
- virtual interaction with the scene;
- *freezing* the scene for legal purposes;
- visual examination of lesions as they were at the time of the retrieval, avoiding the time dependent deterioration.

The optical 3D collection of autopsy data is another interesting application in forensic analysis, for both digital storage and remote collaboration in injury discussion in those cases the autopsy outcome is not immediate.

Medicine and surgery

The number of applications of contactless 3D sensing in medicine and surgery is growing day by day at such a pace they are actually hard to keep abreast of. Miniaturization of 3D sensing probes, such as the miniature Spectrally Encoded Endoscope (SEE) recently published in Nature by a team in Massachusetts General Hospital, Boston (Yelin et al., 2006), or high resolution 3D Optical Coherence Tomography (OCT) (Wojtkowski et al., 2005), are examples of recent advances expected to further increase the application of minimally invasive diagnostic and therapeutic procedures.

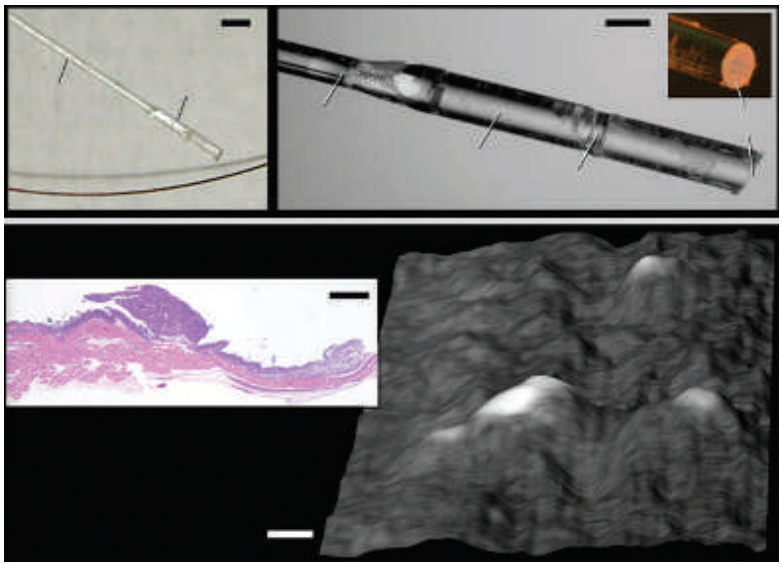

Figure 1.18 - Spectrally Encoded Endoscopy system and probe. The size of the endoscope, which comprises a grating and a GRIN lens is comparable to a hair. 3D images from a rat's ovarian tumour nodules. Courtesy, Dr. Gary Tearney, Massachusetts General Hospital.

Miniature 3D endoscopes can be used to assist in laparoscopic surgical procedures or in diagnostics related to the intestinal or respiratory tracts. But they can also be used to assist in vascular surgery procedures, such as angioplasty or coronary tissue revascularization, to assess the procedure's efficacy in real time.

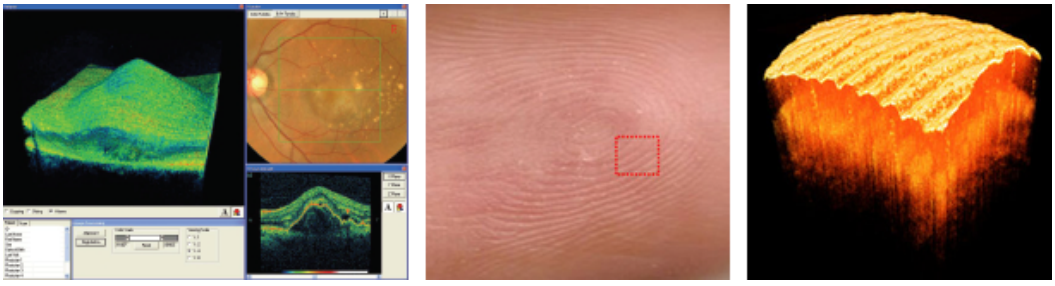

Figure 1.19 - 3D OCT imaging of the eye fundus on a patient with Posterior Vitreous Detachment and on a fingerprint. Courtesy, ThorLabs.

In reconstructive surgery such as mammary or maxillofacial, data may have been collected in advance, in case of a planned intervention such as those in cancer treatment, or may be calculated from similar parts of the body. The necessary adjustments may be calculated from rendered real 3D models as shown in Fig. 1.20.

Plastic surgery for cosmetic reasons follows a very similar reasoning, and the patient may even be called upon to intervene on a CAD modification of the rendered model. Internet services to assist potential patients evaluate the possible outcome of a plastic surgery, can currently be found which require the upload of several photographs and return digitally altered images of that outcome. This work is done by digital imaging experts and plastic surgeons in collaboration. The resulting images can guide the patient's discussion with his own plastic surgeon.

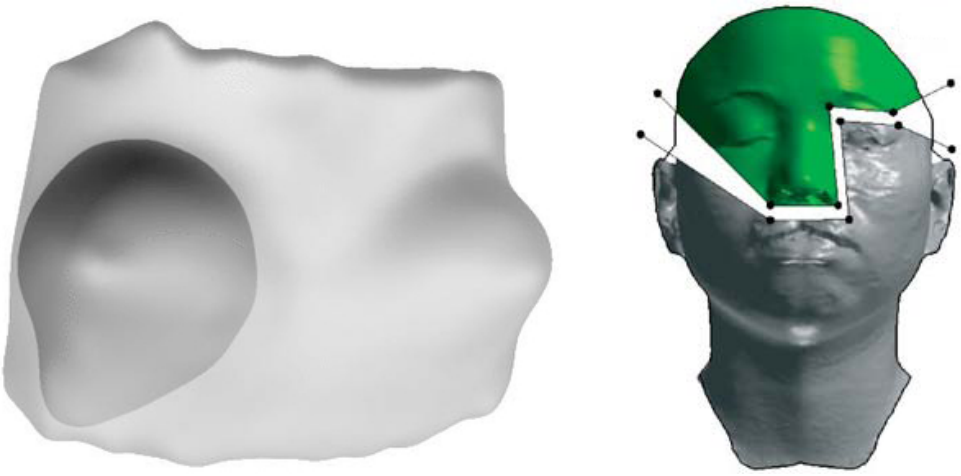

Figure 1.20 - Reconstructive surgery - 3D rendered models from scanned data.

Radiotherapy is another example of an application with multiple benefits from contactless 3D sensing. Both the procedure's immobilization mask and the determination of doses based on volume calculations can be made more precise than with traditional techniques (Kovacs et al., 2007; Rigotti et al., 1998). Repositioning of the radiation sources or measurement of swelling can also be performed with these techniques (Dunn et al., 1989).

A relatively new issue which is due to the advances in 3D imaging is catching the attention of radiotherapists and surgeons alike: the possibility of using image fusion between several different techniques, already with good results with Computed Tomography (CT) and Positron Emission Tomography (PET). Even though image fusion currently applies mainly in diagnostics, the increasing availability of intra-operative 3D imaging supports image fusion in the operating room.applications (Ritter et al., 2007).

In general surgery procedures, 3D contactless sensing can be used to assist the surgeon in real time intra-operative navigation. Usually done with X-Ray sources, in case precise image registration and fusion techniques become available, reposition-

ing pre-surgery volume information based on external optical imaging should soon become a reality.

Orthodontics corrections to dental and facial irregularities are currently planned in advance by the maxillofacial surgeon, so they respect the patients jaw and mouth harmony. A scan is made prior to the intervention which can thus be foreseen in 3D. Digitalization of dental records for subject identification or population study is another application where the use of 3D scans had a dramatic impact.

Figure 1.21 - Dentistry model scanned with temporal phase unwrapping with calculated 3D mesh - LOME.

The development of personalized implants in areas as distinct as Orthopaedics or Otolaryngology, also benefits from advanced 3D scanning technologies to improve on designs and reduce patient discomfort.

1.5 Dissertation plan

This dissertation doesn't exactly correspond to the formal description of one thesis, a hypothesis established at an early stage followed by the experimental work which either proves that thesis or dismisses it completely. Having brewed out of the several difficulties in implementing different three-dimensional surface acquisition methods with structured light fields, it essentially describes these implementations, and the difficulties experienced thereof. Three of these instigated research into novel techniques, which were conducted with success and presented in Appendix E, even

though they are briefly mentioned in Chapters 3 and 4, where the bulk of the acquisition methods implementation is covered.

Chapter 2 is an attempt at describing the current situation of the optical metrology arena. It covers both passive and active imaging techniques in as much as a thesis dissertation allows, although an attempt has been made at reporting the most important and promising methods available at the moment.

Chapter 3 covers the phase methods in greater detail, because these were the methods implemented in this work.

Chapter 4 focuses on the calibration issues behind active image processing three-dimensional surface acquisition, with an accent on phase methods. The acquisition method's result being a phase map, the calibration consists on translating phase into height on the object surface. As such there's no need to explicitly calibrate the video projector. Planar camera calibration is also covered, as it generates the information necessary to the subsequent phase-to-height calibration.

Chapter 5 describes a few applications of the implemented 3D surface acquisition methods, which were also performed at LOME.

Chapter 6 summarizes the present endeavour and suggests some paths to future work in this area.

Apart from the publications, presented in Appendix E, there are four further appendices. Appendix A contains an extensive description of the *Inspect* interface, the computing platform built during this work. Appendix B describes the Coherent Fringe Projector, another project which stemmed from this work. This is a video projector which uses coherent lighting, and is used with a narrow band-pass filter in front of the CCD, to enable fringe pattern acquisition in broad day light. Appendix C contains a complete description of the gradient and Hessian for non-linear intrinsic camera calibration optimization. Finally, Appendix D contains the complete set of numerical results from the two studies, partially presented in § 5.2.

This page intentionally left blank.

Chapter 2

Optical metrology - current state of affairs

Optical metrology has rapidly grown into an unavoidable discipline in most engineering domains. The hallucinating speed of technological development in our days keeps fuelling the advances in optical metrology, as most of them present ever more demanding metrological requirements that only this ubiquitous discipline can provide.

As such, an attempt at describing all the currently available techniques would constitute a formidable task, one well beyond the scope of this manuscript. Instead, only a few of the most prominent will be mentioned next, based on review articles by Blais (Blais, 2004), Chen (Chen et al., 2000) and Dorrío (Dorrío and Fernández, 1999). These are the optical methods on the taxonomy presented in § 1.2. Tiziani published an excellent detailed account of several of these methods (Tiziani, 1997).

2.1 Passive image techniques

The denomination *passive sensing* refers to the measurement of radiation already present in the object being measured, in contrast with *active sensing*, which implies some sort of interaction between the measuring apparatus and the scene, usually in the form of light or energy projection.

Passive image sensing techniques are based on the exploitation of visual cues for depth perception such as accommodation, convergence, binocular disparity or motion parallax, the result of changing positions of an object in space due to either the motion of the object, or of the viewer's. As such, most passive sensing algorithms have been developed to measure shape from texture, shading, focus, parallax, long-range motion, reflection, shadows, symmetry, inter-reflection or polarization. Apart

from photogrammetry, the most prominent approaches to passive 3D photography are Structure from Motion, Shape from Shading, and Photometric Stereo.

Photogrammetry

Photogrammetry, already mentioned in the introduction, dominated the 3D range sensing panorama for most of the 20th century, until both other passive sensing techniques and active sensing were developed, and still is one of the chief range sensing techniques of our days. Most civil and structural engineering activities depend on photogrammetric methods, as it can still be considered one of the most flexible and reliable ranging methods available.

Photogrammetry is the technique of measuring 2D or 3D objects from photograms. These may be either common photographs or electronic images taken with digital cameras and stored in computers. It can be divided in Far-Range Photogrammetry, when the camera lens is set to infinity, as in most of the aerial photogrammetry, or Close-Range Photogrammetry, if it set at a finite distance. Most of the terrestrial photogrammetry is Close-Range. Aerial photogrammetry is mainly used to produce topographical or thematic maps and digital terrain models. Among the users of close-range photogrammetry are architects and civil engineers, to supervise buildings, document their current state, deformations or damages, but it has also been used in archaeology, surgery and forensic projects, amongst others.

The camera model is a central issue in Photogrammetry, as it is this model that establishes the relation between the images and the real world coordinates. The simplest of all models is called the Pinhole model, because it models the simplest of all image forming systems – a pinhole. It is free from image distortion corrections and it models a rigid body transformation followed by a perspective transformation.

Image coordinates within this model can be expressed simply as,

$$\begin{bmatrix} u \\ v \end{bmatrix} = \begin{bmatrix} f\frac{r_{11}(X-X_0)+r_{12}(Y-Y_0)+r_{13}(Z-Z_0)}{r_{31}(X-X_0)+r_{32}(Y-Y_0)+r_{33}(Z-Z_0)} \\ f\frac{r_{21}(X-X_0)+r_{22}(Y-Y_0)+r_{23}(Z-Z_0)}{r_{31}(X-X_0)+r_{32}(Y-Y_0)+r_{33}(Z-Z_0)} \end{bmatrix} \tag{2.1}$$

Most geometric camera models are extensions of this simple model. The Linear Camera Model, also known as Direct Linear Transformation (DLT), extends the pinhole model with a shift of the image coordinate system and a linear distortion in the image plane, which accounts for the aspect ratio and for the eventual skew or lack of orthogonality between the image axes. There is a minimum of eleven variables with this model: six account for the extrinsic or positional parameters, of which there are three translational and three rotational, and five account for the camera intrinsic parameters, focal or principal distance, uncertainty scale factor for xx, origin of image

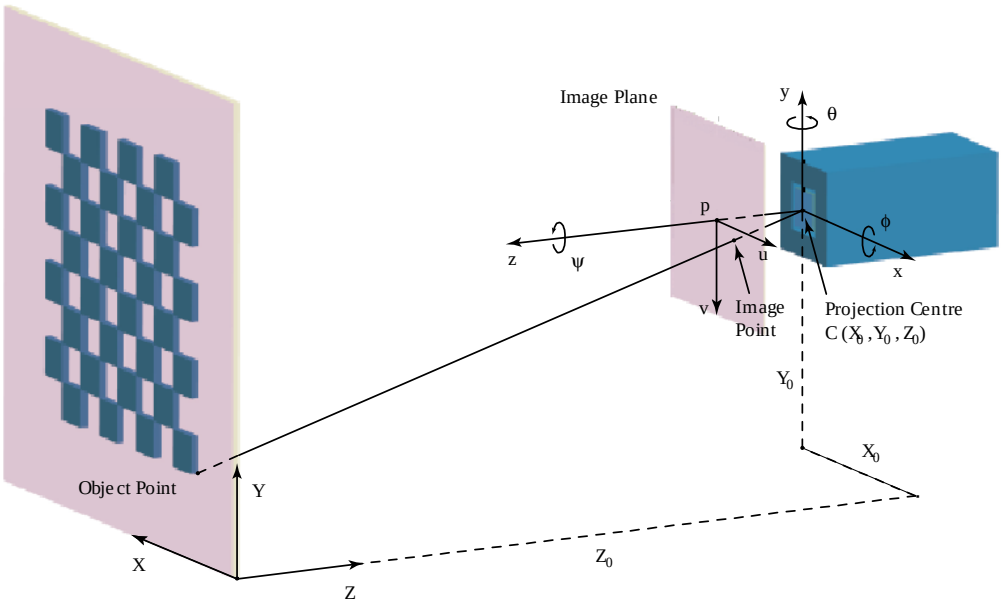

Figure 2.1 - Coordinate systems in projective geometry.

plane and one to five variables for lens distortion, thus modelled in different ways. Two variables for radial and two for tangential distortion are commonplace, yielding the following correction to image coordinates,

$$\begin{bmatrix} i \\ j \end{bmatrix} = \begin{bmatrix} i_0 + \frac{s_u}{d_u} u_d = i_0 + \frac{s_u}{d_u} \left(u - \delta_u^{(r)} - \delta_u^{(t)} \right) \\ j_0 + \frac{1}{d_v} v_d = j_0 + \frac{1}{d_v} \left(v - \delta_v^{(r)} - \delta_v^{(t)} \right) \end{bmatrix} \tag{2.2}$$

where,

$$\begin{aligned} \delta_u^{(r)} &= u_d \left(k_1 r^2 + k_2 r^4 + ... \right); \qquad \delta_v^{(r)} = v_d \left(k_1 r^2 + k_2 r^4 + ... \right); \\ \delta_u^{(t)} &= 2 t_1 u_d v_d + t_2 \left(r^2 + 2 u_d^2 \right); \qquad \delta_v^{(t)} = t_1 \left(r^2 + 2 v_d^2 \right) + 2 t_2 u_d v_d \end{aligned} \tag{2.3}$$

with

$$r = \sqrt{u_d^2 + v_d^2} \tag{2.4}$$

represent the radial and tangential corrections to the optics. This issue will resurface in Chapter 4.

The availability of this knowledge conditions the choice of photographic device as follows:

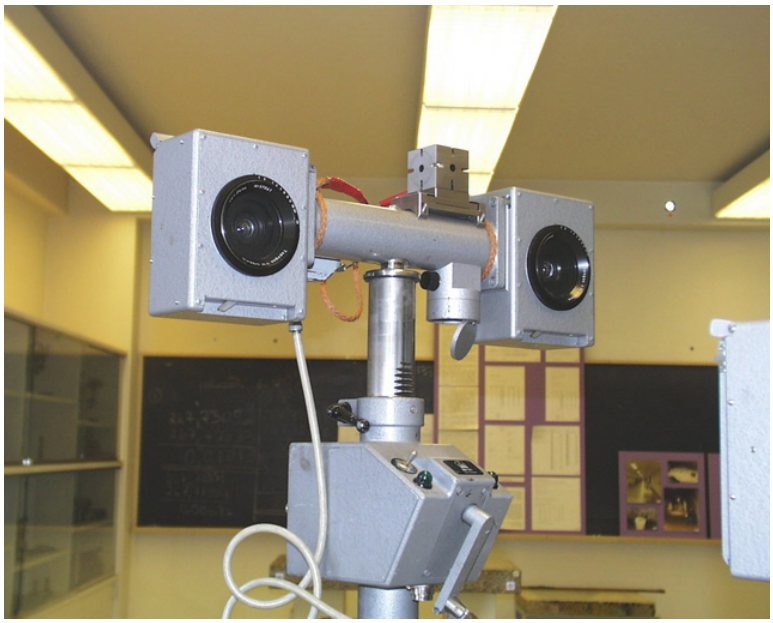

Figure 2.2 - The Stereometric camera from Zeiss.

Metric cameras have stable and precisely known internal geometries and very low lens distortions, and are therefore very expensive devices. The principal distance is constant, which means, that the lens cannot be sharpened when taking photographs. As a result, metric cameras are only usable within a limited range of distances towards the object. The image coordinate system is defined by four fiducial marks mounted on the frame of the camera. Terrestrial cameras can be combined with tripods and theodolites. Aerial metric cameras are built into aeroplanes mostly looking straight downwards. Presently, most of them have an image format of 23 by 23 centimetres.

Stereometric cameras are a practical way of producing stereopairs, already mentioned in the text. Another simple way is to photograph the object from two different positions. The line between the two projection centres is called "base". If both photographs have viewing directions parallel to each other and at a right angle to the base, the "normal case", they have similar properties to the two images of our retinas. The overlapping area of the stereopair, can be seen in 3D, simulating man's stereoscopic vision.

A stereometric camera consists of two metric cameras mounted at both ends of a bar, which has a precisely measured length. Zeiss and Wild cameras, shown in Fig. 2.2, use base lengths of 40 or 120 cm. This bar has the same role as the base line.

Amateur cameras The photogrammetrist speaks of an "amateur" camera, when the internal geometry is not stable and known, as is the case with most commercially available cameras. Photographing a test field with many control points at a repeatedly fixed distance setting, such as infinity, can yield a calibration of the camera. In this case, the four corners of the camera frame function as fiducial marks. However, the precision will never reach that of metric cameras.

There are also several photogrammetric techniques available, which depend on the available camera type and the required result, such as 2D or 3D and the pretended accuracy.

Mapping from a single photograph Only useful for plane 2D objects. Obliquely photographed plane objects show perspective deformations which have to be rectified. There is a broad range of techniques for rectification which can be done numerically, optically or digitally.

Stereophotogrammetry As the term implies, the technique builds on stereopairs. These can be produced using stereometric cameras. If only a single camera is available, two photographs can be made from different positions, to match the conditions of the "normal case". Vertical aerial photographs come mostly close to this situation. They are made using special metric cameras built into the airplane and looking straight downwards. While taking the photographs, the airplane flies over a certain area with a trajectory so that the whole area is covered by overlapping photographs. The overlapping part of each stereopair can be viewed in 3D and consequently mapped in 3D using analogue, analytical or digital techniques, as mentioned in the introduction.

Mapping from several photographs This kind of restitution, which can be done in 3D, has only become possible with the advent of analytical and digital photogrammetry. Here, two or more photographs are used. 3D objects are photographed from several positions around the object, where any object-point should be visible in more than two photographs. The photographs can be taken with different cameras, even amateur cameras, and at different times, if the object doesn't move. The 3D coordinates of each point on the object are reconstructed by intersection of the coordinates determined from each photograph.

Structure from Motion

Structure from Motion is the recovery of scene geometry from the motion of points in the image plane of a moving camera, rather than acquiring multiple images. In a way, the precise information about the camera motion compensates the loss of more images. A central problem to the structure from motion methods is the election and tracking of image features, a problem extensively studied by Kanade, Lucas and Tomasi, who ultimately developed the well known KLT feature tracker (Lucas and Kanade, 1981). Shi and Tomasi further developed a method for feature selection adapted to the tracker characteristics (Shi and Tomasi, 1994).

Shape from Shading

Shape from Shading is the problem of detecting a point's position based solely on its intensity and on the illumination direction, through Lambert's law. It is a typical ill-posed problem, i.e., with no solution or a multitude of solutions, and relies on further information, such as similarity of surface reflectance and orientation at nearby points. An extensive work has been published by Berthold Horn on the subject (Horn, 1970).

Photometric Stereo

Photometric Stereo tries to relieve the ill-posing of the Shape from Shading problem with the acquisition of two or more images of the object under different illumination conditions (Woodham, 1980). Each image provides one constraint on the normal, and therefore two images are sufficient to recover the normal up to a small number of possible solutions, and three images yield a unique solution for each image pixel.

Typical accuracy of high resolution photogrammetry systems is better than 10 ppm or $1 : 100,000$, i.e., 0.050 mm on a 5.0 m object, and the most recent advances in network design, wherefore several cameras are used simultaneously and self- calibrated with bundle adjustment, have enabled accuracies of one part in a million (Fraser, 1992). Target projection, instead of manual placement on the object under evaluation, is a recent addition to the technique which has thus somehow entered the domain of active image processing.

2.2 Active image techniques

Single point and laser scanners

Point laser triangulation is a very pervasive method, suitable for industrial applications in that it offers a simple and robust 3D measurement. These systems determine

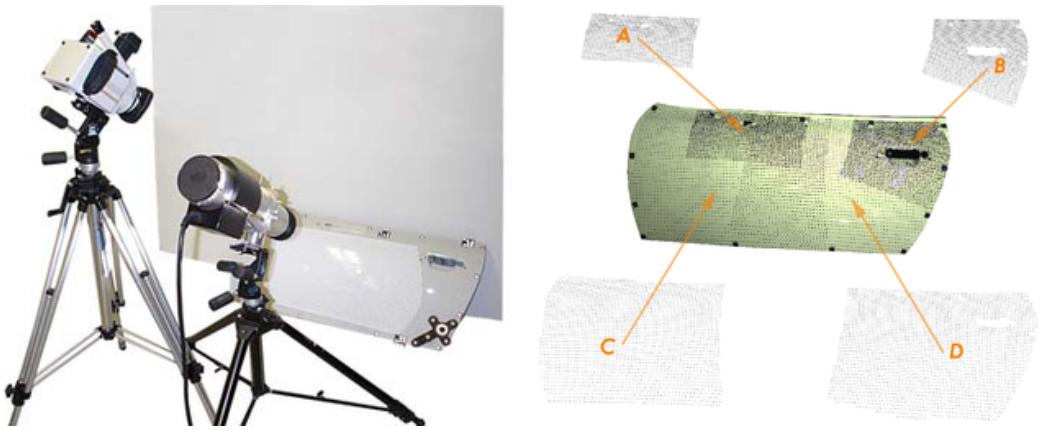

Figure 2.3 - Large scale optics metrology with dot projection. Courtesy, Geodetic Systems.

distance by projecting light from a source onto an object and imaging the resulting illumination pattern onto a detector. Knowing the position of the image on the detector, the lateral separation between the detector lens and the light source, and the projection angle of the source, enables determination of the distance to the object. Sequential measurements at different coordinates lead to a full 3D image of the object surface.

The conventional light triangulation systems cannot simultaneously achieve a large depth measuring range and high horizontal resolution. This is so because the conventional optical lenses that are incorporated in these systems cannot, at the same time, provide both long focal depth and high lateral resolution. Specifically, a high lateral resolution requires high numerical apertures, whereas a large depth of focus requires low numerical apertures (Smith, 2000). Even so, accuracies between 25 and 200 μm for ranges of 40 – 650 mm are attainable with present day technologies. These figures will drop to tenths of a mm when much larger 25 m ranges are required (Blais, 2004).

Slit scanners

Also known as light line or laser stripe projectors, these instruments are a natural extension of the single point detectors. Instead of a multitude of single point detectors or expensive mechanical scanners such as galvanometers, they project a laser line onto the object which is imaged at an angle. The deformation of the profile is a direct function of range. These are by far the most popular triangulation based 3D scanners, partly because of its simplicity and low cost. Their main inconveniences are the tight

compromise between field of view and depth resolution and the relatively poor immunity to ambient light. A field of view above 20 to 30 degrees can only be obtained by expensive anamorphic optical designs (Blais, 2004). Accuracy spans 20 – 300 μm for acquisition ranges of 100 – 600 mm.

Time-of-Flight

As the name implies, Time-of-Flight (TOF) calculates range by determining the amount of time taken by light to travel to the object and back. The measurement is performed by calculating the time difference between the reflection of a pulse of light from the object back to the sensor and a reference pulse passed through an optical fibre directly into the sensor. Typical resolution for this method is around one millimetre, but with sub-picosecond pulses and high resolution electronics, sub-millimetre resolutions have been demonstrated.

This is undoubtedly the preferred method for large structures and long ranges, because range accuracy is relatively constant for the entire volume of measurement, which can range from 5 centimetres to tens of metres. This observation can easily be inferred from the fact that the delay between the outgoing and the incoming signal is given by

$$\tau = \frac{2z}{c} \tag{2.5}$$

where c is the travel speed of the signal and z is the covered distance during time τ. This in turn implies that the measurement accuracy, σ_z, can be approximated by,

$$\sigma_z = \frac{c}{2}\sigma_\tau \tag{2.6}$$

which depends on the delay accuracy, σ_τ, alone.

Different methods have been proposed through the years (Wang, 1987) such as pulse, described above, amplitude modulation (AM), frequency modulation (FM), hybrid detection, self-mixing diodes and single photon counting. Pulse TOF detection is usually done with an avalanche photo-diode. To achieve picosecond resolution, very sensitive high bandwidth electronics, constant group delays and excellent thermal stability have to be employed. In order to reduce noise, multiple pulses are averaged and resolutions of 0.5 to 1 cm are common. With amplitude modulation, range is measured from the phase difference between reference and received pulses, and resolution increases to 3 to 5 mm. In case frequency modulation is used instead, sub-millimetre resolutions are standard of today's equipments, and time correlated single photon counting (Massa et al., 1998; Wallace et al., 2001) reportedly shown a resolution of 15 μm at 1 m ranges.

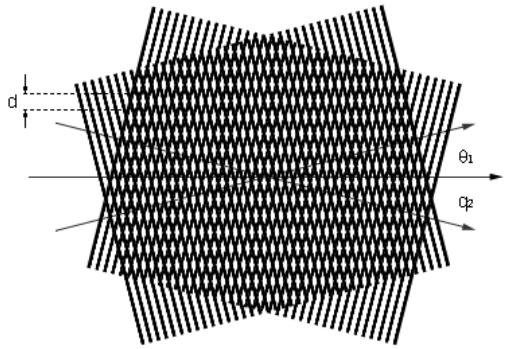

Figure 2.4 - Interference of two plane waves.

Moiré methods

Moiré methods, already mentioned above, map height contours as beats of two gratings, one of which is either attached or projected onto the surface under observation. This is in essence an interferometric method, where the reference grating demodulates the observed amplitude modulated light from the projected or attached grating and creates interference fringes whose phase is proportional to height. Moiré is extensively used in Optics teaching because the gratings can be thought of as instantaneous pictures of interfering plane or spherical waves, the fundamental mathematics being the same.

Where the two waves are in phase, bright fringes result which represent constructive interference and where they are out of phase, dark, destructive interference, fringes are obtained (Creath and Wyant, 1992). This technique is most useful with objects having large flat surfaces and small depth variations, having been extensively used in human body deformation measurements (Takasaki, 1973). The major inconvenience of this method is the use of fixed frequency gratings, although a technique, denominated Logical Moiré, has been introduced by Asundi (Asundi, 1993) using just the projection grating and combining it with a computer generated reference grating

with logic AND and XOR operations to generate multiplicative Moiré patterns.

Very high 100 *nm* accuracy systems for wafer mask alignment (Bouwhuis and Wittekoek, 1979; Liu et al., 1995) and strain field determination in semiconductors (Androussi et al., 2002) have been described. Range varies according to the application, given the Moiré effect can be found in a myriad of applications from microscopy to whole-body system scanners or even larger targets. Applications for large structures are possible, however awkward they may be, due to the technical challenges found in producing large gratings.

Pattern or Structured Light Projection

There are two major classes of pattern projection methods: those which are a natural extension to Projection Moiré, commonly known as Phase Measurement Profilometry methods (PMP), and the Coded Structured Light pattern projection technique. There are also a few proposals to use both methods for completion on a hybrid instrument (Sansoni et al., 1999) where each method would be used according to the given situation, for increased flexibility. PMP has been successfully applied with several methods, other than the fringe projection just mentioned, and will thus be described on a section of its own.

Coded Structured Light

This approach consists of projecting digitally coded light patterns onto the surface under observation (Posdamer and Altschuler, 1982). Since each point in the pattern is encoded in a certain way that uniquely identifies its coordinates, the correspondence problem is solved in a direct way. There are numerous codes available (Pagès et al., 2003) and several different techniques were developed over the years. Time-Multiplexing, also called temporal codification, with a Gray code is the most employed technique. A sequence of Gray coded binary fringe patterns is projected on the object. This divides the object into a number of $2n$ sections, where n is the number of pattern sequences, e.g. 128 sections for $n = 7$. Thus, each pixel is associated with a codeword, which is the sequence of 0's and 1's obtained from the n projected patterns. This codeword establishes the correspondences relating the image pixels with the projector stripe numbers. The object space point coordinates are calculated using the spatial intersection, provided system calibration is known. Resolutions around 400 μm for ranges of 500 x 500 mm and 300 mm depths have been reported. The sequential encoding technique implies a static or quasi-static object, or otherwise the unique encoding at each pixel will be lost. An alternative method codes the bits of information into a small spatial neighbourhood, so that each point in the scene has a

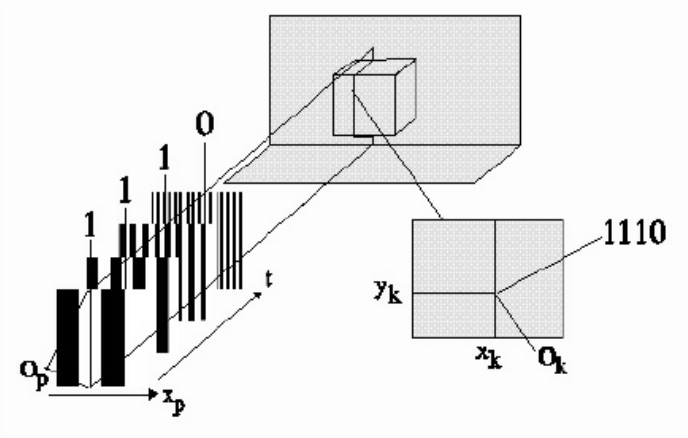

Figure 2.5 - The coded lighting principle.

unique coded pattern projected onto it. Since the pattern is static, fast moving objects can be measured. Still, detection of the correct code requires an assumption of surface continuity in a small neighbourhood around each pattern. If an object edge or depth discontinuity breaks the pattern, range cannot be sensed. This problem seems to have been solved by the introduction of a new method by Young (Young et al., 2007) with additional cameras, each replacing one pattern from the sequence.

2.3 Phase Measurement Profilometry

There are several Phase Measurement Profilometry methods. To gain an insight into the different characteristics of each, Dorrío and Fernández (Dorrío and Fernández, 1999) have elected to separate them into methods *with* or *without* a spatial carrier. The importance of this classification goes to the clear limitations of each class. While methods with a spatial carrier need just a single fringe pattern to perform phase evaluation, and are thus indicated for dynamic situations, they are limited in phase range, or better still, phase gradient range, mainly due to aliasing effects. Methods without a spatial carrier can be very accurate, but cannot cope with dynamic events. The techniques described herein are merely the most prominent, and by no means represent a thorough listing.

Methods with a spatial carrier

The most important amongst these methods are the *FourierTransformfringeanalysis*, the *Spatial Carrier Phase-Shifting* and the *Spatial Synchronous Detection* methods.

Fourier Transform Profilometry

The Fourier transform fringe analysis method is unquestionably one of the most successful techniques of fringe pattern analysis. First introduced by Takeda in 1982 (Takeda et al., 1982), the technique was adapted to two-dimensions by Macy in 1983 (Macy, 1983), although that was essentially a one dimensional extension of the original work by Takeda. Bone provided a full 2D version in 1986, along with a set of very interesting observations regarding the inherent errors of the technique and some suggestions as to how these could be overcome (Bone et al., 1986). A clever suggestion for separation of the information in reciprocal space was also advanced therein. An extensive study on the error sources of the technique has been made by Kujawinska (Kujawinska, 1993; Kujawinska and Wojciak, 1991). Many other works have been published on this method throughout the years, as it remains one of the most elegant and effective methods for shape measurement, including several important contributions for error reduction (Kreis, 1986; Mertz, 1983; Roddier and Roddier, 1987; Takeda and Mutoh, 1983). Another important reason for the plethora of publications is the fact the technique depends on one frame only, contrary to the sequential phase shift methods that need three frames at the very least. This makes it one of the few phase analysis methods capable of dealing with dynamic situations where the target object moves, and taking sequential frames becomes prohibitive. Tavares et al. have recently published FTP results with coherent lighting on object crashing at 3000 frames/s (Tavares et al., 2007).The relevant publication can be found in Appendix E.

The technique can be simply described as follows: a sinusoidal fringe pattern with a known spatial frequency is projected onto the object under test and a two dimensional Fourier Transform of the resulting image is calculated. The spectrum that results from this deformed fringe pattern has two sharp peaks centred at the carrier fringe frequency. In order to remove this carrier and thus obtain an expression for the phase variation, which is a function of the object profile at each image point, a certain amount of frequencies surrounding the carrier are low-pass filtered with a suitable window and this window is moved to the centre of the spectrum. An inverse Fourier transform of the selected frequencies is calculated, which holds the phase information that can finally be calculated as the logarithm of a simple inverse tangent calculation.

Simple as it may be, the method is plagued with several error sources and over

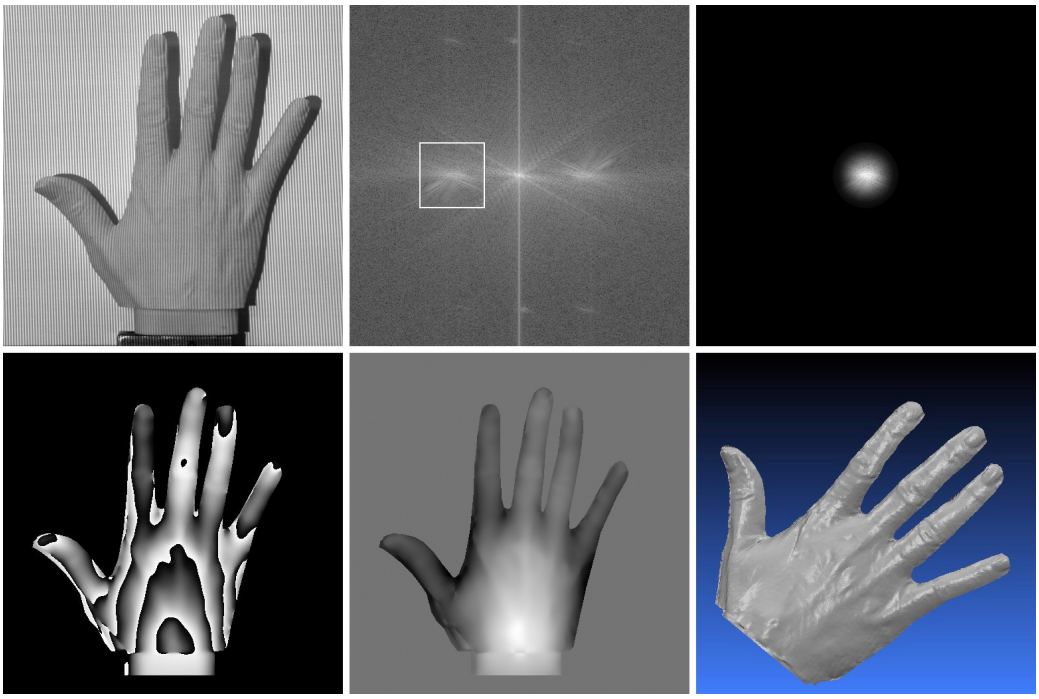

Figure 2.6 - Fourier Transform Fringe Analysis.

the years many contributing efforts have been made to improve its efficacy. A thorough study of the problems and refinement proposals for high accuracy measurements was proposed by Kujawinska, who demonstrated the possibility of attaining $\lambda/100$ accuracy (Kujawinska and Wojciak, 1991).

Spatial Carrier Phase-Shifting Method

Spatial Carrier Phase-Shifting stands amongst the few phase-shift methods that retrieve phase from a single carrier fringe pattern at a low computational cost (Williams et al., 1991). This is an ingenious method wherefore the carrier frequency is specified so that phase can be retrieved from adjacent pixels in the pattern. If the projected frequency is such that a fringe occupies 4 pixels, there will be a $\pi/2$ variation between adjacent pixels. This in turn implies obtaining 64 fringes on a 256 pixel wide image or 128 fringes on a 512 pixel image. For any five consecutive pixels, phase on the central pixel will be calculated from the inverse tangent of an arithmetic function of the intensity at these pixels. Williams suggested other pixel configurations to deal with phase variations along arbitrary directions. This technique was used by Poon and Kujawinska (Poon et al., 1993) on a four beam optical arrangement Moiré setup proposed by Post, for accurate, whole field, strain measurements (Post, 1987). Phase

calculation with this method entails working at or above the Nyquist limit, resulting in a rather noisy process as can be seen on the 3D result in Fig. 2.7. A noise suppression procedure was recently introduced by Kemao which uses a low pass filter through image convolution and can reduce as much as half the noise level (Kemao et al., 2003).

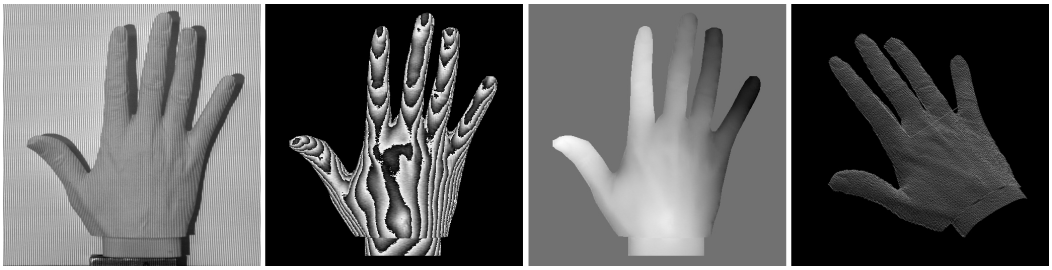

Figure 2.7 - Spatial Carrier Phase-Shift analysis.

Spatial Synchronous Detection

This is a technique similar to Synchronous Detection, described below. The difference lies on the introduction of a spatial carrier into the fringe pattern, multiplying it by sine and cosine functions of a similar frequency. This generates slowly varying beats with amplitudes proportional to the sine and cosine of the fringe pattern phase, upon passing the signals through a low pass filter. Phase determination is done with the usual inverse tangent calculation. The method is prone to errors in case a large phase variation occurs, because the complete separation of the spectral components may become impossible (Womack, 1984).

Methods without a spatial carrier

This class of techniques is relieved from the necessity of employing a carrier frequency, but in turn has to rely on the detection of intensity differences that result from the introduction of phase shifts in object illumination (Creath, 1988). There are numerous techniques for shifting phase, such as moving the reference mirror on a Twyman-Green interferometer, tilting a glass plate on one of the interferometer beams or shifting one of the beams frequency by a number of different manners (Creath, 1993). As to phase determination, Creath separates *electronic real-time systems* such as zero-crossing detection, phase-locked and up-down counters, which monitor the intensity data as the phase is being modulated, from *analytic detectors* which record the data and calculate the phase afterwards. Although the advances in computing

power brought about several innovations in analytical phase detection techniques in the last two decades, it is no less true that, contrary to the electronic ones, these are not real-time, apart from the Fourier method described above. On the other hand, analytical techniques stand as the most reliable, easy to implement and accurate phase measurement interferometric methods.

The phase is either shifted in steps between intensity acquisitions, a method known as *Phase-Stepping*, or continuously, as intensity is being integrated – *Integrated Bucket Phase Shifting*. The recorded intensity data can be described by

$$I = I_0 \left[1 + \gamma \cos\left(\alpha + \phi\right)\right] \tag{2.7}$$

where I_0 is the average background or dc intensity, γ is the fringe visibility, ϕ is the controlled phase shift and α is the sought phase variation which characterizes the object surface, there being three unknown quantities in this equation. As such, the number of necessary intensity measurements varies, from a minimum of three to five or even more, depending on the chosen phase-shifting algorithm. The phase increment is usually specified but it can also be unknown (Carré, 1966) as long as it is maintained constant during the entire measurement. An excellent systematic account of the available phase shifting algorithms is available in the article by Dorrío (Dorrío and Fernández, 1999).

Phase measurement can also be classified according to whether the phase is acquired sequentially or simultaneously, the former methods being known as *Temporal Phase-Shifting* and the latter as *Spatial Phase-Shifting*.

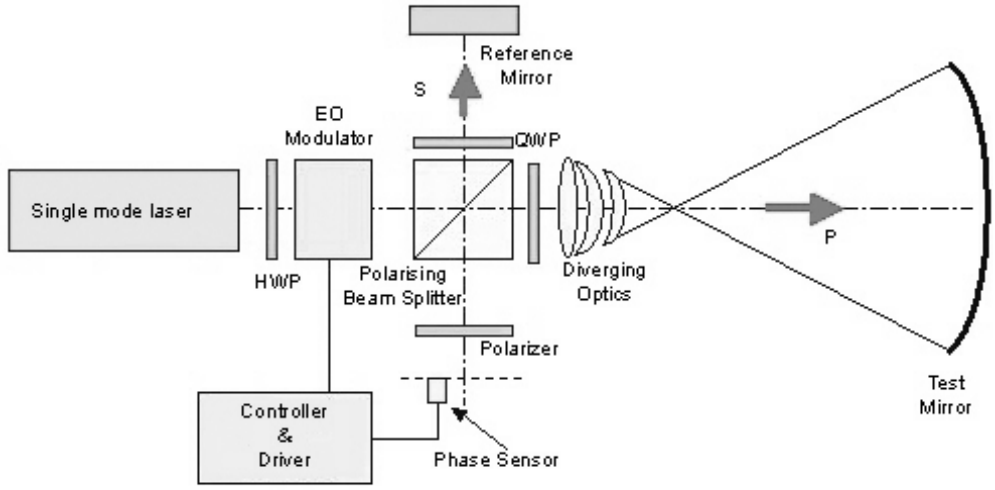

Figure 2.8 - Closed-Loop feedback vibration compensation.

Temporal Phase-Shifting

Temporal Phase-Shifting is the sequential approach to phase-shifting just described (Creath, 1993; Greivenkamp and Bruning, 1992). The technique cannot cope with dynamic situations for obvious reasons but even with static situations, air vibrations or temperature drifts seriously impair overall accuracy, as phase shifts between exposures become different than desired. In controlled environments though, it is still one of the preferred methods for its accuracy and resolution. A number of significant improvements to reduce vibration sensitivity using common-path interferometers and active vibration sensing have also been proposed (North-Morris et al., 2002; Wyant, 2003), such as the one depicted in Fig 2.8.

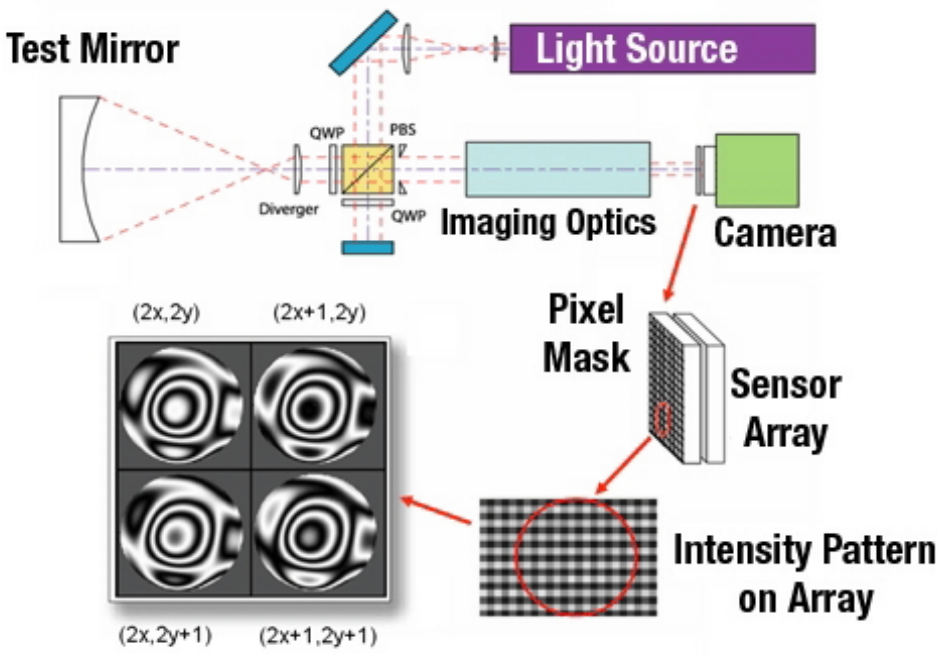

Figure 2.9 - Single shot spatial phase shifter. Courtesy, 4D Technology.

Spatial Phase-Shifting

This method was conceived to circumvent the problems related to the acquisition of sequential patterns at different times of the Temporal Phase-Shifting method, while conserving some of its advantages (Kujawinska, 1993). Central to this technique is the simultaneous acquisition of three or more phase-shifted patterns with different cameras. This is made possible by the use of polarizing optics, such as retarding wave

plates and polarizing beam splitters, in order to impose phase shifts between the reference and the test beams and combining them on a polarizer before each camera. A recent alternative was published by Wyant wherefore an holographic optical element separates the patterns into four quadrants of the same image and a birefringent mask introduces phase shifts of 0, $\pi/2$, π and $3/2\pi$ to each quadrant, as illustrated in Fig. 2.9. The four phase-shifted interferograms are captured by a single camera, thus eliminating the errors inherent to the use of different cameras, such as can be posed by calibration or alignment (Wyant, 2003). A measurement result from an optics part can be seen in Fig. 2.10.

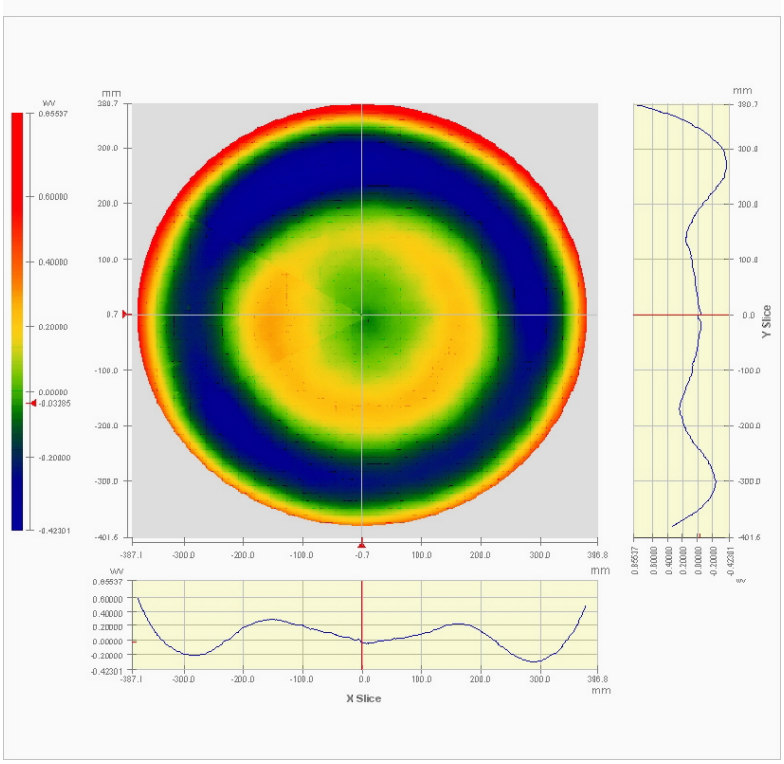

Figure 2.10 - Single shot phase shifter results. Courtesy, 4D Technology.

Synchronous detection

Synchronous detection is a well established communications theory technique for detection of noisy signals, which seems to first have been applied to phase detection by Bruning in 1974 for the measurement of lenses and other optical components to $\lambda/100$ accuracy (Bruning et al., 1974). Basically, it consists of correlating the signal with orthogonal sine and cosine signals of the same frequency and averaging the

result, phase being calculated from a simple inverse tangent calculation, as shown in Fig. 2.11. The averaging process eliminates the effects of turbulence and noise.

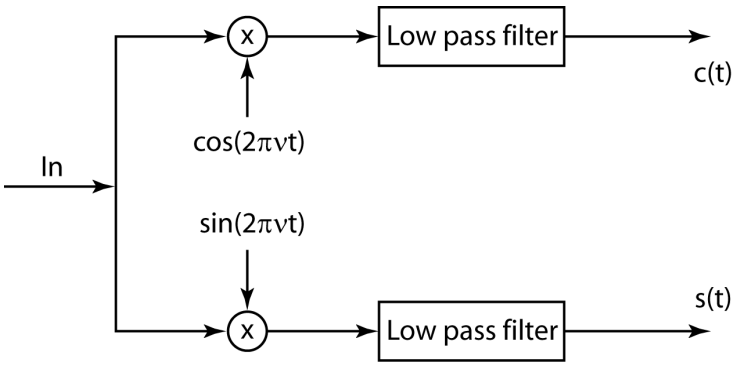

Figure 2.11 - Synchronous demodulation.

Sinusoidal phase modulation

This technique employs either the modulation of the lighting source diode laser injection current or the vibration of the optical setup with piezoelectric transducers in order to achieve phase modulation. The modulation of a laser diode is a simple and effective procedure. The injection current of the laser diode has a dc bias component which determines the central wavelength and a modulation component which changes the wavelength sinusoidally. In a Twyman-Green interferometer configuration, the interference signal reaching the photo-detector is therefore sinusoidal and has a phase component proportional to the object arm dislocation. Phase can then be determined either through a Fourier transform method or through phase-shifting. Ranges of over $\lambda/2$ with very high accuracies on a synchronous detection setup with laser diode modulation efficiencies of $6.0 \times 10^{-3}\ nm/mA$ have been reported with this technique (Suzuki et al., 1993).

Phase-Lock Interferometry

Phase-Lock, or ac Interferometry as it is also known (Servin and Rodriguez-Vera, 1993), uses the phase-locked loop (PLL) principle from communications engineering, benefiting from all the results available from this electronics mature area. A first order PLL works as depicted in Fig. 2.12.

Basically, phase changes to the input signal are followed by monitoring the necessary changes to the signal applied to a voltage controlled oscillator (VCO), so the

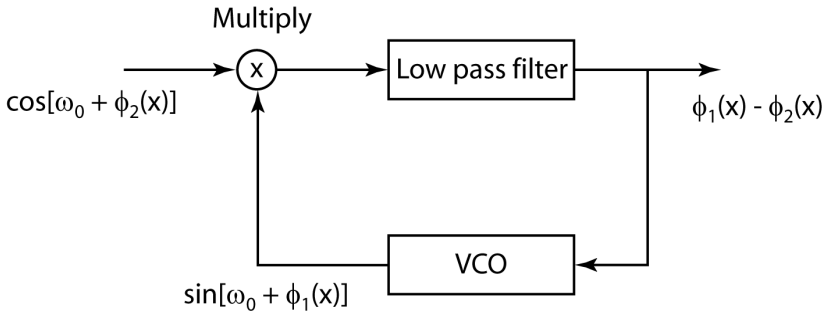

Figure 2.12 - Basic phase-locked loop block scheme.

phase error at the output of the low pass filter vanishes. The correlation signal , p, at the output of the multiplier is,

$$\begin{aligned} p(x) &= 2\cos[\omega_0 + \phi_2(x)]\sin[\omega_0 + \phi_1(x)] \\ &= \sin[2\omega_0 + \phi_1(x) + \phi_2(x)] + \sin[\phi_1(x) - \phi_2(x)] \end{aligned} \tag{2.8}$$

which, after low pass filtering, conserves just the last term. When the PLL operates in lock, this phase difference is sufficiently small to be approximately equal to the signal itself,

$$p_f(x) = \phi_1(x) - \phi_2(x) \tag{2.9}$$

A phase locked interferometer, shown in schematically in Fig. 2.13,.works under the very same principle.

The Twyman-Green interferometer phase is locked onto an initial phase for which object height is zero, changing the laser diode wavelength by controlling its injection current. Object height is proportional to this injection current. Resolutions on the nm scale for 200 μm ranges have been reported (Suzuki et al., 1989).

Heterodyne Interferometry

Heterodyne interferometry is indisputably one of the most flexible and accurate interferometric surface profile or displacement measurement techniques available today, there being current commercial systems available for the measurement of nm ranges with sub-Angstrom accuracy (Sizgoric and Gundjian, 1969; Sommargren, 1981) to 60 m ranges (Gordon and Dukes, 1970) or 100 mm ranges to 1 part in 10^8 accuracy (Jacobs and Shough, 1981). An elegant exposé of a full-field, real time measurement system

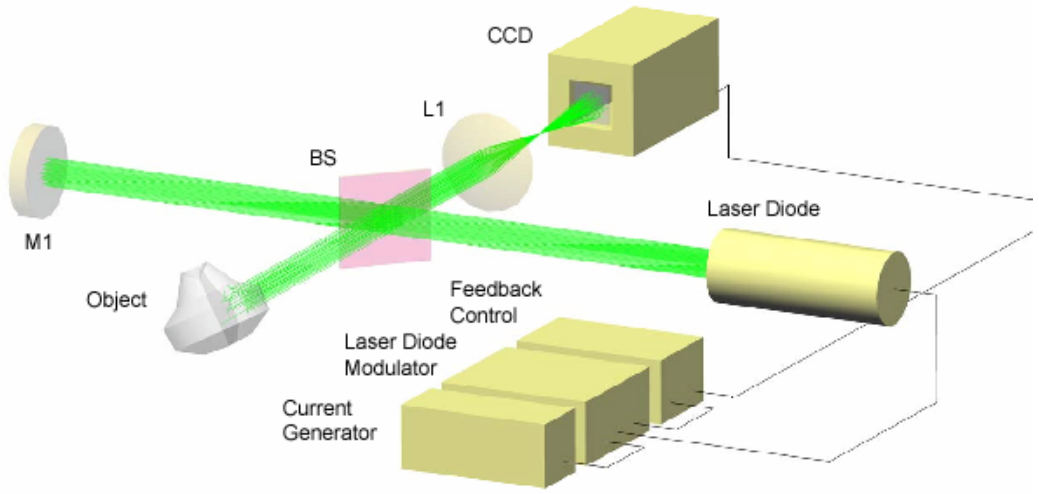

Figure 2.13 - Phase locked laser diode interferometer.

to $\lambda/100$ accuracy tested on 5 cm mirrors was made by Massie in 1979 (Massie et al., 1979). Remarkable 0.1 mm resolution for 100 m ranges have also been reported (Dalhoff et al., 1994) and a Super Heterodyne interferometer using two laser wavelengths and two heterodyning frequencies simultaneously was described by Tiziani with a striking 50 μm resolution for 100 m ranges (Tiziani, 1997).

Heterodyning, or better still Homodyning since two light beams of different frequencies are derived by a frequency offset process from a single, parent laser beam source in this case, is the use of frequency beats from these two very similar frequencies to determine the phase difference introduced by an object onto one of them, as illustrated in Fig. 2.14.

A beam of a single frequency ω_0 is split into two signals, one of which travels to the object surface and suffers a phase shift at each surface point. The other signal is frequency-shifted by a frequency ω_1. The two beams are recombined on a photodetector and produce a sinusoidal signal proportional to the square of the sum of the two signals given by

$$\begin{aligned} i &= \left\langle \{e_0 \cos(\omega_0 t) + e_1 \cos[(\omega_0 + \omega_1) t + \phi]\}^2 \right\rangle \\ &= \frac{e_0^2}{2} + \frac{e_1^2}{2} + e_0 e_1 \cos(\omega_1 t + \phi) \end{aligned} \tag{2.10}$$

where "<>" refers to averaging over one cycle. The third term, which results from

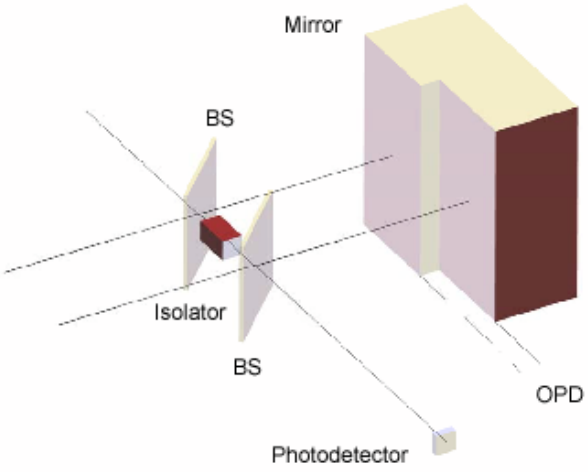

Figure 2.14 - The heterodyning principle.

mixing the electrical fields on a square-law detector, contains the desired phase difference, which is now carried on an electrical, much lower frequency, signal and that can be determined, e.g., on a zero-crossing detector, by comparison with a reference signal with ω_1 frequency from the frequency shifter. The quotient of the difference from the first two zero-crossings to the reference period is given by,

$$\left(\frac{2\pi OPD}{\lambda\omega_1}\right) / \left(\frac{2\pi}{\omega_1}\right) = \frac{OPD}{\lambda} \tag{2.11}$$

which is a direct measure of the surface profile. What's really worth noting in this technique is that a low frequency beat, $(\omega_0 + \omega_1) - \omega_0$ of some 10 kHz can be accurately detected with current electronics, so that obtaining a $\lambda/100$ accuracy is perfectly within reach.

2.4 Other important interferometric methods

A few of the leading optic and holographic interferometry methods are described here below. Though interferometric methods can serve a host of other applications, these very high resolution methods can also be used for three-dimensional sensing purposes.

Holographic Interferometry

Holography is the effective recording and reconstruction of the three-dimensional intensity and phase information of wavefronts scattered from an object surface. Originally discovered by Dennis Gabor in 1947, in an effort to improve the resolution of electron microscopy (Gabor, 1948), Holography had to wait nearly fifteen years before the work of Leith and Upatnieks, with some of the first lasers available at the time, brought it to daylight, by reconstructing the first high quality three-dimensional images ever with an off-axis reference beam technique that solved Gabor's twin-image in-line arrangement problem (Leith and Upatniek, 1962).

Holographic Interferometry, independently explored by Stetson and Powell (Stetson and Powell, 1965), Haines & Hildebrand (Haines and Hildebrand, 1965) as well as Brooks and Heflinger (Brooks et al., 1965) in 1965, is a technique that uses either the interference of the wavefront reconstructed from the hologram with a wavefront from the same object at a later time, or the interference of two wavefronts reconstructed from holograms which were recorded at two different times in the same media, a technique known as *double exposure*. The interference pattern thus obtained contains information about the deformation imposed to the surface at the two different times and can be used to calculate this deformation with a very high accuracy. As such, Holographic Interferometry is extensively used in non-destructive testing, strain and vibration analysis, and also in profile contouring (Vest, 1979).

Several methods for profile contouring, showing the intersection of an object surface with a set of equidistant planes perpendicular to the line of sight, have been described in the literature (Rastogi, 1994), the most popular techniques being the *wavelength difference,* the *immersion* and the *dual beam multiple-sources* methods.

Wavelength difference contouring

Wavelength difference contouring (Hildebrand and Haines, 1967), is based on the use of two slightly different wavelengths. The hologram is first recorded with one wavelength, λ_1, and the object and hologram are later illuminated with λ_2. As a consequence, the reconstructed image is shifted relative to the original object in both lateral and longitudinal directions. The lateral image shifting is eliminated by tilting the reference illumination wave by an angle such that,

$$\frac{\lambda_1}{\sin\theta_1} = \frac{\lambda_2}{\sin\theta_2} \tag{2.12}$$

whilst the longitudinal shift gives rise to a change in magnification which interferes with the original image and produces interference fringes corresponding to contours

of constant altitude. Contour sensitivity, i.e. height variation corresponding to one fringe is given by,

$$\Delta z = \frac{\lambda_1 \lambda_2}{(\lambda_1 - \lambda_2)\,(1 + \cos\theta)} \tag{2.13}$$

where θ is the illumination angle.

Immersion method

This is a technique whereby the hologram is recorded with the object immersed on a glass tank filled with a liquid of a n_1 refractive index. Hologram reconstruction is then made with a different, n_2 refractive index liquid (Zelenka and Varner, 1969). The contour sensitivity of this method is given by,

$$\Delta z = \frac{\lambda}{n_1 - n_2} \tag{2.14}$$

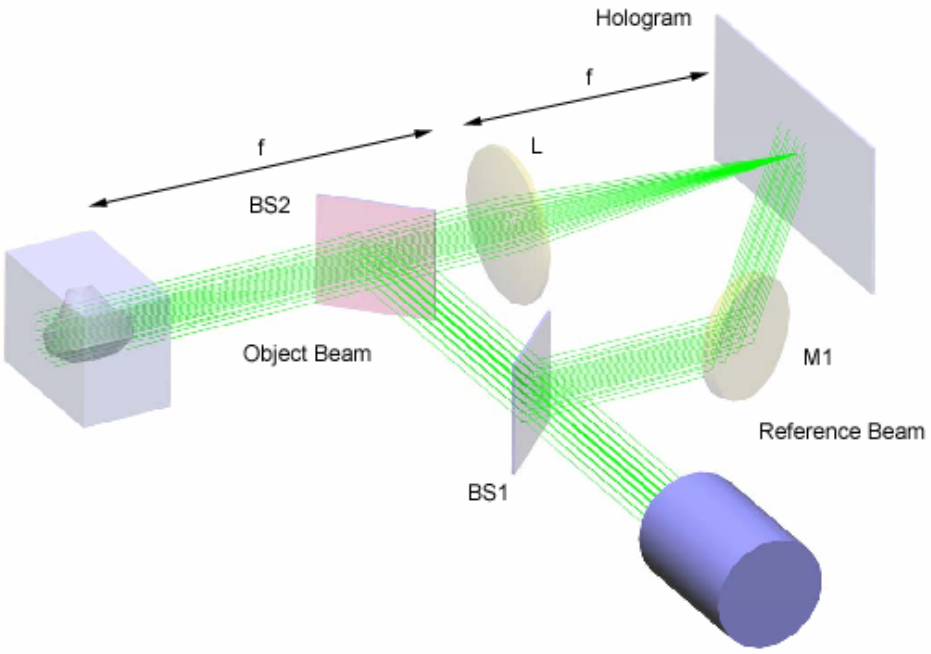

Figure 2.15 - The immersion method for holographic contouring.

Dual beam multiple-sources method

This method uses two equally inclined beams on both sides of the optical axis. The hologram is recorded and the beams are tilted the same amount, $\Delta\theta$, through an axis orthogonal to the plane containing the optical axis and the two illumination directions (Rastogi, 1997). A set of Moiré fringes can then be seen by looking through the hologram, whose incremental height interval is given by,

$$\Delta z = \frac{\lambda}{2 \sin\theta \sin\Delta\theta} \tag{2.15}$$

Speckle Interferometry

Once considered a nuisance by most every holography maker, due to the noisy pattern it bared, speckle was soon to be recognized as one of the most useful characteristics of coherent lighting. An entire field of study, known as Speckle Interferometry, has evolved over the years with such advances as Electronic Speckle Pattern Interferometry (ESPI) or Shearing Interferometry, which are notably two of the most important optical techniques in non-destructive testing and inspection today.

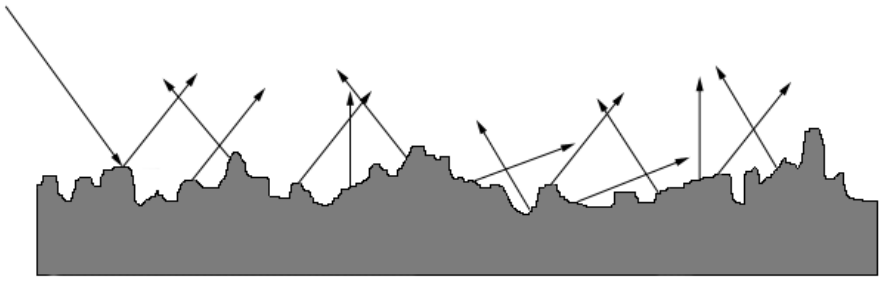

Figure 2.16 - Scattering by an irregular surface.

Speckle, is the random, granular like, spatial variation of intensity, observed whenever a spatially coherent light beam is shone onto an irregular surface with height variations larger than the light wavelength, as can be seen in Fig.2.16. Each

surface point will scatter light in a different direction which will interfere with the neighbour scatters, due to the fact it is spatially coherent. The speckles, or observed light grains, can be objective, if they depend solely on the incident wave and the scatter surface, or subjective, if there's an imaging system involved, in which case, the smaller the aperture size of the imaging system, the larger is the observed speckle size. The example in Fig.2.17 was obtained with a controlled aperture.

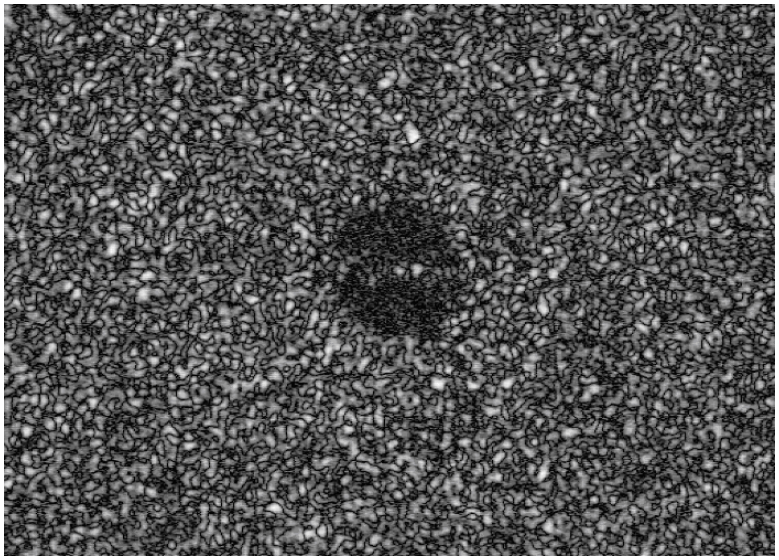

Figure 2.17 - Speckle formation on a diffuse surface. Courtesy, Dr. J. Monteiro - LOME.

Speckle metrology procedures can be broadly classified into three categories: Speckle Photography, Speckle Interferometry and Speckle Shearing Interferometry or Shearography. These techniques are highly flexible when dealing with field problems, therefore being able to cope with large deformation measurements, displacements in and out of the plane, displacement derivatives, surface shape, roughness and dynamic displacement (Joenathan, 1997; Rastogi, 2000).

Speckle Photography (Archbold et al., 1970; Burch and Tokarski, 1968) is the incoherent addition of two speckle patterns corresponding to different states of the object on the same register, and accounts for all the techniques wherefore positional changes of the speckles are monitored. The two most popular Speckle Photography methods differ in the way the resulting specklegram is interrogated. In case a single unexpanded laser beam is used, each speckle pair registration, corresponding to the different object states, behaves as a double slit in a Young's experiment, and parallel equidistant fringes, perpendicular to the displacement or deformation, are observed on the image plan.

This can be deduced from a simple analysis. If the illuminating beam is small, the speckle displacement between the two recordings can be considered uniform within the illuminated area. As such, if the first registered field is $I_1(x,y) = I(x,y)$, the second can be described by $I_2(x,y) = I(x-d,y)$, for a displacement along the xx coordinate. If the observation plane is located at the Fraunhofer region, i.e., a reasonable distance from the illuminated specklegram, the field in this plane will be given by the Fourier transform of the transmittance,

$$u_a = \mathcal{F}\left(I_1 + I_2\right) = \mathcal{F}\left(I_1\right) + \mathcal{F}\left(I_2\right) \tag{2.16}$$

Let,

$$J\left(u,v\right) = \mathcal{F}\left(I\left(x,y\right)\right) \tag{2.17}$$

with spatial frequencies $u = \frac{x}{\lambda z}, v = \frac{y}{\lambda z}$. Then,

$$\begin{aligned} \mathcal{F}\left(I_2\left(x,y\right)\right) &= \int_{-\infty}^{+\infty}\int_{-\infty}^{+\infty} I\left(x-d,y\right) e^{-i2\pi(ux+vy)} dxdy \\ &= \int_{-\infty}^{+\infty}\int_{-\infty}^{+\infty} I\left(x,y\right) e^{-i2\pi(u(x+d)+vy)} dxdy = J\left(u,v\right) e^{-i2\pi ud} \end{aligned} \tag{2.18}$$

so,

$$u_a = J\left(u,v\right)\left(1 + e^{-i2\pi ud}\right) \tag{2.19}$$

and the observed intensity is

$$\begin{aligned} I_a &= |u_a.u_a^*| = 2\left|J(u,v)\right|^2\left(1+\cos\left(2\pi ud\right)\right) \\ &= 2\left|J\left(u,v\right)\right|^2\left(1+\cos\left(2\pi\frac{x}{\lambda z}d\right)\right) \end{aligned} \tag{2.20}$$

which is no other than Young's fringe descriptor with inter-slit distance, d, modulated by $2\left|J(u,v)\right|^2$. From the Wiener-Khinchin, or auto-correlation theorem,

$$\left|J\left(u,v\right)\right|^2 = \mathcal{F}\left\{I\left(x,y\right) \star I\left(x,y\right)\right\} \tag{2.21}$$

so the observed fringe pattern is actually a correlation between the two displaced speckle patterns.

The fringe separation or pitch, indicates the amount of in-plane displacement at the point of the laser beam incidence. Scanning the specklegram throughout, will yield a displacement map for the entire object.

The whole-field alternative, illustrated in Fig. 2.18, consists of placing the registered specklegram on a Fourier filtering arrangement, and removing all but one single frequency on the spectrum plane, with a band-pass filter, i.e., a hole (Archbold and Ennos, 1972). This corresponds, after Fourier transformation by the second lens, to a single frequency grating modulation of the speckle pattern on the object surface. A displacement or deformation will originate an observable phase variation on the observed fringe pattern, which will have a maxima every

$$s\left(x,y\right)=\sqrt{u^{2}\left(x\right)+v^{2}\left(y\right)}=n\lambda_{0}f\sqrt{\left(\frac{1}{x_{f}}\right)^{2}+\left(\frac{1}{y_{f}}\right)^{2}} \tag{2.22}$$

and a minima every

$$s\left(x,y\right)=\left(n+\frac{1}{2}\right)\lambda_{0}f\sqrt{\left(\frac{1}{x_{f}}\right)^{2}+\left(\frac{1}{y_{f}}\right)^{2}} \tag{2.23}$$

where x_f and y_f are the filter's coordinates. This enables a displacement measurement along an angle to the x axis given by $\tan^{-1}\left(x_f/y_f\right)$.

The greater the hole distance to the spectrum plane centre, the larger the number of observable fringes and the greater the method's resolution. At the edge of the spectrum, it can be shown this corresponds to a resolution around $1\mu m$ (Gasvik, 2000).

The remaining two categories, Speckle Interferometry and Speckle Shearing Interferometry, represent methods based on the measurement of irradiance changes. In Speckle Interferometry, two interference fields, corresponding to object states before and after deformation, are compared, each one having been generated by the coherent superposition of object and reference waves (Rastogi, 2000; Sirohi, 1993). The reference field can be either a plane wave or another speckle field, usually by means of switching the reference field mirror by a diffuse reflector on a Michelson interferometer configuration, in case of out-of-plane displacement detection. In case in-plane detection is envisaged, the object is illuminated by two collimated waves aligned symmetrically and making an angle with respect to the surface normal. The resulting speckle pattern in the image plane is generated by the coherent superposition of the speckle fields corresponding to each of the two illumination beams. When the object is deformed, the phase difference between the illuminating waves at any point will change. The corresponding fringes represent contours of constant in-plane displacement (Leendertz, 1970).

Speckle Shearing Interferometry, or Shearography as it is also known, is a technique whereby the two interfering speckles originate from the same object and are sheared laterally with respect to each other (Hung, 1974; Leendertz and Butters, 1973).

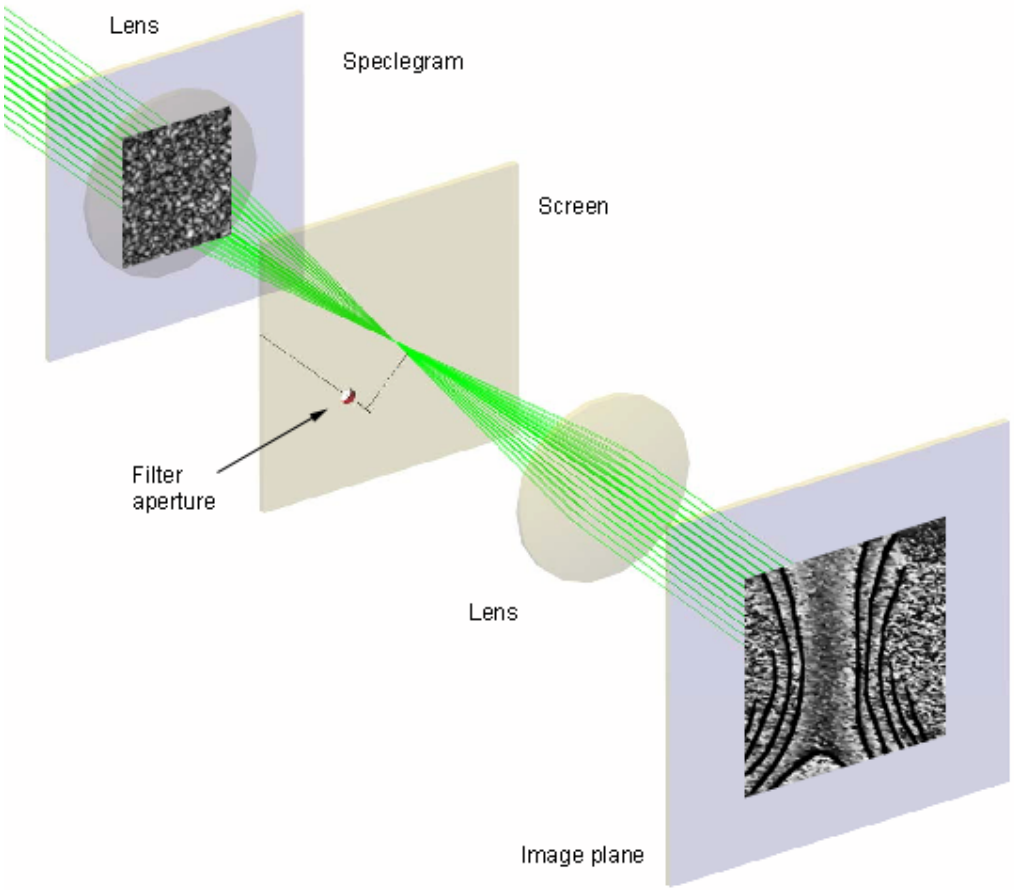

Figure 2.18 - Fourier filtering setup for whole-field recovery in Speckle Photography.

A wealth of speckle interferometry methods has been reported over the years, as can easily be confirmed in the literature (Joenathan, 1997; Rastogi, 2000).

Contouring is done in much the same way as described in the holographic interferometry technique, except for the reference beam which is now contained in the speckle fields themselves. Both the Dual Beam and the Immersion techniques can be used with speckle fields (Joenathan et al., 1990; Rastogi, 1993). Although the fringes contrast decreases rapidly as the viewing angle increases and the diffusing surfaces becomes rougher, due to speckle decorrelation, resolutions near $\lambda/10$ with phase analysis on ESPI setups have been reported (Joenathan et al., 1990).

ESPI

Electronic Speckle Pattern Interferometry, also known by several other names such as TV Holography or Electronic Holography, made its debut in the decade of 1970 with

the pioneer works at Loghborough (Leendertz, 1970), Stanford (Macovski et al., 1971) and Wien (Schwomma, 1972), as well as several important contributions in vibration measurement from the Trondheim group (Høgmoen and Løkberg, 1977; Pedersen et al., 1974). The importance of the technique cannot be overstated, and the hundreds of contributions, originating virtually all over the world, from Tsukuba to La Plata, from Luleä to Singapore, is a clear indication of the impact it had on interferometry. The introduction of digital imaging devices in the end of the 1980s brought about yet another denomination change, and the method is presently designated Digital Speckle Pattern Interferometry (DSPI).

Two main disadvantages of this technique are the fact the recorded hologram can't be interrogated by a reference beam any longer, which means the hologram cannot be reconstructed, and the inferior resolution of CCD cameras: present day 8.3 Mb camera sensors with a 3326 x 2504 pixel resolution, exhibit pixel sizes of 5.4 μm. To comply with the Nyquist limit, each interference fringe has to be greater than twice the pixel size,

$$2p \leq d = \frac{\lambda}{2\sin\left(\frac{\alpha}{2}\right)} \tag{2.24}$$

where α is the angle between reference and object field directions. For the small angle approximation, $\sin(\alpha) \approx \alpha$, this implies

$$\alpha \leq \frac{\lambda}{2p} \tag{2.25}$$

For p=5.4 μm, α has to be less than 3.4 degrees, which requires a near parallel incidence setup, characteristic of the technique, as illustrated in Fig. 2.19.

Deformation analysis in real-time is accomplished by subtracting the interference intensity distribution from the object and the reference fields after deformation to the distribution at an initial state, at the system frame rate.

Let the wave scattered by the object be described by

$$u_1 = U_o e^{i\phi_o} \tag{2.26}$$

prior to deformation and

$$u_2 = U_o e^{i(\phi_o + 2kd)} \tag{2.27}$$

afterwards. If the reference wave is given by

$$u_r = U_r e^{i\phi_r} \tag{2.28}$$

the intensity distribution seen by the CCD at the initial state will be,

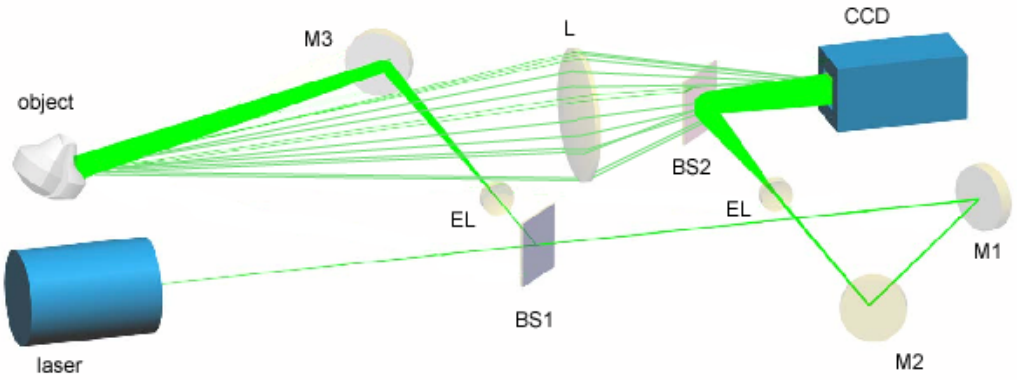

Figure 2.19 - Typical ESPI setup: BS - beam splitter; M - mirror; L - imaging lens; EL - expanding beam lens. Mirror M2 can be tilted.

$$I_1 = U_r^2 + U_o^2 + 2U_rU_o\cos(\phi_r - \phi_o) \tag{2.29}$$

which will be stored in frame memory. After deformation the intensity distribution can be described by

$$I_2 = U_r^2 + U_o^2 + 2U_rU_o\cos(\phi_r - \phi_o - 2kd) \tag{2.30}$$

The subtraction in real-time yields a signal proportional to,

$$\begin{aligned} I_1 - I_2 &= 2U_rU_o\left|\cos(\phi_r - \phi_o) - \cos(\phi_r - \phi_o - 2kd)\right| \\ &= 4U_rU_o\left|\sin(\phi_r - \phi_o - kd)\sin(kd)\right| \end{aligned} \tag{2.31}$$

where the absolute value was taken. This expression reveals the presence of a background illumination term, a stochastic speckle noise, which varies randomly from pixel to pixel, and a modulation term whose frequency is proportional to the displacement at each object point.

ESPI can also be used in 3D contouring and over the years several methods have been reported, such as dual beam illumination (Rodriguez-Vera et al., 1992), changing the illumination angle between exposures, two wavelength contouring (Tatam et al., 1990), immersion (Rastogi, 1993), and others. Resolutions of $\lambda/20$ have been reported (Creath, 1985).

Digital Image Correlation

Also known as Digital Speckle Photography, this is a technique which evolved from White Light Speckle Interference, a close technique to Speckle Photography described before.

The first computer based speckle photography system was presented in the early 1980's by Peters and Ranson.(Peters and Ranson, 1982). The images, recorded by a CCD-detector and stored on separate frames in the computer, are submitted to a cross-correlation algorithm to determine the displacement field. The result is obtained much faster since no film processing or reconstruction with laser light is needed.

Speckle correlation requires that the surface has a random texture of some kind, obtained by either using a laser light to produce speckle from the surface or a random pattern that can be projected (Sjodahl and Synnergren, 1999) or painted on the surface. These white light speckles have one advantage over the laser speckle in that they are more robust to decorrelation.

The technique uses two images from the object, one taken before and one after the object has been deformed or moved in some way. The images are divided into small sub-images. The size of these sub-images determines the spatial resolution of the final result, making it important not to use too large sub-images. However, if too small sub images are chosen, there will be difficulties in finding the corresponding sub-image and the correlation value will drop. The cross-correlation algorithm evaluates the statistical similarity between the sub-image from the reference image and the corresponding sub-image from the displaced image. Actually, a sub-image is let to sweep over the displaced image and when an area is found where the statistical similarity is the highest, this area is taken as the new sub-image. The displacement can then be calculated for all the sub-images displacements over the entire image – the displacement field. The height of each correlation peak is a measure of how similar the cross-correlated sub-images are, and hence a value of the accuracy of the measurement.

Conoscopic Holography

Conoscopic Holography is a point scanning holographic technique wherefore the light from each object point interferes with a delayed version of itself by use of a uniaxial crystal such as calcite. The ordinary and the extraordinary rays are made to interfere at the crystal exit by combination onto a polarizer. The technique was invented by Demetri Psaltis and Gabriel Sirat in 1985 at CALTECH (Sirat and Psaltis,

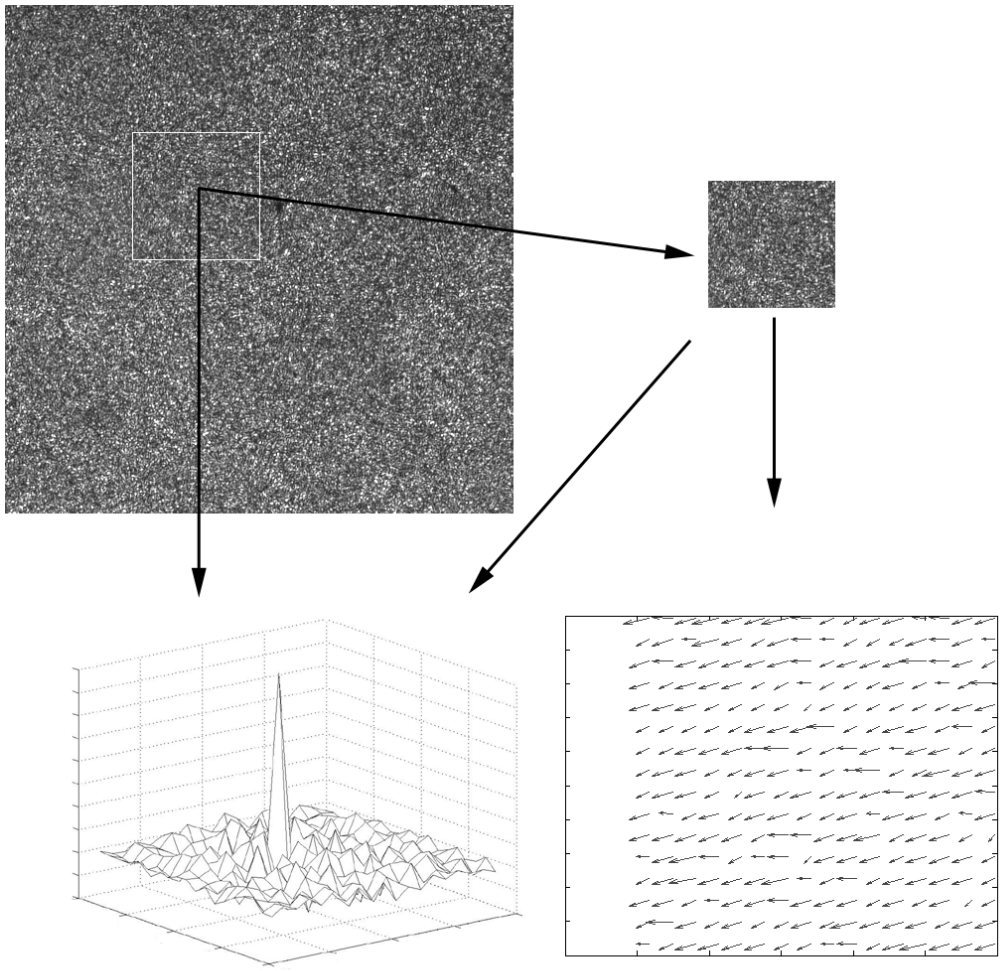

Figure 2.20 - A typical speckle correlation result. Although the movement is clearly detected, the correlation vector field can look very disordered.

1985) and further developed at the École Nationale Supérieure des Telecommunications in Paris. The Israelite company Optimet commercializes this type of interferometer and claims resolutions under 1 micron for 1 to 120 mm ranges on both point or line scan configurations.

White Light Interferometry

White light interferometry, be it Coherence Scanning Microscopy (Davidson et al., 1987; Lee and Strand, 1990), Spectroscopic Analysis Interferometry (Sandoz et al., 1996) or Fourier Transform Spectroscopy of white light interferograms (Hart et al.,

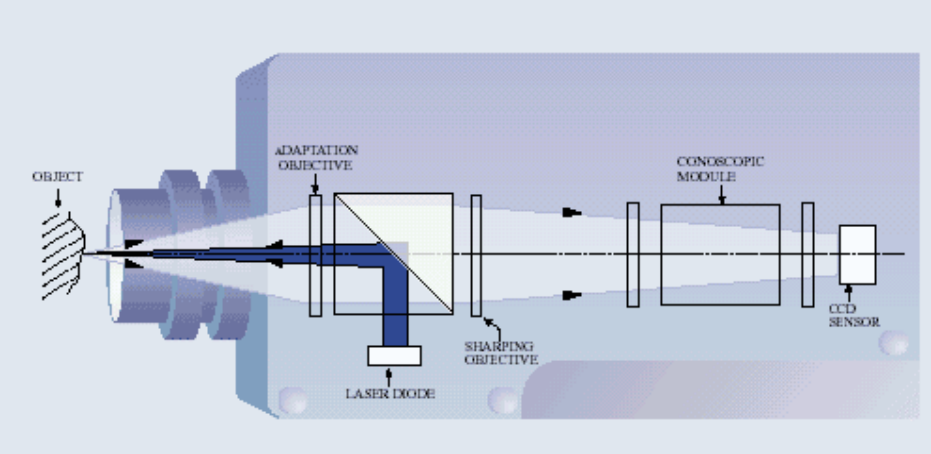

Figure 2.21 - Conoprobe sensor diagram. Courtesy, Optimet.

1998), can measure surface depth profiles with vertical nanometre resolutions and lateral resolutions twice the ones from conventional optical microscopy.

The principle of the white light interferometer is based on the otherwise annoying fact that a Michelson interferometer, when used with white light, can only produce interference fringes with an almost exact match of both reference and object arms (Wyant, 2002).

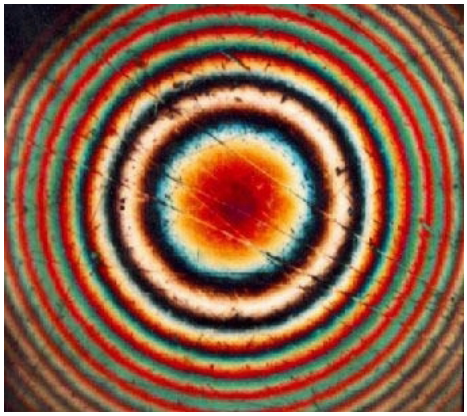

Figure 2.22 - White light fringes on a matched interferometer.

Scanning either the reference or the object arm will result in focused interference fringes whenever each object point height is matched through the scanning. Actually, the amplitude at each object point will fluctuate as depicted in Fig. 2.23. Peak amplitude at each object point is determined along with the corresponding optical path difference. A high resolution surface profile of the object is thus obtained from the

scanning height map corresponding to the fringe peak at every object point. Reduced crosstalk between laterally adjacent surface points, due to the spatial incoherence of the illumination, ensures a lateral resolution similar to that found in confocal microscopy. Depth resolutions of some nm for ranges of several μm have been reported (Lee and Strand, 1990). However, the physical scan, which can take as long as a few seconds, limits the instruments application to the measurement of static surfaces in mechanically stable environments.

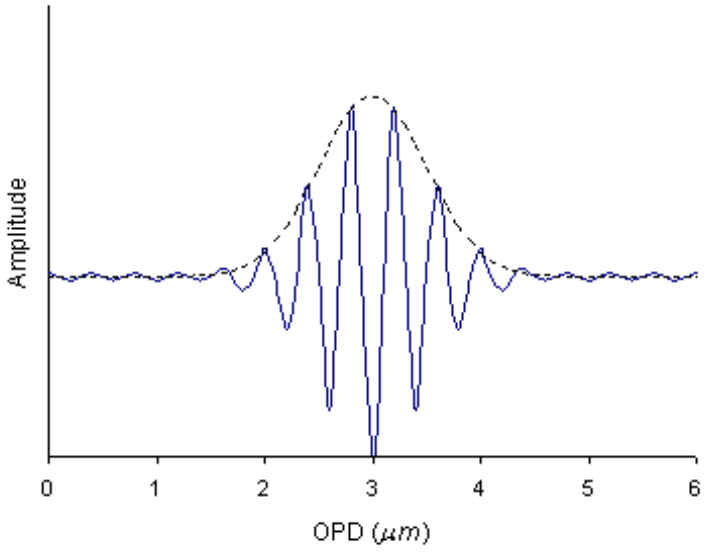

Figure 2.23 - Output signal of a white light interferometer as a function of optical path difference.

Chapter 3

Phase Measurement Methods

3.1 Introduction– ubiquitous phase

Phase information is responsible for many aspects of image formation. In fact, phase information is the fundamental difference between coherent and incoherent image formation. Whereas phase interdependence gives rise to a sinusoidal varying term in coherent imaging, whose argument is the difference in phase between the two interfering waves, this term averages to zero in incoherent addition of two waves.

In some instances, phase information may even be regarded as more prominent than intensity, as depicted in Fig. 3.1, where the complex phase and amplitudes from the original images were switched as indicated. Retaining phase enables a quite understandable image reconstruction, whereas retaining amplitude doesn't.

Oppenheim has shown that, under special circumstances, a signal can be entirely reconstructed, to within a scale factor, by phase information alone (Oppenheim and Lim, 1981) .

In coherent imaging, phase difference can be regarded as a delay between waves that emanate from the same source and travel different paths. Even if this isn't true in incoherent systems, an artificial phase shift can be introduced and put to use, if a sinusoidal pattern is projected onto an object and a reference plane. The sinusoidal fringes will suffer a shift or distortion due to the surface irregularities, which is perfectly quantifiable. This is the principle of triangulation which can be explained with help from Fig. 3.2.

A fringe pattern with a known spatial frequency is projected onto the object under test by projector P and the image is captured at camera C. E_p and E_c refer to the nodal points of the projection and imaging systems, respectively. The optical axis of these systems cross at point O on a reference plane R_0. L_0 is the distance from the camera – projector plane to the reference plane, d is the distance between

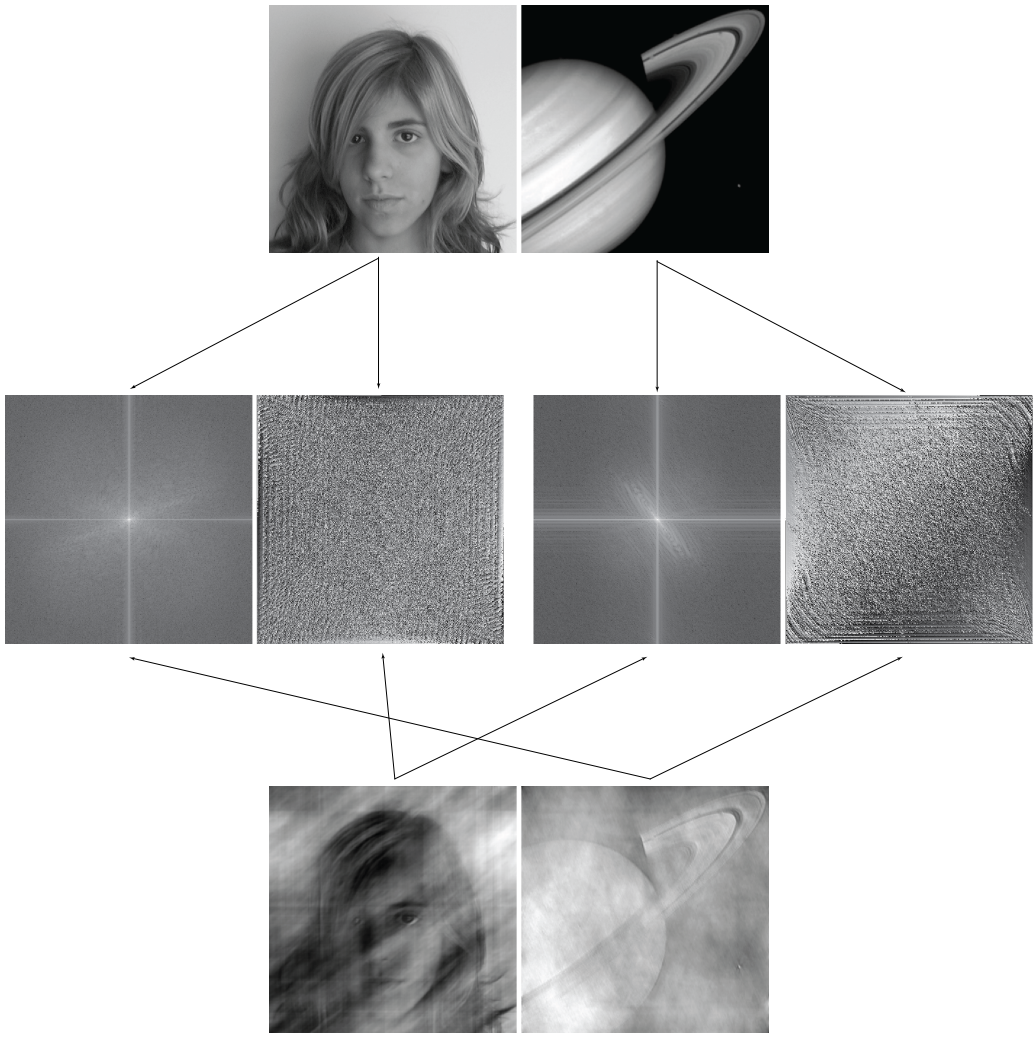

Figure 3.1 - Image reconstruction from switched phase and amplitude information

centers of projection, θ is the angle between projector and camera and s represents the intersection of $\overline{E_pB}$ with the object surface. $\overline{E_tD}$ represents a telecentric projection through s, as if E_t was located at infinity, described by,

$$g_t(x,y) = a(x,y) + b(x,y)\cos[2\pi f_0 x] \tag{3.1}$$

where $a(x,y)$ and $b(x,y)/a(x,y)$ represent the average intensity and fringe visibility or modulation on the surface of the object, f_0 is the fundamental frequency of the observed grating image, and the fringes run perpendicular to the paper plane. In the non-telecentric case, the pattern on the reference plane has a pitch increase with xx direction even for the flat reference plane, and can be described by,

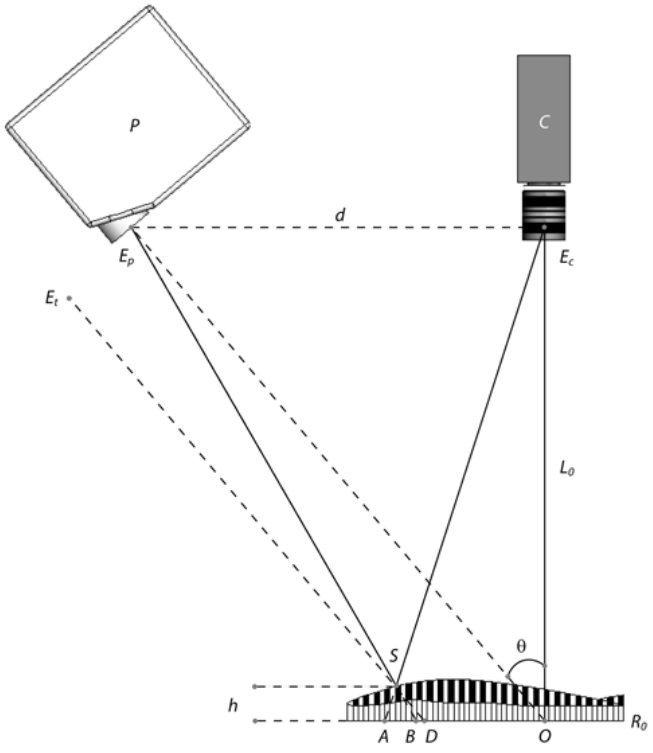

Figure 3.2 - Typical crossed axis phase measurement setup for structured lighting

$$g_0(x,y) = a(x,y) + b(x,y)\cos\left[2\pi f_0 x + \phi_0(x,y)\right] \tag{3.2}$$

with,

$$\phi_0\left(x,y\right) = 2\pi f_0 \overline{BD} \tag{3.3}$$

When the object is in place, the ray from E_p that strikes the reference plane at B is seen from the camera as coming from A and the phase expression for $h(x,y)$ is therefore,

$$\phi\left(x,y\right) = 2\pi f_0 \overline{AD} \tag{3.4}$$

As such, the fringe pattern on the object surface is expressed by,

$$g_s\left(x,y\right) = a\left(x,y\right) + b\left(x,y\right)\cos\left[2\pi f_0 x + \phi\left(x,y\right)\right] \tag{3.5}$$

and the phase difference between reference plane and object surface is,

$$\Delta\phi\left(x,y\right)=2\pi f_0\left[\overline{AD}-\overline{BD}\right]=2\pi f_0\overline{AB} \tag{3.6}$$

In order to establish a relation between phase and height one uses the fact triangles E_psE_c and AsB are similar,

$$\overline{AB}=\frac{dh}{L_0-h} \tag{3.7}$$

so,

$$\Delta\phi\left(x,y\right)=2\pi f_0\overline{AB}\Longrightarrow h=\frac{L_0\Delta\phi\left(x,y\right)}{\Delta\phi\left(x,y\right)+2\pi f_0 d} \tag{3.8}$$

or,

$$\Delta\phi\left(x,y\right)=\frac{2\pi f_0 dh}{L_0-h} \tag{3.9}$$

3.2 Phase shifting

Phase can be artificially changed on the object surface by moving the fringe pattern a specified amount. This is the basis of the Phase Shift methods, of which there are as many as the shift and recover methods developed over the years. There are two different classes of phase shift methods, which bear names that reflect the shift and recover procedures:

Temporal Phase Measurement (TPM) techniques measure the phase of a single point in an interferogram as the phase difference between the test and reference beams is changed in a controlled way. These techniques are also known as *n-steps* or *n-frames* techniques, because they use a sequence of n interferograms with known relative phase shifts. Spatial Phase Measurement (SPM) techniques extract the phase information from a single interferogram which has a large number of tilt fringes acting as a carrier frequency.

Phase shift can be accomplished by different techniques. Typical interferometer setups for fringe generation can use techniques such as moving a mirror, tilting a glass plane, moving a grating or rotating a half-wave plate, as described by Creath, or using an up-shift converter multi-frequency Zeeman laser (Creath, 1993).

In case a white light video projector is used, phase shift is accomplished by direct manipulation of the fringe calculation algorithm, which is currently the case with LOME's fringe projection system. In this case, the projected fringe lines correspond to the co-sinusoidal function,

$$\cos\left\{2\pi\left[t\left(\frac{i}{n}-\frac{1}{2}\right)+\frac{k-1}{4}\right]\right\} \tag{3.10}$$

where t is the number of projected fringes, i represents horizontal image pixels, n is the total number of horizontal image pixels and k is the amount of $\pi/2$ phase delay. These fringe pattern have a maximum at the middle of the image and grow or shrink outwards, as can be seen in Fig. 3.3.

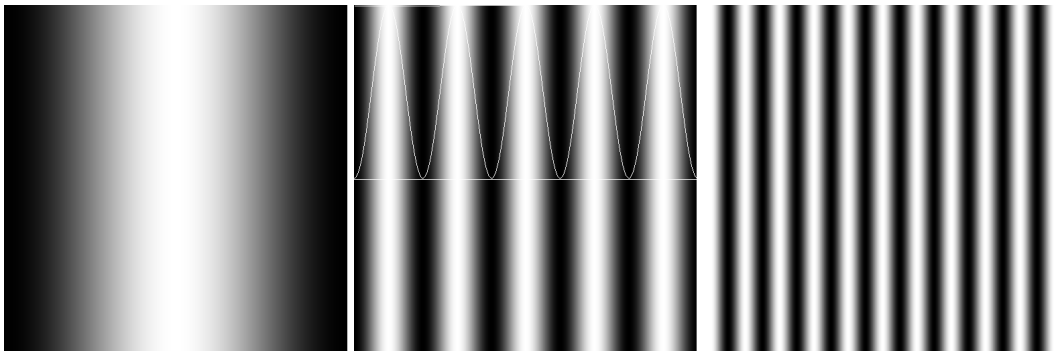

Figure 3.3 - Projected fringe patterns on LOME's prototype

The projected patterns can be tilted at will, and the fringes can be sinusoidal or square. Spagnolo has shown that under most circumstances, a sinusoidal pattern can be replaced by a Ronchi grating (Spagnolo et al., 2002).

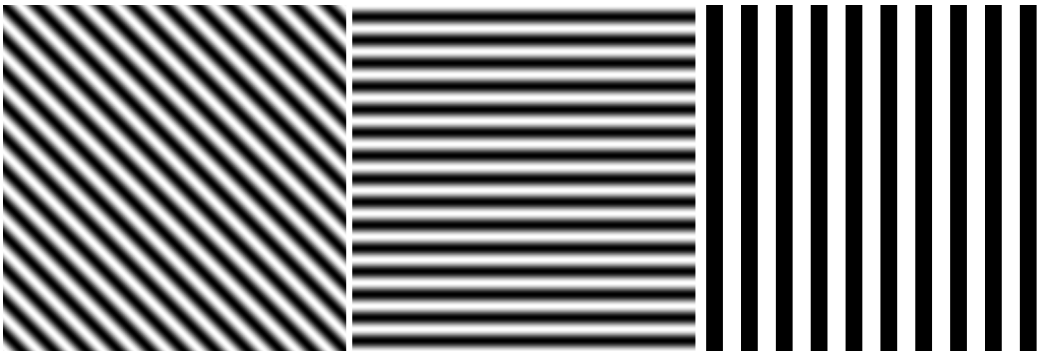

Figure 3.4 - Fringes tilt and shape control

The patterns can further be zoomed to a large extent, in order to accommodate to different object sizes or camera lens magnification.

3.3 Temporal phase shifting

Many algorithms for the determination of wavefront phase have been published over the years, as well as thorough studies on the calibration and expected errors from the use of these patterns (Creath and Schmit, 1996). If the phase is shifted between image grabbing or intensity measurements, the technique is known as phase stepping, whereas if it is linearly ramped while intensity is integrated, it is known as integrated bucket phase shifting.

The general *n-step* case

The general case can be described as follows (Gasvik, 2000). A minimum of three measurements is necessary, for there are three unknowns in intensity data, as mentioned in § 2.3:

$$I = I_0 \left[1 + \gamma \cos\left(\alpha + \phi\right)\right] \tag{3.11}$$

where I_0 is the average background or dc intensity, γ is the fringe visibility, ϕ is the controlled phase shift and α is the sought phase variation. For arbitrary phase shifts ϕ_1, ϕ_2 and ϕ_3, Eq.3.11 can be explicitly written as,

$$\begin{aligned} I_1 &= I_0 \left[1 + \gamma \cos\left(\alpha + \phi_1\right)\right] \\ I_2 &= I_0 \left[1 + \gamma \cos\left(\alpha + \phi_2\right)\right] \\ I_3 &= I_0 \left[1 + \gamma \cos\left(\alpha + \phi_3\right)\right] \end{aligned} \tag{3.12}$$

from which the phase, α, can be calculated as,

$$\alpha = \tan^{-1}\left(\frac{\left(I_2 - I_3\right)\cos\left(\phi_1\right) - \left(I_1 - I_3\right)\cos\left(\phi_2\right) + \left(I_1 - I_2\right)\cos\left(\phi_3\right)}{\left(I_2 - I_3\right)\sin\left(\phi_1\right) - \left(I_1 - I_3\right)\sin\left(\phi_2\right) + \left(I_1 - I_2\right)\sin\left(\phi_3\right)}\right) \tag{3.13}$$

For phase shifts of $\pi/2$, with $\phi_1 = \pi/4$, $\phi_2 = 3/4\ \pi$ and $\phi_3 = 5/4\ \pi$, α is given by,

$$\alpha = \tan^{-1}\left(\frac{I_3 - I_2}{I_1 - I_2}\right) \tag{3.14}$$

and the fringe visibility, γ, is

$$\gamma = \frac{\sqrt{\left(I_3 - I_2\right)^2 + \left(I_1 - I_2\right)^2}}{\sqrt{2} I_0} \tag{3.15}$$

Morgan has shown that the general n steps case can be solved by a least squares procedure as follows (Morgan, 1982). The ith step is written,

$$I_i = I_0 \left[1 + \gamma \cos\left(\alpha + \phi_i\right)\right] = a_0 + a_1 \cos\phi_i + a_2 \sin\phi_i \tag{3.16}$$

where

$$\begin{aligned} a_0 &= I_0 \\ a_1 &= I_0 \gamma \cos\alpha \\ a_2 &= -I_0 \gamma \sin\alpha \end{aligned} \tag{3.17}$$

For the n steps, Eq. 3.16 can be written in matrix form as,

$$\begin{bmatrix} I_1 \\ I_2 \\ \vdots \\ I_n \end{bmatrix} = \begin{bmatrix} 1 & \cos\phi_1 & \sin\phi_1 \\ 1 & \cos\phi_2 & \sin\phi_2 \\ \vdots & \vdots & \vdots \\ 1 & \cos\phi_n & \sin\phi_n \end{bmatrix} \begin{bmatrix} a_0 \\ a_1 \\ a_2 \end{bmatrix} \tag{3.18}$$

Using ordinary least squares analysis, the coefficients a_i are given by,

$$\begin{bmatrix} a_0 \\ a_1 \\ a_2 \end{bmatrix} = \mathbf{A}^{-1}\mathbf{B} \tag{3.19}$$

where

$$\mathbf{A} = \begin{bmatrix} n & \sum\cos\phi_i & \sum\sin\phi_i \\ \sum\cos\phi_i & \sum\cos^2\phi_i & \sum\cos\phi_i \sin\phi_i \\ \sum\sin\phi_i & \sum\cos\phi_i \sin\phi_i & \sum\sin^2\phi_i \end{bmatrix} \tag{3.20}$$

and

$$\mathbf{B} = \begin{bmatrix} \sum I_i \\ \sum I_i \cos\phi_i \\ \sum I_i \sin\phi_i \end{bmatrix} \tag{3.21}$$

A needs to be calculated and inverted just once, because it depends on the phase shifts alone. The phase at each (x, y) point is obtained through,

$$\alpha = \tan^{-1}\left(-\frac{a_2(x,y)}{a_1(x,y)}\right) \tag{3.22}$$

and the fringe visibility by,

$$\gamma = \frac{\sqrt{a_1^2(x,y) + a_2^2(x,y)}}{a_0(x,y)} \tag{3.23}$$

The $n = 3$ case

Instead of $\pi/2$ phase shifts, illustrated above, if a $2/3\pi$ phase shift is used with $\phi_i = 2/3\pi$, 0 and $2/3\pi$,

$$\alpha = \tan^{-1}\left(\sqrt{3}\frac{I_1 - I_3}{2I_1 - I_2 - I_3}\right) \tag{3.24}$$

and

$$\gamma = \frac{\sqrt{3\left(I_1 - I_3\right)^2 + \left(2I_2 - I_1 - I_3\right)^2}}{3I_0} \tag{3.25}$$

The $n = 4$ case

The most common procedure with four frames uses $\pi/4$ phase shifts with $\phi_i = 0$, $\pi/2$, π and $3/2\pi$. Phase and visibility are found as,

$$\alpha = \tan^{-1}\left(\frac{I_4 - I_2}{I_1 - I_3}\right) \tag{3.26}$$

and

$$\gamma = \frac{\sqrt{\left(I_4 - I_2\right)^2 + \left(I_1 - I_3\right)^2}}{2I_0} \tag{3.27}$$

The $n = 5$ case

This technique was first described by Schwider and later refined by Hariharan in an attempt to reduce the uncertainty in the phase calculation when the phase difference between the two interferometer arms is close to integer multiples of π (Hariharan et al., 1987; Schwider et al., 1983). It is still one of the most robust methods available, except in sensitivity to dc intensity variations across the image, where the three frames or the Carré method seems to perform marginally better. For $\phi_i = -\pi$, $-\pi/2$, 0, $\pi/2$, and π, phase and visibility are found as,

$$\alpha = \tan^{-1}\left(\frac{2\left(I_2 - I_4\right)}{2I_3 - I_5 - I_1}\right) \tag{3.28}$$

and

$$\gamma = \frac{\sqrt{\left(2\left(I_2 - I_4\right)\right)^2 + \left(2I_3 - I_5 - I_1\right)^2}}{4I_0} \tag{3.29}$$

The Carré technique

Carré proposed an ingenious technique which is independent of the amount of phase shift, as long as it is a linear shift (Carré, 1966):

$$\begin{aligned} I_1 &= I_0\left[1+\gamma\cos\left(\alpha-\frac{3}{2}\phi\right)\right] \\ I_2 &= I_0\left[1+\gamma\cos\left(\alpha-\frac{1}{2}\phi\right)\right] \\ I_3 &= I_0\left[1+\gamma\cos\left(\alpha+\frac{1}{2}\phi\right)\right] \\ I_4 &= I_0\left[1+\gamma\cos\left(\alpha+\frac{3}{2}\phi\right)\right] \end{aligned} \tag{3.30}$$

It is straightforward to see that the phase shift is given by,

$$\phi = 2\tan^{-1}\left(\sqrt{\frac{3\left(I_2-I_3\right)-\left(I_1-I_4\right)}{\left(I_2-I_3\right)+\left(I_1-I_4\right)}}\right) \tag{3.31}$$

and the phase by,

$$\alpha = \tan^{-1}\left\{\tan\left(\frac{\phi}{2}\right)\left[\frac{\left(I_2-I_3\right)+\left(I_1-I_4\right)}{\left(I_2-I_3\right)+\left(I_1-I_4\right)}\right]\right\} \tag{3.32}$$

Creath has shown that, in case the phase shift is $\pi/2$, the visibility is given by,

$$\gamma = \frac{1}{2I_0}\sqrt{\frac{\sqrt{\left[\left(I_2-I_3\right)+\left(I_1-I_4\right)\right]^2+\left[\left(I_2+I_3\right)-\left(I_1+I_4\right)\right]^2}}{2}} \tag{3.33}$$

In case the phase shift is offset by 10° the estimation of γ will be offset by $\pm 10\%$. Besides being one of the methods least sensitive to errors, it has the advantage of foregoing phase shift calibration (Creath, 1988).

Temporal methods are best suited to high accuracy static measurements, even though error sources such as vibration or air turbulence can severely impair this accuracy. As referred in § 2.3, there are some configurations such as common path interferometers or vibration sensing setups, which render these methods somewhat more immune to this type of noise, but a more appropriate answer to this problems seems to be given be the Spatial Phase Shift approach.

3.4 Spatial phase shift

Spatial techniques were designed to handle dynamic events, by relying on the use of one interferogram alone or several interferograms taken simultaneously. These meth-

ods can best be described by separating them into spatial carrier methods, currently comprising both the Fourier Transform and the Spatial Carrier Phase Shift methods, and the spatial analogue of the temporal phase shift – Spatial Phase Stepping.

Spatial Phase Stepping

Different methods to generate simultaneous phase stepped patterns into parallel channels have been proposed and include the use of polarising optics (Bareket, 1985; Smythe and Moore, 1984) or diffraction gratings (Kujawinska, 1987; Kujawinska and Robinson, 1988; Kwon, 1984). The polarisation method delays the interference of object and reference beams up until the appropriate phase shift has been introduced on each channel. Interference then occurs by mixing both waves on a polariser oriented at 45 degrees to the polarisation axis. Other configurations have also been advanced, which use a dielectric beam splitter and introduce a relative phase shift between the xx and yy components of the reference and object interference term (Millerd et al., 2005).

The two most widespread configurations use three or four channels. Fig. 3.5 depicts the 3-channel implementation by Bareket. The polarisation interferometer reference and object beams acquire orthogonal polarisations after passing twice on quarter-wave plates (QWP) with orientations at $\pi/4$ to each other. The beams are then analysed on a Direct Phase Measurement module (DPM), by means of further retarders and a final polariser before each camera, at $\pi/4$ to the polarisation axis. Channel 3 combines the beams as they come out of the polarisation interferometer, whilst the QWP after the beam splitter introduces a further $\pi/2$ phase delay and the one before channel 2, another. The final captured intensity patterns can be described by,

$$\begin{aligned} I_1 &= I_0\left[1+\gamma\cos\left(\alpha+\frac{\pi}{2}\right)\right] = I_0\left[1-\gamma\sin\alpha\right] \\ I_2 &= I_0\left[1+\gamma\cos\left(\alpha+\pi\right)\right] = I_0\left[1-\gamma\cos\alpha\right] \\ I_3 &= I_0\left[1+\gamma\cos\alpha\right] \end{aligned} \tag{3.34}$$

and the phase can be calculated as,

$$\alpha = \tan^{-1}\left[\frac{2I_1 - I_2 - I_3}{I_2 - I_3}\right] \tag{3.35}$$

The most prominent errors of the multi-channel configurations are related to adverse conditions that affect each channel separately, such as those that can result from detector variations, channel attenuation or camera calibration adjustments.

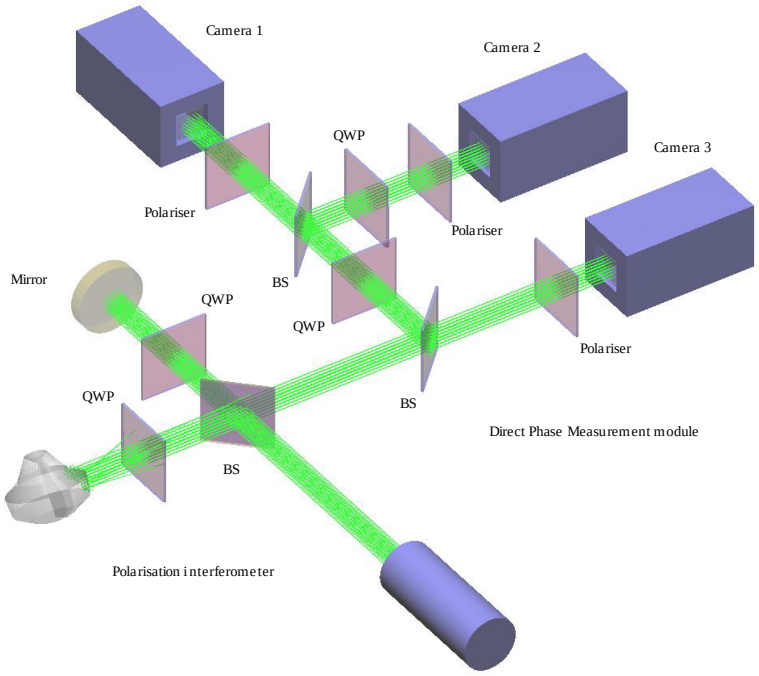

Figure 3.5 - Three-channel direct phase measurement module

Spatial Carrier Phase Shifting

Spatial carrier phase-shifting (Poon et al., 1993; Williams et al., 1991) is the spatial analogue of the temporal phase-stepping principle reviewed in § 3.3. It is a spatial phase-shifting method, but instead of shifting the phase, the concept makes use of the fact a repetitive pattern - the carrier - covers the entire object and can be seen as being continuously shifted over it.

Let the spatial frequency in *fringes per pixel* be given by $f_0 = n/N$, with n fringes on a N pixel wide image. The wavelength, λ, of each fringe will be given by a number of pixels equal to $1/f_0$. For instance, in order to use Hariharan's *5-step* technique, n is chosen so as to make λ proportional to 4 or,

$$n = \frac{N}{4a} \tag{3.36}$$

where a is chosen in advance. Take $a = 1$, without loss of generality. Then each fringe will occupy exactly 4 pixels, which means $2\pi f_0 x = x\pi/2$. Say pixel 3 on a 5 pixel

wide set of pixels, has zero phase shift. Intensity variation on the two adjacent pixels to each side can then be described by,

$$\begin{aligned}
I_1 &= I_0\left[1+\gamma\cos\left(\frac{\pi}{2}x-\pi+\phi\right)\right] = I_0\left(1-\gamma\cos\left(\frac{\pi}{2}x+\phi\right)\right)\\
I_2 &= I_0\left[1+\gamma\cos\left(\frac{\pi}{2}x-\frac{\pi}{2}+\phi\right)\right] = I_0\left(1+\gamma\sin\left(\frac{\pi}{2}x+\phi\right)\right)\\
I_3 &= I_0\left[1+\gamma\cos\left(\frac{\pi}{2}x+\phi\right)\right]\\
I_4 &= I_0\left[1+\gamma\cos\left(\frac{\pi}{2}x+\frac{\pi}{2}+\phi\right)\right] = I_0\left(1-\gamma\sin\left(\frac{\pi}{2}x+\phi\right)\right)\\
I_5 &= I_0\left[1+\gamma\cos\left(\frac{\pi}{2}x+\pi+\phi\right)\right] = I_0\left(1-\gamma\cos\left(\frac{\pi}{2}x+\phi\right)\right)
\end{aligned} \tag{3.37}$$

and the phase at pixel 3 can be calculated as usual by Eq. 3.28,

$$\phi = \tan^{-1}\left(\frac{2\left(I_2-I_4\right)}{2I_3-I_5-I_1}\right)-\frac{\pi}{2}x \tag{3.38}$$

The $\frac{\pi}{2}$ phase ramp per pixel has to be subtracted to obtain the final phase variation.

The same reasoning can be applied to any *n-step* technique, as long as the Nyquist limit is not violated, i.e., as long as there are 2 pixels for each fringe.

For a *4-step* technique, the number of fringes would be such that the period would be proportional to 4 pixels, and Eq. 3.26 would apply. Pedrini used a *3-step* technique for evaluation of ESPI data(Pedrini et al., 1993).

Williams expanded the concept by proposing other sampling geometries to cope with fringe inclination and increased frequency. A cruciform geometry for a *5-step* technique, such as the one if Fig. 3.6, requires a fringe pattern with a phase variation in xx twice as slower as slower as that in yy for equal pixel spacing, which means the fringe inclination must be chosen as $tan^{-1}\left(1/2\right)$ as can be seen in the figure. This configuration allows a significant reduction in fringe spacing, but can be rather noisy, in case the frequency is close to the Sampling Theorem's limit.

Measurement errors of *n-step* spatial phase-shifting techniques

One of the chief disadvantages of the spatial phase-shifting techniques is the relative poor immunity to noise, due to the fact the detector has to resolve a large number of fringes and must perform uniformly across the entire useful area. Even if this is the case, several error sources, inherent to the fringe projection and shifting, plague these techniques. An extensive simulation study was presented by Creath, which emphasises the issue must not be overlooked and advances four major error sources which can, and do, hinder the measurements and render their validity questionable altogether (Creath and Schmit, 1996):

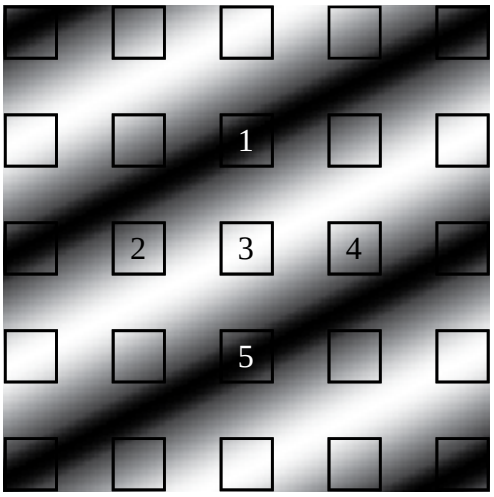

Figure 3.6 - Cruciform pixel arrangement for a 5-step technique

- Phase shifter miscalibration;
- Unequal fringe spacing;
- Detector non-linearity;
- DC intensity variation across fringes.

A wrong or absent phase shifter calibration implies the phase shift may not be as expected at each detector pixel, suffering a supplementary shift. This error will be noticed in the retrieved phase as both a high frequency error at twice the carrier frequency and a modulation error function at four times the error frequency, and is discussed below.

Unequal fringe spaces, which can be due to both detector or projector non-uniformity across the useful area, or a wrong or poor calibration procedure, produces a similar effect to phase shift miscalibration, except for the fact it is not uniform across the entire detector.

Detector non-linearity, or source for that matter if a projector is used, can be a serious concern, by distorting the intensity readings. The distortion is usually modelled as a square intensity error term and can be reduced if it is possible to work on the linear part of the gain curve. Creath remarks that there is also a high frequency error related to the detector non-linearity which seems to depend on the initial phase of the first sampling point, one which will worsen in case unequal fringe spacing or phase shifter miscalibration is also present, but which has an amplitude similar to an equivalent temporal phase-shift technique.

Phase errors will also occur in case there is a dc intensity variation across the imaging plane. This error will increase as expected from the centre to the edges but can be kept at below 0.01 wavelengths if the intensity at the edges is kept within a factor of 2 to the intensity at the centre of the image. The illumination calibration procedure for projector sources developed in LOME and presented in § 4.4 can further reduce this effect to acceptable levels.

Creath makes a comparative study on the behaviour of some of the most popular *n-step* techniques, such as the *3-step*, *3-step* at 120°, *4-step*, *5-step* and *Carré*, and concludes that both *5-step* and *Carré* perform appreciably better than the remaining.

n-Step averaging and extended averaging

While studying the *n-step* techniques, Schwider stressed the fact that most of the errors, especially those related to phase-shifter calibration, occur at twice the carrier frequency (Schwider et al., 1983). Therefore, performing the measurements twice, with $\pi/2$ phase shifts and averaging the results, should produce errors π out of phase which would readily cancel each other out. Actually, using $\pi/2$ phase shifts would make it necessary to take only one further data point and use the first 1 to $N-1$ frames for the first measurement and 2 to N for the second, then averaging the results. Schwider further noted that, rather than averaging the measurement results after calculating the inverse tangent, the numerators and denominators of the function argument could themselves be averaged. For the *5-step* case above, that meant using the first 1 to 4 frames in a *4-step* algorithm,

$$\frac{n_1}{d_1} = \frac{I_4 - I_2}{I_1 - I_3} \tag{3.39}$$

frames 2 to 5 also on a *4-step* algorithm,

$$\frac{n_2}{d_2} = \frac{I_4 - I_2}{I_5 - I_3} \tag{3.40}$$

and calculating

$$\tan\alpha = \frac{n_1 + n_2}{d_1 + d_2} = \frac{2\,(I_2 - I_4)}{2I_3 - I_5 - I_1} \tag{3.41}$$

which is the Schwider-Hariharan algorithm in Eq. 3.28. This technique is widely known as *n-step averaging*. Schwider's analysis of the residual phase error, ε, caused by phase-shift miscalibration used a first-order approximation for $\sin(\varepsilon)$ and $\cos(\varepsilon)$, therefore concluding the residual error is just a constant offset with no impact on measurement. Hariharan revised this method and used a second-order approximation for the sine and cosine functions, showing that the peak-to-valley residual phase

error has a dependence on phase as $\sin(2\varepsilon)$. The error of the *5-step* technique is significantly smaller than the one in the conventional *4-step* technique, although the double frequency dependence is still the same (Hariharan et al., 1987).

Schmit and Creath further developed Schwider's concept into what they called *extended n-step averaging*, generating new algorithms from the sequential application of the averaging technique (Schmit and Creath, 1995). Each new algorithm has a smaller phase error than the algorithm from which it developed. Two different classes of algorithms were presented, which were generated from the *4-step* and the *3-step* techniques, respectively, the *A* and *B* algorithms.

Take,

$$\begin{aligned}
I_1 &= I_0\left[1+\gamma\cos\alpha\right] \\
I_2 &= I_0\left[1+\gamma\cos\left(\alpha+\frac{1}{2}\pi\right)\right] = I_0\left[1-\gamma\sin\alpha\right] \\
I_3 &= I_0\left[1+\gamma\cos\left(\alpha+\pi\right)\right] = I_0\left[1-\gamma\cos\alpha\right] \\
I_4 &= I_0\left[1+\gamma\cos\left(\alpha+\frac{3}{2}\pi\right)\right] = I_0\left[1+\gamma\sin\alpha\right] \\
I_5 &= I_0\left[1+\gamma\cos\left(\alpha+2\pi\right)\right] = I_0\left[1+\gamma\cos\alpha\right] \\
I_6 &= I_0\left[1+\gamma\cos\left(\alpha+\frac{5}{2}\pi\right)\right] = I_0\left[1-\gamma\sin\alpha\right]
\end{aligned} \tag{3.42}$$

With a *4-step* technique, the ratios obtained with frames 2 to 5 and 3 to 6,

$$\begin{aligned}
\frac{n_2}{d_2} &= \frac{I_4-I_2}{I_5-I_3} \\
\frac{n_3}{d_3} &= \frac{I_4-I_6}{I_5-I_3}
\end{aligned} \tag{3.43}$$

result in,

$$\frac{n_2+n_3}{d_2+d_3} = \frac{2I_4-I_2-I_6}{2\left(I_5-I_3\right)} \tag{3.44}$$

Adding Eq. 3.41 with Eq. 3.44 generates the *6-step*, *A*, algorithm,

$$\frac{(n_1+n_2)+(n_2+n3)}{(d_1+d_2)+(d_2+d_3)} = \frac{-3I_2+4I_4-I_6}{I_1-4I_3+3I_5} \tag{3.45}$$

The *3-step*, *B*, algorithms result from

$$\begin{aligned}
\frac{n_1}{d_1} &= \frac{I_1 - 2I_2 + I_3}{I_1 - I_3} \\
\frac{n_2}{d_2} &= \frac{-I_2 + I_4}{I_2 - 2I_3 + I_4} \\
\frac{n_3}{d_3} &= \frac{-I_3 + 2I_4 - I_5}{-I_3 + I_5} \\
\frac{n_4}{d_4} &= \frac{I_4 - I_6}{-I_4 + 2I_5 - I_6}
\end{aligned} \tag{3.46}$$

for 3 steps,

$$\begin{aligned}
\frac{n_1 + n_2}{d_1 + d_2} &= \frac{I_1 - 3I_2 + I_3 + I_4}{I_1 + I_2 - 3I_3 + I_4} \\
\frac{n_2 + n_3}{d_2 + d_3} &= \frac{-I_2 - I_3 + 3I_4 - I_5}{I_2 - 3I_3 + I_4 + I_5} \\
\frac{n_3 + n_4}{d_3 + d_4} &= \frac{-I_3 + 3I_4 - I_5 - I_6}{-I_3 - I_4 + 3I_5 - I_6}
\end{aligned} \tag{3.47}$$

for 4 steps,

$$\begin{aligned}
\frac{(n_1 + n_2) + (n_2 + n3)}{(d_1 + d_2) + (d_2 + d_3)} &= \frac{I_1 - 4I_2 + 4I_4 - I_5}{I_1 + 2I_2 - 6I_3 + 2I_4 + I_5} \\
\frac{(n_2 + n3) + (n_3 + n_4)}{(d_2 + d_3) + (d_3 + d_4)} &= \frac{-I_2 - 2I_3 + 6I_4 - 2I_5 - I_6}{I_2 - 4I_3 + 4I_5 - I_6}
\end{aligned} \tag{3.48}$$

for 5 steps and,

$$\frac{I_1 - 5I_2 - 2I_3 + 10I_4 - 3I_5 - I_6}{I_1 + 3I_2 - 10I_3 + 2I_4 + 5I_5 - I_6} \tag{3.49}$$

for 6 steps.

Alternative equations could have been issued if different numerators and denominators had been adopted, or different signals chosen for the n/d ratios. For instance, $d_4 = I_4 + 2I_5 + I_6$ or $n_3 = I_3 + 2I_4 + I_5$, could have been used instead, which would have produced different algorithms, but perfectly equivalent to the ones shown herein. This principle can be carried on to higher step numbers, but at some point the error reduction doesn't improve significantely. Table 3.1 summarizes these results and figures 3.7 to 3.10 illustrate the application to miscalibration correction on a image with a very small miscalibration, under 1%.

	Class A - *4-step* based	Class B - *3-step* based
Three steps	—	$\frac{I_1-2I_2+I_3}{I_1-I_3}$
Four steps	$\frac{I_4-I_2}{I_1-I_3}$	$\frac{I_1-3I_2+I_3+I_4}{I_1+I_2-3I_3+I_4}$
Five steps	$\frac{2(I_2-I_4)}{2I_3-I_5-I_1}$	$\frac{I_1-4I_2+4I_4-I_5}{I_1+2I_2-6I_3+2I_4+I_5}$
Six steps	$\frac{-3I_2+4I_4-I_6}{I_1-4I_3+3I_5}$	$\frac{I_1-5I_2-2I_3+10I_4-3I_5-I_6}{I_1+3I_2-10I_3+2I_4+5I_5-I_6}$

Table 3.1 - Extended Averaging algorithms for classes A and B up to 6 steps

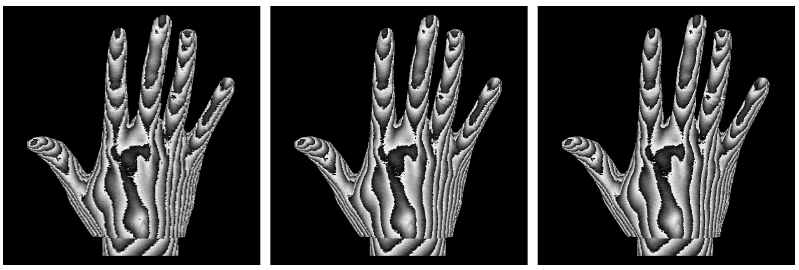

Figure 3.7 - Error reduction with 4-step, A4 to A6, extended averaging algorithms.

Fourier Transform Profilometry

Despite being also a spatial carrier method, the different nature of the Fourier transform fringe analysis method amply justifies illustrating this method separately from the remaining.

The Fourier transform fringe analysis method is unquestionably one of the most successful techniques for fringe pattern analysis. First introduced by Takeda in 1982 (Takeda et al., 1982), the technique was adapted to two-dimensions by Macy (Macy, 1983) in 1983, although that was in essence a slice extension of the one-dimensional model originally proposed by Takeda. Bone (Bone et al., 1986), provided a full 2D version in 1986, along with a set of very interesting observations regarding the inherent errors of the technique and some suggestions as to how these could be overcome. A clever suggestion for separation of the information in reciprocal space was also advanced therein. An extensive study on the error sources of the technique has been made by Kujawinska (Kujawinska, 1993; Kujawinska and Wojciak, 1991). Many other works have been published on this method throughout the years, as it remains one of the most elegant and effective methods for shape measurement, including several important contributions for error reduction (Kreis, 1986; Mertz, 1983; Roddier and

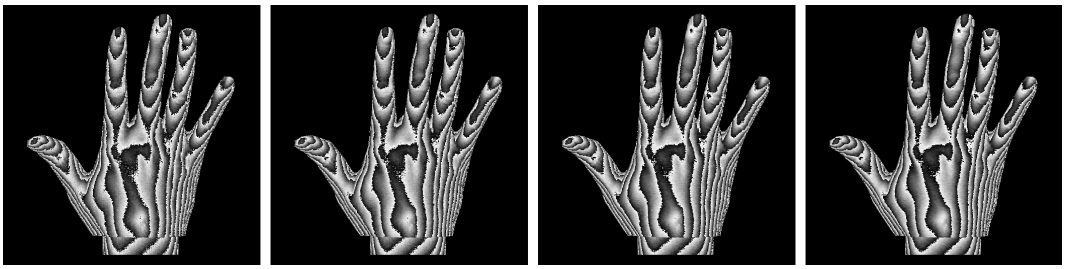

Figure 3.8 - Error reduction with 3-step, B3 to B6, extended averaging algorithms.

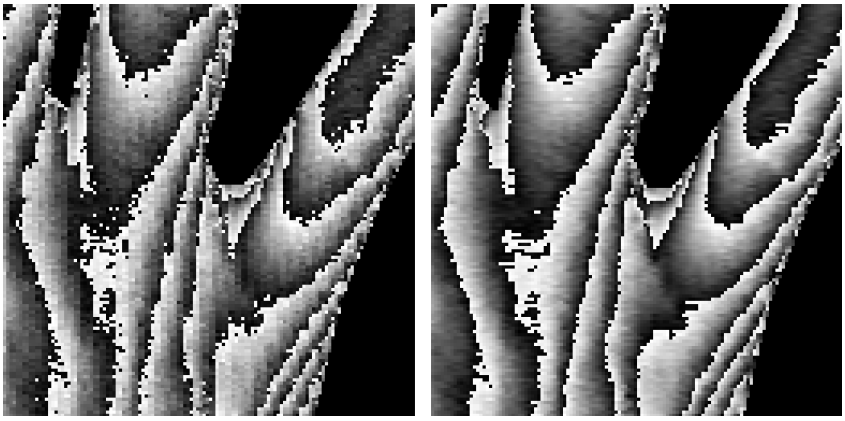

Figure 3.9 - Phase detail for B3 and B6 algorithms showing the double frequency error with the B3 algorithm.

Roddier, 1987; Takeda and Mutoh, 1983).

The full 2D description presented here follows the reasoning by Bone (Bone et al., 1986), or Roddier (Roddier and Roddier, 1987), even if it doesn't add much to the illustration, in case the setup from § 4.3 is used and the fringe pattern is required to lay orthogonal to the xx axis, which is acceptable for most cases.

A sinusoidal fringe pattern projected onto the object under study, such as shown in Fig. 3.11, can be described as before by,

$$g(x,y) = a(x,y) + b(x,y)\cos\left[2\pi f_0 x + \phi(x,y)\right] \tag{3.50}$$

where $a(x,y)$ and $b(x,y)/a(x,y)$ represent the average intensity and fringe visibility or modulation on the surface of the object, f_0 is the fundamental frequency of the observed grating image, and $\phi(x,y)$ is the phase modulation resulting from the object height distribution. The fringes run perpendicular to the paper plane. For convenience of analysis, this fringe pattern can be rewritten as

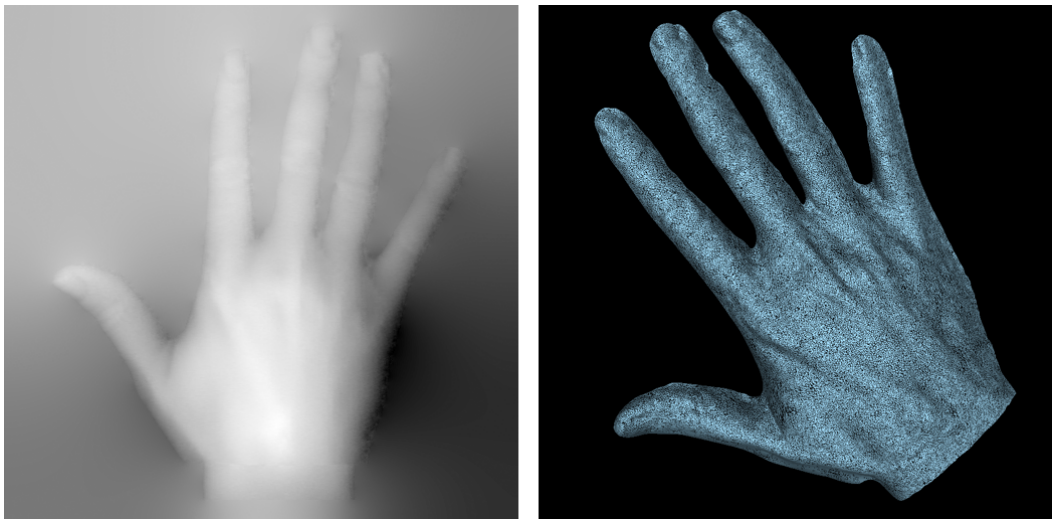

Figure 3.10 - B6 algorithm image after unwrapping and 3D rendering, with visible mesh.

$$g(x,y) = a(x,y) + c(x,y)\exp(2\pi i f_0 x) + c^*(x,y)\exp(-2\pi i f_0 x) \tag{3.51}$$

with the understanding that,

$$c(x,y) = \frac{b(x,y)\exp(i\phi(x,y))}{2} \tag{3.52}$$

and * denotes complex conjugation. The function $c(x,y)$ is known as Complex Fringe Visibility. The Fourier transform of the deformed fringe pattern in the xx direction is,

$$G(u,v) = A(u,v) + C(u - f_0, v) + C^*(u + f_0, v) \tag{3.53}$$

Fig. 3.12 shows a typical log scaled amplitude of a sinusoidal signal, showing the central, dc, term and the two symmetrical terms at $\pm f_0$. As explained by Takeda, these terms, which correspond to the transform of the average intensity and the sinusoidal components, are clearly identifiable in reciprocal space because the spatial variation of $a(x,y)$, $b(x,y)$ and $\phi(x,y)$ is slow when compared to the carrier frequency, f_0. Either of the two sinusoid transform components, shown in Fig. 3.12, can now be isolated from the rest of the spectrum by a filter window and shifted to the origin, to remove the carrier frequency and obtain $C(u,v)$, as illustrated in Fig 3.13.

The inverse transform of $C(u,v)$ yields the complex visibility from Eq. 3.52. The phase map, shown in Fig. 3.14, can be obtained in two distinct ways, either from the real and imaginary parts of $c(x,y)$ as

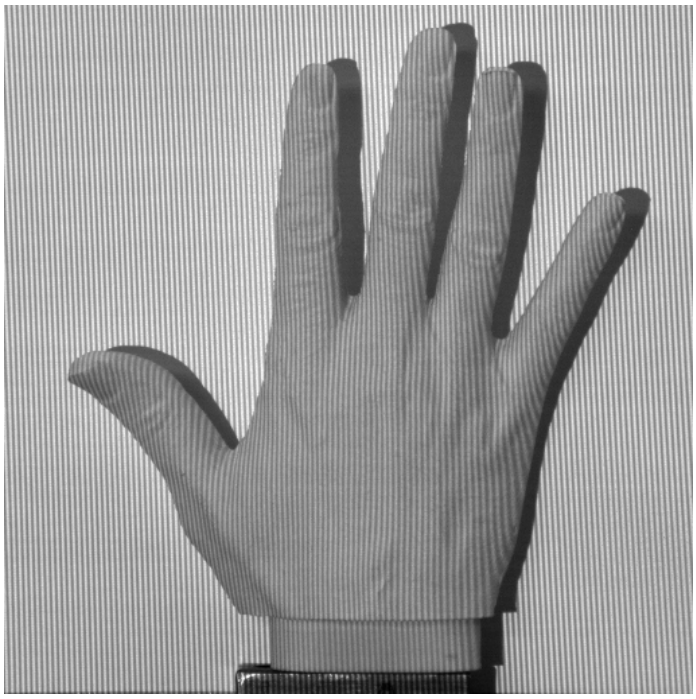

Figure 3.11 - A 128 fringes sinusoidal pattern.

$$\phi(x,y) = \tan^{-1}\left\{\frac{\mathrm{Im}\left[c(x,y)\right]}{\mathrm{Re}\left[c(x,y)\right]}\right\} \tag{3.54}$$

or from the imaginary part of the complex logarithm of $c(x,y)$,

$$\log\left[c(x,y)\right] = \log\left[\frac{b(x,y)}{2}\right] + i\phi(x,y) \tag{3.55}$$

Now, phase is a quantity defined over the interval $[-\pi,\pi]$ and must be demodulated or *unwrapped* before any use can be made of it. The unwrapped phase map is shown on the right in Fig. 3.14. The unwrapping algorithms are discussed in § 3.5.

Measurement errors of the Fourier Transform method

Imaging systems are constrained to physical limitations, such as the image capture device size or the sampling rate on digital systems. These constrains, which impair the image quality in different ways, are shared by every method, not just Fourier analysis, but due to their nature, it seems natural to discuss them here. Other error sources, such as *picket-fence* and *scalloping loss*, are characteristic of the Fourier analysis method, and will be discussed next. An extensive study of the problems relating

Figure 3.12 - FFT of a sinusoidal fringe pattern. Scale is logarithmic and the spectrum origin has been shifted to the center.

to the Fourier Fringe Analysis method was presented by Kujawinska (Kujawinska, 1993; Kujawinska and Wojciak, 1991).

Sampling Digital images are captured by imaging sensors composed of discrete elements. A continuous image is thus sampled by these elements at a rate which is dependent on the device's characteristics. Even if there are sampling geometries more effective than rectangular grids, most digital systems use rectangular grids. A rectangular sampling function at periods Δx and Δy, such as

$$Comb\left(\frac{x}{\Delta x}\right) Comb\left(\frac{y}{\Delta y}\right) \tag{3.56}$$

may then be used to represent sampling, and the discretized image version becomes,

$$g_s(x,y) = g(x,y)\, Comb\left(\frac{x}{\Delta x}\right) Comb\left(\frac{y}{\Delta y}\right) \tag{3.57}$$

The Fourier transform of $g_s(x,y)$ is

$$G_s(u,v) = G(u,v) \otimes \Delta x \Delta y Comb(\Delta x u)\, Comb(\Delta y v) \tag{3.58}$$

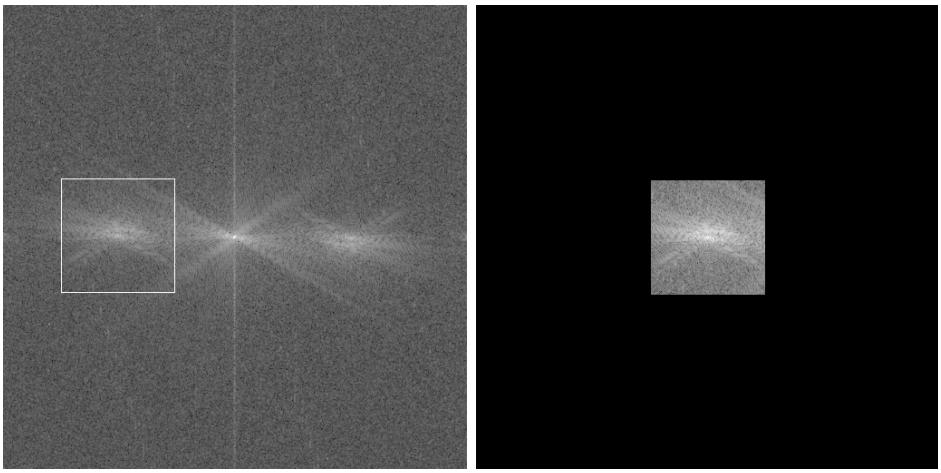

Figure 3.13 - Carrier removal by filtering and shifting the useful spectrum.

or,

$$\begin{aligned} I_s(u,v) &= I(u,v) \otimes \sum_{n=-\infty}^{+\infty} \sum_{m=-\infty}^{+\infty} \delta\left(u - \frac{n}{\Delta x}, v - \frac{m}{\Delta y}\right) = \\ &= \sum_{n=-\infty}^{+\infty} \sum_{m=-\infty}^{+\infty} I\left(u - \frac{n}{\Delta x}, v - \frac{m}{\Delta y}\right) \end{aligned} \tag{3.59}$$

To the extent that the imaging system can be considered Linear Shift Invariant (LSI), this convolution may be regarded as the frequency response modification due to the sampling operation. Physically, it corresponds to erecting replicas of the $G(u,v)$ spectrum at each $(n/\Delta x, m/\Delta y)$ point on the (u,v) frequency plane, i.e., separated by $1/\Delta x$ in uu and $1/\Delta y$ in vv. It is noteworthy that this fact is a consequence of the sampling itself, and will happen independently of the method elected for retrieving phase.

In case the signal $g(x,y)$ is band limited within a square of sides $2B_x$ and $2B_y$, these band replicas will be separable in frequency space as long as,

$$\frac{1}{\Delta x} \geq 2B_x \text{ and } \frac{1}{\Delta y} \geq 2B_y \tag{3.60}$$

and

$$G_s(u,v) = G(u,v) \text{ for } |u| \leq B_x \text{ and } |v| \leq B_y \tag{3.61}$$

which amounts to saying the original $g(x,y)$ signal will be fully recoverable by interpolation if the samples are taken at a rate superior to $\left(1/2B_x, 1/2B_y\right)$.

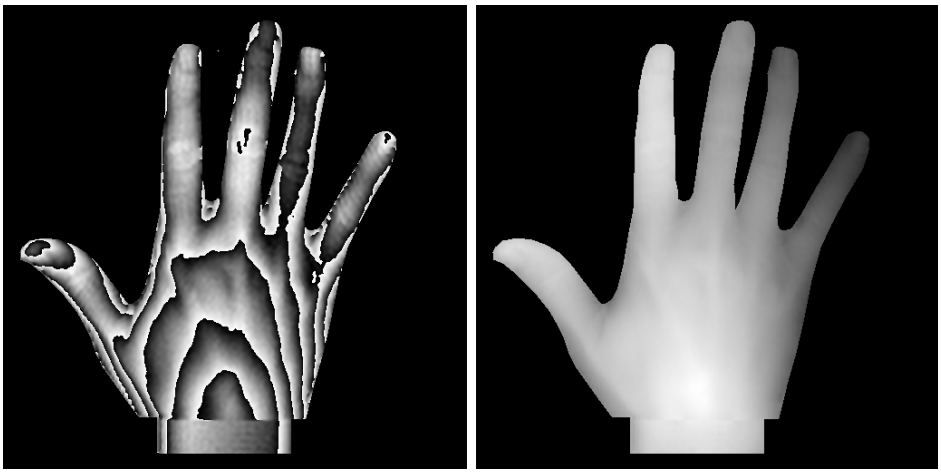

Figure 3.14 - Phase map obtained with the Fourier fringe analysis method.

In case a rectangular or boxcar function, Π, is used to isolate one of the spectrum replicas in frequency space, such as the one at the origin, without loss of generality,

$$H(u,v) = \Pi\left(\frac{u}{2Bx}\right)\Pi\left(\frac{v}{2By}\right) \Longrightarrow h(x,y) = 4B_xB_y sinc\left(2B_x x\right) sinc\left(2B_y y\right) \quad (3.62)$$

then,

$$G_s(u,v)\,\Pi\left(\frac{u}{2Bx}\right)\Pi\left(\frac{v}{2By}\right) = G(u,v) \quad (3.63)$$

or

$$\begin{aligned} g(x,y) &= g_s(x,y) \otimes h(x,y) = \\ &= \left[g(x,y)\, Comb\left(\frac{x}{\Delta x}\right) Comb\left(\frac{y}{\Delta y}\right)\right] \otimes h(x,y) \end{aligned} \quad (3.64)$$

and finally,

$$\begin{aligned} g(x,y) = &\sum_{n=-\infty}^{+\infty}\sum_{m=-\infty}^{+\infty} g\left(\frac{n}{2Bx}, \frac{m}{2By}\right) \\ &sinc\left[2Bx\left(x - \frac{n}{2Bx}\right)\right] sinc\left[2By\left(y - \frac{m}{2By}\right)\right] \end{aligned} \quad (3.65)$$

The interpolation functions in this case are *sinc* functions weighted by the sampled values of $g(x,y)$ at each $\left(n/2B_x, m/2B_y\right)$ point.

This is a fundamental result from sampling theory known as the *Whittaker-Shannon* sampling theorem. In two dimensions this result isn't unique, for other sampling geometries or filter functions may be chosen. Dudgeon and Mersereau treat the problem of multidimensional sampling with variable sampling geometries and notice that hexagonal sampling may be up to 13.4% more efficient than rectangular sampling in two dimensions (Dudgeon and Mersereau, 1984).

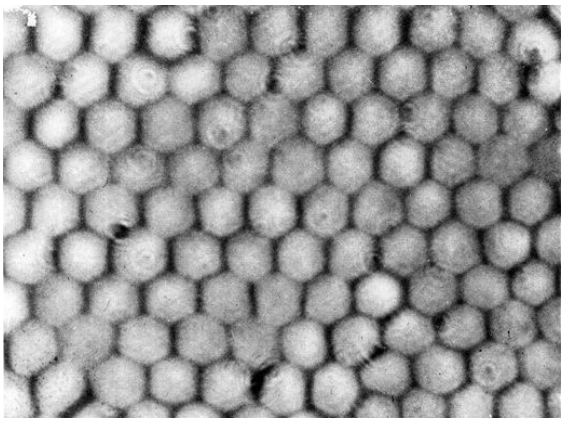

Figure 3.15 - Efficient image sampling - the foveal cone distribution in human eye.

If the sampling rate is not enough to separate the bands in frequency space, an error known as *aliasing* will occur, and higher frequencies will show up as low frequency beats in the final image. Moiré beats or the perception of a car wheel rotating in the wrong sense, are but two examples of aliasing problems.

When applied to fringe projection, this constraint means there must be at least two pixels for discriminating one fringe.

Windowing or apodization A band limited signal requires an infinite support region in reciprocal space. But due to practical reasons this is simply not possible to achieve. It is thus, at best, an approximation to real signals, which are captured by finite sized sensors. The sampled signal isn't really as described in Eq. 3.57 but must be represented by

$$g_s(x,y)\, w(x,y) \tag{3.66}$$

where $w(x,y)$ is a window function taking the value 1 inside a limited space region and 0 otherwise. The transform of this sampled and windowed image is

$$G_s(u,v) \otimes W(u,v) \tag{3.67}$$

where $W(u,v)$ is the Fourier transform of the window $w(x,y)$.

As such, $G_s(u,v)$ will be spread in frequency space according to the transform of the chosen window, a fact known as *leakage*. The ideal window would then be one whose transform is a Dirac delta, but that would correspond to no window at all.

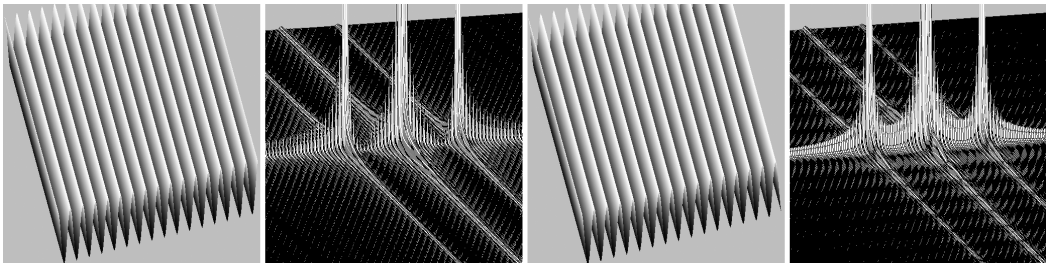

Figure 3.16 - Apodization by a rectangular window - complete vs. incomplete number of wavelengths.

Many windows have been proposed and used for signal analysis over the years. An excellent account of window effects in signal processing can be found in the classical article by Harris who notices that in case a sinusoidal signal has an incomplete number of wavelengths, the spreading of the original transform due to high frequency components is much worse (Harris, 1978). This is shown in Fig. 3.16 where the transform of the ideal cosinusoidal fringe pattern

$$g(x,y) = g_0 \left[1 + \gamma \cos\left(2\pi f_0 x\right)\right] w(x,y) \tag{3.68}$$

is seen with a complete number of wavelengths on the left, showing the dc term and two symmetric peaks which correspond to $C(u - f_0, v)$ and $C^*(u + f_0, v)$, and an incomplete number of wavelengths on the right. The window function, $w(x,y)$, used to build these images was a rectangular window. Fig. 3.17 shows the transform of the exact same function apodized by a Hann window, which is described by,

$$w(x,y) = \frac{1}{2}\left[1 - \cos\left(\frac{2\pi x}{N-1}\right)\right] \tag{3.69}$$

where N represents the total number of pixels in xx direction. The diminishing of the leakage effect is quite noticeable, as is the effect of using an incomplete number of wavelengths. Although the Hann function transform main lobe has a larger half-width than the one from the *sinc* transform of the rectangular function, it goes to zero much faster, which allows a better discrimination of nearby frequencies.

This *feet removal* process of the Fourier transform components is the origin of the word *apodization*.

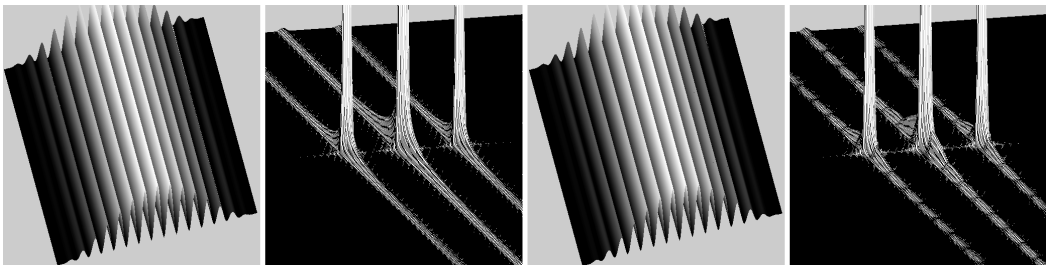

Figure 3.17 - Apodization by a Hann window - complete vs. incomplete number of wavelengths.

The choice of an appropriate window is a matter of trade-off between three criteria, namely:

- the *main lobe width*, which limits the resolution of closely-spaced peaks of approximate height;
- the *height of the first side lobe*, which limits the ability to discriminate a small peak near a larger one;
- the *slope of side lobe drop-off*, which limits the ability to see small peaks further away from a large peak.

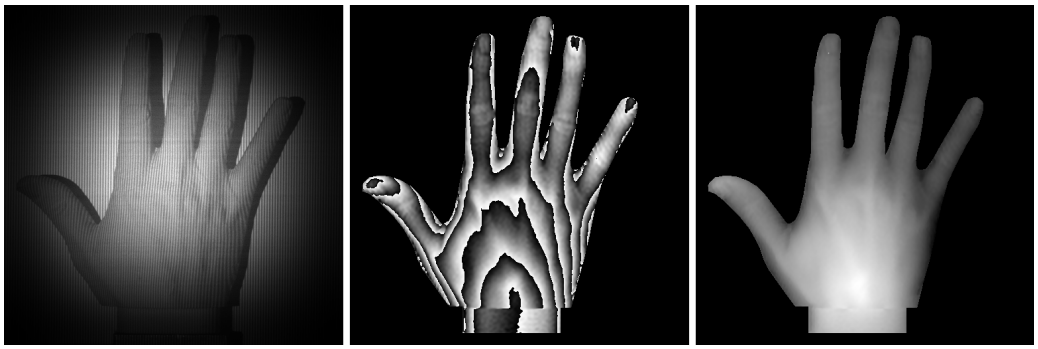

Figure 3.18 - Bidimensional Hann window apodization. Leakage reduction near the border of the object is quite appreciable.

Even if it could be possible to control the number of wavelengths present in the image, this isn't always possible for finite sized objects inside the image, particularly if they are composed of separated parts as in the hand example above. The leakage effect is thus unavoidable and it can be clearly seen on the finger limits of the hand phase map in Figs 3.14 and 3.18.

A class of solutions to this problem has been proposed and became known as *analytic continuation* or *fringe extrapolation* techniques. These solutions are based on the work by Harris who shown that because a finite support function has an analytic spectrum, knowing a portion of this spectrum can, in principle, lead to knowledge of the entire spectrum (Harris, 1964).

An iterative technique for analytic continuation has been proposed independently by Gerchberg and Papoulis (Gerchberg, 1974; Papoulis, 1975), and later improved by Kany and Dainty (Kani and Dainty, 1988). Roddier and Roddier proposed a modified technique which was followed in this work (Roddier and Roddier, 1987).

These techniques are based on the fact that the transform of a sinusoidal signal like the one from Eq. 3.68, modulated by a finite sized window, such as a rectangular window

$$g(x,y) = g_0 \left[1 + \gamma \cos\left(2\pi f_0 x\right)\right] \Pi\left(\frac{x}{a}\right) \tag{3.70}$$

is

$$G(u,v) = sinc(au) + \gamma sinc\left[a\left(u - f_0\right)\right] + \gamma sinc\left[a\left(u + f_0\right)\right] \tag{3.71}$$

spreading or *leaking* energy under the lobes of the *sinc* functions, where a continuous, infinite support, sinusoid would show delta functions instead. Limiting the two symmetrical *sinc* functions to a circle the size of their own cut-off frequency, dropping off the rest of the spectrum and reverse transforming the result will yield a sinusoidal pattern with extended fringes. In case $g(x,y)$ corresponds to a finite sized object, the iterative algorithm keeps on reinforcing the original limited fringes. This is done by switching the region occupied by the object on the extended fringe interferogram by the original fringe covered object and Fourier transforming the result. The new transform will now have reinforced symmetrical peaks and the algorithm is maintained until the change on either the spectrum or the image is less than some pre-established threshold.

A simple intuitive explanation for this result, based on Parseval's energy conservation theorem, is found by considering both the known and unknown object and spectrum energies. Reducing the unknown object energy, by replacing the region occupied by the object with the original interferogram, implies the reduction of the unknown spectrum energy. But this is exactly that part of the spectrum outside the radius of the cut-off frequency. In fact, as can be seen in Fig. 3.19, the spectrum energy outside of the two original selected circles is reduced as the algorithm iterates.

The technique is depicted in Fig. 3.20. The initial image without dc term was obtained with the two steps technique described below.

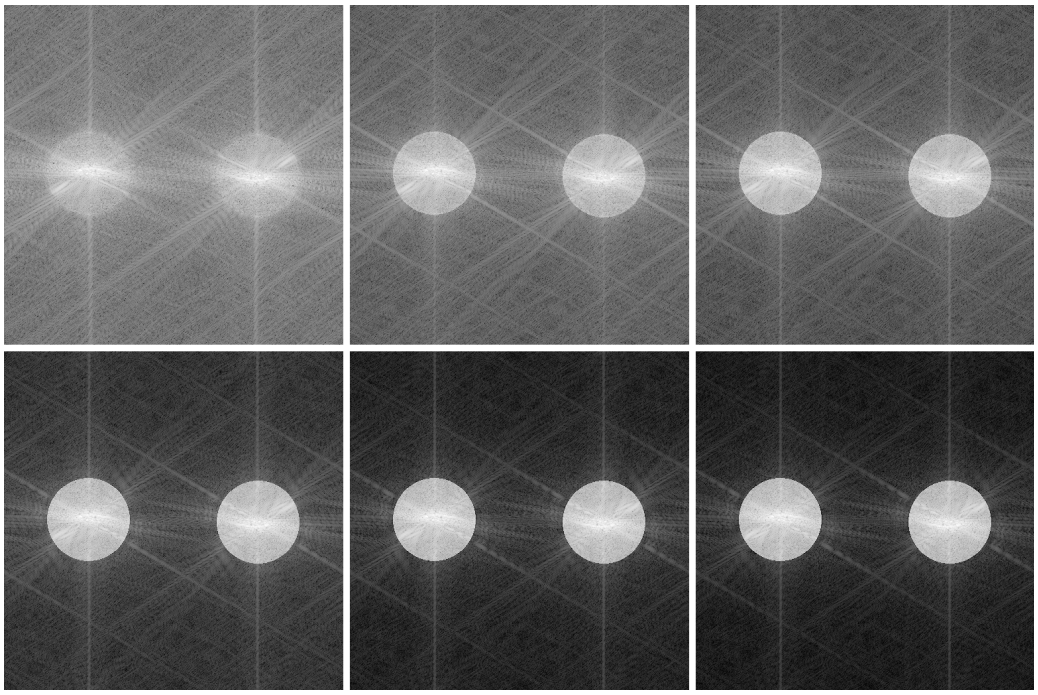

Figure 3.19 - Fourier spectra in Gerchberg iteration algorithm taken after 1, 10, 100, 5000 and 10000 cycles. The energy concentrates more and more inside the cut-off frequency circles.

The reduction of the leakage effect with this technique is quite appreciable as can be seen in Fig. 3.21. The problem with the technique is the necessary number of iterations, which can be as high as some thousands. The improvement to the technique proposed by Kany and Dainty is basically the same as Gerchberg's algorithm, but carried out in a number of steps. After a number of iterations, the region close to the known part of the spectrum is kept and the remainder is set to zero. The algorithm continues to iterate until the next step, at which point a larger portion of the spectrum is kept and so forth.

Another technique for fringe continuation has been proposed by Kujawinska which calculates dummy fringes with the same frequency of the orininal ones at the object, and smoothly extrapolates the data up to the image boundary (Kujawinska, 1993).

***Picket-fence, scalloping loss* and the *zero-padding* technique** The picket-fence effect is the loss of discrimination capacity between nearby frequency peaks which results from the fact the frequency resolution in reciprocal space is too low. In a way, it can be thought of as the frequency counterpart of the aliasing problem, as it is due

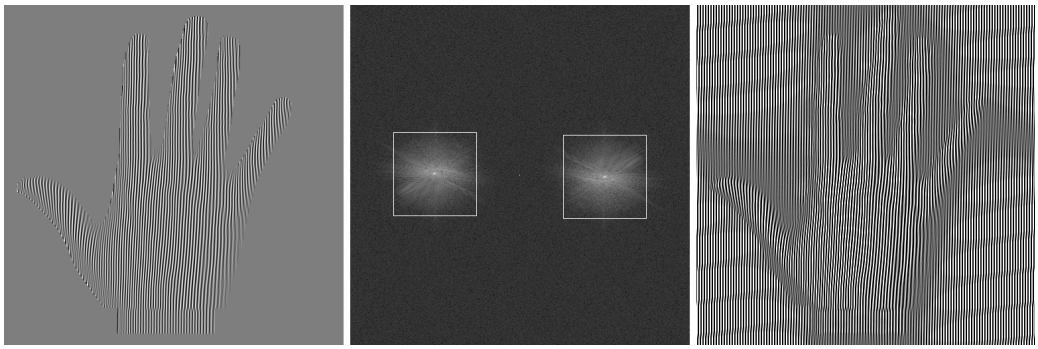

Figure 3.20 - The Gerchberg technique. The picture on the left shows the initial continuousless image, the centre image shows the Fourier transform and the isolation of the two peaks and the picture on the right shows the result after 10000 iterations.

to lack of resolution in the frequency plane, and it causes the mixing up of very similar frequencies. This phenomenon is inherent to the Fourier analysis method and it is depicted in Fig. 3.22. The image on the left was produced with two very close frequencies at 0.25 and 0.275 Hz on a 32 by 32 points cosinusoidal signal sampled at every half-point. The image shows the beat produced by the addition of the two cosines, and the first image to the right shows the Fourier transform of this signal. Although it seems to be composed of just one frequency, a closer look reveals that the peaks are not symmetric, denoting the presence of a nearby frequency. Adding 64 zeros to each side of the original signal, on both dimensions will increase the resolution of the DFT, as required by the fact the DFT has the same size of the original signal. The transform of the twice zero-padded signal is shown in the third image, and the presence of two frequencies is clearly given away here. Still, the problem remains as to whether the peaks of these frequencies show the correct values, a problem known as *Scalloping Loss*. A larger zero padding of 16 times or 1024 points, shown on the last image, shows the frequency peaks are really very similar.

Two step projection technique for resolution enhancement

The size of the filter window poses a severe limitation on the Fourier transform phase analysis method's resolution. Even though the spectrum region centred at the projected frequency is band-limited, its size may extend below the cut-off frequency of the continuum dc term. It is thus desirable to eliminate this term in order to enlarge the window as much as possible.

On the other hand, as already mentioned above, the application of a filter window on a spectrum region is a frequency space analogue of the window limitation

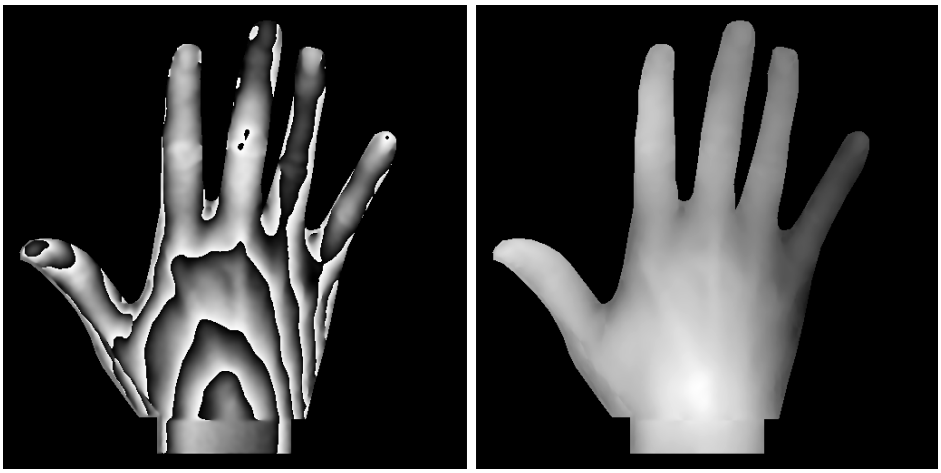

Figure 3.21 - The result from the Gerchber algorithm. A considerable reduction in leakage is readily seen at the object boundary.

on the image space. Some sort of leakage is expected to occur upon inverse Fourier transformation, as noted by Kreis (Kreis, 2005). Enlarging the filter window size after eliminating the dc term is similar to zero-padding this window, which is bound to improve the resolution of the reverse transform for phase determination.

A method for removing the dc term was developed at LOME which is based on the acquisition of two images with projected fringe patterns at right angles (Tavares and Vaz, 2006). The technique is simply described as follows.

Let $g_x(x,y)$ and $g_y(x,y)$ describe two object images with fringe patterns running at right angles such that,

$$g_x(x,y) = a(x,y) + c(x,y)\exp(2\pi i f_0 x) + c^*(x,y)\exp(-2\pi i f_0 x) \tag{3.72}$$

and

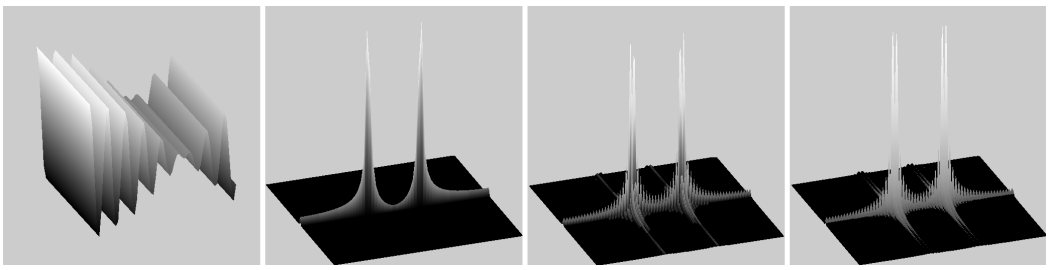

Figure 3.22 - Picket fence and Scalloping loss. The effect of zero-padding with different sizes.

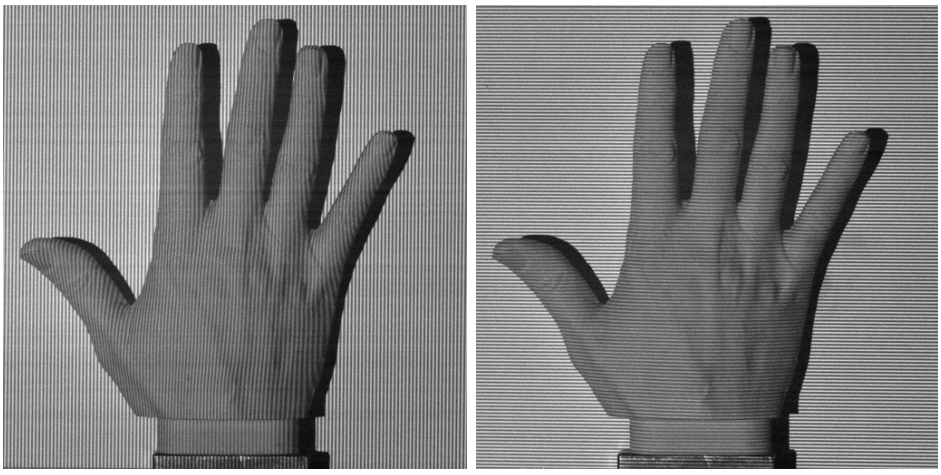

Figure 3.23 - Orthogonal fringe patterns with 128 fringes.

$$g_y(x,y) = a(x,y) + c(x,y)\exp(2\pi i f_0 y) + c^*(x,y)\exp(-2\pi i f_0 y) \tag{3.73}$$

as before. The Fourier transforms of the two images are described by,

$$G_u(u,v) = A(u,v) + C(u - f_0, v) + C^*(u + f_0, v) \tag{3.74}$$

and

$$G_v(u,v) = A(u,v) + C(u, v - f_0) + C^*(u, v + f_0) \tag{3.75}$$

as shown on the left and centre images in Fig. 3.24.

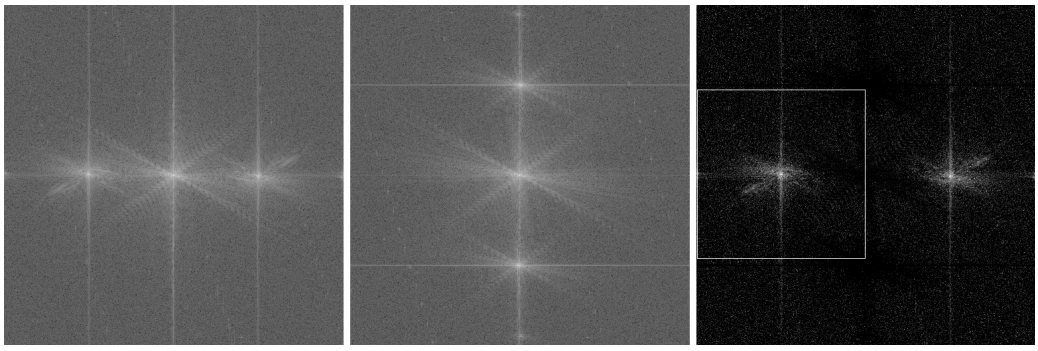

Figure 3.24 - Orthogonal projection spectra and clipping result.

It is clear from the transform equations above and the examination of both spectra that the central dc term is equal in both cases, in case the contrast and gain of the

two fringe patterns is kept constant and the background intensity variation under control, which suggest a simple form to remove it. Subtraction of equations 3.74 and 3.75 above produces,

$$\begin{aligned} G_u(u,v) - G_v(u,v) &= C(u-f_0,v) + C^*(u+f_0,v) \\ &\quad -C(u,v-f_0) - C^*(u,v+f_0) \end{aligned} \tag{3.76}$$

which means that keeping just the positive part of this equation, i.e., dropping the negative part of the resulting image altogether, results in

$$G(u,v) = C(u-f_0,v) + C^*(u+f_0,v) \tag{3.77}$$

It is interesting to note that any visibility variation between the two original images will be totally eliminated by this clipping operation. The resulting spectrum can be seen on the right in Fig. 3.24, together with the mask limits that can now be used for carrier removal. The outcome of this mask enlargement is a higher resolution phase map that can be seen in Fig. 3.25 together with the unwrapping result.

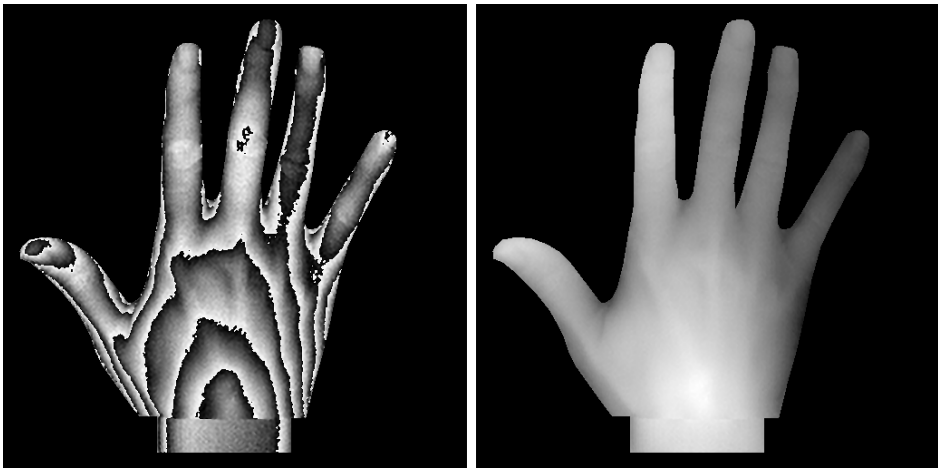

Figure 3.25 - Phase map and unwrapping result obtained with the orthogonal projection technique.

Pirga had already suggested two-directional phase acquisition in Spatial Carrier Phase-Shift, with a very systematic description of proper bandwidth boundaries (Pirga and Kujawinska, 1995).

The relevant publication can be found in Appendix E.

Spatial analogues of the Fourier Transform method

A space domain processing procedure equivalent to the frequency domain Fourier transform method was first advanced by Ichioka and Inuiya in 1972 based on an analogue electronic synchronous detection system. The method was refined by Mertz several years later, also with the use of electronic hardware (Mertz, 1983) and Womack one year later, who introduced the digital synchronous demodulation of interferograms with a linear carrier (Womack, 1984).

The synchronous spatial method proposed by Womack can be described as follows. Let the interferogram irradiance be described as usual by

$$I(x,y) = I_0 \left[1 + \gamma \cos\left(w_0 x + \phi(x,y)\right)\right] \tag{3.78}$$

Multiplying the intensity by $\sin(w_0 x)$ and $\cos(w_0 x)$ results in

$$\begin{aligned} I_s(x,y) &= I(x,y)\sin(w_0 x) = \\ &= I_0 \left\{ \sin(w_0 x) + \frac{\gamma}{2}\left[\sin\left(2w_0 x + \phi(x,y)\right) - \sin\left(\phi(x,y)\right)\right] \right\} \\ I_c(x,y) &= I(x,y)\cos(w_0 x) = \\ &= I_0 \left\{ \cos(w_0 x) + \frac{\gamma}{2}\left[\cos\left(2w_0 x + \phi(x,y)\right) + \cos\left(\phi(x,y)\right)\right] \right\} \end{aligned} \tag{3.79}$$

I_s and I_c contain three harmonics at frequencies 0, w_0 and $2w_0$. Supposing the carrier frequency is much larger than the ϕ variation, i.e.,

$$w_0 \gg \frac{d\phi}{dx} \tag{3.80}$$

the ϕ component can be separated by the remaining spectrum by low pass filtering of I_s and I_c,

$$\begin{aligned} LPF\left[I_s(x,y)\right] &= I(x,y)\sin(w_0 x) = -I_0 \frac{\gamma}{2}\sin\left(\phi(x,y)\right) \\ LPF\left[I_c(x,y)\right] &= I(x,y)\sin(w_0 x) = I_0 \frac{\gamma}{2}\cos\left(\phi(x,y)\right) \end{aligned} \tag{3.81}$$

and

$$\phi(x,y) = \arctan\left\{ -\frac{LPF\left[I_s(x,y)\right]}{LPF\left[I_c(x,y)\right]} \right\} \tag{3.82}$$

The spatial domain technique doesn't require the calculation of Fourier transforms and their inverses, which renders the technique considerably faster. The problem with this technique is the presence of high frequency errors in the filtered Fourier

spectrum, due to the fact that there is always some leakage present which causes a finite spread around the zero gain frequencies of the low-pass filter.

A technique which doesn't make use of a carrier was proposed by Moore and Mendoza-Santoyo (Moore and Mendoza-Santoyo, 1995), inspired on the work by Kreis on the Fourier transform method (Kreis, 1986). In case the carrier frequency is dispensed, the interferogram irradiance can be described by

$$I(x,y) = I_0 \left[1 + \gamma \cos\left(\phi(x,y)\right)\right] \tag{3.83}$$

Now, I_s and I_c become,

$$\begin{aligned} I_s(x,y) &= I(x,y)\sin(w_0 x) = \\ &= I_0 \left\{ \sin(w_0 x) + \frac{\gamma}{2}\left[\sin\left(w_0 x + \phi(x,y)\right) + \sin\left(w_0 x - \phi(x,y)\right)\right] \right\} \\ I_c(x,y) &= I(x,y)\cos(w_0 x) = \\ &= I_0 \left\{ \cos(w_0 x) + \frac{\gamma}{2}\left[\cos\left(w_0 x + \phi(x,y)\right) + \cos\left(w_0 x - \phi(x,y)\right)\right] \right\} \end{aligned} \tag{3.84}$$

The lowest frequency terms are the third on both expressions, i.e., the frequency difference terms, and a low pass filter will yield,

$$\begin{aligned} LPF\left[I_s(x,y)\right] &= I_0 \frac{\gamma}{2}\sin\left(w_0 x - \phi(x,y)\right) \\ LPF\left[I_c(x,y)\right] &= I_0 \frac{\gamma}{2}\cos\left(w_0 x - \phi(x,y)\right) \end{aligned} \tag{3.85}$$

An inclined phase map can thus be obtained as,

$$\phi(x,y) - w_0 x = \arctan\left\{ -\frac{LPF\left[I_s(x,y)\right]}{LPF\left[I_c(x,y)\right]} \right\} \tag{3.86}$$

This method shows a phase signal ambiguity and has limited application.

Yanez-Mendiola proposed a very interesting iterative method for reducing the boundary errors that result from the unavoidable imaging window. The method starts with an estimate of true phase given by the synchronous method, and iterates in order to find the optimum phase value that minimize the least-squares error in interferogram intensity (Yanez-Mendiola et al., 2001). Let this error be given by,

$$\chi^2(x,y) = \left\{ I_n(x,y) - \cos\left[w_0 x + \phi(x,y)\right] \right\}^2 \tag{3.87}$$

where $I_n(x,y)$ is the normalized interferogram intensity without dc term,

$$I_n(x,y) = \cos\left[w_0 x + \phi(x,y)\right] \tag{3.88}$$

Using a steepest descent method, $\phi_i(x,y)$ is determined by setting

$$\phi_{i+1} = \phi_i - \eta \frac{\partial \chi^2}{\partial \phi_i} \tag{3.89}$$

where the error derivative is,

$$\frac{\partial \chi^2}{\partial \phi_i} = 2\left\{I_n(x,y) - \cos\left[w_0 x + \phi_i(x,y)\right]\right\} \sin\left[w_0 x + \phi_i(x,y)\right] \tag{3.90}$$

and the initial phase estimate, $\phi_0(x,y)$, is found with the synchronous method, Eq. 3.82.

3.5 Phase unwrapping

A camera cannot measure three-dimensional coordinates. Two cameras in a triangulation setup, typical of photogrammetric devices, are necessary to do so. In PMP, this ability is achieved through the use of a pattern projection device and a camera, but then, the information retained by the instrument is *phase*, which is a lot more than the intensity information a camera is capable of capturing. Phase is the fundamental difference between a hologram and a photograph. The hologram successfully retains the object and reference wave fields phase and intensity information, and that's about all that's needed to reconstruct its real and virtual 3D images.

Now, phase is not a signal but a *property* of a signal instead. It has to be calculated, as it relates to the temporal or spatial wavelengths and influences the signal through phase principal values, i.e., those values lying between $\pm\pi$ radians. These values are called *wrapped* phase values because the absolute phase is wrapped into $[-\pi, +\pi]$. Thus, the calculated function isn't really phase but a highly non-linear function called *wrapped phase*, which relates to phase through,

$$\psi(x,y) = \phi(x,y) + 2\pi n(x,y) \tag{3.91}$$

In order to find an estimate for the phase, $\phi(x,y)$, this function has to be demodulated or unwrapped before further use.

A very significant effort has been put into the issue of phase unwrapping over the last few decades, simply because it is a problem which arises in many different contexts. From magnetic permeability studies to radar detection, Magnetic Resonance Imaging (MRI) or electron holography, phase, or better still phase shift, is the physical property at hand, and must invariably be unwrapped at some point. It shouldn't come as a surprise then that different approaches have been taken to solve this problem. One-dimensional phase unwrapping, for example, arising in

the context of signal analysis, has different constraints than does the two-dimension problem, typical of image processing. And the type of noise arising in different contexts can be utterly different too, which poses an additional burden on the chosen algorithms. Even in engineering applications which require image processing, such as surface metrology, different image acquisition methods may imply different approaches for unwrapping. Interferometric methods using coherent light, subject to high noise speckle images, may require filtering prior to unwrapping in order to obtain meaningful results. The problem with filtering prior to unwrapping is a sensitive one, because the fringe structure has to be maintained, or otherwise unwrapping will become meaningless altogether. Kemao developed a filtering methodology based on the Windowed Fourier Transform (WFT), with impressive results, which renders the unwrapping operation much simpler (Kemao, 2007; Qian et al., 2005). The WFT is also known as Gabor Transform, in case the transform kernel is obtained with a Gaussian window and it is a close cousin of the Orthogonal Wavelet Transform (OWT), also used in noise reduction (Mallat, 1999).

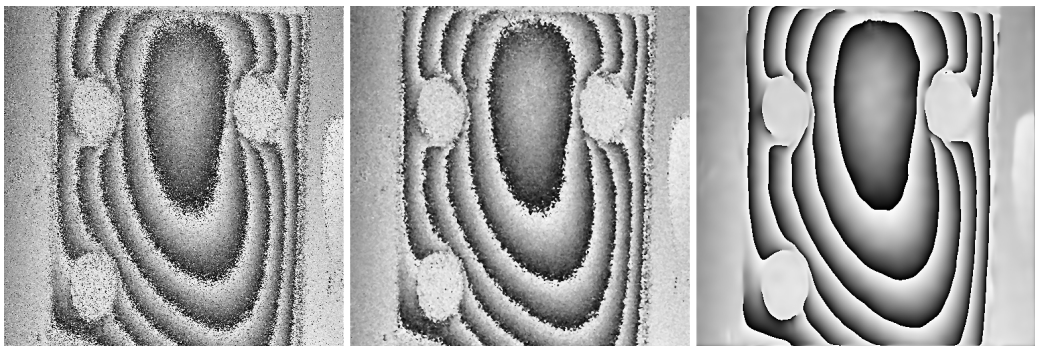

Figure 3.26 - Data processing prior to unwrapping. A noisy phase map filtered with a 3x3 median filter and a WFT at LOME.

Many other filter approaches had been used previously, such as the median filter, known to effectively remove the type of noise known as *salt and pepper*, i.e., isolated pixels or small clusters of data (Creath, 1985; Vikhagen, 1990). In interferometric applications using high quality apparatus, the quality of the phase map is already very good, requiring little or no filtering at all.

Phase unwrapping in the context of 3D surface metrology, is a problem characterized by clean, low noise, phase maps, which facilitates the unwrapping procedure. On the other hand, simple, continuous surfaces with smooth phase gradients, typical of stress analysis for example, cannot be expected, as the engineering surfaces under analysis span a wide range of more or less complicated shapes. A steep shape or a step, for instance, may present phase gradients far greater than the resolution limit

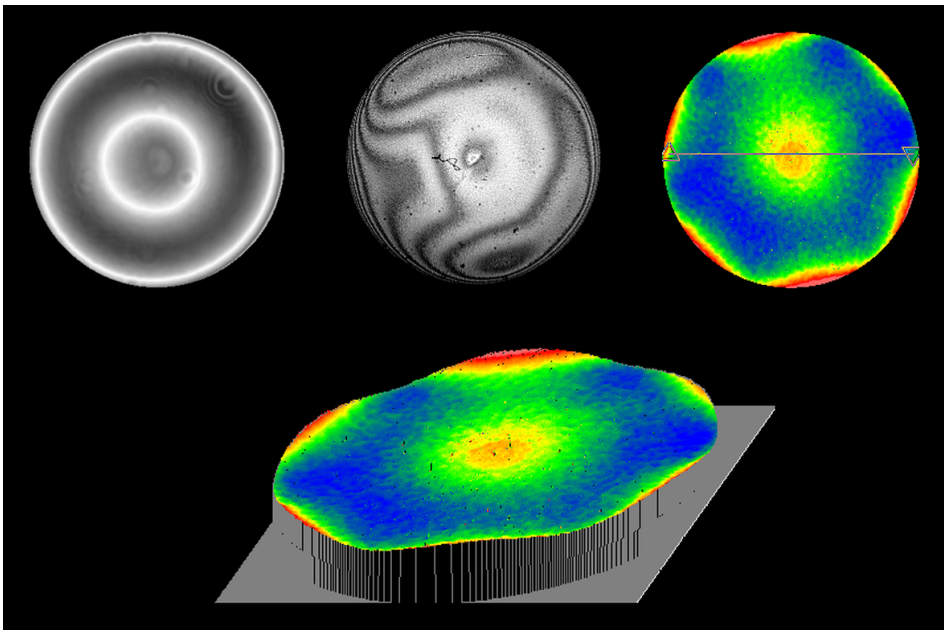

Figure 3.27 - Interferometric optics measurement and control. Courtesy, Zygo Corp.

imposed by the image sampling capabilities. In such cases, phase discontinuities are bound to appear which render the unwrapping task a formidable one.

Phase unwrapping techniques are best characterized by splitting them into two classes. The techniques known as *path-following*, which integrate phase along a prescribed path that can either depend or not on the data and *full-field* methods, which are global, in the sense that phase is calculated independently for every pixel. The description that follows is merely included for completion of the present dissertation, the only method implemented in the course of this work having been *Volkov's deterministic method*. This method is a low computational burden global method, robust to every application it has been tested with, and well suited for 3D surface metrology, as far as the applications in this work go. An excellent in-depth analysis of several methods and quality measures of phase unwrapping can be found in Ghiglia and Pritt's book (Ghiglia and Pritt, 1998), and in the review articles by Robinson (Robinson, 1993), and Judge (Judge and Bryanston-Cross, 1994).

Path-following methods

Phase map fringe discontinuities, which represent poles in the complex exponential phase function, seem to be the central problem in phase unwrapping. The phase difference between any two points of an interferogram must remain constant, inde-

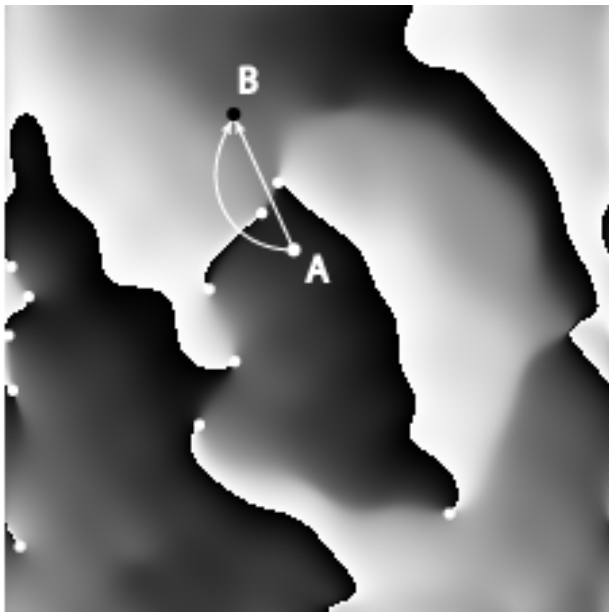

Figure 3.28 - Discontinuities in a phase map marked with white dots. The number of phase transitions from A to B depend on the chosen path.

pendently of the path followed by the fringe counting procedure, unless this path goes through such a discontinuity, as shown in Fig. 3.28. Discontinuities seem to arise as a result of either shape steep changes, aliasing or noise corrupted phase gradients, all three of which can generate the equivalent of local rotational components on the phase gradient field, thus compromising the necessary condition for path independence, $\nabla \times \nabla\phi \equiv \mathbf{0}$ (Ghiglia and Pritt, 1998).

The success of the unwrapping operation is thus dependent on the chosen path, except of course if some way to avoid erroneous or inconsistent data is built into the procedure. This is in fact the principle behind most of path-following methods proposed to date. In a way, phase residues are the problem and the solution to phase unwrapping at the same time, for they alone can indicate the proper paths.

Linear Scanning

The simplest of all phase unwrapping models is an extension of the algorithm originally advanced by Itoh while analysing the one dimensional problem (Itoh, 1982). It involves a line by line data scan, integrating the wrapped phase differences along each line. The phase on all scanned lines can be related to by either determining the phase difference between pixels on two lines at the end of each line or by scanning through a vertical line at the end of the line by line scanning procedure. A variation of

this method, used by Robinson and Williams to unwrap ESPI and holographic phase maps, calculates the phase gradient at each point in two simultaneous directions and if the fringe order agrees with the order from the previous unwrapped pixels, the process continues to the next pixel, otherwise the pixel is marked to avoid influencing the next pixel calculation (Robinson and Williams, 1986).

The success of this approach is related to one of the major problems with path integration methods, i.e., the fact that one error may propagate along the scanning path.

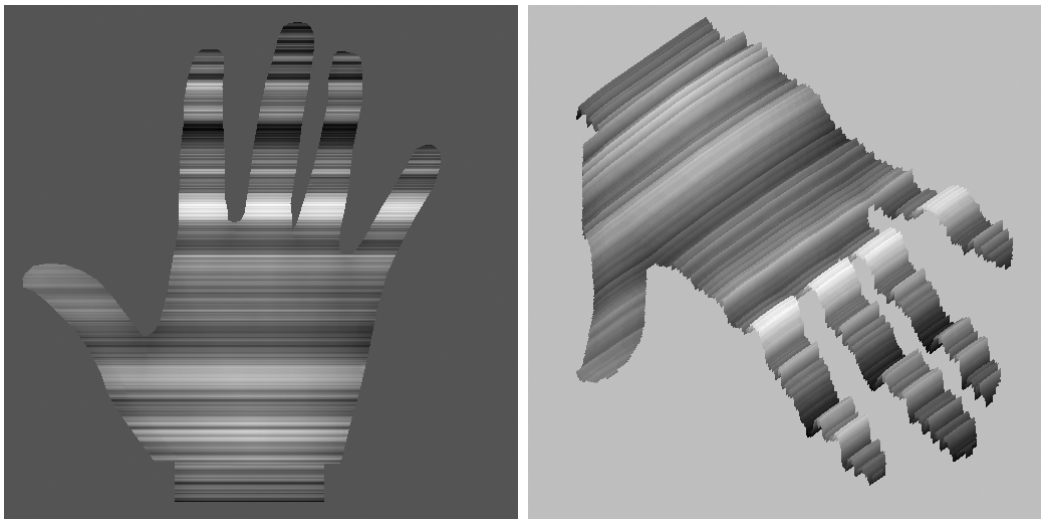

Figure 3.29 - Simple linear scanning phase unwrapping. The effect of error propagation is evident. Courtesy, H. Lopes.

Spiral Scanning

The previous approach was extended by several authors to a set of spiral paths, starting at a central pixel and measuring the phase gradient between the current pixel and a nxn neighbourhood of pixels that have already been unwrapped. This technique is prone to problems with irregularly shaped clusters of masked pixels.

Pixel queuing

Queuing refers to a method of building a list of "good" and "bad" pixels to unwrapp, prior to unwrapping. The pixels selected as being "good" pixels are less likely to propagate errors and are unwrapped first. Queues can be built in different ways, such as comparing the phase difference between each pixel and its neighbours and labelling as good the ones with the smallest phase difference, or examining the fringe contrast

at each point and selecting the ones with the highest contrast first. The complete phase map may then be considered an undirected graph and a Minimum Spanning Tree (MST) established which links pixels with smallest phase gradient first.

Region Scanning

Phase unwrapping can also be processed by regions, istead of isolated pixels, as suggested by Kwon (Kwon et al., 1987). Phase consistent pixels are grouped into regions which are merged into larger regions in case there are no inconsistencies accross boundaries. This approach reduces calculation burden by minimizing the number of decisions about phase relationships. A combination of region scanning and pixel queuing was advanced by Towers which divides the entire phase map into square tiles that are unwrapped independently to each other. Phase data across tile boundaries is compared to adjacent tiles in order to assemble the tiles together with a MST (Towers et al., 1991).

Branch Cutting

Branch cutting refers to a method which looks for phase data residues and places cuts on all pairs or, if that fails, onto the data border. These cuts prevent the unwrapping path from going through data discontinuities and ensures a correct phase unwrapping. At first, that seems to be path dependent, but Goldstein developed the algorithm in such a way as to make sure all the residue polarities are balanced, which in turn implies their sum is zero as is the integral along any closed contour of the phase data (Goldstein et al., 1988). This makes the method path independent. Goldstein's method is not full-proof, as shown by Ghiglia with a simple shear example (Ghiglia and Pritt, 1998). An improved version of Goldstein's method was proposed by Ghiglia, which uses a pre-processing nearest-neighbour procedure to connect adjoining residues and remove them before applying Goldstein's method.

Quality-Guided methods

A number of quality driven phase unwrapping techniques have been proposed over the years. In some phase calculation methods, such as the temporal phase unwrapping below, a quality measure seems to be the most appropriate approach to reduce or even decimate data. The reasoning behind the application of a quality measure to phase unwrapping is guided by the fact that residues tend to show low quality values and so, a good quality map should be able to guide integration without going through unbalanced residue pairs. Quality measures such as the second order

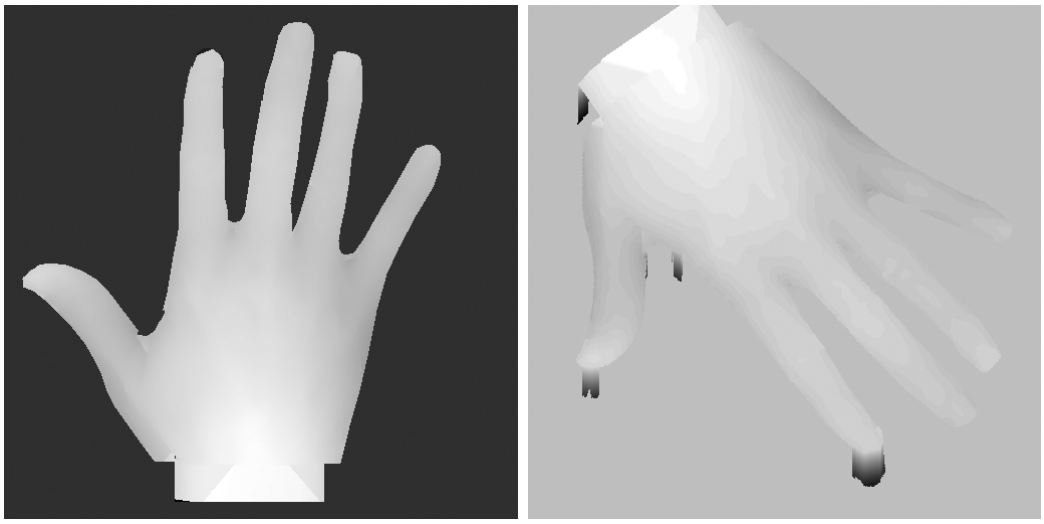

Figure 3.30 - Goldstein's branch cut method. Courtesy, H. Lopes

partial derivatives, the modulation of interference fringes or even variance of phase derivatives has been proposed (Ghiglia and Pritt, 1998).

Mask-Cutting

Mask-cutting is the combination of Goldstein's branch cut method with Quality-guiding, to produce a steering method for placing the branch cuts. The quality-guided branch cuts can be elected in different ways. Either by defining a cost function for each cut, by analysing the placement path correlation or by growing pixel masks through regions identified as being "low-quality". In the latter case, the mask starts at a residue and terminates whenever the total residue charge it connects is zero or when it reaches the image border, ensuring path independence either way.

Flynn's Minimum Discontinuity

Flynn's approach is a technique that iterates through the image, identifying discontinuities on the data that are joined into loops, and adding the necessary multiple of 2π to the pixels enclosed in each loop, until no loops remain. Flynn further advocates the use of an array of weights that indicates data reliability, constraining the discontinuities to low quality regions - the *minimum weighted discontinuity* solution.

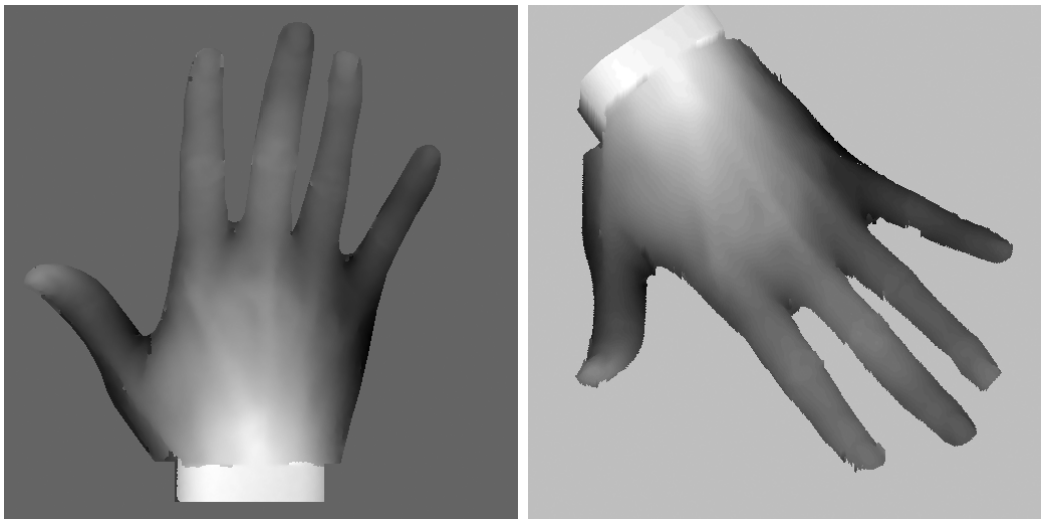

Figure 3.31 - Quality-guided phase unwrapping. The few errors that remain seem to occur near border regions, where noise may occur. Courtesy, H. Lopes.

Cellular Automata

A Cellular Automaton is a discrete dynamical system composed of cells disposed in a regular spatial grid. Each cell can have a finite number of states and is updated according to a local rule, so that the state of a cell at a given time depends only on its own state one time step previously, and the states of its nearby neighbours at the previous time step. All cells on the lattice are updated synchronously. Thus the state of the entire lattice advances in discrete time steps.

Ghiglia et al proposed a Cellular Automaton for phase unwrapping where the test for a 2π phase jump at each pixel is determined based on the value of each pixel and it's 4 nearest neighbours in vertical and horizontal directions, as depicted in Fig. 3.34 (Ghiglia et al., 1987).

The rule for growth entails computing the difference between the central pixel and its 4 neighbours so that whenever it is greater than π, a $+1$ or -1 vote is recorded depending on the sign of that difference. The 4 votes are then summed and $+2\pi$ or -2π is added to the central pixel according to the resultant sum sign. When the four votes are balanced and sum up to zero, an arbitrary decision of adding 2π is made and if any of the pixels in the cell has been masked as invalid phase, its vote is ignored. The cell moves through the entire image modifying it and each application to the entire image is considered one iteration. After several iterations the growth mechanism seems to stall. Then, an averaging between the last two iterations is kept on each pixel and the resulting phase map has one fringe less. The entire map is thus

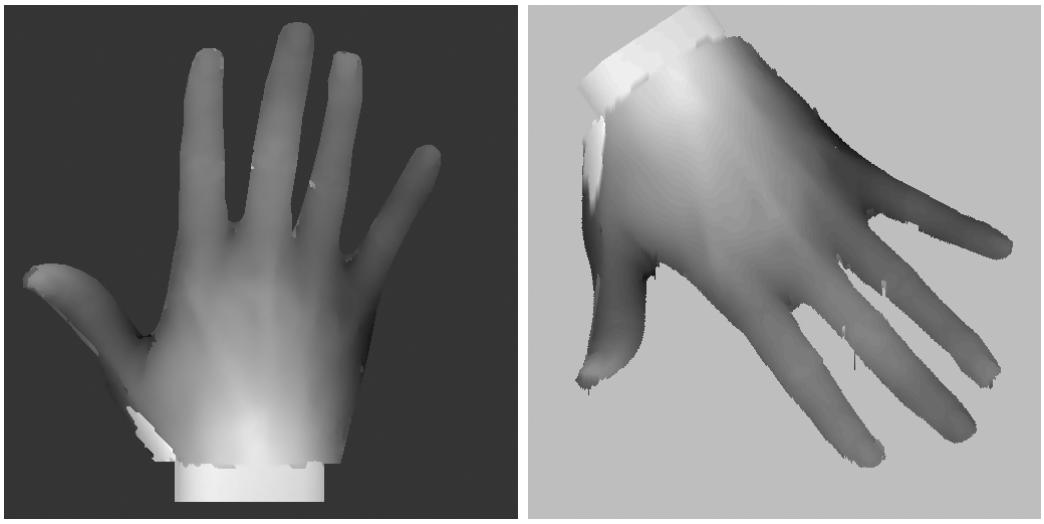

Figure 3.32 - Mask-Cutting phase unwrapping. Courtesy, H. Lopes.

gradually unwrapped and the method seems to be fairly immune to noise (Robinson and Williams, 1986). However, the method doesn't always converge to an unwrapped solution and, in some situations, it doesn't seem to be able to reduce the number of fringe discontinuities. This is particularly so in the presence of object discontinuities, such as cracks or steep height changes.

Full field methods

Full Field methods, are methods which look at the phase unwrapping problem from a global standpoint, and thus process the entire image or field at once, independently of any paths through the data. Three different approaches have been included here below, because these seem to be the most generally accepted global methods. These are very different approaches, based on different circumstances and backgrounds, even though Volkov's deterministic approach bears some resemblance to minimum-norm techniques.

Minimum-Norm methods

Minimum-Norm refers to a class of optimization methods that attempt to minimize the error between wrapped and unwrapped phase gradients or, stated differently, that seek the unwrapped phase whose gradient matches the wrapped gradient as closely as possible.

Let $\psi_{i,j}$ and $\phi_{i,j}$ represent the wrapped and unwrapped phase values on a rec-

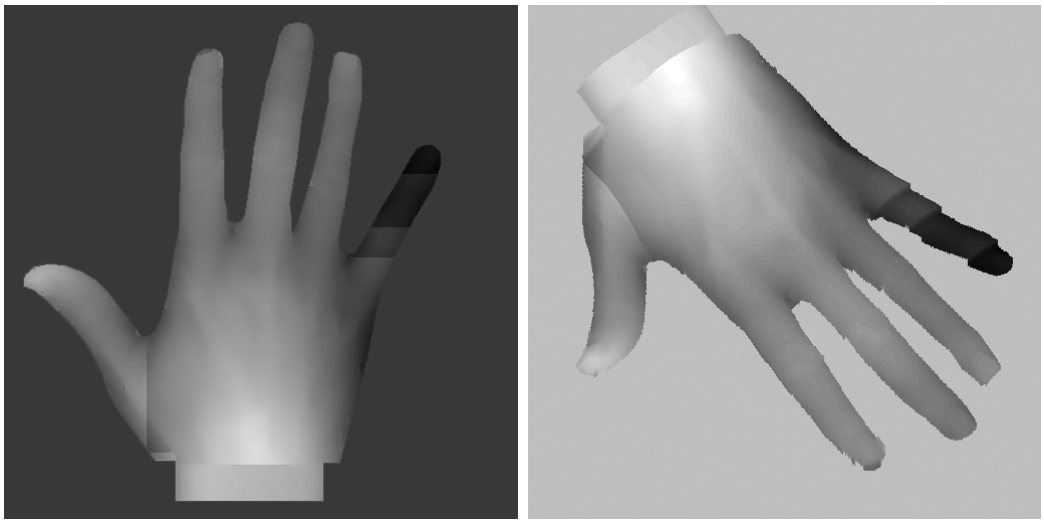

Figure 3.33 - Flynn's Minimum Discontinuity approach to phase unwrapping. The errors are clearly related to a poor weight mask definition. Courtesy, H. Lopes.

tangular $M \times N$ grid. The minimum L^p norm solution, $\phi_{i,j}$, must minimize the error (Ghiglia and Pritt, 1998),

$$J = \varepsilon^p = \sum_{i=0}^{M-2} \sum_{j=0}^{N-1} \left| \phi_{i+1,j} - \phi_{i,j} - \Delta_{i,j}^x \right|^p + \sum_{i=0}^{M-1} \sum_{j=0}^{N-2} \left| \phi_{i,,j+1} - \phi_{i,j} - \Delta_{i,j}^y \right|^p \tag{3.92}$$

where $\Delta_{i,j}^x$ and $\Delta_{i,j}^y$ represent wrapped phase differences in xx and yy respectively. It can be proved that the solution to the minimum L^p norm problem is the solution of the equation

$$\begin{aligned} &U(i,j)\left(\phi_{i+1,j} - \phi_{i,j} - \Delta_{i,j}^x\right) + V(i,j)\left(\phi_{i,,j+1} - \phi_{i,j} - \Delta_{i,j}^y\right) - \\ &-U(i-1,j)\left(\phi_{i,j} - \phi_{i-1,j} - \Delta_{i-1,j}^x\right) - V(i,j-1)\left(\phi_{i,,j} - \phi_{i,j-1} - \Delta_{i,j-1}^y\right) = 0 \end{aligned} \tag{3.93}$$

with

$$U(i,j) = \left| \phi_{i+1,j} - \phi_{i,j} - \Delta_{i,j}^x \right|^{p-2} \text{ for } i = 0,\ldots,M-2 \text{ and } j = 0,\ldots,N-1 \tag{3.94}$$

and

$$V(i,j) = \left| \phi_{i,,j+1} - \phi_{i,j} - \Delta_{i,j}^y \right|^{p-2} \text{ for } i = 0,\ldots,M \text{ and } j = 0,\ldots,N-2 \tag{3.95}$$

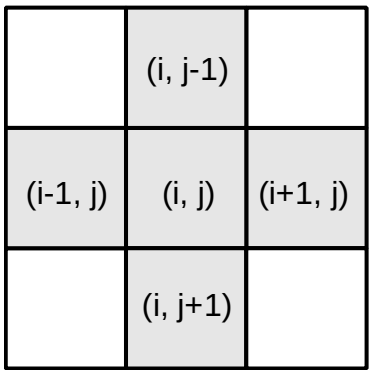

Figure 3.34 - Cellular Automaton operator.

and zero otherwise, and the boundary conditions,

$$\begin{aligned}
&\phi_{-1,j} - \phi_{0,j} = \psi_{-1,j} - \psi_{0,j} \\
&\phi_{M,j} - \phi_{M-1,j} = \psi_{M,j} - \psi_{M-1,j} \quad 0 \leq j \leq N-1 \\
&\phi_{i,-1} - \phi_{i,0} = \psi_{i,-1} - \psi_{i,0} \\
&\phi_{i,N} - \phi_{i,N-1} = \psi_{i,N} - \psi_{i,N-1} \quad 0 \leq i \leq M-1
\end{aligned} \tag{3.96}$$

For the least-squares case with $p = 2$, Eq. 3.93 reduces to,

$$\left(\phi_{i+1,j} - 2\phi_{i,j} - \phi_{i-1,j}\right) + \left(\phi_{i,j+1} - 2\phi_{i,j} - \phi_{i,j-1}\right) = \rho_{i,j} \tag{3.97}$$

where

$$\rho_{i,j} = \left(\Delta^x_{i,j} - \Delta^x_{i-1,j}\right) + \left(\Delta^y_{i,j} - \Delta^y_{i,j-1}\right) \tag{3.98}$$

which is a discrete version of Poisson's Equation,

$$\nabla^2 \phi = \rho \tag{3.99}$$

where ρ represents the Laplacian of the wrapped phase values, ψ.

Ghiglia proposes five different solutions to this Least Squares problem. Two are based on Fourier methods on two differently even symmetrised periodic extensions of the wrapped function, and another two are the Discrete Cosine Transform versions of these Fourier methods. The fifth method is an iterative multi-grid method based on the classical Gauss-Seidel relaxation technique for solving the Poisson equation.

Even though the least-aquares solution is inherently *unweighted*, the reintroduction of the weights $U(i,j)$ and $V(i,j)$, back into Eq. 3.93 based on quality measures such as masks or the quality maps referred to above, avoids integration through the residues. The methods that accomplish this are known as *weighted* Least Squares, and

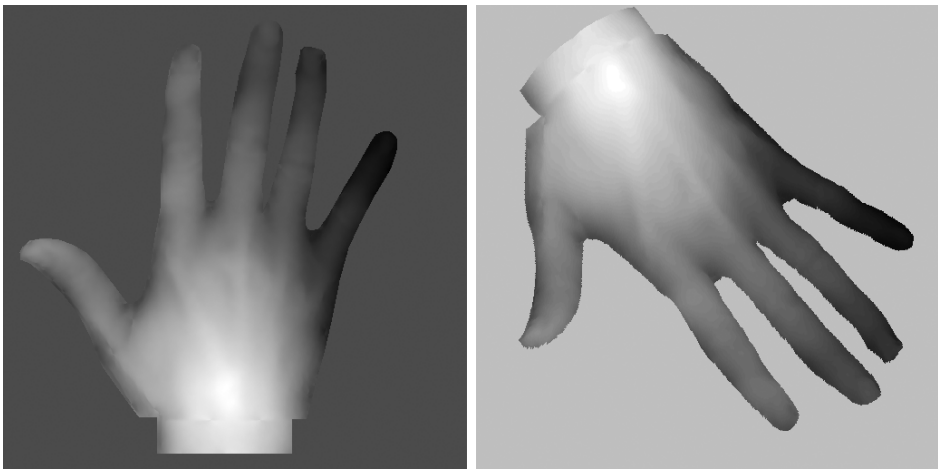

Figure 3.35 - PCG weighted least-squares phase unwrapping. Courtesy, H. Lopes.

the fastest amongst these seem to be the Preconditioned Conjugate Gradient (PCG), shown in Fig. 3.35 and the Weighted Multi-grid methods.

The Conjugate Gradient method (CG) is the oldest and most well known of all non-stationary methods for solving linear systems. On each iteration it generates a sequence of conjugate residuals, which are also the gradients of the quadratic error function to be minimized. It is a very effective method if the coefficient matrix is similar to the identity matrix, that being the reason to employ a preconditioning step, which transforms the coefficient matrix to one very close to the identity matrix.

The general L^p norm phase unwrapping problem is also solved under an iterative technique, but now the weights are extracted from the data itself. Specifically, $U_0(x,y)$ and $V_0(x,y)$ are obtained from the wrapped phase, ψ, and an initial estimate for the true phase, ϕ_0. The partial differential equation that results from the residue minimization problem, i.e. the continuous version of Eq. 3.93,

$$\frac{\partial}{\partial x}\left[U(x,y)\left(\frac{\partial \phi}{\partial x}-\frac{\partial \psi}{\partial x}\right)\right]+\frac{\partial}{\partial y}\left[V(x,y)\left(\frac{\partial \phi}{\partial y}-\frac{\partial \psi}{\partial y}\right)\right]=0 \tag{3.100}$$

is then solved by either a PCG or a multi-grid method and the solution, ϕ_1, is used with the original ψ to find a new set of weights, $U_1(x,y)$ and $V_1(x,y)$. This process is repeated until convergence is achieved. According to Ghiglia, this seems to be the most effective of the Minimum-Norm solutions, even though the computing requirements may rapidly become prohibitive for a medium-sized 512x512 image.

A thorough study of the Minimum-Norm methods was recently presented by Lopes, with performance comparisons in several applications (Lopes, 2008).

Deterministic phase unwrapping

Volkov proposes a solution to the phase unwrapping problem based on the periodicity characteristics of the complex phase function and the Fourier transform itself. This solution is unique, to an additive constant term, and is free from the boundary constraints required by the solution of the Poisson equation (Volkov and Zhu, 2003).

Let

$$(x, y) \leftrightarrow (u, v) \tag{3.101}$$

represent space and frequency coordinates and

$$\psi(x, y) = \phi(x, y) + 2\pi n(x, y) \tag{3.102}$$

be the wrapped and unwrapped phase values and $n(x, y)$ the solution to the integer field. The 2D Fourier transform differentiation theorem can be written

$$\left(\mathcal{F}\left\{\frac{\partial\phi(x,y)}{\partial x}\right\}, \mathcal{F}\left\{\frac{\partial\phi(x,y)}{\partial y}\right\}\right) \equiv \mathcal{F}\left\{\nabla\left[\phi(x,y)\right]\right\} = (2\pi ju, 2\pi jv)\,\Phi(u, v) \tag{3.103}$$

and the fact that the complex exponential phase is periodic can be stated as

$$\exp\left[j\phi(x,y)\right] = \exp\left[j\psi(x,y) - 2\pi jn(x,y)\right] \equiv \exp\left[j\psi(x,y)\right] \tag{3.104}$$

Performing the internal product with (u, v) on both sides of Eq. 3.103, dividing by the square radius and reverse transforming, results in

$$\phi(x, y) = \mathrm{Re}\left\{\frac{1}{2\pi j}\mathcal{F}^{-1}\left(\frac{u\mathcal{F}\left\{\frac{\partial\phi(x,y)}{\partial x}\right\} + v\mathcal{F}\left\{\frac{\partial\phi(x,y)}{\partial y}\right\}}{u^2 + v^2}\right)\right\} \tag{3.105}$$

This solution is unique, up to a constant, since the behaviour of $\phi(x, y)$ is entirely determined by the Neumann boundary conditions on its derivatives, or better still by its Fourier Transforms. A solution of Eq. 3.105 can be obtained by even or odd symmetrisation of the wrapped phase, $\psi(x, y)$, similar to Ghiglia's proposal on the unweighted least squares solution above (Volkov et al., 2002).

All that's left to calculate is the true phase gradient components. Let

$$P(x, y) = \exp\left[j\phi(x,y)\right] \equiv \exp\left[j\psi(x,y)\right] \tag{3.106}$$

The gradient of $P(x, y)$ is given by

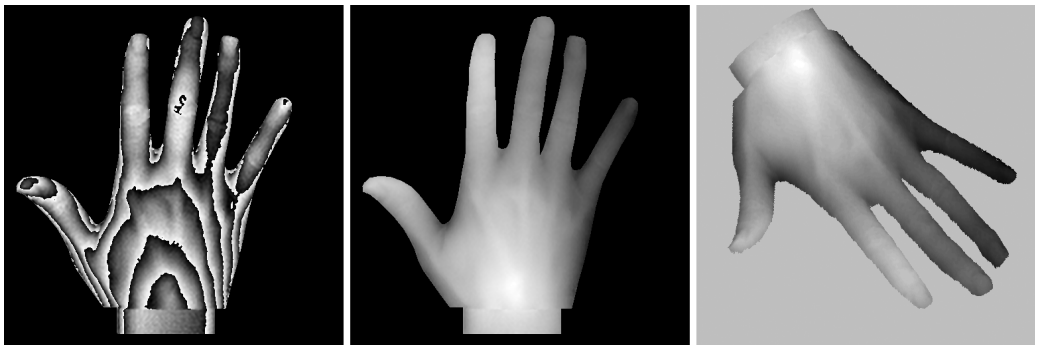

Figure 3.36 - Unwrapping with Volkov's deterministic method.

$$\nabla\left[P(x,y)\right] = j\nabla\left[\phi(x,y)\right]\exp\left[j\phi\left(x,y\right)\right] \equiv \exp\left[j\psi\left(x,y\right)\right] \tag{3.107}$$

from which the true phase gradient components can be calculated as

$$\nabla\left[\phi(x,y)\right] = \mathrm{Re}\left\{\frac{\nabla\left[P(x,y)\right]}{jP(x,y)}\right\} = \cos\psi\left(x,y\right)\nabla\left[\sin\psi(x,y)\right] - \sin\psi(x,y)\nabla\left[\cos\psi(x,y)\right] \tag{3.108}$$

These gradient components are directly inserted into Eq. 3.105 to obtain the exact unwrapped phase field. The procedure is pixel independent, which means it is totally immune to noise propagation. It also quite fast. A 512×512 pixel image takes less than $20s$ to unwrap on a common Pentium IV personal computer with the code developed in LOME, and even less than that when using MatLab with optimized FFT routines. Figs. 3.36 and 3.37 show the application to phase maps with different noise contents. An iterative solution to this problem via the Laplace transform and appropriate periodic boundary conditions, once more with the use of a symmetrisation rule, had already been suggested by Schofield (Schofield and Zhu, 2003).

Temporal phase unwrapping

Temporal phase unwrapping (TPU) is actually more than an unwrapping method. It is a phase acquisition technique that dispenses with phase unwrapping altogether, introduced by Huntley and Saldner in 1993 and later perfected in many respects by Huntley, Coggrave and Saldner (Coggrave and Huntley, 1999; Huntley and Saldner, 1997; Saldner and Huntley, 1997). The method unwraps phase, pixel by pixel along a time axis by stacking a number of phase maps taken at different times and frequencies, and observing the phase variation at each pixel.

Let the phase at pixel (x, y) at time t be described by $\phi(t)$ and assume that during the measurement, phase undergoes a total number N of 2π phase jumps. If $t = 1, 2, \ldots, s$, the total number of 2π discontinuities pixel (x, y) goes through, can be calculated by summing all the phase differences between consecutive phase maps

$$N(s) = \frac{1}{2\pi} \sum_{t=1}^{s} \Delta\phi(t) \tag{3.109}$$

where

$$\Delta\phi(t) = \phi(t) - \phi(t-1) \tag{3.110}$$

The phase at pixel (x, y) could then be found by subtracting $2\pi N(s)$ to $\phi(s)$, in the sense of Eq. 3.91, which is simply the fringe counting procedure that the first unwrapping methods relied upon.

In practice, the phase at time t is found by phase-stepping. For a 4-step method

$$\phi(t) = \tan^{-1}\left(\frac{I_4(t) - I_2(t)}{I_1(t) - I_3(t)}\right) \equiv \tan^{-1}\left(\frac{\Delta I_{42}(t)}{\Delta I_{13}(t)}\right) \tag{3.111}$$

but in such case the phase differences would span 4π, as given by Eq. 3.110, because the inverse tangent operation yields phase values between $-\pi$ and $+\pi$. A clever way around this had previously been suggested by Stetson (Stetson, 1990) by observing that

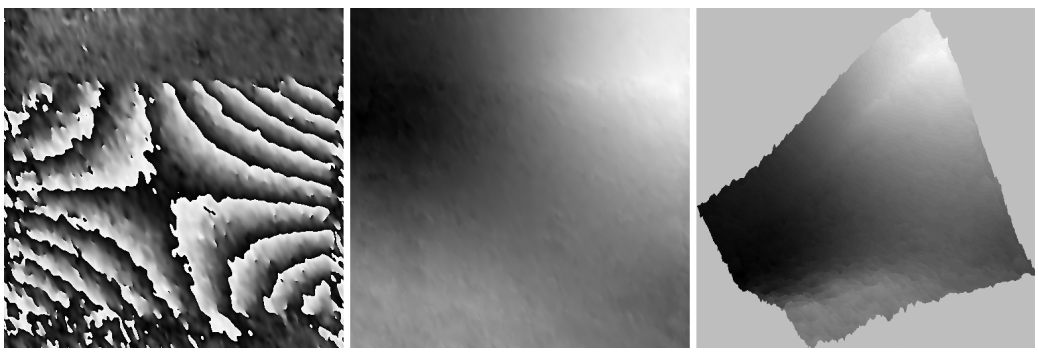

Figure 3.37 - Unwrapping with Volkov's deterministic method. Pixel-independency prevents noise and discontinuities from propagating.

Figure 3.38 - Fringe projection in TPU with 1, 5 and 10 fringes and $\pi/2$ phase shifts.

$$\begin{aligned}
\tan\Delta\phi\left(t\right) &= \frac{\sin\left[\phi\left(t\right)-\phi\left(t-1\right)\right]}{\cos\left[\phi\left(t\right)-\phi\left(t-1\right)\right]} \\
&= \frac{1}{\frac{1}{\tan\phi(t)}+\tan\phi\left(t-1\right)} - \frac{1}{\frac{1}{\tan\phi(t-1)}+\tan\phi\left(t\right)} \\
&= \frac{1}{\frac{\Delta I_{13}(t)}{\Delta I_{42}(t)}+\frac{\Delta I_{42}(t-1)}{\Delta I_{13}(t-1)}} - \frac{1}{\frac{\Delta I_{13}(t-1)}{\Delta I_{42}(t-1)}+\frac{\Delta I_{42}(t)}{\Delta I_{13}(t)}} \\
&= \frac{\Delta I_{42}\left(t\right)\Delta I_{13}\left(t-1\right)-\Delta I_{13}\left(t\right)\Delta I_{42}\left(t-1\right)}{\Delta I_{13}\left(t\right)\Delta I_{13}\left(t-1\right)+\Delta I_{42}\left(t\right)\Delta I_{42}\left(t-1\right)}
\end{aligned} \tag{3.112}$$

and the phase difference thus calculated lies between $-\pi$ and $+\pi$. This is an important point because now the s^{th} phase map can be calculated by summing the consecutive phase differences that don't show 2π discontinuities any further. Fringe projection and filtered 3D maps can be seen in Figs. 3.38 and 3.39.

The inexistence of a relationship between pixels, which is inherent in the other phase acquisition methods, makes this method particularly noisy. This problem has to be dealt with afterwards, upon mesh creation, but this in fact reduces the apparent high resolution advantage of the method.

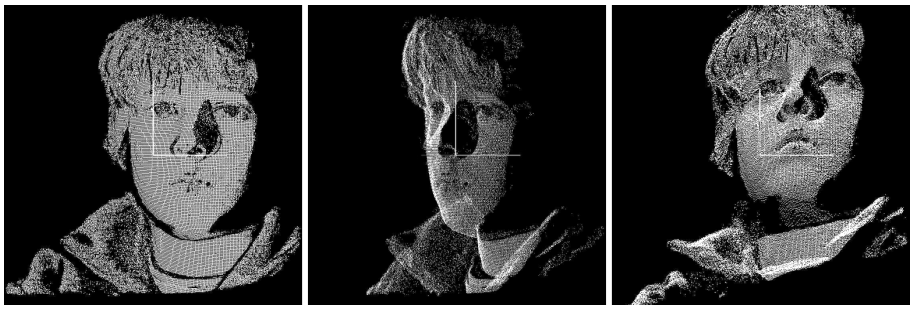

Figure 3.39 - 3D maps obtained with TPU after filtering.

This page intentionally left blank.

Chapter 4

Calibration

Everything is vague to a degree you do not realize,
till you have tried to make it precise...
Bertrand Russell - The Philosophy of Logical Atomism

4.1 3D acquisition calibration with phase methods

Calibration of Phase Measurement Profilometry (PMP) instruments has a fundamental difference from typical imaging device calibration procedures: PMP instruments calculate *phase* information from distorted fringe patterns and transform it into object surface elevation.

As already mentioned in § 3.5, this calculated phase estimate is always relative to some reference, unless some artefact is provided in the imaging scene, such as the rubber band in Abramson's experiment to confer absolute measurements throughout the interferogram (Abramson, 1972). There have been several proposals to measure absolute phase wherefore a correspondence has to be established between projector pixels and camera pixels (Legarda-Saenz et al., 2004; Nadeborn et al., 1996; Osten and Jüptner, 1997; Schreiber and Notni, 2000). These methods have the significant advantage of yielding an unwrapped phase estimate directly, albeit at the expense of added complexity of the calibration procedure. Although this is a very important advantage, they do so by either projecting the structured patterns at different angles or different frequencies, which requires time, making these methods not adapted to non-stationary objects.

The method proposed and implemented in LOME calculates phase relative to a reference plane, which has to be subtracted in the end to calculate phase difference. Thus, besides the camera calibration procedure, a phase-to-height relation has to be established and calibrated in order to recover the object surface elevation. This issue

was the subject of a study presented in § 4.3, which led to the introduction of a new technique.

Two camera calibration methods have been implemented. Complete extrinsic and intrinsic calibration is done with a modification of Tsai's method, a two step method which involves a direct solution for most of the camera parameters and a nonlinear iterative solution for the remaining. This method uses a radial alignment constraint to determine part of the calibration parameters. The modification of Tsai's method consists of making full use of the calibration data on both xx and yy directions on the error function at the optimization step, instead of just on one direction, as originally proposed by Tsai. Further calibration of the external parameters for camera repositioning is done by a standard Direct Linear Transformation (DLT) algorithm, which is a closed-form solution, obtained simply by solving a set of linear equations. This is a faster method, which ignores the nonlinear radial and tangential distortions but is quite capable of handling repositioning when there are no changes to the camera lens.

4.2 Camera calibration

Camera calibration, in the context of three-dimensional machine vision, is the process of determining the internal camera geometric and optical characteristics, denominated intrinsic parameters, and the 3D position and orientation of the camera frame relative to a certain world coordinate system, so called extrinsic parameters. Although the simple DLT model doesn't support image distortion corrections, it is nevertheless a very powerful method for the situations where those corrections are not required, such as rigid body movements of either the camera or the object under scrutiny. This method will be discussed first and the nonlinear Tsai's method will be reviewed next.

The Pinhole and DLT camera models

The DLT was first introduced by Abdel-Aziz and Karara in 1971 (Abdel-Aziz and Karara, 1971), based on the simplest of all models, already known to the painters of Middle Age – the pinhole model. The pinhole model represents a simple rigid body transformation, i.e., rotation and translation, followed by a perspective transformation. It can be explained with Fig. 4.1:

- Object space coordinates are represented by (X, Y, Z);

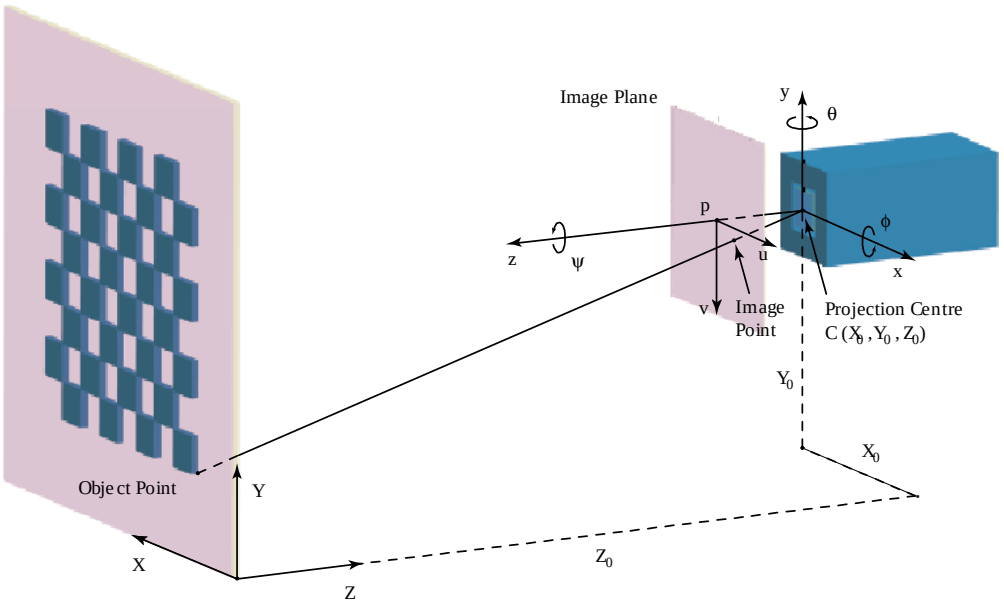

Figure 4.1 - Coordinate systems for camera models. The *pinhole* model.

- Image space coordinates are represented by (u, v) This plane is called *retinal* or image plane;
- Camera coordinates are represented by (x, y, z). All object point rays go through this coordinate system's origin, C, denominated *Optical Centre*;
- The point p in retinal plane, pierced by the camera coordinate zz axis is called *Principal Point*;
- The distance between camera and retinal or image plane is the focal length or *Principal Distance*, f;
- The positive, counter-clockwise, rotation angles around respectively the xx, yy and zz axes are ϕ, θ and ψ, as defined in the figure.

This is just a convenient way of modelling image formation on the retinal plane as if a lens, or a pinhole for that matter, had been placed at the Optical Centre, the origin of the camera coordinate system. The retinal plane is drawn in front of the camera plane so the lateral coordinates become positive.

Using homogeneous coordinates, the rigid body transformation can be modelled linearly as,

$$\begin{bmatrix} x \\ y \\ z \\ 1 \end{bmatrix} = \mathbf{T}_r \begin{bmatrix} X \\ Y \\ Z \\ 1 \end{bmatrix} \tag{4.1}$$

where the transformation,

$$\mathbf{T}_r = \mathbf{RT} = \begin{bmatrix} r_{11} & r_{12} & r_{13} & x_0 \\ r_{21} & r_{22} & r_{23} & y_0 \\ r_{31} & r_{32} & r_{33} & z_0 \\ 0 & 0 & 0 & 1 \end{bmatrix}. \tag{4.2}$$

R and T are the rotation and translation matrices, respectively,

$$\mathbf{R}= \begin{bmatrix} r_{11} & r_{12} & r_{13} & 0 \\ r_{21} & r_{22} & r_{23} & 0 \\ r_{31} & r_{32} & r_{33} & 0 \\ 0 & 0 & 0 & 1 \end{bmatrix} \text{ and } \mathbf{T}= \begin{bmatrix} 1 & 0 & 0 & -X_0 \\ 0 & 1 & 0 & -Y_0 \\ 0 & 0 & 1 & -Z_0 \\ 0 & 0 & 0 & 1 \end{bmatrix} \tag{4.3}$$

with,

$$\begin{aligned} r_{11} &= \cos(\theta)\cos(\psi) & r_{31} &= -\sin(\theta) \\ r_{12} &= \sin(\phi)\sin(\theta)\cos(\psi) - \cos(\phi)\sin(\psi) & r_{32} &= \sin(\phi)\cos(\theta) \\ r_{13} &= \cos(\phi)\sin(\theta)\cos(\psi) + \sin(\phi)\sin(\psi) & r_{33} &= \cos(\phi)\cos(\theta) \\ r_{21} &= \cos(\theta)\sin(\psi) & x_0 &= -r_{11}X_0 - r_{12}Y_0 - r_{13}Z_0 \\ r_{22} &= \sin(\phi)\sin(\theta)\sin(\psi) + \cos(\phi)\cos(\psi) & y_0 &= -r_{21}X_0 - r_{22}Y_0 - r_{23}Z_0 \\ r_{23} &= \cos(\phi)\sin(\theta)\sin(\psi) - \sin(\phi)\cos(\psi) & z_0 &= -r_{31}X_0 - r_{32}Y_0 - r_{33}Z_0 \end{aligned} \tag{4.4}$$

The rotation matrix $\mathbf{R}$ is a special orthogonal matrix. $\mathbf{R}.\mathbf{R}^t = \mathbf{I}$ and $\det(\mathbf{R}) = 1$. These properties can be very useful to verify the calibration data. Had the rotation angles been defined on the object coordinate system, the rotation would have been the inverse of the one presented here, i.e., the transpose of $\mathbf{R}$.

The perspective transformation from camera to retinal planes is just an application of Thales's theorem, and represents the perspective transformation,

$$u = f\frac{x}{z} \quad \text{and} \quad v = f\frac{y}{z} \tag{4.5}$$

In matrix notation , if f is represented by,

$$\mathbf{F} = \begin{bmatrix} f & 0 & 0 & 0 \\ 0 & f & 0 & 0 \\ 0 & 0 & 1 & 0 \end{bmatrix} \tag{4.6}$$

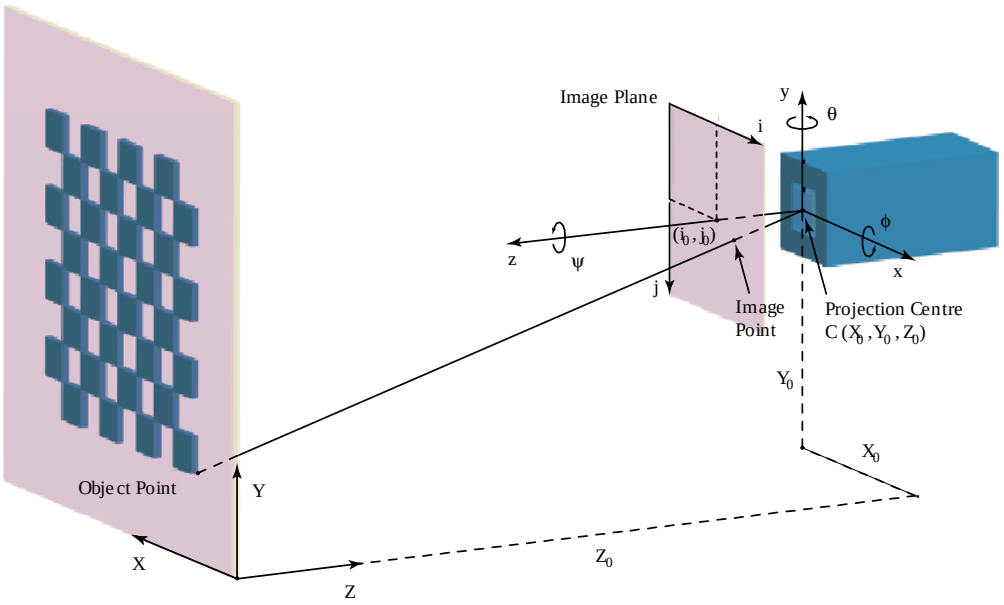

Figure 4.2 - The Direct Linear Transformation model.

the image space relates to object space through,

$$\begin{bmatrix} zu \\ zv \\ z \end{bmatrix} = \mathbf{F} \begin{bmatrix} x \\ y \\ z \\ 1 \end{bmatrix} = \mathbf{FT}_r \begin{bmatrix} X \\ Y \\ Z \\ 1 \end{bmatrix} \tag{4.7}$$

The DLT model is an extension of the simple pinhole model, to accommodate a shift in image origin, due to the fact that image pixel origin is usually set at the top left corner of the image, and a linear image distortion, to account for pixel skew and scaling from metric to pixel data: The model looks as the one depicted in Fig. 4.2.

The transformation is described by,

$$\begin{bmatrix} u \\ v \\ 1 \end{bmatrix} = \mathbf{DS} \begin{bmatrix} i \\ j \\ 1 \end{bmatrix} \tag{4.8}$$

where, **S** is represents the coordinate shift,

$$\mathbf{S} = \begin{bmatrix} 1 & 0 & -i_0 \\ 0 & 1 & -j_0 \\ 0 & 0 & 1 \end{bmatrix}, \tag{4.9}$$

and **D**, is the skew and scale correction,

$$\mathbf{D} = \begin{bmatrix} 1+b_1 & b_2 & 0 \\ b_2 & 1-b_1 & 0 \\ 0 & 0 & 1 \end{bmatrix}. \tag{4.10}$$

Here, b_1 controls scaling and b_2 controls pixel skew. Image pixel coordinates can then be calculated by,

$$\begin{bmatrix} i \\ j \\ 1 \end{bmatrix} = \mathbf{D}^{-1}\mathbf{S}^{-1} \begin{bmatrix} u \\ v \\ 1 \end{bmatrix} = \begin{bmatrix} \frac{1-b_1}{1-b_1^2-b_2^2} & \frac{-b_2}{1-b_1^2-b_2^2} & 0 \\ \frac{-b_2}{1-b_1^2-b_2^2} & \frac{1+b_1}{1-b_1^2-b_2^2} & 0 \\ 0 & 0 & 1 \end{bmatrix} \begin{bmatrix} 1 & 0 & i_0 \\ 0 & 1 & j_0 \\ 0 & 0 & 1 \end{bmatrix} \begin{bmatrix} u \\ v \\ 1 \end{bmatrix}, \tag{4.11}$$

provided, **D** and **S** can be inverted.

The complete transformation from object to image space can now be written as,

$$\begin{bmatrix} \omega.i \\ \omega.j \\ \omega \end{bmatrix} = \mathbf{A} \begin{bmatrix} X \\ Y \\ Z \\ 1 \end{bmatrix} = \begin{bmatrix} a_{11} & a_{12} & a_{13} & a_{14} \\ a_{21} & a_{22} & a_{23} & a_{24} \\ a_{31} & a_{32} & a_{33} & a_{34} \end{bmatrix} \begin{bmatrix} X \\ Y \\ Z \\ 1 \end{bmatrix} \tag{4.12}$$

where,

$$\mathbf{A} = \lambda \mathbf{D}^{-1}\mathbf{S}^{-1}\mathbf{F}\mathbf{T}_r, \tag{4.13}$$

and λ is simply a general scaling factor (Melen, 1994). It can be shown the components of **A** are given by,

$$
\begin{aligned}
a_{11} &= i_0.r_{31} + f.r_{11}\tfrac{1-b_1}{1-b_1^2-b_2^2} - f.r_{21}\tfrac{b_2}{1-b_1^2-b_2^2} \\
a_{12} &= i_0.r_{32} + f.r_{12}\tfrac{1-b_1}{1-b_1^2-b_2^2} - f.r_{22}\tfrac{b_2}{1-b_1^2-b_2^2} \\
a_{12} &= i_0.r_{33} + f.r_{13}\tfrac{1-b_1}{1-b_1^2-b_2^2} - f.r_{23}\tfrac{b_2}{1-b_1^2-b_2^2} \\
a_{14} &= -f.(r_{11}X0 + r_{12}Y0 + r_{13}Z0).\tfrac{1-b_1}{1-b_1^2-b_2^2} + f.(r_{21}X0 + r_{22}Y0 + r_{23}Z0).\tfrac{b_2}{1-b_1^2-b_2^2} \\
&\quad -i_0.(r_{31}X0 + r_{32}Y0 + r_{33}Z0) \\
a_{21} &= j_0.r_{31} - f.r_{11}\tfrac{b_2}{1-b_1^2-b_2^2} + f.r_{21}\tfrac{1+b_1}{1-b_1^2-b_2^2} \\
a_{22} &= j_0.r_{32} - f.r_{12}\tfrac{b_2}{1-b_1^2-b_2^2} + f.r_{22}\tfrac{1+b_1}{1-b_1^2-b_2^2} \\
a_{23} &= j_0.r_{33} - f.r_{13}\tfrac{b_2}{1-b_1^2-b_2^2} + f.r_{23}\tfrac{1+b_1}{1-b_1^2-b_2^2} \\
a_{24} &= f.(r_{11}X0 + r_{12}Y0 + r_{13}Z0).\tfrac{b_2}{1-b_1^2-b_2^2} - f.(r_{21}X0 + r_{22}Y0 + r_{23}Z0).\tfrac{1+b_1}{1-b_1^2-b_2^2} \\
&\quad -j_0.(r_{31}X0 + r_{32}Y0 + r_{33}Z0) \\
a_{31} &= r_{31} \\
a_{32} &= r_{32} \\
a_{33} &= r_{33} \\
a_{34} &= -(r_{31}X0 + r_{32}Y0 + r_{33}Z0)
\end{aligned}
\tag{4.14}
$$

In order to find the linear model parameters a_{ij}, ω is eliminated from Eq. 4.12,

$$
\begin{aligned}
(a_{31}X + a_{32}Y + a_{33}Z + a_{34}).i &= a_{11}X + a_{12}Y + a_{13}Z + a_{14} \\
(a_{31}X + a_{32}Y + a_{33}Z + a_{34}).j &= a_{21}X + a_{22}Y + a_{23}Z + a_{24}
\end{aligned}
\tag{4.15}
$$

which can be put in matrix form for n control points (X_i, Y_i, Z_i), and the corresponding image points (i_i, j_i),

$$
\mathbf{LA} = \mathbf{0} \tag{4.16}
$$

$$\begin{bmatrix} X_1 & Y_1 & Z_1 & 1 & 0 & 0 & 0 & 0 & -X_1.i_1 & -Y_1.i_1 & -Z_1.i_1 & -i_1 \\ 0 & 0 & 0 & 0 & X_1 & Y_1 & Z_1 & 1 & -X_1.j_1 & -Y_1.j_1 & -Z_1.j_1 & -j_1 \\ \vdots & & & & \vdots & & & & \vdots & & & \\ X_i & Y_i & Z_i & 1 & 0 & 0 & 0 & 0 & -X_i.i_i & -Y_i.i_i & -Z_i.i_i & -i_i \\ 0 & 0 & 0 & 0 & X_i & Y_i & Z_i & 1 & -X_i.j_i & -Y_i.j_i & -Z_i.j_i & -j_i \\ \vdots & & & & \vdots & & & & \vdots & & & \\ X_n & Y_n & Z_n & 1 & 0 & 0 & 0 & 0 & -X_n.i_n & -Y_n.i_n & -Z_n.i_n & -i_n \\ 0 & 0 & 0 & 0 & X_n & Y_n & Z_n & 1 & -X_n.j_n & -Y_n.j_n & -Z_n.j_n & -j_n \end{bmatrix} \begin{bmatrix} a_{11} \\ a_{12} \\ a_{13} \\ a_{14} \\ a_{21} \\ a_{22} \\ a_{23} \\ a_{24} \\ a_{31} \\ a_{32} \\ a_{33} \\ a_{34} \end{bmatrix} = \begin{bmatrix} 0 \\ 0 \\ \vdots \\ 0 \\ 0 \\ \vdots \\ 0 \\ 0 \end{bmatrix}, \tag{4.17}$$

each point contributing two equations.

When a calibration target is used, with a set of known object space coordinates, the observed image coordinates for each of these points can be used to recover the a_{ij} coefficients from this equation in a least squares algorithm. In order to avoid the trivial $a_{ij} = 0$ solution, a normalization procedure has to be applied. Abdel-Aziz and Mahmhoud Karara suggested using the constraint $a_{34} = 1$, which will make,

$$\mathbf{LA} = \mathbf{u} \tag{4.18}$$

or,

$$\begin{bmatrix} X_1 & Y_1 & Z_1 & 1 & 0 & 0 & 0 & 0 & -X_1.i_1 & -Y_1.i_1 & -Z_1.i_1 \\ 0 & 0 & 0 & 0 & X_1 & Y_1 & Z_1 & 1 & -X_1.j_1 & -Y_1.j_1 & -Z_1.j_1 \\ \vdots & & & & \vdots & & & & \vdots & & \\ X_i & Y_i & Z_i & 1 & 0 & 0 & 0 & 0 & -X_i.i_i & -Y_i.i_i & -Z_i.i_i \\ 0 & 0 & 0 & 0 & X_i & Y_i & Z_i & 1 & -X_i.j_i & -Y_i.j_i & -Z_i.j_i \\ \vdots & & & & \vdots & & & & \vdots & & \\ X_n & Y_n & Z_n & 1 & 0 & 0 & 0 & 0 & -X_n.i_n & -Y_n.i_n & -Z_n.i_n \\ 0 & 0 & 0 & 0 & X_n & Y_n & Z_n & 1 & -X_n.j_n & -Y_n.j_n & -Z_n.j_n \end{bmatrix} \begin{bmatrix} a_{11} \\ a_{12} \\ a_{13} \\ a_{14} \\ a_{21} \\ a_{22} \\ a_{23} \\ a_{24} \\ a_{31} \\ a_{32} \\ a_{33} \end{bmatrix} = \begin{bmatrix} i_1 \\ j_1 \\ \vdots \\ i_i \\ j_i \\ \vdots \\ i_n \\ j_n \end{bmatrix}, \tag{4.19}$$

In this case, a minimum of six control points are necessary for the system to have full rank eleven. The solution is found by calculating the pseudo-inverse of **L**,

$$\mathbf{A} = \left(\mathbf{L}^t\mathbf{L}\right)^{-1}\mathbf{L}^t\mathbf{u} \tag{4.20}$$

Melen has shown the minimum operations cost for six control points is, $O(6) = 3036$. Other constraints have also been proposed, which are computationally less costly (Faugeras and Toscani, 1987).

In the case of a coplanar control point structure, one of the control points coordinate, such as Zi, can be set to 0, and the 3x4 DLT matrix becomes singular. A 3x3 matrix with nine unknown parameters must be used instead. In this case, the translation matrix will be,

$$\mathbf{T}= \begin{bmatrix} 1 & 0 & -X_0 \\ 0 & 1 & -Y_0 \\ 0 & 0 & -Z_0 \\ 0 & 0 & 1 \end{bmatrix} \tag{4.21}$$

and its non-homogeneous 3x3 version will be invertible as long as Z_0 is different from 0, i.e., the camera is out of the object space. The $\mathbf{A} = \left(\mathbf{L}^t\mathbf{L}\right)^{-1}\mathbf{L}^t\mathbf{u}$ solution will now bear $O(n) = 144n + 576$ operations.

Linear methods are very fast owing to the fact no iteration is required. On the other hand, they can't handle lens distortions directly. These methods are thus indicated for either estimating the extrinsic camera parameters or for use after the intrinsic parameters have been calculated. Wei and Ma first corrected the lens distortion and then applied a linear calibration method for corrected image coordinates (Wei and Ma, 1994). The prototype built in LOME uses the DLT for camera or object repositioning, after the intrinsic camera parameters has been calculated with Tsai's two step method, described below.

Tsai's two step model

Tsai proposed a method based on a Radial Alignment Constraint (RAC), which states the direction of the vector $\overrightarrow{OP_d}$ extending from the image centre O to the image point $P_d(u_d, v_d)$ remains unchanged, and is radially aligned with the vector extending from the point $P_0(0, 0, z_i)$ in the optical axis to the point $P(x_i, y_i, z_i)$.

According to this model, only radial distortion is taken into consideration and a correction is due, after the perspective transformation,

$$u = f\frac{x}{z} \quad \text{and} \quad v = f\frac{y}{z} \tag{4.22}$$

such that the point P is *distorted* or corrected according to,

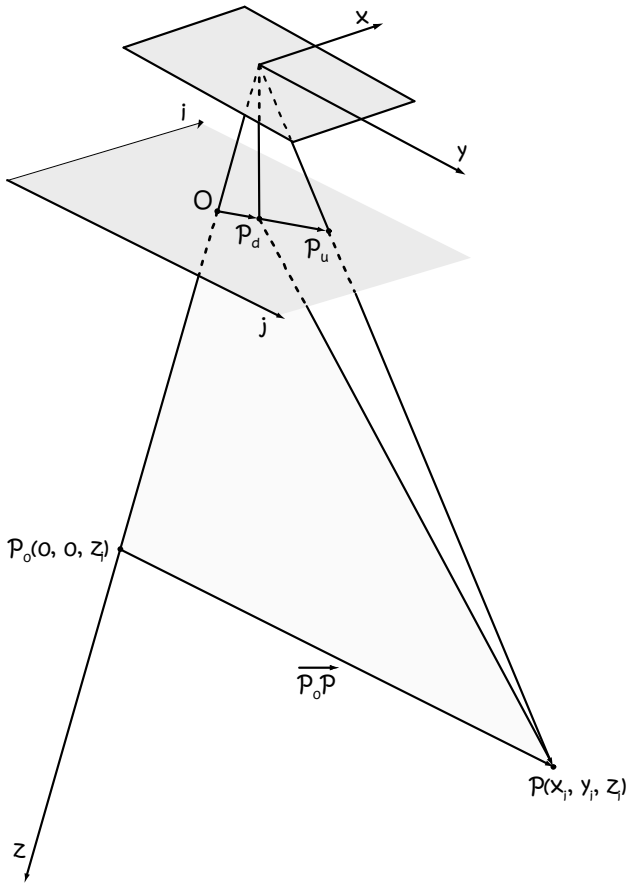

Figure 4.3 - The Radial Alignment Constraint

$$u = u_d + D_x \quad and \quad v = v_d + D_y \tag{4.23}$$

where (u, v) represent the uncorrected image coordinates, given by Eq. 4.5 or Eq. 4.22 above. The radial corrections are given by,

$$D_x = u_d(k_1 r^2 + k_2 r^4 + ...), \quad D_y = v_d(k_1 r^2 + k_2 r^4 + ...), \quad and \quad r^2 = u_d^2 + v_d^2. \tag{4.24}$$

The transformation to pixel coordinates is done through the introduction of scale factors for uu and vv, d_u and d_v, which are none other than the centre-to-centre distances between adjacent sensor pixels, and an uncertainty factor, s_u, on one of the lateral dimensions, to account for several factors such as timing mismatch between camera and grabber or the imprecision of the grabber itself,

$$i = \frac{s_u}{d_u} u_d + i_0 \quad and \quad j = \frac{1}{d_v} v_d + j_0. \tag{4.25}$$

Even if just the first term of the radial correction, k_1, is used, the transformation from object space to image space has now become non-linear, and can't be accomplished before D_x and D_y are known. It is thus not possible anymore to estimate image space from object coordinates.

Considering now the RAC constraint, the requirement the two vectors (u_d, v_d) and $(x, y) = \overrightarrow{P_0P}$ are parallel, can be written,

$$(u_d, v_d) \times (x, y) = \overrightarrow{0} \quad \text{or} \quad u_d y - v_d x = 0. \tag{4.26}$$

Substituting x and y from Eq.4.4,

$$u_d(r_{21}X + r_{22}Y + r_{23}Z + y_0) = v_d(r_{11}X + r_{12}Y + r_{23}Z + x_0) \tag{4.27}$$

or in matrix form for n points and a coplanar object, such as a planar calibration rig with $Z = 0$,

$$\begin{bmatrix} v_{d1}X_1 & v_{d1}Y_1 & v_{d1} & -u_{d1}X_1 & -u_{d1}Y_1 \\ \vdots & & & \vdots & \\ v_{di}X_i & v_{di}Y_i & v_{di} & -u_{di}X_i & -u_{di}Y_i \\ \vdots & & & \vdots & \\ v_{dn}X_n & v_{dn}Y_n & v_{dn} & -u_{dn}X_n & -u_{dn}Y_n \end{bmatrix} \begin{bmatrix} \frac{r_{11}}{y_0} \\ \frac{r_{12}}{y_0} \\ \frac{x_0}{y_0} \\ \frac{r_{21}}{y_0} \\ \frac{r_{22}}{y_0} \end{bmatrix} = \begin{bmatrix} u_{d1} \\ \vdots \\ u_{di} \\ \vdots \\ u_{dn} \end{bmatrix} \tag{4.28}$$

With more than five control points, the five quantities r_{11}/y_0, r_{12}/y_0, x_0/y_0, r_{21}/y_0, r_{22}/y_0, can be calculated with a least squares algorithm. Using one more control point and the fact that both u_d and x as well as v_d and y have the same sign, results in one further constraint that can be used to determine r_{11}, r_{12}, r_{21}, r_{22}, x_0 and y_0 unambiguously. The fact that the rotation matrix is a special orthogonal matrix contributes the necessary constraints to determine its missing elements. All that's left to be determined are the focal distance, f, z_0 and the radial distortion coefficient, k_1.

At this point, Tsai's proposal considers an initial estimate for f and z_0 by taking D_x and D_y to be zero in Eq. 4.23 and establishing the following identities for all control points:

$$\begin{aligned} f\frac{x}{z} &= f\frac{r_{11}X + r_{12}Y + r_{13}Z}{r_{31}X + r_{32}Y + r_{33}Z} = \frac{d_u}{s_u}(i - i_0) \\ f\frac{y}{z} &= f\frac{r_{21}X + r_{22}Y + r_{23}Z}{r_{31}X + r_{32}Y + r_{33}Z} = d_v(j - j_0) \end{aligned} \tag{4.29}$$

In particular, for $Z = 0$, the 2$^{\text{nd}}$ equation results in,

$$\begin{bmatrix} y_1 & -d_v\,(j_1 - j_0) \\ \vdots & \\ y_i & -d_v\,(j_i - j_0) \\ \vdots & \\ y_n & -d_v\,(j_n - j_0) \end{bmatrix} \begin{bmatrix} f \\ z_0 \end{bmatrix} = \begin{bmatrix} w_1 d_v\,(j_1 - j_0) \\ \vdots \\ w_i d_v\,(j_i - j_0) \\ \vdots \\ w_n d_v\,(j_n - j_0) \end{bmatrix} \tag{4.30}$$

with,

$$y_i = r_{21}X + r_{22}Y + y_0 \quad \text{and} \quad w_i = r_{31}X + r_{32}Y \tag{4.31}$$

which can be solved for f and z_0.

The exact solution for f, k_1 and z_0 is then found by a standard optimization scheme, using the f and z_0 estimates and $k_1 = 0$ as initial guesses.

The intersection of the camera lens optical axis, zz, and the image plane,(i_0, j_0), has to be known in advance. As seen in image 4.2, this point is the normal projection of point C in image plane. For most modern cameras, this estimate can be fairly approximated by the image centre coordinates but, as shown by Willson, there are different centres to be considered depending on the property at stake (Willson, 1994). Willson proposed a taxonomy where he identified fifteen different image centres, along with the necessary procedures for measuring ten of these. Tsai and Lenz proposed a method for determining an optimized image centre, i.e., one that minimizes the RAC residue error caused by an image centre offset (Lenz and Tsai, 1988).

The prototype built in LOME during this dissertation uses several improvements to Tsai's method:

- Non-linear search is done with a Levenberg-Marquardt algorithm, implemented with Singular Value Decomposition (SVD), which proved to be a very robust algorithm even for small angles between camera and calibration target, that introduce a linear dependence and a singularity in Eq 4.30. The algorithm is very fast, converging in two or three iterations;

- As suggested by Willson, full use of both xx and yy calibration data is made in the non-linear optimization step (Willson, 1994). The merit function becomes,

$$\begin{aligned} \chi^2 &= \left[(u - u')^2 + (v - v')^2 \right] \\ &= \left[\frac{d_u}{s_u} (i - i_0) \left(1 + k_1 r^2\right) - f\frac{x}{z} \right]^2 + \left[d_v\,(j - j_0) \left(1 + k_1 r^2\right) - f\frac{y}{z} \right]^2 \end{aligned} \tag{4.32}$$

  with,

$$r^2 = \left[\frac{d_u}{s_u} (i - i_0) \right]^2 + \left[d_v\,(j - j_0) \right]^2 \tag{4.33}$$

instead of just the 2nd term as suggested by Tsai. This error function, denominated undistorted image plane error (UIPE) by Willson, represents the sum of squared differences between the undistorted coordinates, as calculated from the image data, (u, v), and from the known object coordinates, (u', v');

- The prescribed preliminary non-linear search for the image centre also minimizes UIPE error. The algorithm was compared against the one proposed by Tsai and Lenz with favourable results. This step isn't really very important in face of the final optimization step described next;

- A full non-linear optimization of the intrinsic camera parameters via Levenberg-Marquardt is done after the previous estimates have been found, that minimizes UIPE error by optimizing $f; z_0, k_1, k_2, t_1, t_2, s_u, i_0$ and j_0. Even though Tsai's method can only deal with radial distortion, UIPE can still be optimized on a model comprehending both radial and tangential distortion given by,

$$\begin{aligned} \delta_u^{(r)} &= u_d \left(k_1 r^2 + k_2 r^4 + ...\right); \qquad \delta_v^{(r)} = v_d \left(k_1 r^2 + k_2 r^4 + ...\right); \\ \delta_u^{(t)} &= 2t_1 u_d v_d + t_2 \left(r^2 + 2u_d^2\right); \qquad \delta_v^{(t)} = t_1 \left(r^2 + 2v_d^2\right) + 2t_2 u_d v_d \end{aligned} \tag{4.34}$$

such that the final image coordinates are given by,

$$\begin{bmatrix} i \\ j \end{bmatrix} = \begin{bmatrix} i_0 + \frac{s_u}{d_u} u_d = i_0 + \frac{s_u}{d_u} \left[u - \delta_u^{(r)} - \delta_u^{(t)}\right] \\ j_0 + \frac{1}{d_v} v_d = j_0 + \frac{1}{d_v} \left[v - \delta_v^{(r)} - \delta_v^{(t)}\right] \end{bmatrix} \tag{4.35}$$

Both radial, $\delta^{(r)}$, and tangential, $\delta^{(t)}$, distortions are modelled by two components. The obtained results indicate the 2nd higher order terms are one to two orders of magnitude smaller.

The planar calibration target currently under use in LOME is a checkerboard pattern with 64 inner corners used as control points, as described in the next section, which makes the complete calibration operation time fairly acceptable on a vulgar personal computer, taking under 1s to complete.

The complete non-linear model gradient and Hessian calculations are shown in Appendix C, as they are rather extensive to be presented in the text, and can be made available upon request.

Control points detection

Control points detection is a critical part of the calibration procedure. The necessary points can be either on a calibration target or can be extracted from the image scene

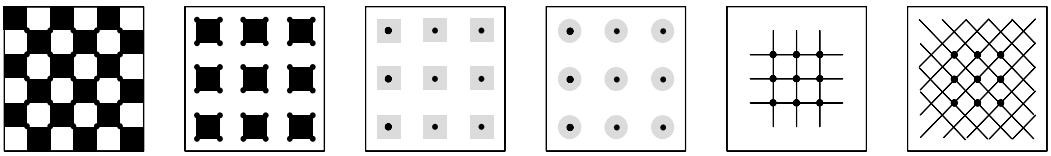

Figure 4.4 - Typical camera calibration patterns range from chequerboard to simple squares, centroid detection or line intersection. Dots represent sought locations.

itself. Either way, the procedure has to detect features within a scene, an ample study subject. Feature detection is also important for object tracking, which adds to the interest in this issue but is beyond the scope of the present work.

A calibration target is an assembly of visually detectable features such as those in Fig. 4.4. The location of the control points can be calculated from a centre of gravity, an intersection of lines or the location of a corner. The automatic detection of either one of these poses different problems such as can arise for instance from an incorrect threshold upon binary conversion or a super position of features, illustrated in Fig. 4.5. Sub-pixel detection capability is often a necessity in camera calibration systems, for the accuracy requirements of most camera metrology based systems goes well beyond the pixel limit.

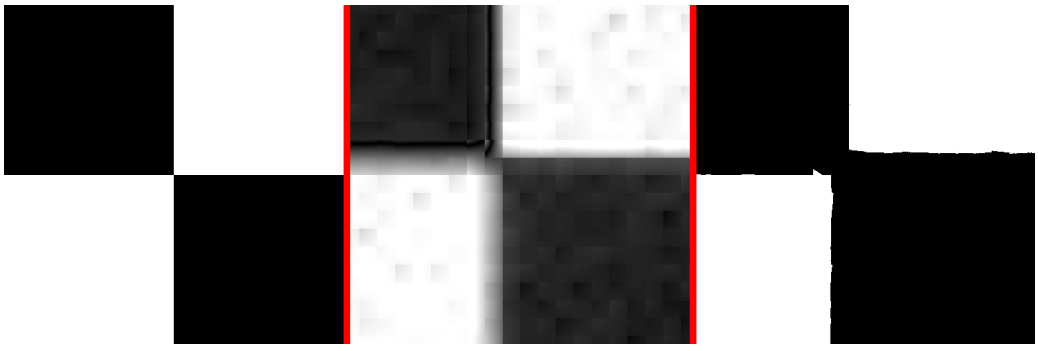

Figure 4.5 - Ideal corner, imaged through a CCD and incorrectly binarized.

Feature detection techniques can be separated into three broad categories, namely, contour-based, intensity-based, and parametric-modelling methods (Schmid et al., 2000). Contour methods rely on the extraction of a contour around the interest point and a search along that contour of maximal inflection or curvature points (Asada and Brady, 1986; Mokhtarian and Mackworth, 1986), intensity methods stipulate a measure of interest point detection from the image gray values (Harris and Stephens, 1988; Lucas and Kanade, 1981; Moravec, 1980) and parametric modelling methods fit

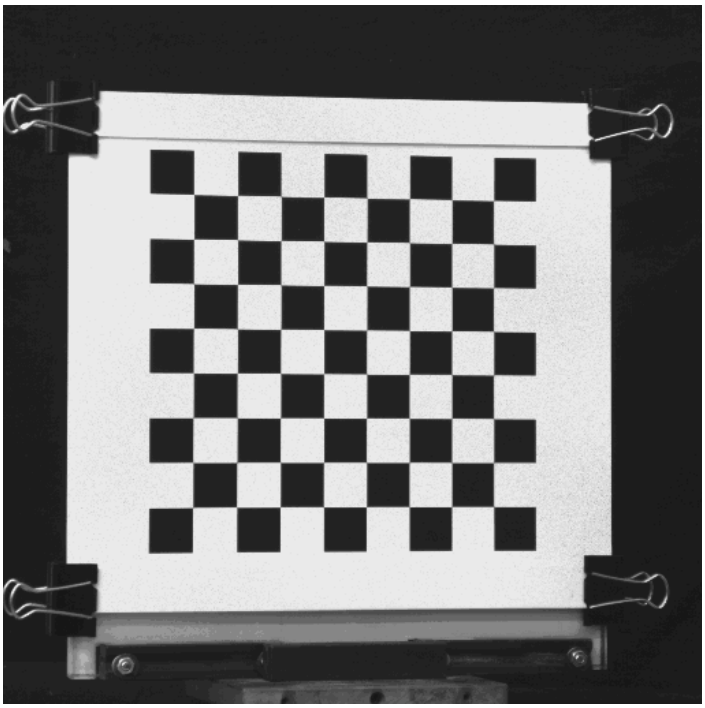

Figure 4.6 - LOME's planar camera calibration target

an intensity model to the original image by varying a certain number of the model's parameters, usually through an optimization process (Kohlmann, 1996; Mohr and Brand, 1994).

An accurate sub-pixel corner detector based on the Hilbert transform was developed in LOME and is currently being used for camera calibration therein (Tavares and Vaz, 2007b). The method uses a planner checkerboard calibration target and detects double corner locations using a bi-dimensional Hilbert transform, a method based on Kohlmann's proposal. The Hilbert transform results in a peak at each corner location and a sub-pixel algorithm is then applied at these positions. Both a squared centroid and a ridge peak detection by paraboloid fitting were used with no appreciable differences.

The principle can be described as follows.

Let $s(t_1, t_2)$ be a real integrable function and its Fourier transform given by,

$$S(\omega_1, \omega_2) = \int_{-\infty}^{+\infty} \int_{-\infty}^{+\infty} s(t_1, t_2) \exp(-j\omega_1 t_1) \exp(-j\omega_2 t_2)\, dt_1 dt_2 \tag{4.36}$$

Its Hilbert transform is,

$$\widehat{s}(t_1,t_2) = \frac{1}{\pi^2} p.v. \int_{-\infty}^{+\infty}\int_{-\infty}^{+\infty} \frac{s(\tau_1,\tau_2)}{(t_1-\tau_1)(t_2-\tau_2)} d\tau_1 d\tau_2 = \frac{1}{\pi^2 t_1 t_2} \otimes s(t_1,t_2) \quad (4.37)$$

where $p.v.$ refers to the principal value of the integral, and $\otimes$ is the convolution operator. The Fourier transform of $1/\left(\pi^2 t_1 t_2\right)$ is,

$$F\left\{\frac{1}{\pi^2 t_1 t_2}\right\} = -sgn(\omega_1).sgn(\omega_2) \quad (4.38)$$

where $sgn(x)$ is the signum function:

$$sgn(x) = \begin{cases} -1 & \text{for } x < 0 \\ 0 & \text{for } x = 0 \\ 1 & \text{for } x > 0 \end{cases} \quad (4.39)$$

By the convolution theorem, the Fourier transform of the Hilbert transform of $s(t_1,t_2)$ is related to the Fourier transform of $s(t_1,t_2)$, $S(\omega_1,\omega_2)$, by,

$$\widehat{S}(\omega_1,\omega_2) = F\{\widehat{s}(t_1,t_2)\} = -sgn(\omega_1).sgn(\omega_2).S(\omega_1,\omega_2) \quad (4.40)$$

For a Linear Shift Invariant (LSI) system with impulse response $1/\left(\pi^2 t_1 t_2\right)$, the function $-sgn(\omega_1).sgn(\omega_2)$ represents the corresponding frequency response and serves as a Hilbert Transformator. This system responds to steep changes in image frequency, such as those in edges, in a way very similar to spatial differentiation, except for the fact that it is more stable to frequency oscillations.

If the calibration pattern is composed of squares, such as the one in Fig. 4.6, the Hilbert transform can be thought of as a separable function in a 2D space. When applied along direction xx, it detects the edges in that direction, as shown in Fig. 4.7.

If it is now applied along the yy direction to the result of the first transformation, it will detect the edges along the new direction, i.e., the corners of the given squares, as shown in Fig. 4.8. The absolute values are retained after calculating the transforms.

Regions of interest are established around each peak through a simple method. A Gaussian filter is first applied to the Hilbert transform, reducing most of the unwanted peaks. The resulting image is binarized to retain just the central, stronger peak regions. The peak detection algorithm is then applied to the regions of interest in the original peaks image, centred at the intensity maxima of sub-regions around each binary region, to find exact sub-pixel locations of the respective corner.

The method's accuracy was established at or beyond 0.1 pixels, and extensive testing has shown maximum standard deviation below 0.09 pixels. 3-D reconstruction accuracy was calculated, performing camera calibration with the acquired corner positions, which were then projected back through the camera calibration matrix to

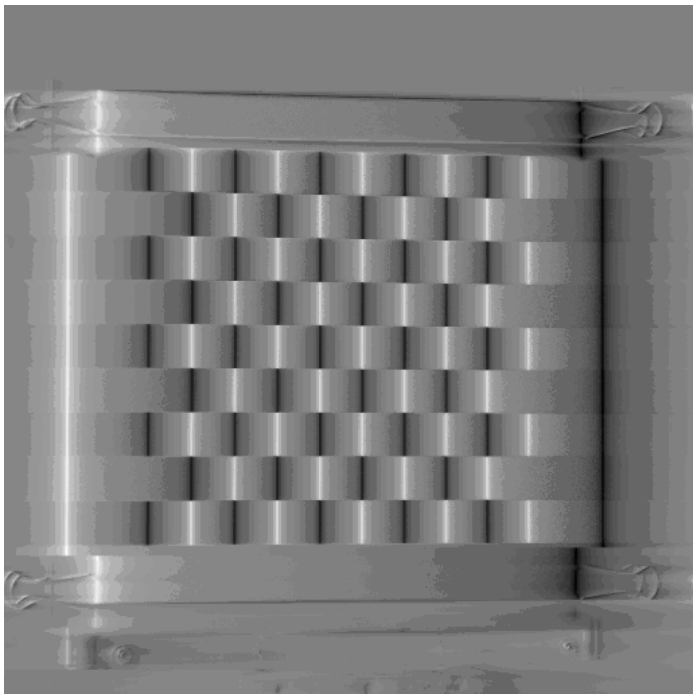

Figure 4.7 - Hilbert transform of the checkerboard target along one direction

determine the world coordinates of the observed corners. The distance between these coordinates and the given target locations was calculated for each corner and the ratio of these distances to the image scene width was established at or below 1/2000, which is a fair estimate of 3D reconstruction accuracy.

The overall accuracy of the proposed method was analysed through cross ratio analysis of the detected corner locations. Non existence of a bias between cross ratios was first established statistically and an accuracy measure introduced by Mohr, based on the re-projected point distances, was then employed to show the expected accuracy is always below 0.1 pixels.

The relevant publication can be found in Appendix E.

4.3 Phase-to-height translation

Camera calibration is but one part of the calibration procedure of a phase measurement instrument.

Phase measurement techniques calculate phase shift mappings of surface deformations or profile-to-reference differences, and rely, at some point, on the translation of the obtained phase map to either a dislocation or a height measurement. The rela-

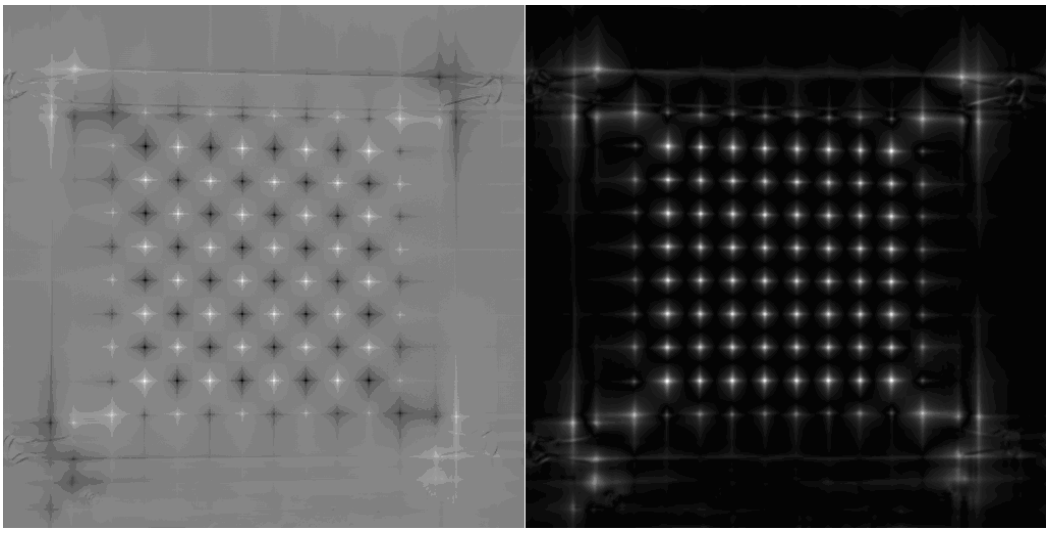

Figure 4.8 - Hilbert transform on both directions and absolute value

tion between phase and height has thus been the subject of a large number of works over the years, due to its impact on the overall method's accuracy. These works can be divided in *analytical* (Rajoub et al., 2005; Takeda and Mutoh, 1983) and *empirical* approaches (Legarda-Saenz et al., 2004; Sitnik et al., 2002).

Analytical methods, simple to apply as they may be, rely on a precise determination of camera and projector locations and do not explicitly account for the distortions of both projection and imaging optics. This can become a major issue, in those cases where the aberrations are either unidentified or known to severely impact the final result. The former argument can also be decisive to final accuracy, when even small changes between projector and camera positions can result in erroneous measurements.

On the other hand, most of the phase-to-depth empirical calibration methods proposed to date interpolate the results from a set of reference plane dislocations and respective phase maps. The accuracy of this procedure depends on the precision of the travelling stage that carries the reference plane and is fairly awkward to manoeuvre outside of laboratory premises.

In face of the findings relating to the shape of the function which governs the phase-to-height relation, an empirical solution is proposed in this work, which has been implemented and tested, and is currently being used in LOME. This solution uses just two views of a planar calibration plane and a linear fitting calculation.

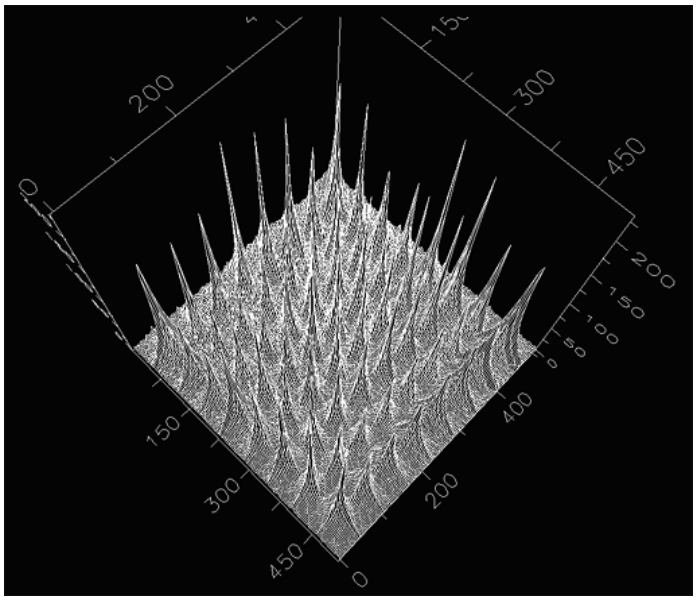

Figure 4.9 - The 3D result of the Hilbert transform

Analytical phase-to-depth methods

Fig. 3.2, reproduced here above for convenience, depicts a typical optical crossed axis fringe projection setup for phase measurement. A fringe pattern with a known spatial frequency is projected onto the object under test by projector P and the image is captured at camera C. E_p and E_c refer to the nodal points of the projection and imaging systems, respectively. The optical axis of these systems cross at point O on a reference plane R_0. L_0 is the distance from the camera – projector plane to the reference plane, d is the distance between centres of projection, θ is the angle between projector and camera and s represents the intersection of $\overline{E_pB}$ with the object surface. $\overline{E_tD}$ represents a telecentric projection through s, described by,

$$g_t(x,y) = a(x,y) + b(x,y)\cos[2\pi f_0 x] \tag{4.41}$$

where $a(x,y)$ and $b(x,y)/a(x,y)$ represent the average intensity and fringe visibility or modulation on the surface of the object, f_0 is the fundamental frequency of the observed grating image, and the fringes run perpendicular to the paper plane. In the non-telecentric case, the pattern on the reference plane can be described by,

$$g_0(x,y) = a(x,y) + b(x,y)\cos[2\pi f_0 x + \phi_0(x,y)] \tag{4.42}$$

with

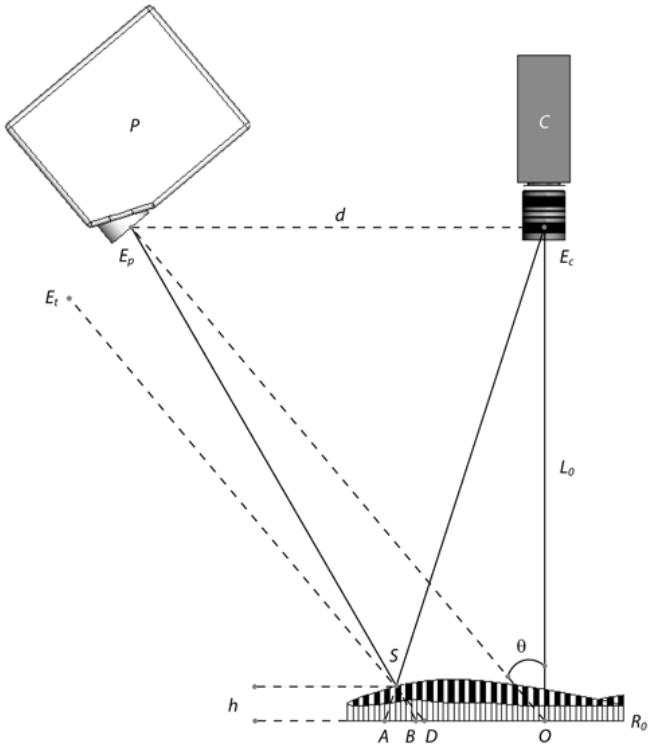

Figure 4.10 - Typical crossed axis phase measurement setup for structured lighting

$$\phi_0(x,y) = 2\pi f_0 \overline{BD} \tag{4.43}$$

When the object is in place, the ray from E_p that strikes the reference plane at B is seen from the camera as coming from A and the phase expression for $h(x,y)$ is therefore,

$$\phi(x,y) = 2\pi f_0 \overline{AD} \tag{4.44}$$

The fringe pattern on the object surface is expressed by,

$$g_s(x,y) = a(x,y) + b(x,y)\cos\left[2\pi f_0 x + \phi(x,y)\right] \tag{4.45}$$

and the phase difference between reference plane and object surface is,

$$\Delta\phi(x,y) = 2\pi f_0 \left[\overline{AD} - \overline{BD}\right] = 2\pi f_0 \overline{AB} \tag{4.46}$$

As shown by Takeda, this phase difference is completely recovered as,

$$\Delta\phi\left(x,y\right)=\mathrm{Im}\left\{\log\left[G_s\left(u,v\right)G_0^*\left(u,v\right)\right]\right\} \tag{4.47}$$

where $G(u,v)$ is the Fourier Transform of the fringe pattern and $*$ denotes complex conjugation.

In order to establish a relation between phase and height one uses the fact triangles E_psE_c and AsB are similar,

$$\overline{AB}=\frac{dh}{L_0-h} \tag{4.48}$$

so,

$$\Delta\phi\left(x,y\right)=2\pi f_0\overline{AB}\Longrightarrow h=\frac{L_0\Delta\phi\left(x,y\right)}{\Delta\phi\left(x,y\right)+2\pi f_0 d} \tag{4.49}$$

or,

$$\Delta\phi\left(x,y\right)=\frac{2\pi f_0 dh}{L_0-h} \tag{4.50}$$

A thorough analysis in (Zhang et al., 2004) indicates $h\left(x,y\right)$ is in fact a function of the lateral coordinate xx and the angle between projector and camera h as,

$$h=\frac{L_0}{\frac{2\pi L_0^2 d\cos(\theta)}{P_0\Delta\phi(x,y)(L_0+x\cos(\theta)\sin(\theta))^2}-\frac{d\cos(\theta)\sin(\theta)}{L_0+x\cos(\theta)\sin(\theta)}+1} \tag{4.51}$$

with,

$$P_0=\frac{1}{f_0}=\frac{P}{\cos\left(\theta\right)} \tag{4.52}$$

P being the projected grating period.

An analysis of either expression for $h\left(x,y\right)$ will reveal they are not that much different for a plausible application range. Reversing the equation for $h(x,y)$ above yields $\Delta\phi$ as,

$$\Delta\phi=\frac{2\pi hL_0^2 d\cos\left(\theta\right)}{P_0\left\{hA+L_0^3+B\right\}} \tag{4.53}$$

where,

$$A=dL_0\cos\left(\theta\right)\sin\left(\theta\right)+dx\cos^2\left(\theta\right)\sin^2\left(\theta\right)-L_0^2 \tag{4.54}$$

and

$$B=\left(L_0-h\right)x\cos\left(\theta\right)\sin\left(\theta\right)\left[2L_0+x\cos\left(\theta\right)\sin\left(\theta\right)\right] \tag{4.55}$$

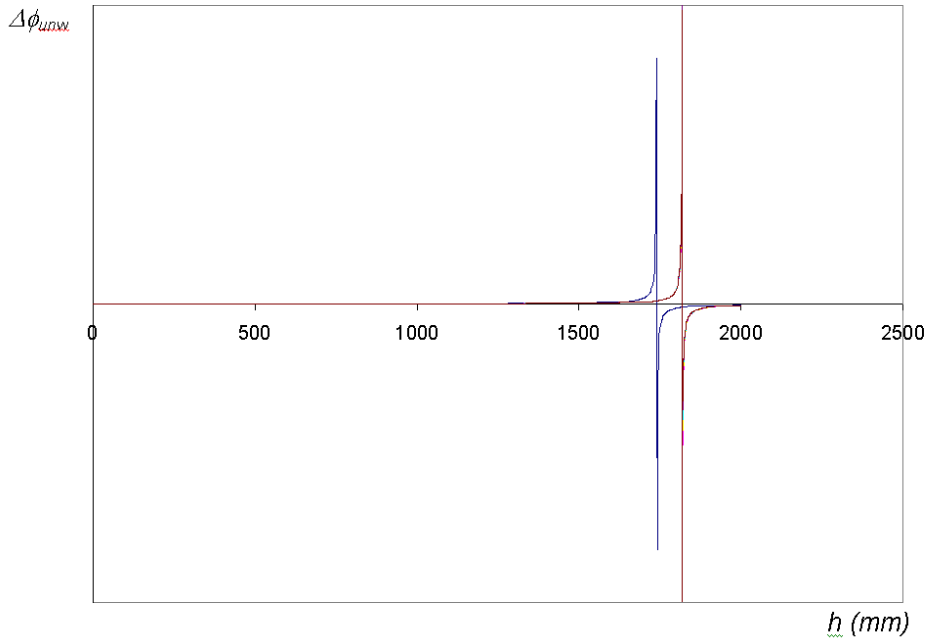

Figure 4.11 - $\Delta\phi\,(x, y)$ versus $h\,(x, y)$

Fig. 4.11 shows a comparison of the expressions for $\Delta\phi\,(x, y)$ in Eqs. 4.50 and 4.53, taken as functions of $h\,(x, y)$.

Several plots of Eq. 4.53 corresponding to different values of xx ranging from 0 to 100 mm are presented, although they cannot be distinguished at this scale. This plot was done for $L_0 = 1740$ mm, $d = 370$ mm, $f_0 = 0.6$ fringes/mm and a field size of 160 mm. The plots are nearly identical except for the region around camera location. Expression 4.50 has a discontinuity at the camera location, $h = L_0$, whereas the discontinuity for the phase expression in Eq. 4.53 with $x = 0$ is located at,

$$h = \frac{L_0^2}{L_0 - d\cos(\theta)\sin(\theta)} \tag{4.56}$$

Either way, the highly non-linear discontinuity regions occur near or past the camera location and are totally out of reach for ordinary phase measuring techniques. Comparison of the plot for the region of 0 to 100 mm shows the plots are very similar, as can be confirmed in Fig. 4.11.

Moreover, the analytical plots are strikingly linear at these regimes. The correlation coefficient for h in Eq. 4.49 and the first 120 mm is $R^2 = 0.9997$ in the plot shown in Fig. 4.12.

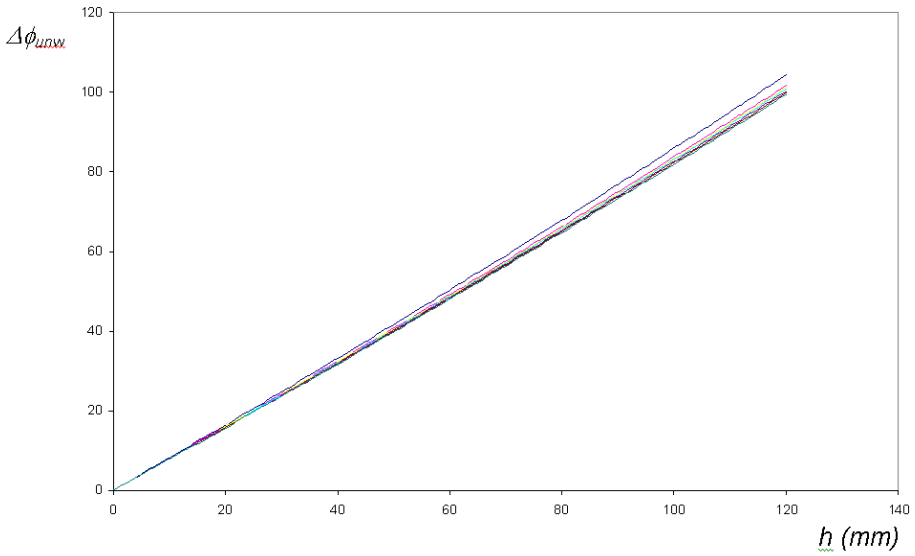

Figure 4.12 - The plot of $\Delta\phi\,(x,y)$ versus $h\,(x,y)$ – detail for 0 .. 120 mm

Empirical phase-to-depth methods

Experimental methods are based on the assumption the relation between height and phase for every point of the calibration volume can be described by an expression of the following type (Guo et al., 2005; Zhou and Su, 1994):

$$\frac{1}{h\,(x,y)} = a\,(x,y) + b\,(x,y)\,\frac{1}{\Delta\phi\,(x,y)} \tag{4.57}$$

The estimation of coefficients $a\,(x,y)$ and $b\,(x,y)$ then proceeds by sampling the calibration volume at regular intervals and calculating phase maps for a reference plane in each position, as illustrated in Fig. 4.13. For every (x,y) position there will be several phase values corresponding to the number of chosen height positions. The coefficients can then be calculated by linear interpolation (Zhang et al., 2005; Zhou and Su, 1994), least squares (Guo et al., 2005) or higher order polynomial fitting (Sitnik et al., 2002).

Fig. 4.14 shows the plot of the phase values obtained for one particular (i,j) image point as the reference plane was moved forward by 100, 1 mm steps. The field size was approximately 160 mm, L_0 was 1857 mm and d was 370 mm. There were 97 fringes across the field of view so the spatial frequency f_0 was 0.606 fr/mm. The fringe period P_0 was 1.649 mm and the dislocation of the fringe pattern over the image, $z * \tan(\theta) = 0.199$, so one complete fringe period elapsed every 8.277 mm of forward zz movement of the reference plane. This effect is also evident from Fig. 4.14

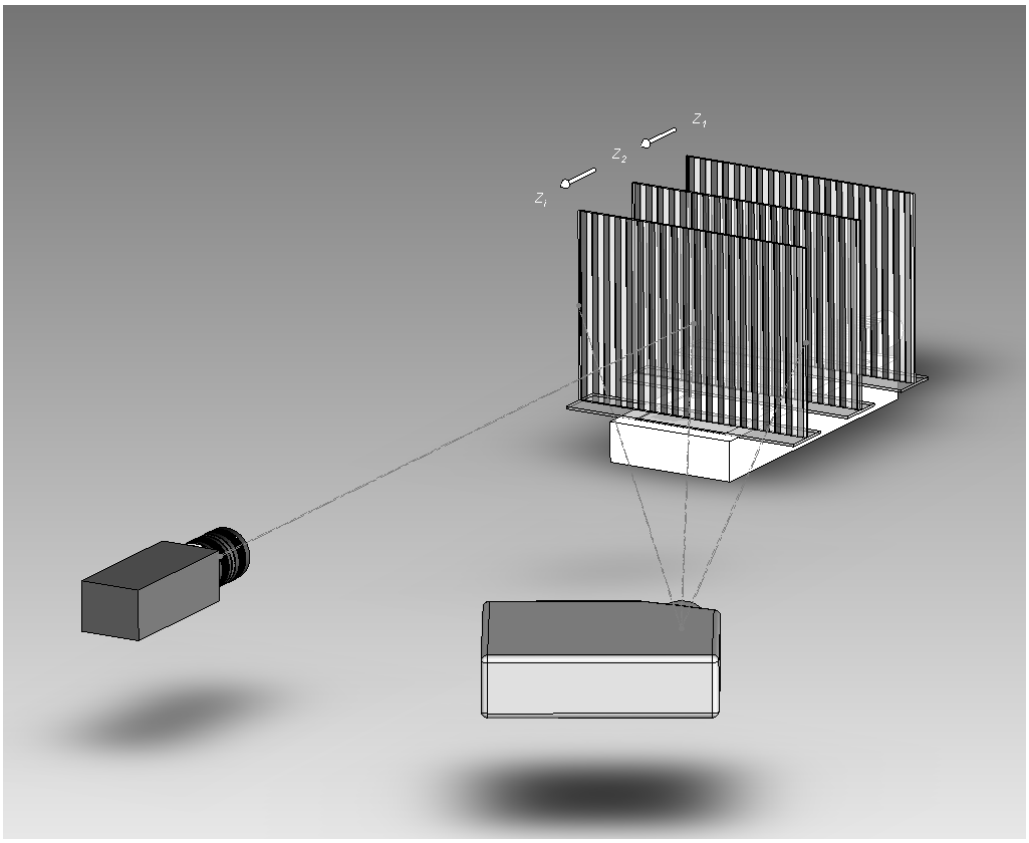

Figure 4.13 - Phase-to-height setup for zz interpolation

and has been reported in (Asundi and Chan, 1994).

To normalize the previous phase results, one has to add 2π to the phase values every 8.277 mm.

The final result is plotted in Fig. 4.15 along with the theoretical values predicted for that range in Eqs. 4.50 and 4.53. It is thus reasonable to conclude, from either the experimental data or the analytical solutions, that at these ranges phase varies linearly with height, and therefore the phase-to-height relation can be calibrated with either a linear or a least squares calibration procedure. Higher order polynomial interpolation will not improve the method significantly.

Two planes calibration

In view of the fact a linear calibration procedure is satisfactory for the plausible working depth, a simple phase-to-height calibration procedure has been devised in LOME (Tavares and Vaz, 2007a). Although the procedure described herein requires a priori accurate camera calibration and the possibility to calibrate for rigid body motion

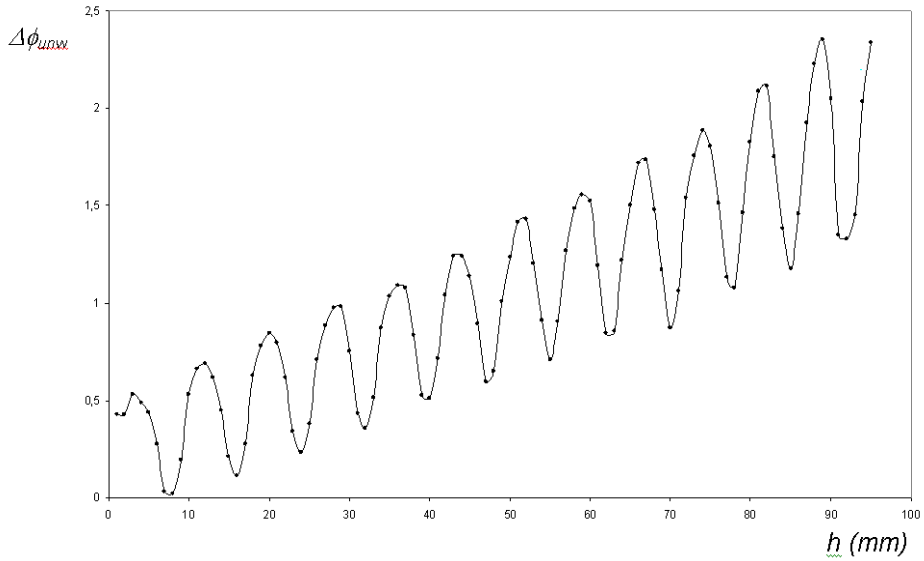

Figure 4.14 - $\Delta\phi\,(x, y)$ versus the interpolating zz

within the depth of field, it has the advantage of requiring just one further phase map of an inclined reference plane and can thus accelerate the complete process of calibrating phase-to-height. A necessary step for camera calibration is the acquisition of the image location of a set of points, traditionally on some sort of calibration pattern. The result from extrinsic camera calibration is a set of data describing a rigid body transformation. Basically it transforms the object space coordinate system (X_1, Y_1, Z_1), here denominated OCS_1, into a camera coordinate system (x, y, z), CCS, as depicted in Fig. 4.16. If the calibration plane is rotated to a new position and the camera is recalibrated, a new transformation is obtained, OCS_2, this time from (X_2, Y_2, Z_2) to CCS.

As before, the transformation is described in projective space with homogeneous coordinates, so the complete transformation, consisting of one rotation followed by one translation is reduced to just one operation:

$$\mathbf{T}_r = \mathbf{RT} = \begin{bmatrix} r_{11} & r_{12} & r_{13} & x_0 \\ r_{21} & r_{22} & r_{23} & y_0 \\ r_{31} & r_{32} & r_{33} & z_0 \\ 0 & 0 & 0 & 1 \end{bmatrix}. \tag{4.58}$$

with,

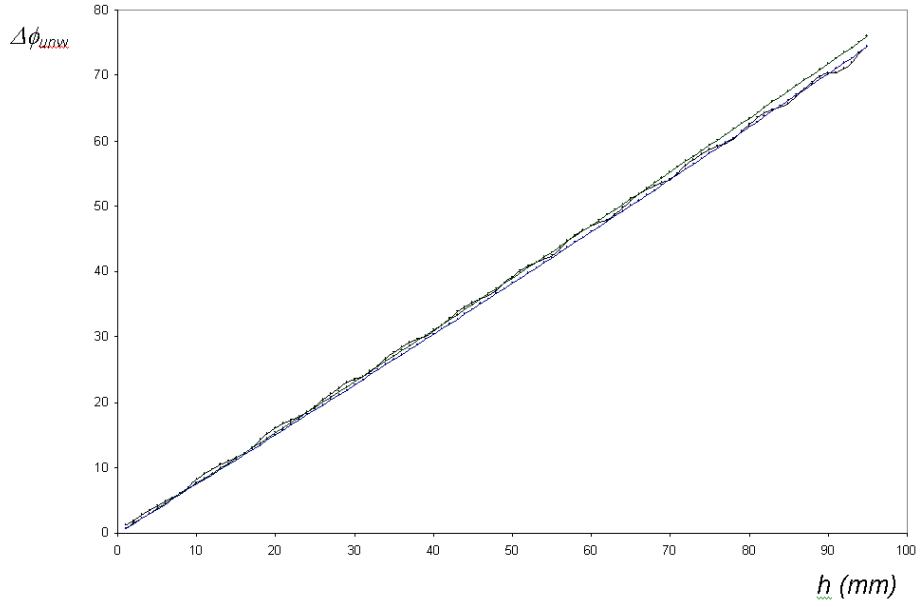

Figure 4.15 - Experimental versus predicted phase-to-height variation from 0 to 100 mm.

$$\mathbf{R}=\begin{bmatrix} r_{11} & r_{12} & r_{13} & 0 \\ r_{21} & r_{22} & r_{23} & 0 \\ r_{31} & r_{32} & r_{33} & 0 \\ 0 & 0 & 0 & 1 \end{bmatrix} \text{ and } \mathbf{T}=\begin{bmatrix} 1 & 0 & 0 & -X_0 \\ 0 & 1 & 0 & -Y_0 \\ 0 & 0 & 1 & -Z_0 \\ 0 & 0 & 0 & 1 \end{bmatrix} \tag{4.59}$$

If $\mathbf{T}_{r1}$ describes the transformation from OCS_1 to CCS and $\mathbf{T}_{r2}$ the transformation from OCS_2 to CCS, the transformation we seek, describing points of OCS_2 in OCS_1, will be given by,

$$\begin{bmatrix} X_1 \\ Y_1 \\ Z_1 \\ 1 \end{bmatrix} = \mathbf{T}_r \begin{bmatrix} X_2 \\ Y_2 \\ Z_2 \\ 1 \end{bmatrix} = \mathbf{T}_{r1}^{-1}\mathbf{T}_{r2} \begin{bmatrix} X_2 \\ Y_2 \\ Z_2 \\ 1 \end{bmatrix} \tag{4.60}$$

The transformation above calculates the position of the rotated calibration points on OCS_1. A phase map is calculated at each position and subtracted to obtain a phase difference map between both planes. If zz is taken as 0 on OCS_1, this procedure returns a set of points with different zz coordinates, to each of which there is a corresponding phase difference, $\Delta\phi\,(x, y)$. A simple least squares fitting of zz coordinates to phase differences will result in a couple of global coefficients a and b for all (x, y),

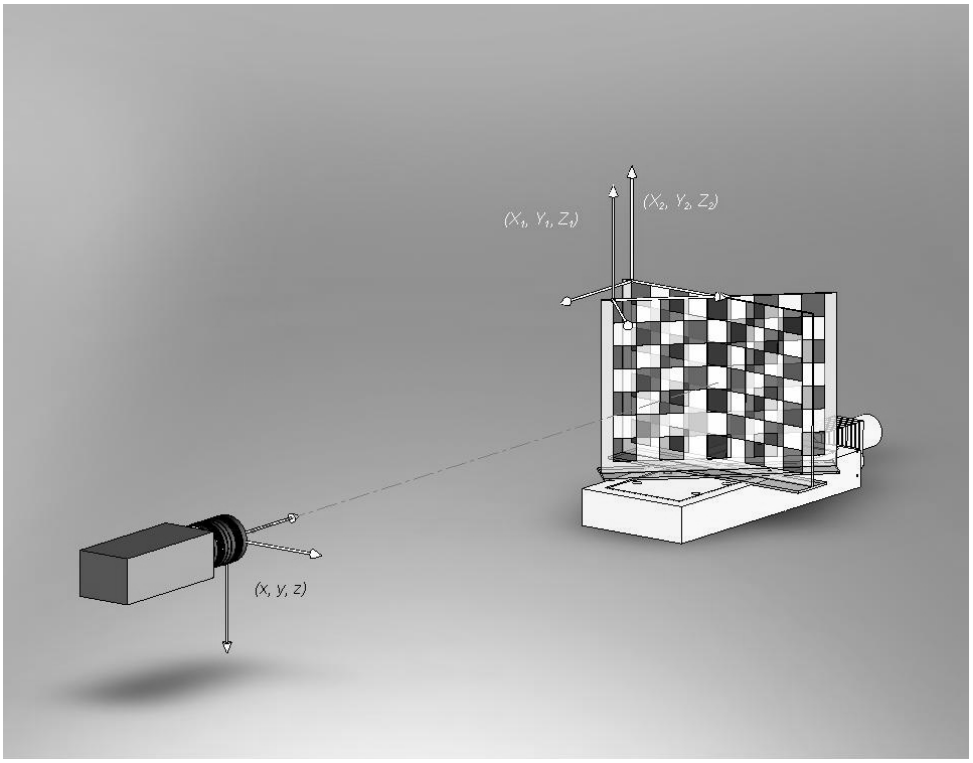

Figure 4.16 - Two planes phase-to-height calibration setup

such that,

$$h(x,y) = a + b\Delta\phi(x,y) \tag{4.61}$$

This procedure was tested against the least squares z-shift described by Guo on the plaster mold shown in Fig. 4.17. This part is 70 mm thick and 55 mm high. The lateral dimension recovered was 160 mm. Though most of its relief is quite simple to handle, the plaster model has both a very steep border and a high surface curvature. The z-shift phase-to-height relation was calibrated using the full 100, 1 mm shift reference plans mentioned earlier and with the proposed technique, placing the reference plane at 0 and 42 degrees. The results can be seen in Figures 4.18 and 4.19 for line and column numbers 255 on a 512 by 512 pixels image. Small deviations under 2% between both methods can be noticed at the begin and end of the plots which seem to be related to radial camera calibration.

The final surface was also compared against a high resolution 3D model of the part, made by contact profiling. The differences, both in height and in lateral coordinates, between the 3D models seem to indicate very small errors, between 0.01 and

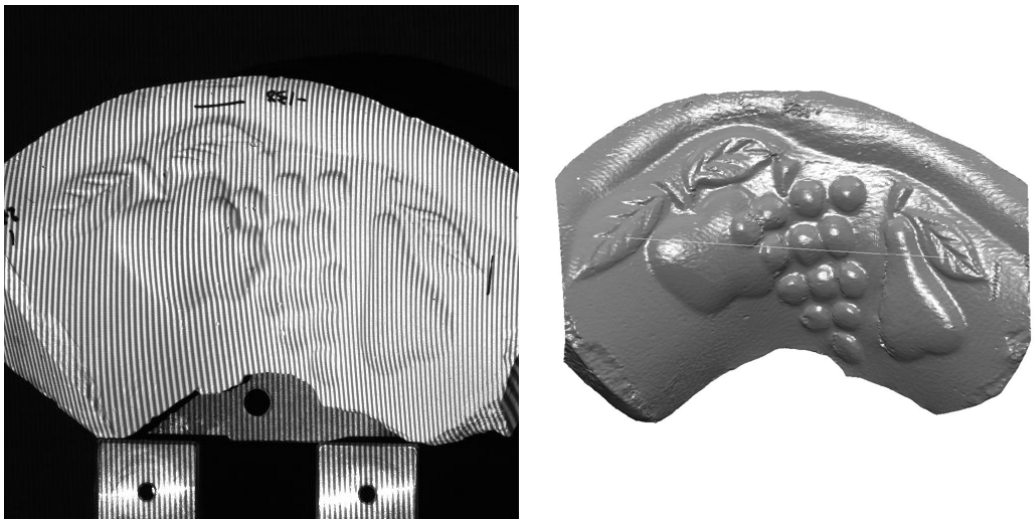

Figure 4.17 - Dimension controlled plaster model. Courtesy, Norcam Portugal. Fringe projection and final 3D surface obtained in LOME.

0.1 mm, though the exact positioning of the measurement markers on the 3D models may not be as accurate. The relevant publication can be found in Appendix E, and the method has been used in all phase-to-height calibration occasions thereafter.

4.4 Illumination and the Optical Transfer Function

The performance of full-field fringe projection methods can also be impaired the projection system contrast degradation, a physical imposition of real systems finite impulse response width. This problem has been studied in LOME and a simple technique to limit these effects has been proposed, which makes use of an Optical Transfer Function analysis.

It is not uncommon to observe imaging distortion artefacts in full-field fringe projection systems, due to the system's inability to reproduce the ideal sinusoidal patterns projected onto the object. This is a particularly stringent problem with multi-frequency methods such as Temporal Phase Unwrapping, because an inadequate fringe width results in wrong or incomplete fringe superposition, necessarily impairing the results of the phase-shift algorithm. A less visible effect, but one which can still degrade final image quality, is contrast degradation imposed by the system's finite impulse response width - the response of an incoherent system to a single frequency sinusoidal pattern degrades the object contrast or modulation by the complex Optical Transfer Function (OTF) amplitude, known as Modulation Transfer Function (MTF).

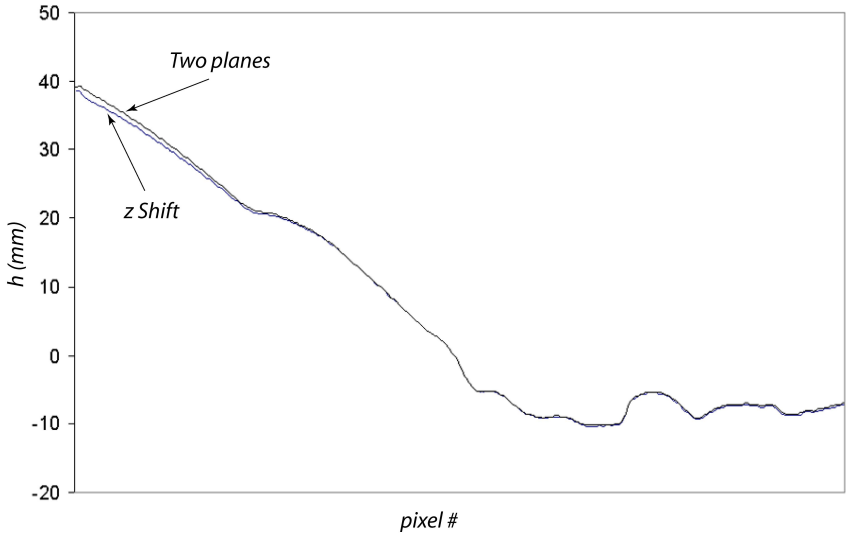

Figure 4.18 - Profile height along line# 255 of the plaster's model 3D point cloud.

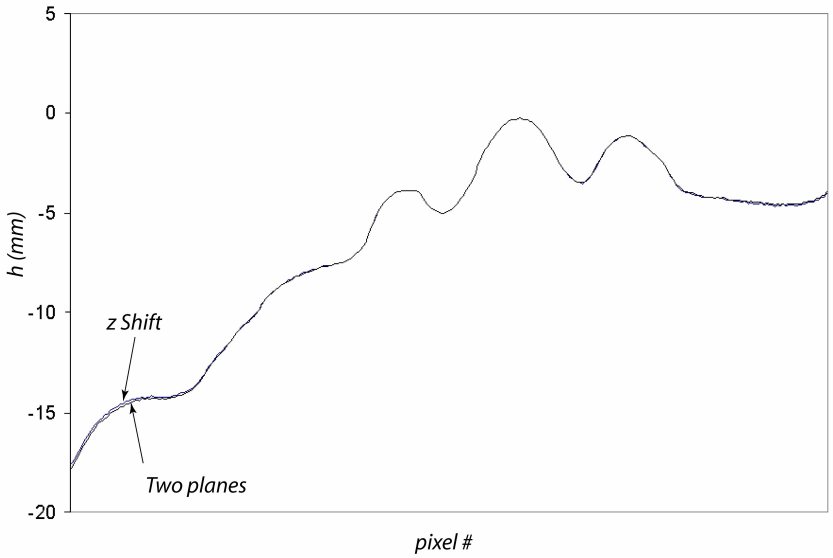

Figure 4.19 - Profile height along column# 255 of the plaster's model 3D point cloud.

An example of such image degradation can be seen in Fig. 4.20, which shows the effect of a typical projector device on an ideal sinusoidal pattern and the consequences on the final acquired 3D surface.

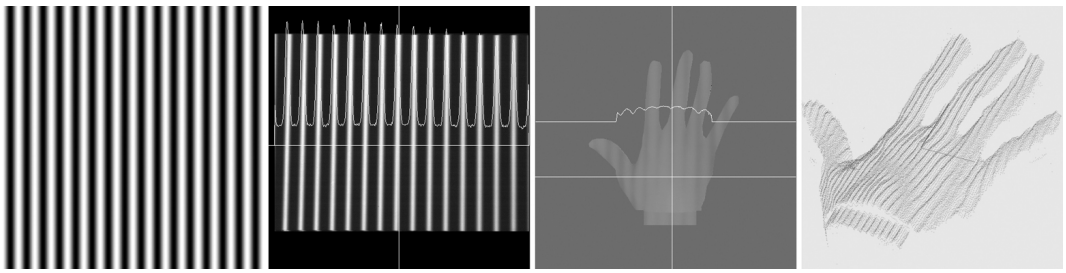

Figure 4.20 - Imaging artefacts in Temporal Phase Unwrapping.

There are other causes to contrast degradation, although it seems the limiting factor is the reduced contrast ratio of Digital Light Processors (DLP) or Liquid Crystal Displays (LCD) currently being used as light modulators. In particular, the high black level observed with these projectors, due to the fact that either the crossed polarisers in LCD displays or the partial "ON" duty cycle, even in no signal black scenes in DLPs, results in some unintended light always being transmitted to the scene.

A simple solution to this problem is suggested by OTF analysis, and has been successfully applied to the TPU method in LOME. Basically it is a seek for the periodic function which has to be projected so the final image is a near perfect sinusoid.

In order to find the image necessary for each projected frequency, the complex OTF for the projection and imaging system, henceforth called imaging system, is first calculated. The OTF of an incoherent imaging system can be defined as the systems ability to transfer contrast from object to image. It is the Fourier transform of the system's impulse response, i.e., the imaging of a single point source, which can be obtained by using the Huygens-Fresnel integral to follow the propagation of light from the point source through the system. Incoherent imaging systems can be considered linear in intensity. This means that,

$$I(x,y) = I_o(x,y) \otimes IR(x,y) = \int_{-\infty}^{+\infty} \int_{-\infty}^{+\infty} I_o(u,v)\, IR(x-u, y-v)\, dudv \qquad (4.62)$$

where I is the image intensity, I_o is the object intensity, IR is the system's impulse response and $\otimes$ is the convolution operator. In reciprocal space, the use of the convolution theorem implies the Fourier transform of the image intensity is equal to the product of the Fourier transform of the object intensity and the Fourier transform of the Impulse Response, which is the OTF of the imaging system,

$$\mathcal{F}\{I(x,y)\} = \mathcal{F}\{I_o(x,y)\}\, OTF(u,v) \tag{4.63}$$

This provides a simple way to calculate the complex OTF of the imaging system. Now, for each ideal sinusoid pattern, there must be some artificially distorted image, I_{unkn}, which, when sent to the projector and imaged through the system, will result in a perfect sinusoid, I_{ideal},

$$I_{ideal}(x,y) = I_{unkn}(x,y) \otimes IR(x,y) \tag{4.64}$$

This in turn implies,

$$\begin{aligned} \mathcal{F}\{I_{unkn}(x,y)\} &= \frac{\mathcal{F}\{I_{ideal}(x,y)\}}{OTF(u,v)} \iff \\ \iff I_{unkn}(x,y) &= \mathcal{F}^{-1}\left\{\frac{\mathcal{F}\{I_{ideal}(x,y)\}}{OTF(u,v)}\right\} \end{aligned} \tag{4.65}$$

An InFocus LP70R DLP projector and a Kodak ES1.0 camera have been used to produce these images. The artificial images have been created as described above and saved for later projection. As shown in Fig.4.21 for 5 and 16 fringes these images are, as expected, much narrower on the black level, which is bound to compensate for the limited contrast ratio of the projector.

The effect on the objects used in Fig. 4.20 can be seen in Fig. 4.22, now free from the previous artefacts. Both the images taken from the reference plane at either 5 or 16 fringes and the hand surface show a clear improvement over the original ones. The drawback of the method lies in having to calculate and record the fringe patterns in advance, but even so the benefits seem to be worth the effort, particularly in repetitive

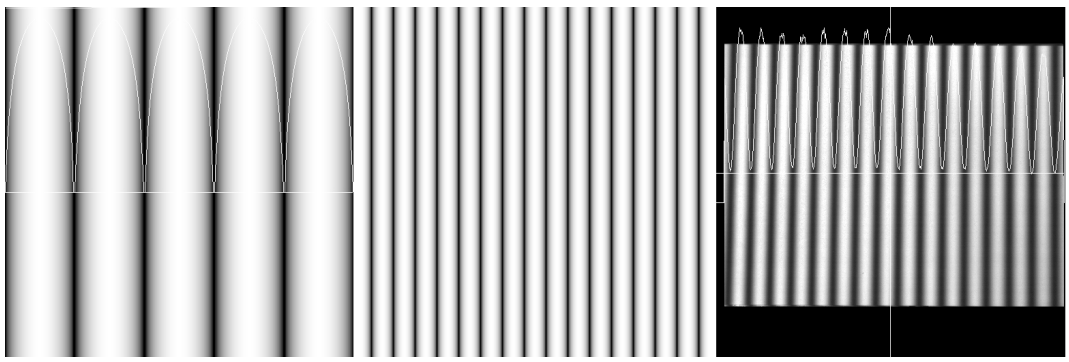

Figure 4.21 - Artificially created patterns to obtain sinusoidal fringes when sent through the imaging system.

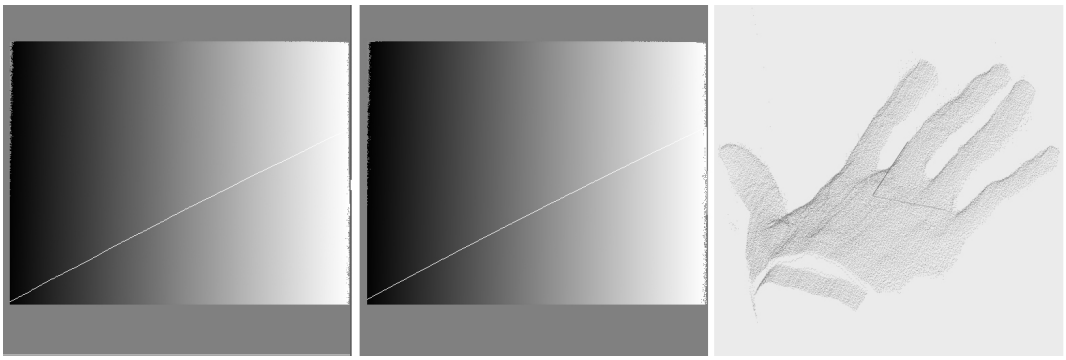

Figure 4.22 - Corrected images with artificial fringe patterns.

tasks where the same patterns can be reused several times. A publication was issued from this work, which can be found in Appendix E.

Chapter 5

Applications

During the course of the present work, several applications have been targeted, with different degrees of success. Although it was never intended to develop image registration and integration techniques, it is no less true that this is a crucial step, as far as concerns real world applications, for if a single view is acquired, the possible application range will be severely compromised. Thence, some of the applications of the present prototype required some sort of manual registration, achieved with specialised software packages. Two of the Experimental Mechanics applications discussed below were made possible due to this effort and in some occasions image registration would have been helpful in other applications too.

5.1 LOME's 3D Cart

A flexible, cart like structure was built at LOME to accommodate the projector and the camera, which can be seen in Fig. 5.1. This structure was assembled with Bosch strut profiles due to their versatility, and is fairly simple to operate. The cart can be moved around the laboratory for 3D acquisition of rather large objects, which can't easily be moved. It is composed of a central pillar with an attached arm which can slide both vertically and horizontally. One further degree of freedom enables the inclination of the bar, attached to the end of the front arm, where both camera and projector can themselves slide. A versatile ball-head socket which allows 360 degree orientation and 180 degree tilt, connects both camera and projector to this bar, to facilitate alignment of both components.

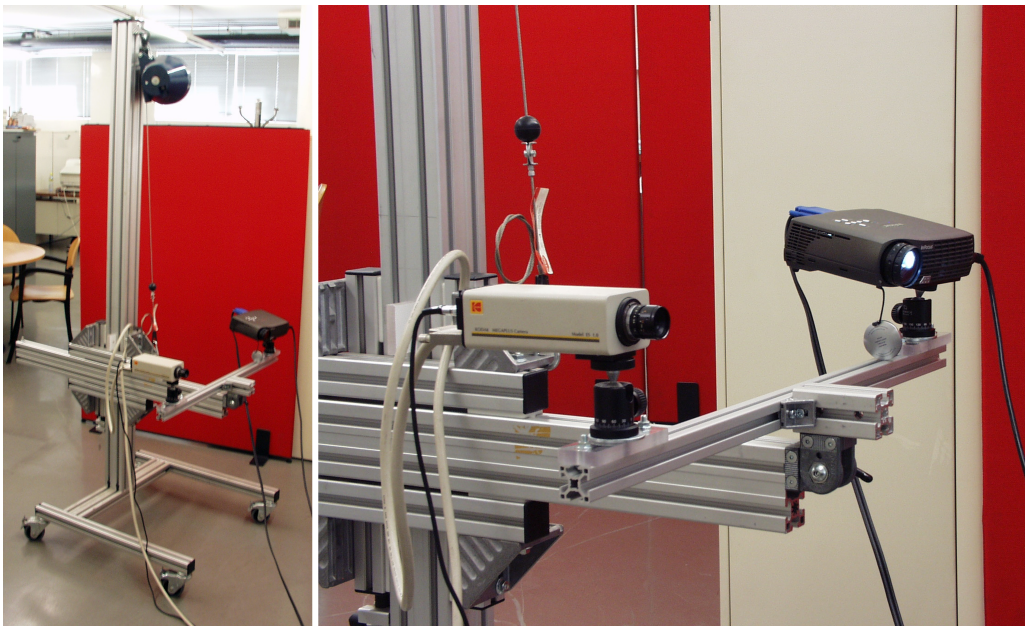

Figure 5.1 - LOME's 3D cart.

5.2 Experimental Mechanics

With the advent of Finite Element Analysis (FEA), a typical experimental mechanics study of the natural vibration modes of an object such a bar or a plate, became much simpler. An elementary mesh is created on the three-dimensional shape with different degrees of complexity according to the problem at hand, which is subsequently subjected to elementary analysis. This is a fairly straightforward procedure if the 3D shape is available, as is often the case when access to the mechanical project is granted. Still, there are several practical situations which can benefit from the possibility of 3D shape acquisition, either because the part doesn't have a mechanical project or simply because the three-dimensional information isn't readily available, even when there is a project. In these situations, the analyst can turn to optical techniques, such as Time Average Holography or ESPI, which can be complemented by proven mechanical methods and numerical analysis (Lopes, 2008; Santos, 2008; Vaz, 1995). Whenever these situations occur, FEA based on acquired 3D shape on location, can greatly improve data reliability, by providing a redundant method to ascertain the results obtained through experimental means.

This line of thought was followed herein. The shape of two very different objects was acquired and used in a FEA software, and the results compared with the ones obtained through experimental techniques. The first is a turbine blade from a

Hercules C-130 AE2100 turbo prop engine and the second is a timing belt cover from a Renault R5 1100 cc motor.

The gas turbine blade study

The gas turbine principle has been known for thousand of years. Hero of Alexandria is credited as the first to document a reaction gas turbine, the aeolipile, which used steam to propel a rotating air chamber, in the first century. Apparently, the idea of using the reaction torque of a steam engine had already been used some 400 years before, by another Greek, Archytas of Tarentum, who demonstrated the principle by flying a mechanical pigeon made of wood. However, the truly great achievements in the development of gas turbines that eventually led to the birth of jet propulsion with Sir Frank Whittle in 1937, were to happen at or after the industrial revolution.

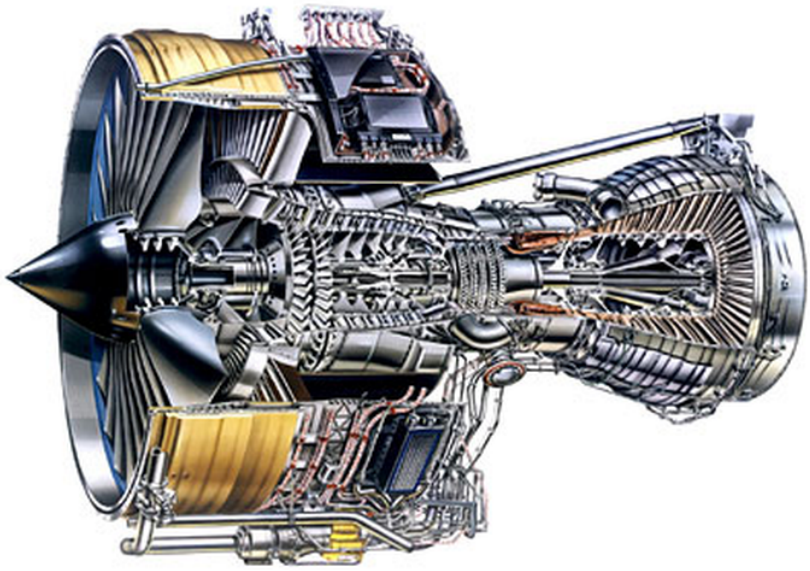

Figure 5.2 - The Rolls Royce Trent 800 gas turbine engine. Courtesy, Rolls Royce PLC.

A gas turbine works under a simple thermodynamic cycle known as a Brayton cycle, originally described by George Brayton in 1872. Ideally a constant entropy process, the actual Brayton cycle is truly composed of two adiabatic and two isobaric processes. Intake air is adiabatically compressed and driven through an open combustion chamber where fuel is added at high temperature. The mixture is burned at constant pressure and the exhaust gases are adiabatically expanded to atmospheric

pressure through a turbine. Part of the turbine work is used to drive a compressor, whilst the remaining produces the resulting thrust from the engine. Gas turbines are used in commercial and military aviation, trains, ships, tanks and electrical generation. A turbo fan engine from Rolls Royce, in use in most of the Boeing 777 airplanes, is depicted in the cutaway Fig. 5.2. This is a 14 stage compressor and 7 stage turbine engine, which can be seen behind the combustion chamber and in the schematic in Fig. 5.3.

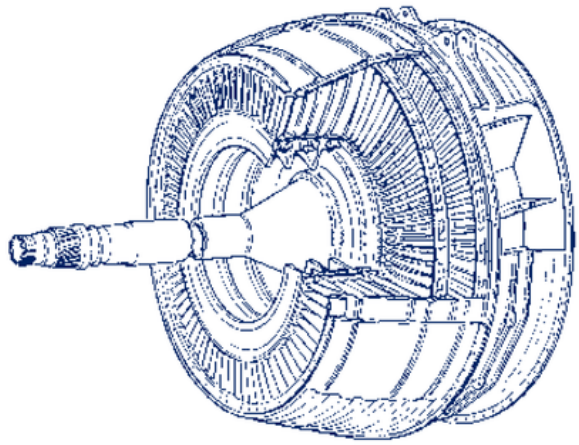

Figure 5.3 - Trent 800 multi-stage turbine cutaway showing the central shaft, the 5 stage low power turbine and the single stage intermediate and high power turbines. Courtesy, Rolls Royce PLC.

Analyses of the deformation of gas turbine components are very pertinent, because deformed components can lead to reduced air flow efficiency throughout the entire engine. Furthermore, these engines operate at unusually high regimes, which create all sorts of solicitations to the various components and can lead to High-Cycle Fatigue (HCF). HCF is avoided in rotating turbine blades by controlling vibratory stresses. The blades are designed by tuning the lower natural frequencies to avoid operating near strong excitations and high vibratory stresses. When the natural frequency variance is greater than an acceptable band, the blades must be designed with

sufficient stiffness to limit stresses at or near resonance conditions. HCF failures can occur when these conditions are not met, or if excessive excitations occur due to other causes such as rubbing. Not only does the variability of blade fabrication influence natural frequencies on assembly, but also wear and erosion can reduce resonant frequency margins over time, leading to HCF damage.

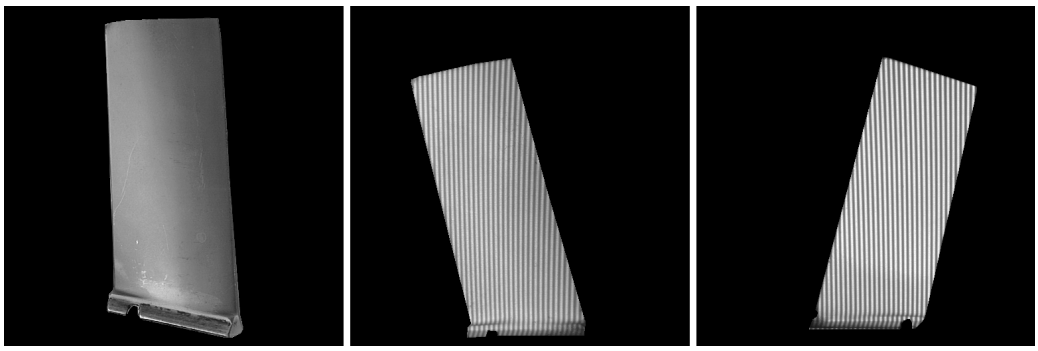

Figure 5.4 - Turbine blade. The centre and right pictures show the fringe pattern on both sides of the blade.

A vibration analysis was conducted on a turbine blade from a AE 2100 Rolls Royce engine in LOME. The AE 2100 turboprop, shown in Fig. 5.5, is a two shaft gas turbine with a 14-stage high pressure compressor. The low pressure shaft, driven by a two-stage power turbine, drives itself a compound planetary reduction gearbox connected to the propeller. The AE 2100 was developed to power military transports, long-range maritime patrol and high-speed regional aircrafts.

Figure 5.5 - The AE2100 turbo prop engine, used by the military transportation C130 airplane. Courtesy, Rolls Royce PLC.

The shape of a blade, depicted in Fig. 5.4, is rather irregular, which makes it difficult to reproduce in mechanical 3D drawing. After point cloud acquisition from both sides, the points from both clouds were combined by a simple manual registration process, which required close contact of most of the edge points. The complete

point cloud was transformed into a single surface, which was then closed. A solid part was generated from this surface and refined through mechanical drawing. A FEA software package was then used to create an elementary mesh with 2918 elements and 6040 nodes. The rendered 3D model and the mesh can be seen in Fig. 5.6.

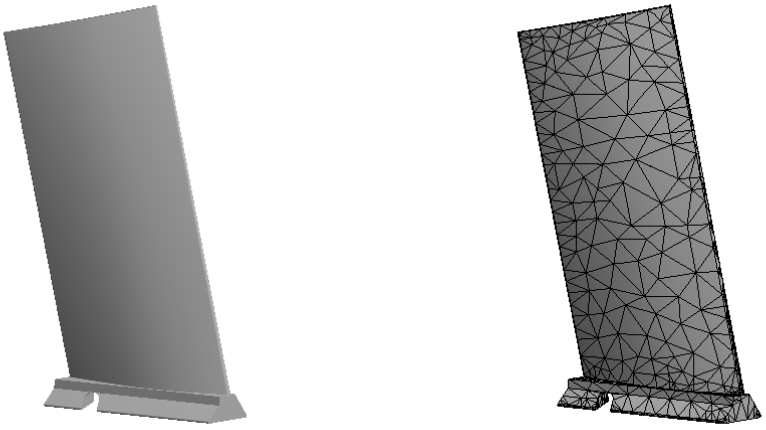

Figure 5.6 - Turbine blade 3D rendered model and mesh for FEA.

This blade had already been the subject of another study with ESPI, for observation of the natural vibration frequencies, conducted in LOME (Santos, 2008). A comparison of the first few natural vibration modes found experimentally and with FEA can be seen in Figs. 5.7 to 5.11. Table 5.1 presents the results from both studies and the graphic in Fig. 5.12 shows a comparison of the frequencies found in both cases. Although there's a slight shift in some frequencies and several modes are missing in the experimental data, the overall resemblance is quite remarkable.

The experimental excitation mechanism was a piezoelectric transducer attached to one side of the blade. These transducers have a finite size and are known to mask some frequencies, such as those which have a nodal line that goes through the transducer. At any rate, some modes are difficult to excite and assess, because they are very close to one another. In these cases, mixed modes may appear which are difficult to characterize.

These blades are fabricated in a NiCo alloy and show a rather high stiffness, with a Young coefficient of $200x10^9$ Pa, and a density of 8.89 g/cm^3. This stiffness is necessary for the tuning of the natural vibration modes, since jet engine solicitations cover a very wide frequency range, given the very high operational regimes of tens of

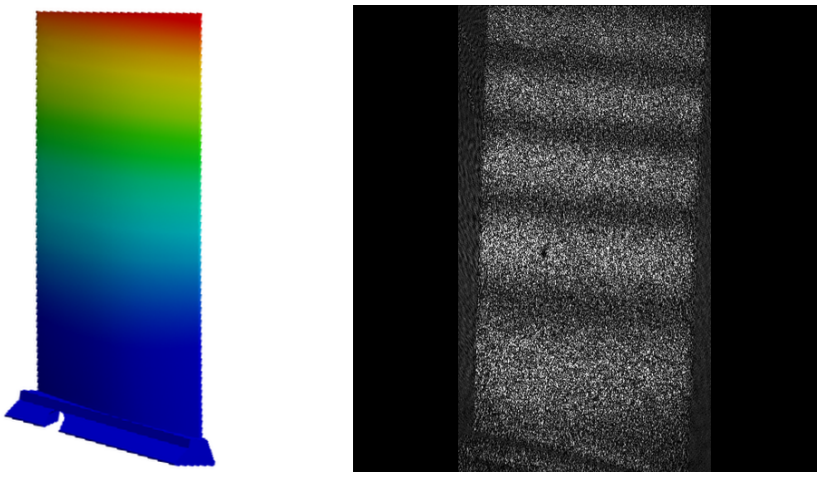

Figure 5.7 - 1^{st} mode at 460 Hz.

thousands of rotations per minute (RPM) in some cases. The first 24 natural vibration modes obtained through FEA can be found in Appendix D.

Timing belt cover study

A second comparative study between experimental determination of natural vibration frequencies and numerical results based on an acquired shape, was carried out on a timing belt cover from a Renault R5 engine, shown in Fig. 5.13. The experimental study was carried out in LOME some years ago after a request from Renault, upon detection of a leakage from the border of the cover seal. The cover is a low cost part built by sheet metal forming on St37 steel with 1.2 mm thickness. The hole on the cover is crossed by the end of the crankshaft which connects to the water pump pulley. The border of the hole is obtained during metal forming and is used as case support for a oil seal. It was a leakage on this seal that triggered the study of the component.

Amongst other analysis, a time average ESPI study was conducted on the cover using a piezo-electric transducer bonded to the cover as an excitation source. The cover was fastened to the engine block by its own screws, so as to reproduce working conditions as closely as possible, as can be seen in Fig. 5.14 (Vaz et al., 1996).

The cover shape was acquired with an FTP technique. The resulting point cloud can be seen in Fig. 5.13. This point cloud was used to create a triangular mesh and a surface was build from that mesh. A 1.2 mm offset was given to that surface and the border was closed. A solid part, shown in Fig. 5.15 was obtained from that shell which served as the starting point to a FEA analysis. The finite element mesh with

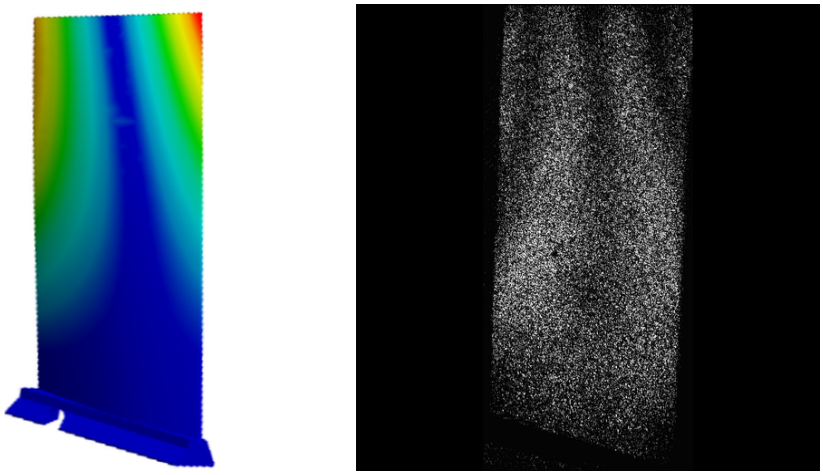

Figure 5.8 - 2^{nd} mode at 1815 Hz.

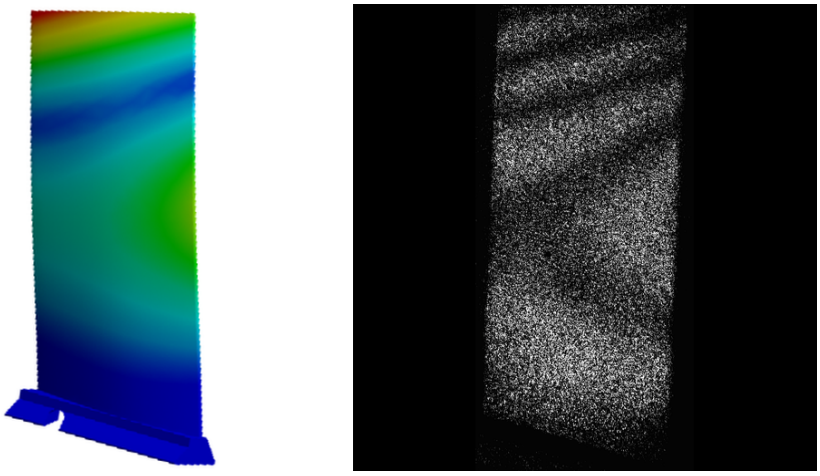

Figure 5.9 - 3^{rd} mode at 2150 Hz.

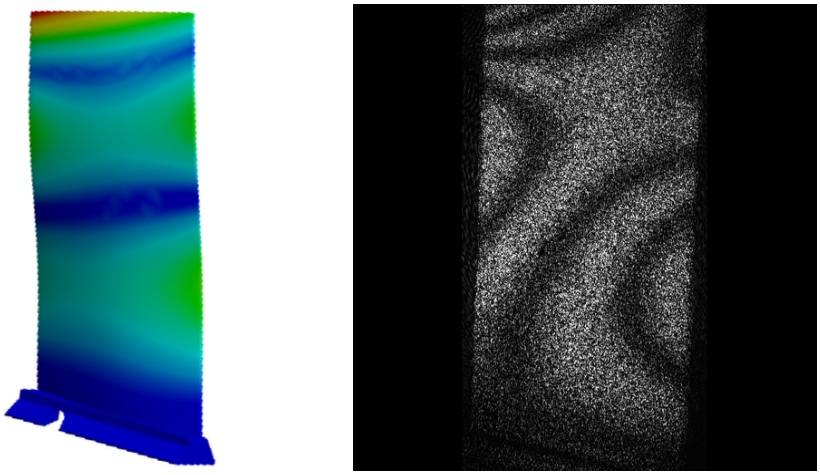

Figure 5.10 - 6^{th} mode at 5385 Hz.

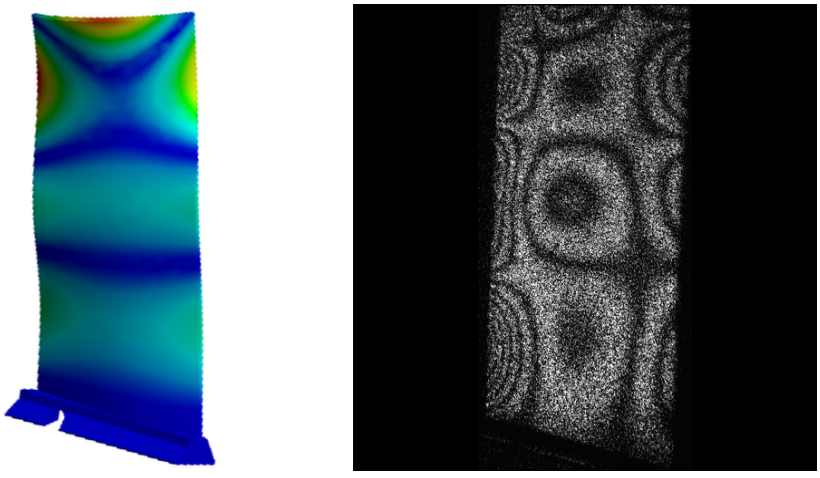

Figure 5.11 - 8^{th} mode at 9409 Hz.

Mode #	FEA (Hz)	ESPI (Hz)
1	460	490
2	1815	2384
3	2150	2680
4	4263	—
5	4683	—
6	5385	6256
7	8020	—
8	9409	9009
9	10339	—
10	12247	—
11	14265	—
12	15071	—
13	16598	—
14	17299	—
15	17997	—
16	18577	—
17	21289	—
18	22356	22427

Table 5.1 - Gas turbine helix blade - natural vibration frequencies

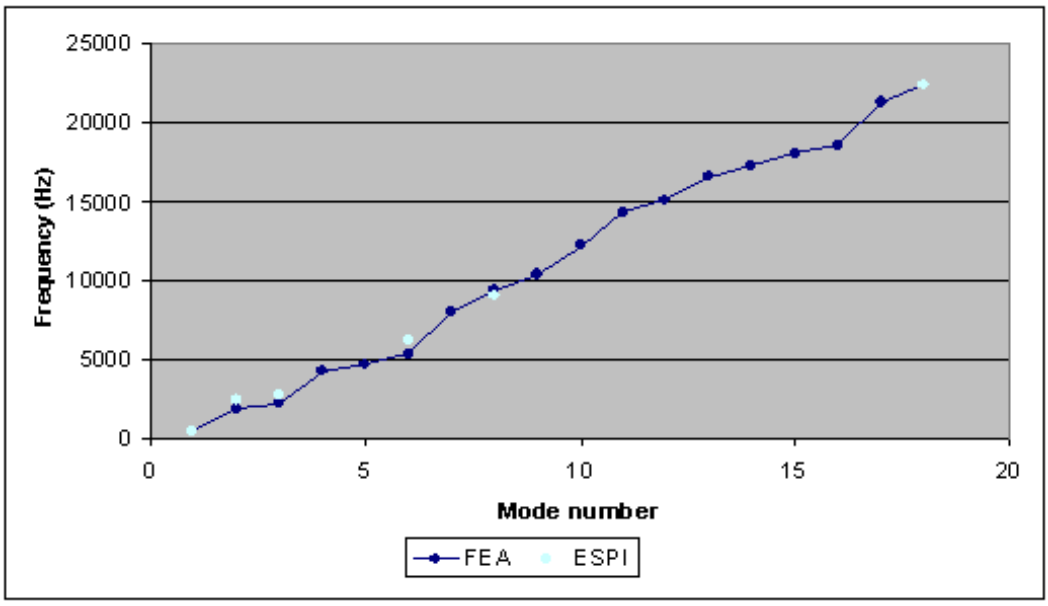

Figure 5.12 - Gas turbine helix blade - comparison of numerical and experimental results.

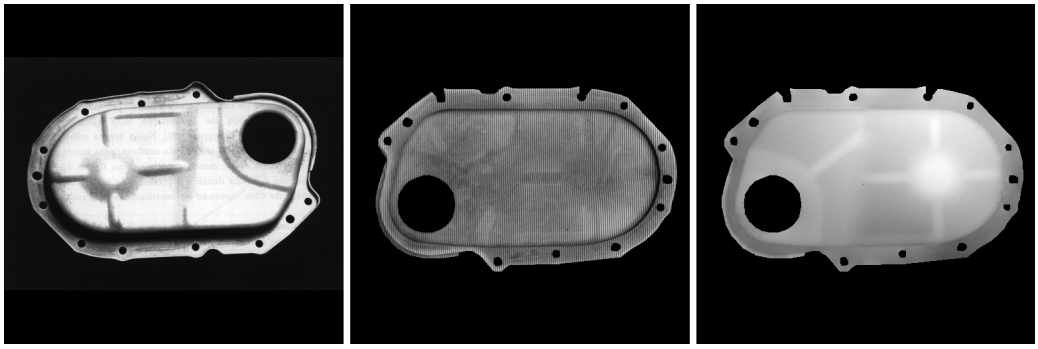

Figure 5.13 - The timing belt cover. The centre picture shows the fringe pattern and the rightmost picture shows the obtained point cloud.

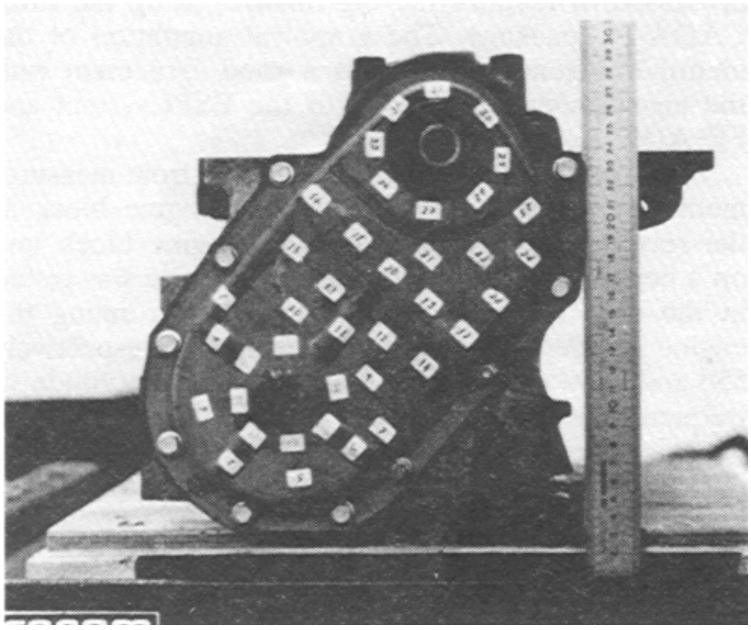

Figure 5.14 Timing belt cover fastened to the engine block - LOME.

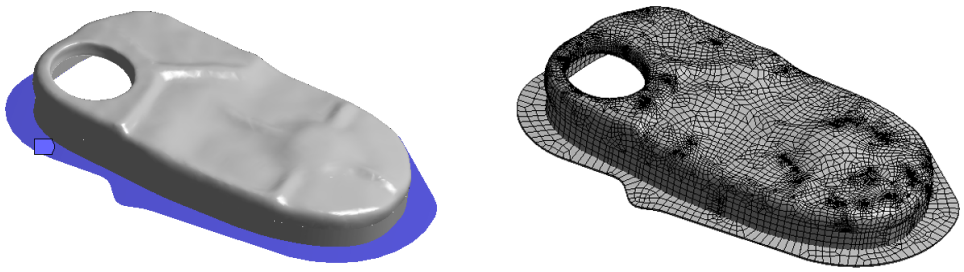

Figure 5.15 - Timing belt cover 3D rendered model and mesh for FEA.

11628 elements and 11787 nodes can also be seen in Fig. 5.15.

The cover solid 3D model was fixed at the joint shown in blue in Fig. 5.15, so as to simulate fastening to the engine block. Some of the first natural vibration modes can be seen in Figs. 5.16 to 5.21 along with the corresponding modes found with ESPI.

Although the kind of exciting mechanisms in a vehicle engine is very different from the ones found in gas turbine engines, it is also true that higher harmonics can be picked-up by this sort of components, starting vibration phenomena at higher frequencies. The results found by numerical study on the 3D shape acquired by the methods in this work, show also here a very close approximation to the interferometric results found in earlier studies. The comparison is shown in Table 5.2 and in graphical form in Fig. 5.22.

The complete FEA analysis results can be found in Appendix D.

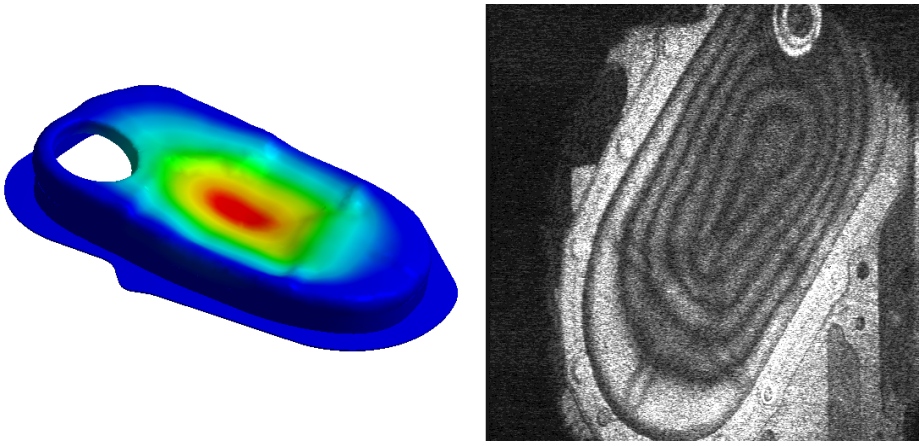

Figure 5.16 - 1^{st} mode at 677 Hz.

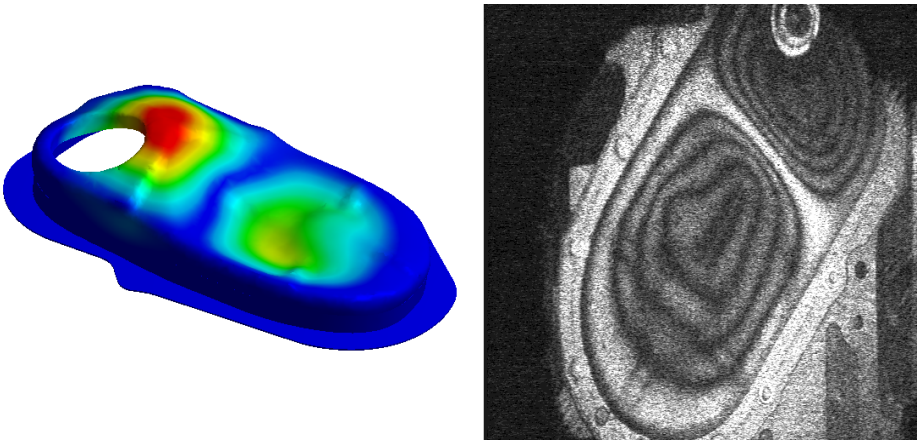

Figure 5.17 - 2^{nd} mode at 1204 Hz.

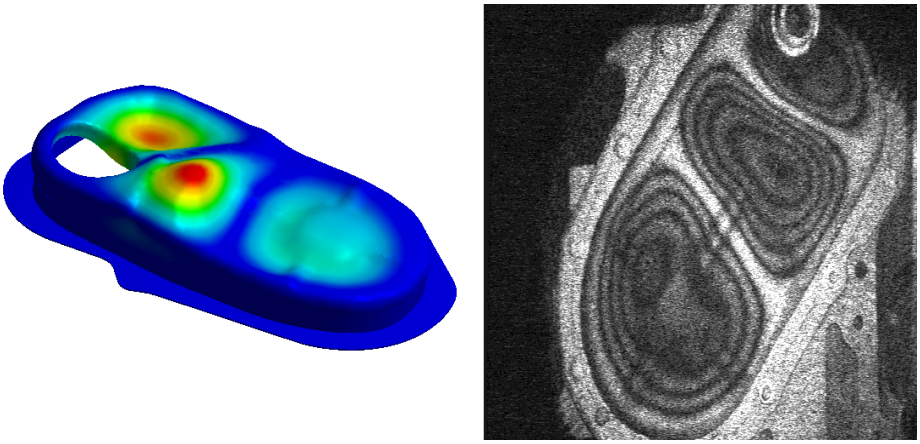

Figure 5.18 - 3^{rd} mode at 1596 Hz.

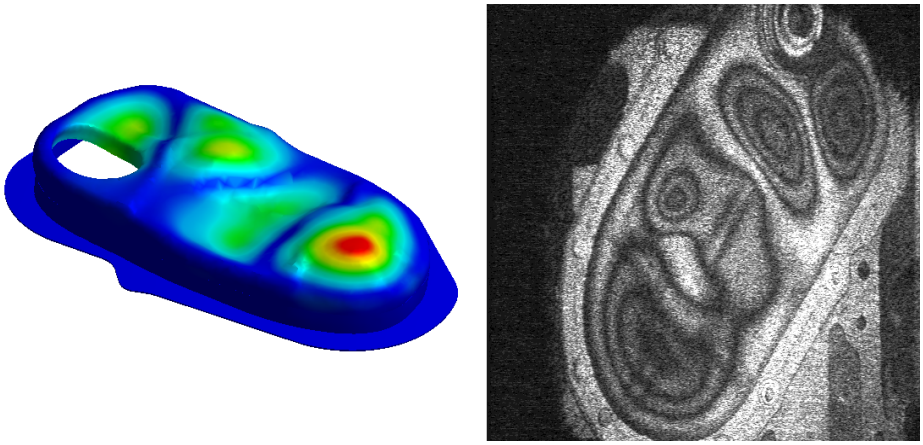

Figure 5.19 - 6^{th} mode at 2303 Hz.

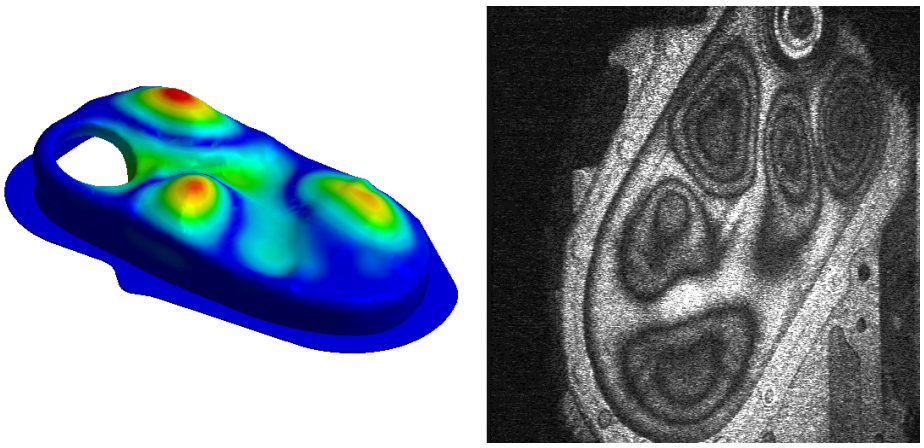

Figure 5.20 - 8^{th} mode at 2626 Hz.

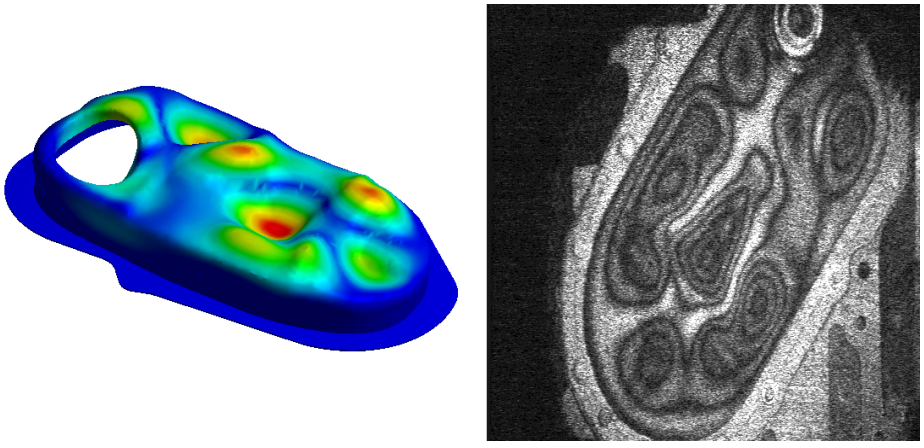

Figure 5.21 - 9^{th} mode at 2822 Hz.

Mode #	FEA (Hz)	ESPI (Hz)
1	677	650
2	1204	847
3	1596	1530
4	1884	—
5	2162	—
6	2303	2277
7	2463	—
8	2626	2613
9	2822	—
10	2863	—
11	3039	—
12	3270	3172

Table 5.2 - Timing belt cover - natural vibration frequencies

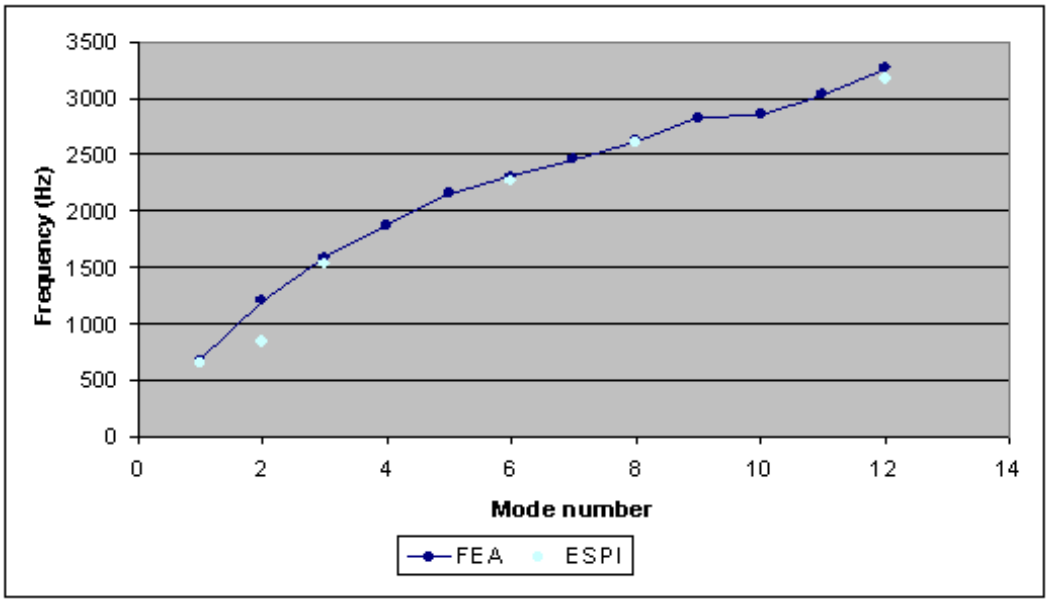

Figure 5.22 - Timing belt cover - comparison of numerical and experimental results.

5.3 Biomedical and Biomechanical

The biomedical and biomechanical areas have long been targeted by 3D imaging. The shear possibility of 3D visualization has started an entire research area in medical imaging, as it stands in direct support of numerous possibilities for new diagnostic and prophylactic techniques. From Computerized Axial Tomography (CAT) to Magnetic Resonance Imaging (MRI) to Cone Beam Computerized Tomography for planning and even real-time guidance of maxillofacial surgery, or 3D Positron Emission Tomography (PET) for differentiated tissue detection, many recent advances in 3D imaging make this one of the most exciting areas for image research.

3D surface acquisition can play a very important role in medical imaging. Image fusion is a relatively new technique for combining images from different sources, such as PET and external 3D surface, further increasing the potential of the new techniques. LOME has been involved in biomechanical applications for some years and now adds the capability of 3D imaging to the existing techniques. Research is underway to combine 3D surface acquisition with existing radiographic imaging capabilities in local medical facilities and research centres. Soft tissue finite element modelling provides the missing link for position determination of differentiated tissues in dynamical situations, where the patient has to be moved between radiographic analysis and surgical intervention, but external 3D image registration can be secured.

Volume calculation for radiation and medical dosimetry is another important application of the current techniques, which doesn't require any further developments.

Dentistry

LOME has recently started a collaboration with the Medical Dentistry School of Porto University, which may benefit from this work. So far, the 3D measurement of dental models such as the one in Fig. 5.23, has been executed in support of a population study that is set to classify dental palate measurements, such as the anteroposterior length, molar linear distance or inter-papillary distance. The measurements have been conducted on plaster models from normal subjects, but the creation of a tool to perform the measurements directly is envisaged, that will prevent going through the production of plaster models.

Body deformation

Another area of active collaboration in 3D studies lies with the swimming laboratory of the Faculty of Sports of Porto University. LOME is involved in a study of swimmers

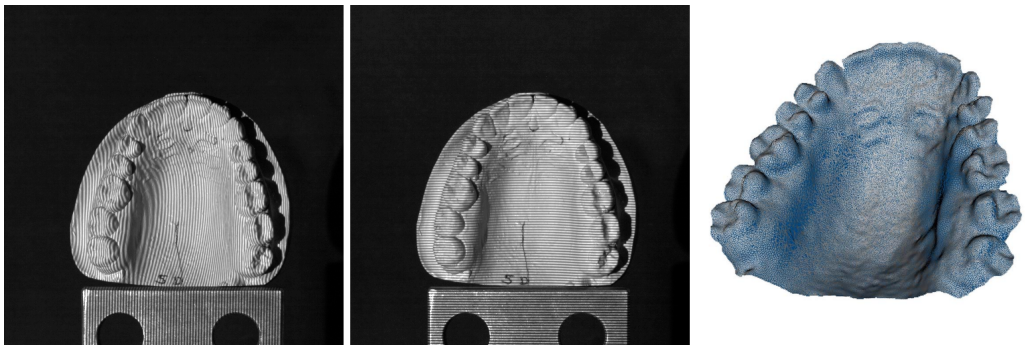

Figure 5.23 - 3D surface obtained from a dentistry plaster model - LOME.

body deformation equipped with competitive swimwear that drastically improves water sliding by holding the body in a more hydrodynamic position, while repelling water, cf. Fig. 5.24. While still in a very insipient phase, this collaboration has proven itself valuable by clearly indicating there are observable volume differences on the swimmer under different swimwear use.

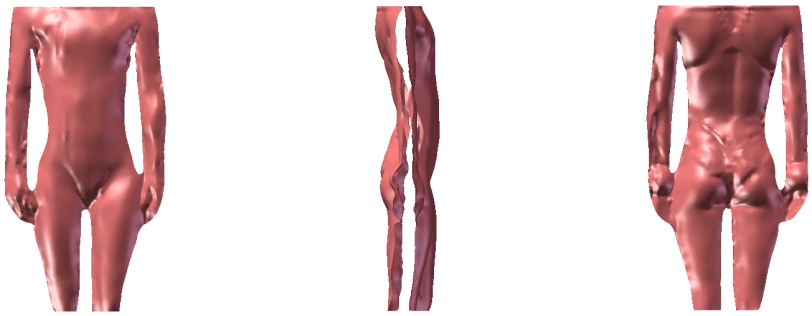

Figure 5.24 - Rendered combination of front and back views of a swimmer.

With the advent of dynamical 3D measurements with one-frame techniques, complete body volume deformation under dynamical conditions is now being targeted by this project, which will help understand, amongst other, the extent of the hydrodynamic deformation of the swimmers body. Using finite element analysis for fluid dynamics, as illustrated in Fig. 5.25, body volumes can be further characterized in numerical simulation studies to reveal whether an obtained body volume deformation is as hydrodynamic as foreseen.

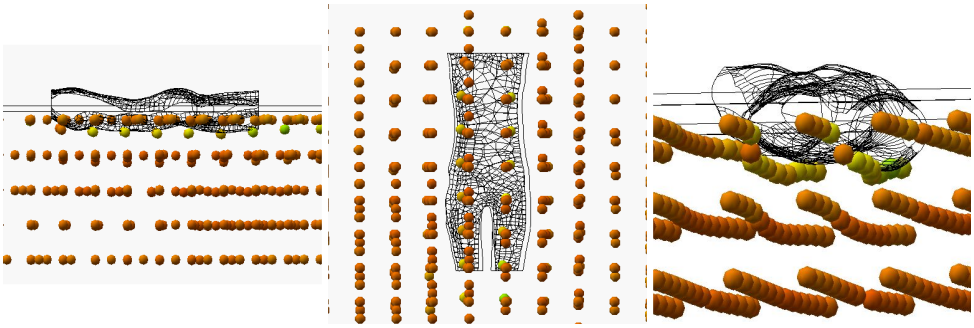

Figure 5.25 - Hydrodinamical study of water volume deformation.

5.4 Moulding and Clothing

Moulding and clothing are natural targets for 3D surface acquisition. Having completed and tested the calibration procedures, the LOME prototype was used, on occasions, for surface acquisition tasks of very different nature, each of which revealed different constraints. These were really opportunities to test the implemented procedures over and over, perfecting them or further developing accessory procedures as the need arose. The following are a few examples of the tasks accomplished to date.

Bowl mould

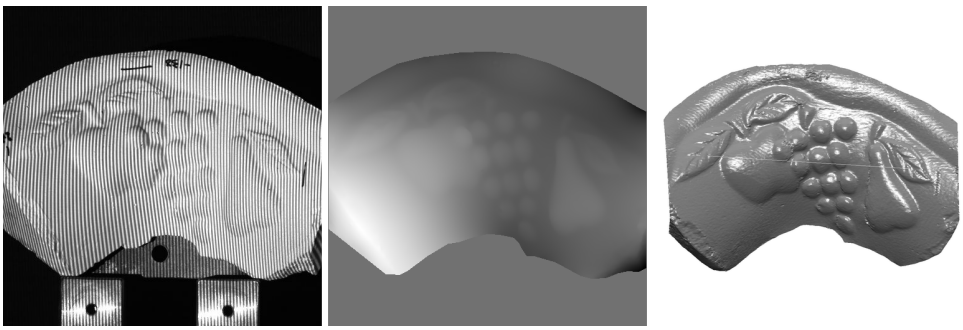

Figure 5.26 - Bowl mould positive in plaster. Original part, courtesy of Norcam.

This was a very important task, which helped optimize the calibration procedure. This part had been measured by local 3D coordinate measurement company Norcam, who graciously granted access to their coordinate data. The measurements in LOME were made with an FTP technique and compared to Norcam's. The resulting error was established at or below 1/1000 of the largest dimension, according to Norcam's data, which was taken to be exact.

Apparel manikin

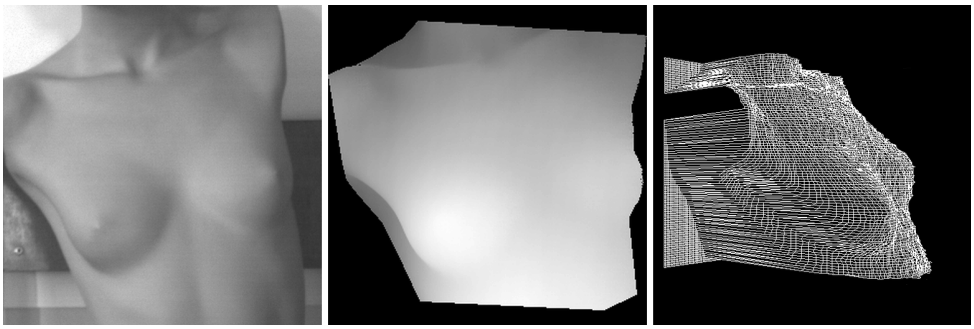

Figure 5.27 - Clothing manikin.

Apparel industry can use 3D surface imaging to target niche markets where tailored clothing is becoming mandatory. In that respect, 3D imaging could probably help revitalize a market which practically disappeared with the emergence of made-to-fit clothing. A recent public discussion on whether special swimming suits with the ability to shape the athlete's body, is influencing competition results, can be resolved resorting to these technologies. A very recent attempt at measuring one such suit revealed several difficulties related to the colour of the suits, which are usually very dark. Still, with some leakage preventing efforts, the results shown herein can well become the starting point for full field measurements in swimming. The enormous advantage of one-frame dependence, presented by either spatial carrier or Fourier methods, makes these methods particularly suited for the dynamical situations found in sports competition.

5.5 Outdoor applications

Real world applications are seldom as controlled as laboratory measurements can be. The addition of a coherent light source has further increased the potential of these methods, which now become capable of working under broad day light. Some applications can be seen in Appendix B, where the projector developed in LOME during this work has been detailed.

5.6 Dynamical object data

Both spatial carrier and Fourier transform methods can be applied to dynamical situations. This is so because these methods need a single frame, or several frames cap-

tured at one moment in time, to build a complete phase map and a 3D point cloud. One of the most successful applications of the present work, briefly mentioned in § 2.3, was the recording of 110 frames with a high speed camera at 3000 frames/s of a crashing event on a split Hopkinson bar. Post experiment processing of the fringe patterns resulted in 110 phase maps and point clouds, which registered the entire event. Three images from the 110 image sequence can be seen in Fig. 5.28. This sort of experiment demonstrates the methods used herein can be applied to most types of dynamical events such as crash tests or projectile impacts.

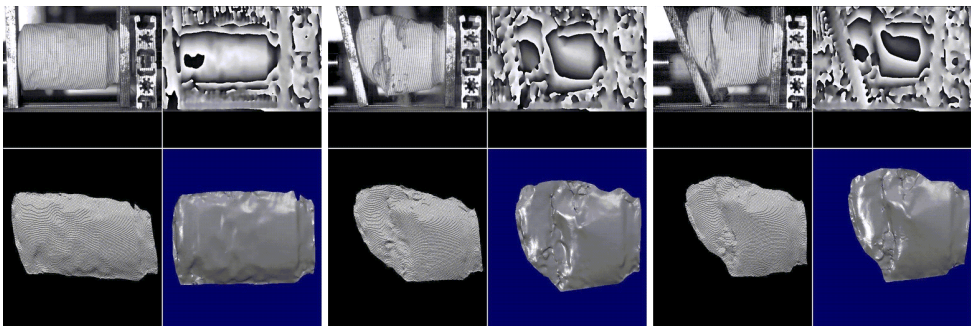

Figure 5.28 - Dynamical 3D imaging of a crash event at 3000 frames/s. High speed camera, courtesy of MRA.

This page intentionally left blank.

Chapter 6

Conclusions and suggestions for future research

This work set up to study and implement full field, structured light surface acquisition methods. Under that assumption, the initial objectives were duly fulfilled for, having studied most of the full field active image processing methodologies, implementation and testing of three of the most successful techniques then followed. Real world applications with moderate success have been conducted that indicate the usefulness of the work from several perspectives.

6.1 Versatility

One of the guidelines of the present work was to conduct it in such a way that it could culminate in a versatile 3D surface acquisition instrument. The question of whether or not it should acquire full 360° object surfaces was not posed initially, simply because development started out from a very insipient local status. In fact, save for a few inspired but very hard work and somewhat limited scope attempts to acquire 3D surfaces prior to this work, not much had been done in LOME previously. This alone required a lengthy start, in order to build the necessary software tools, before the first results ever came to light. Software and hardware options had to be made at the time which, although not entirely regretted, would probably have been taken differently today.

Be that as it may, an instrument was build that can be considered reasonably versatile from three different perspectives: speed, illumination and object size.

Speed

Three different algorithms have been successfully implemented that can deal with the binomial *speed* vs. *resolution*. TPU is a temporal phase shift based method that has the potential to ensure a height resolution better that 1/10000 of the field of view. Lateral resolution is obviously limited by the image acquisition device alone, and is therefore not an issue here. The application of TPU can unfortunately be done only on static or quasi-static situations because, like all temporal phase shift techniques, it requires capturing several frames. Another drawback of the TPU technique is the amount of noise generated by this technique, which is due to the pixel wise independency of the temporal unwrapping procedure, generating independent 3D information for every pixel.

FTP is a very promising Fourier based method, but one which still has to be perfected in order to achieve its full potential. True, it is a single-frame technique which can cope with dynamical events, but post-processing necessary to attain accurate results can be too software-intensive to consider it a real-time method. An attempt at improving the resolution of this method has been carried out herein which is described in § 3.4, but at the expense of acquiring a second frame with fringes at a right angle from the fringes on the first frame. Acquiring two images is unfortunately not an option, when dynamical events are taken upon, so the application of this technique is also limited in scope.

The third technique is a SCPS method which is also a single frame technique but prone to noise artefacts. Unless some post-processing is considered, which can be detrimental to real-time applications, the technique is also rather limited in that respect. On the other hand, even very fast phenomena, such as those dealt with at the end of Chapter 5, can be analysed at a later time, which amply justifies investing in further development of the latter two techniques.

Illumination

Most of the experiments and applications carried out during this research were performed under a lighting controlled environment in LOME with a common DLP device, which can be seen in Fig. 5.1. Given the success of the structured light field techniques, it was only natural that exterior, broad-day light applications became envisaged sooner or later. In order to accomplish that, a coherent light projector, whose wavelength is filtered in front of the CCD, was devised and built, which is thoroughly described in Appendix B. Initial testing with this projector was rather encouraging, but several mechanical problems led to a complete redesign of the entire projector, which can already be seen at the end of Appendix B.

Object size

Versatility of the profilometre, regarding object size, is utterly important in laboratory work. From auto vehicle doors or entire persons to ventricle heart valves or even smaller sized objects, a large choice of objects with differing sizes have been measured with this prototype. Accommodation to object size is provided by switching camera objectives with different magnifications and recalibrating the entire setup. Although this versatility is obtained at the expense of some calibration work, the capacity to address most object sizes amply justifies it.

6.2 Resolution

Resolution is perhaps the one characteristic most people look for in a profilometre. While not necessarily the most important characteristic, a poor resolution may certainly be detrimental to the application of the device in many instances.

The methods implemented herein, have all been scrutinized in that regard, and they are amongst the active methods with the highest potential resolutions currently available.

Resolution is to be understood as depth discernment, and is usually presented as a fraction of the largest dimension on the acquisition volume. It should be made clear that the choice of the method has an impact on resolution, simply because the method itself can pose restrictions in resolution. The Fourier Transform methods, for instance, show limitations which depend on the available bandwidth as well as on the carrier frequency (Asundi, 2000). Typical resolutions for the methods currently addressed by LOME's prototype seem to be between 1/2000 and 1/20000 of the field of view, depending on the chosen method.

Resolution was not ascertained in the present work, because attaining a particular resolution simply wasn't amongst the work objectives, but the tests carried out on numerous occasions with different object sizes and different lenses all seem to confirm the prototype resolution is, or can be made, near the limiting resolutions indicated above.

6.3 Future directions

Recent trends and materials

Current environmental concerns regarding the consumption of energetic resources, stress the necessity of optimizing transport vehicles, by reducing structure weight and increasing engine efficiency, which, in turn, enable larger transport capacity and

Figure 6.1 - The A380 continuous geometry variation wing. The wing tip detail on the right shows a blended winglet.

range without an equivalent increase in fuel consumption. In aeronautics, new materials and aerodynamic solutions, such as winglet structures or otherwise optimized wing geometries to support reduction of engine pylons, add to the flight efficiency and lower the take-off wakeup vortex, allowing reduced separation between aeroplanes. New traffic control methodologies heavily supported by better information systems, enable the increase of passenger flows and drive the overall efficacy of civil aerial transportation.

Modern aeroplane projects impose severe geometrical restrictions on the aerodynamic surfaces, to reduce air drag and turbulence. A number of complex geometry aerodynamic appendices have been introduced in recent years to increase air flow, due only to new engineering resources, which enabled reduced horizontal aeroplane separation and a further increase in flight frequency. New techniques that seek to lower vertical flight separation and the optimization of traffic management in aerial corridors, such as the Single European Sky ATM Research programme (SESAR), receive a special attention from both flight authorities and private investment groups, and will condition the general approach to flight management in the future.

The search for higher resistance and lower weight structures, led industry into research on new composite materials. Recent projects for both military and civilian applications, such as the RAFALE, the Eurofighter or the emblematic A380 and the 787 Dreamliner aeroplanes, make an extensive use of composite materials in both aerodynamic and structural elements. The A380, for instance, features a 25% weight in composite materials. Fibre carbon and fibre quartz reinforced composites are extensively used in wing structures, fuselage sections, tail surfaces and exterior doors.

Fibreglass/aluminium and even some special composites such as GLAss-REinforced fibre metal laminate (GLARE), have been developed for this aeroplane. It was also the first time the central wing box was totally developed in composite materials. The 80m span wings, have a continuous profile variation to increase aerodynamic efficiency, as can be seen in Fig. 6.1.

LOME has long been involved in both mechanical project and structural testing for the aeronautics and the automotive industries, participating in European projects and national R&D initiatives, and maintaining research activities in Non Destructive Testing (NDT) and project support methodologies. Shape characterization plays an important role, as part of an integrated set of methodologies that cover the mechanical project in its entirety.

Three-dimensional surface acquisition is currently being used in two different ways: in finite-element based numerical simulations for characterizing part behaviour in face of both static and dynamical solicitations, and thus ascertain both response and structural integrity; and shape modification, in view of either structure or response optimization, or simply due to aesthetic requirements. Once the point cloud is acquired, filtered, reduced and, eventually, decimated, a triangle mesh can be extracted and used in numerical simulations. The response to external solicitations, such as heat or vibration, can thereafter be simulated with different software applications in support of decisions regarding the part structure or shape. Once the surface has been closed into a solid object, shape modifications can also be easily obtained with dedicated CAD applications.

On the other hand, LOME developed, over the years, an expertise in holographic interferometry techniques (Monteiro et al., 2001; Santos, 2008; Santos et al., 2004; Vaz, 1995; Vaz et al., 1996), gathering a set of tools for NDT which can detect both structural deformations and superficial damages or defects with sub-micrometre resolution (Lopes, 2008). Shape acquisition now bridges this capacity with the mechanical project and the numerical simulation, enabling cross-checking of the obtained testing data with the numerical simulations performed on the acquired 3D shapes, which can thus be validated.

In order to extend this coverage between simulation and testing, there is further work yet to be done in two different directions: *3D image registration and fusion*; and further developments towards an *integrated set of tools for image sensing*.

Surface registration and fusion

A logical and necessary evolution of the current work, vital for all applications that require acquisition of the full object three-dimensional shape into a closed surface, and

most often into a solid henceforth, is 3D image registration and fusion for surfaces which have been captured either with two cameras, a typical Stereo Vision problem, or with two different positions of the same camera, a task known as Structure from Motion.

Apart from being a very powerful tool for 3D shape acquisition in short-range photogrammetry, surface fusion into closed surfaces will enable the downstream profusion of experimental mechanics methodologies that depend on shape, such as structural studies, vibration response or even surface drag characterization with finite element modelling.

Image registration has been the subject of thousands of works in recent years, due to its importance, namely in the medical field. Apparently there are several different strategies to address this problem, none of which totally satisfactory in all situations (Zitová and Flusser, 2003). Most of the methodologies employ either intensity based or feature based approaches to determining best matches between range data. The problem with both approaches, to the extent that both choices depend on rendered surfaces, seems to lie on the fact that most of the times a simple geometric transformation consisting of translations and rotations isn't sufficient to accomplish registration. Distortion may have to be considered, and in this case the use of area-based methods seems to be inappropriate.

When considering just geometric transformations, and allowing a certain amount of overlap between point clouds, a simple approach, being used by most commercial solutions, is to place markers on the complete surface and use a photogrammetric technique to produce a course approximation to the 3D surface, as seen in Figs. 6.2 and 6.3. The range data sets, acquired afterwards, are then brought in to fill the 3D space between the markers.

Recent point based tactics, employing feature recognition nonetheless, seems to faster and more effective than the remaining methodologies (Zitová and Flusser, 2003). Being point based, these techniques use smaller data sets to recognize and match surface features, and pose a smaller computational burden to the involved calculations.

A different feature based approach could be put forward by establishing the three-dimensional homographies between physical points in different surfaces. To establish these homographies, a correct description of the relevant projective geometry must be previously established, and this has to be supported by automatic detection of 3D features in both images. LOME is currently taking the first steps in this area and a PhD program is currently being developed to address this issue.

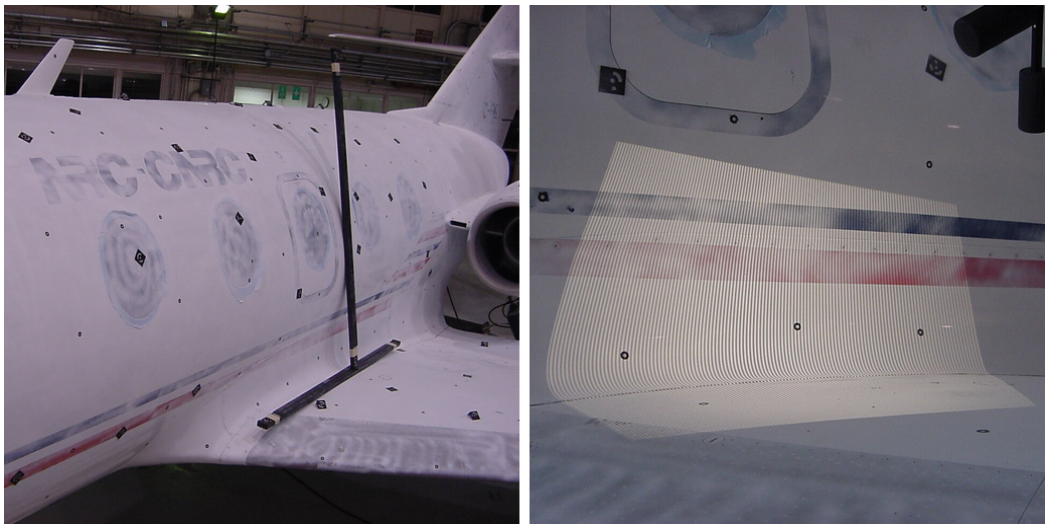

Figure 6.2 - Surface profiling of a Falcon jet. Photogrammetric markers and fringe projection. Courtesy, GOM, mbH.

Towards an image sensing discipline

Having closed the mechanical project cycle, from testing with interferometric techniques to numerical simulation based on the acquired 3D shapes, looking ahead means developing further tools for testing different material and structural characteristics, such as thermal response or large area deformations in all types of surfaces, under all conditions of field lighting. Portability is one of the issues to be addressed first. LOME has been actively involved in the design of new shearography systems but lighting still has to be coherent, which adds to the size of a final equipment. Digital Image Correlation, already focused in § 2.4, seems to be an interesting option to this end. With the ability to perform both in-plane and out-of-the-plane deformation measurements with one camera and one projector alone (Sutton et al., 2001), the technique, which had already been used in surface profiling (McNeill et al., 1997), became a powerful alternative to other interferometric methods. There is still some room for improvement on both the differentiation and the correlation algorithms themselves, in order to fully exploit the method's potential. Combined with LOME's coherent projection system, DIC can be applied under all sorts of lighting conditions, independent of the fact the surface texture is actually adequate or not and without having to modify superficial characteristics. Another area for improvement seems to be the camera model adopted by Sutton et al, which was simply a pinhole model. In case a more complex model is used, a further degree of data accuracy and reliability can be expected. In this case, correcting for the optics distortions becomes possible, even

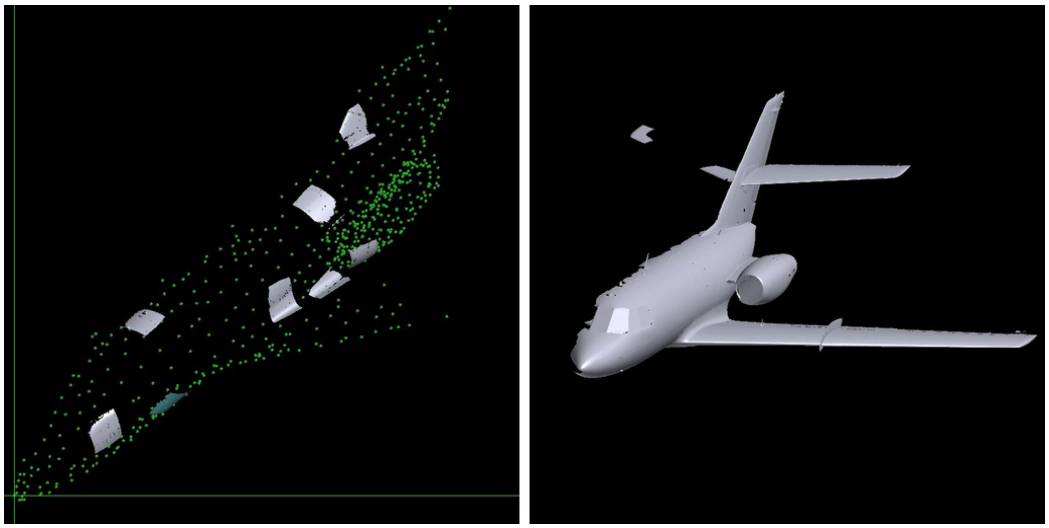

Figure 6.3 - Surface profiling of a Falcon jet. Photogrammetric mesh with attached scans. Courtesy, GOM, mbH.

with low cost optics such as can be found on webcams, paving the way to a breadth of applications that require telemetry and enabling the leap from measurement alone to remote measurement and control. LOME is also preparing a PhD program along these lines.

Bibliography

Y. I. Abdel-Aziz and H. M. Karara. Direct linear transformation into object space coordinates in close-range photogrammetry. In *Symposium on Close-Range Photogrammetry*, Proc. ASP, pages 1–18, 1971.

N. Abramson. The Holo-Diagram. V: a device for practical interpreting of hologram interference fringes. *Applied Optics*, 11(5):1143–1147, 1972.

Y. Androussi, T. Benabbas, and A. Lefebvre. Moiré-like fringes in transmission electron microscopy images of coherently strained semiconductor islands. *Ultramicroscopy*, 93(2):161–167, 2002.

E. Archbold and A. E. Ennos. Displacement measurement from double-exposure laser photographs. *Optica Acta*, 19(4):253–271, 1972.

E. Archbold, J. M. Burch, and A. E. Ennos. Recording of in-plane surface displacement by double-exposure speckle photography. *Optica Acta*, 17(12):883–898, 1970.

H. Asada and M. Brady. The curvature primal sketch. *IEEE Trans. Pattern Anal. Mach. Intell.*, 8(1):2–14, 1986.

A. Asundi. Discussion on spatial resolution and sensitivity of Fourier transform fringe detection. *Optics and Lasers in Engineering*, 39(10):2715–2719, 2000.

A. Asundi. Computer-aided Moiré methods. *Optics and Lasers in Engineering*, 18(3): 213–238, 1993.

A. Asundi and C. S. Chan. Phase-shifted projection grid - effect of pitch and profile. *Optics and Lasers in Engihneering*, 21(1-2):31–47, 1994.

N. Bareket. 3-channel phase-detector for pulsed wave-front sensing. *Proceedings of the Society of Photo-Optical Instrumentation Engineers*, 551:12–16, 1985.

F. Blais. Review of 20 years of range sensor development. *Journal of Electronic Imaging*, 13(1):231–243, 2004.

D. J. Bone, H. A. Bachor, and R. J. Sandeman. Fringe-pattern analysis using a 2D Fourier transform. *Applied Optics*, 25(10):1653–1660, 1986.

T. Bothe, W. Osten, A. Gesierich, and W. P. Jueptner. Compact 3D camera. In W. Osten, editor, *Interferometry XI: applications*, volume 4778 of *Proc. SPIE*, pages 48–59, jun 2002.

G. Bouwhuis and S. Wittekoek. Automatic alignment system for optical projection printing. *IEEE Transactions on Electron Devices*, 26(4):723–728, 1979.

R. E. Brooks and L. O. Heflinger. Moiré gauging using optical interference patterns. *Applied Optics*, 8(5):935–939, 1969.

R. E. Brooks, L. O. Heflinger, and R. F. Wuerker. Interferometry with a holographically reconstructed comparison beam. *Applied Physics Letters*, 7(9):248–249, 1965.

J. H. Bruning, D. R. Herriott, J. E. Gallagher, D. P. Rosenfeld, A. D. White, and D. J. Brangaccio. Digital wavefront measuring interferometer for testing optical surfaces and lenses. *Applied Optics*, 13(11):2693–2703, 1974.

J. M. Burch. Outlines of optical metrology. In E. R. Robertson, editor, *The engineering uses of coherent optics*, Proceedings of the Conference, University of Strathclyde, Glasgow, Scotland, pages 1–22. Cambridge University Press, 1975.

J. M. Burch and J. M. Tokarski. Production of multiple beam fringes from photographic scatterers. *Optica Acta*, 15(2):101–111, 1968.

P. Carré. Installation et utilisation du comparateur photoélectrique et interférentiel du Bureau international des Poids et Mesures. *Metrologia*, 2(1):13–23, 1966.

F. Chen, G. M. Brown, and M. M. Song. Overview of three-dimensional shape measurement using optical methods. *Optical Engineering*, 39(1):10–22, 2000.

T. A. Clarke and M. R. Williams. Buyers guide to six non-contact distance measuring techniques. *Quality Today*, pages 145–149, 1999.

C. R. Coggrave and J. M. Huntley. High-speed surface profilometer based on a spatial light modulator and pipeline image processor. *Optical Engineering*, 38(9):1573–1581, 1999.

K. Creath. Phase-shifting speckle interferometry. *Applied Optics*, 24(18):3053–3058, 1985.

K. Creath. Phase-measurement interferometry techniques. In E. Wolf, editor, *Progress in Optics*, volume XXVI, chapter 5. Elsevier Science Publishers, Amsterdam, 1988.

K. Creath. Temporal phase measurement methods. In D. W. Robinson and G. T. Reid, editors, *Interferogram Analysis: Digital Fringe Pattern Measurement Techniques*, chapter 4. Institute of Physics, Bristol, 1993.

K. Creath and J. Schmit. N-point spatial phase-measurement techniques for non-destructive testing. *Optics and Lasers in Engineering*, 24(5-6):365–379, 1996.

K. Creath and J. C. Wyant. Moiré and fringe projection techniques. In D. Malacara, editor, *Optical shop testing, 2nd ed.*, chapter 16. Wiley, New York, 1992.

E. Dalhoff, E. Fischer, S. Heim, and H. J. Tiziani. Double heterodyne interferometry for high-precision distance measurements. In A. Gruen and H. Kahmen, editors, *Optical 3D Measurement Techniques II: Applications in Inspection, Quality Control, and Robotics*, volume 2252 of *Proc. SPIE*, pages 379–385, 1994.

M. Davidson, K. Kaufman, and I. Mazor. The coherence probe microscope. *Solid State Technology*, 30(9):57–59, 1987.

B. V. Dorrío and J. L. Fernández. Phase-evaluation methods in whole-field optical measurement techniques. *Measurement Science and Technology*, 10(3):33–55, 1999.

D. E. Dudgeon and R. M. Mersereau. *Multidimensional digital signal processing*. Prentice-Hall signal processing series. Prentice-Hall, Englewood Cliffs, N.J., 1st edition, 1984.

S. M. Dunn, R. L. Keizer, and J. Yu. Measuring the area and volume of the human body with structured light. *IEEE Transactions on Systems, Man and Cybernetics*, 19 (6):1350–1364, 1989.

O. Faugeras and G. Toscani. Camera calibration for 3D computer vision. In *Int. Workshop on Industrial Applications of Machine Vision and Machine Intelligence*, Proc., pages 240–247, 1987.

R. Fontana, M. Greco, M. Materazzi, E. Pampaloni, L. Pezzati, C. Rocchini, and R. Scopigno. Three-dimensional modelling of statues: the Minerva of Arezzo. *Journal of Cultural Heritage*, 3(4):325–331, 2002.

G. Frankowski and M. Stenzel. DLP based fringe projection as an optical 3D inline measuring method for inspection in manufacturing. In W. Osten, editor, *Optical Measurement Systems for Industrial Inspection V*, volume 6616 of *Proc. SPIE*, pages 1–12, 2007.

C. S. Fraser. Photogrammetric measurement to one part in a million. *Photogrammetric Engineering and Remote Sensing*, 58(3):305–310, 1992.

D. Gabor. A new microscopic principle. *Nature*, 161(4098):777–778, 1948.

K. J. Gasvik. *Optical metrology*. John Wiley and Sons, Inc., New York, 3rd edition, 2000.

R. W. Gerchberg. Super-resolution through error energy reduction. *Optica Acta*, 21(9): 709–720, 1974.

D. C. Ghiglia and M. D. Pritt. *Two-dimensional phase unwrapping: theory, algorithms, and software*. Wiley, New York, 1998.

D. C. Ghiglia, G. A. Mastin, and L. A. Romero. Cellular-automata method for phase unwrapping. *Journal of the Optical Society of America A: Optics, Image Science and Vision*, 4(1):267–280, 1987.

R. M. Goldstein, H. A. Zebker, and C. L. Werner. Satellite radar interferometry - two-dimensional phase unwrapping. *Radio Science*, 23(4):713–720, 1988.

J. N. Gordon and G. B. Dukes. A two-hundred-foot yardstick with graduations every microinch. *Hewlett-Packard Journal*, 21(12):2–9, 1970.

J. E. Greivenkamp and J. H. Bruning. Phase shifting interferometry. In D. Malacara, editor, *Optical shop testing, 2nd ed.*, chapter 14. Wiley, New York, 1992.

A. Gruen, F. Remondino, and L. Zhang. 3D modeling and visualization of large cultural heritage sites at very high resolution: the Bamiyan valley and its standing Buddhas. In O. Altan, editor, *Geo-Imagery Bridging Continents - the XXth ISPRS Congress*, volume XXXV-B5 of *Proc. ISPRS*, pages 603–608, 2004.

J. Guild. *The interference systems of crossed diffraction gratings; theory of Moiré fringes*. Clarendon Press, Oxford, 1st edition, 1956.

H. W. Guo, H. T. He, Y. J. Yu, and M. Y. Chen. Least-squares calibration method for fringe projection profilometry. *Optical Engineering*, 44(3):6031–6039, 2005.

K. Haines and B. P. Hildebrand. Contour generation by wavefront reconstruction. *Physics Letters*, 19(1):10–11, 1965.

P. Hariharan, B. F. Oreb, and T. Eiju. Digital phase-shifting interferometry - a simple error-compensating phase calculation algorithm. *Applied Optics*, 26(13):2504–2506, 1987.

C. Harris and M. Stephens. A combined corner and edge detection. In *Proceedings of The Fourth Alvey Vision Conference*, Proc. British Machine Vision Association, pages 147–151, 1988.

F. J. Harris. Use of windows for harmonic analysis with discrete Fourier-transform. *Proceedings of the IEEE*, 66(1):51–83, 1978.

J. L. Harris. Diffraction and resolving power. *Journal of the Optical Society of America*, 54(7):931–936, 1964.

M. Hart, D. G. Vass, and M. L. Begbie. Fast surface profiling by spectral analysis of white-light interferograms with Fourier transform spectroscopy. *Applied Optics*, 37 (10):1764–1769, 1998.

B. P. Hildebrand and K. A. Haines. Multiple-wavelength and multiple-source holography applied to contour generation. *Journal of the Optical Society of America*, 57(2): 155–162, 1967.

K. Høgmoen and O. J. Løkberg. Detection and measurement of small vibrations using electronic speckle pattern interferometry. *Applied Optics*, 16(7):1869–1875, 1977.

B. Horn. *Shape from shading: a method for obtaining the shape of a smooth opaque object from one view*. PhD thesis, Massachusetts Institute of Technology, Cambridge, MA, 1970.

E. Horn and N. Kiryati. Toward optimal structured light patterns. *Image and Vision Computing*, 17(2):87–97, 1999.

Y. Y. Hung. Speckle-shearing interferometer - a tool for measuring derivatives of surface displacements. *Optics Communications*, 11(2):132–135, 1974.

J. M. Huntley and H. O. Saldner. Error-reduction methods for shape measurement by temporal phase unwrapping. *Journal of the Optical Society of America A: Optics, Image Science and Vision*, 14(12):3188–3196, 1997.

K. Itoh. Analysis of the phase unwrapping algorithm. *Applied Optics*, 21(14):2470–2470, 1982.

S. F. Jacobs and D. Shough. Thermal-expansion uniformity of Heraeus-Amersil TO8E fused silica. *Applied Optics*, 20(20):3461–3463, 1981.

C. Joenathan. Speckle photography, shearography, and espi. In P. K. Rastogi, editor, *Optical Measurement Techniques and Applications*, chapter 6. Artech-House, Norwood, MA, 1997.

C. Joenathan, B. Pfister, and H. J. Tiziani. Contouring by electronic speckle pattern interferometry employing dual beam illumination. *Applied Optics*, 29(13):1905–1911, 1990.

T. R. Judge and P. J. Bryanston-Cross. A review of phase unwrapping techniques in fringe analysis. *Optics and Lasers in Engineering*, 21(4):199–239, 1994.

L. M. Kani and J. C. Dainty. Super-resolution using the Gerchberg algorithm. *Optics Communications*, 68(1):11–17, 1988.

Q. Kemao. Two-dimensional windowed Fourier transform for fringe pattern analysis: principles, applications and implementation. *Optics and Lasers in Engineering*, 45(2): 304–317, 2007.

Q. Kemao, S. H. Soon, and A. Asundi. Noise suppression in Spatial Carrier Phase Shifting method. *Optical Engineering*, 42(9):2642–2645, 2003.

K. Kohlmann. Corner detection in natural images based on the 2D Hilbert transform. *Signal Process.*, 48(3):225–234, 1996.

L. Kovacs, M. Eder, R. Hollweck, A. Zimmermann, M. Settles, A. Schneider, M. Endlich, A. Mueller, K. Schwenzer-Zimmerer, N. A. Papadopulos, and E. Biemer. Comparison between breast volume measurement using 3D surface imaging and classical techniques. *Breast*, 16(2):137–145, 2007.

T. Kreis. *Handbook of holographic interferometry: optical and digital methods*. Wiley-VCH, Weinheim, 2005.

T. Kreis. Digital holographic interference-phase measurement using the Fourier transform method. *Journal of the Optical Society of America A: Optics, Image Science and Vision*, 3(6):847–855, 1986.

M. Kujawinska. Use of phase-stepping automatic fringe analysis in Moiré interferometry. *Applied Optics*, 26(22):4712–4714, 1987.

M. Kujawinska. Spatial phase measurement methods. In D. W. Robinson and G. T. Reid, editors, *Interferogram Analysis: Digital Fringe Pattern Measurement Techniques*, chapter 5. Institute of Physics, Bristol, 1993.

M. Kujawinska and D. W. Robinson. Multichannel phase-stepped holographic interferometry. *Applied Optics*, 27(2):312–320, 1988.

M. Kujawinska and J. Wojciak. High-accuracy Fourier transform fringe pattern analysis. *Optics and Lasers in Engineering*, 14(4-5):325–339, 1991.

O. Y. Kwon. Multichannel phase-shifted interferometer. *Optics Letters*, 9(2):59–61, 1984.

O. Y. Kwon, D. M. Shough, and R. A. Williams. Stroboscopic phase-shifting interferometry. *Optics Letters*, 12(11):855–857, 1987.

B. S. Lee and T. C. Strand. Profilometry with a coherence scanning microscope. *Applied Optics*, 29(26):3784–3788, 1990.

J. A. Leendertz. Interferometric displacement measurement on scattering surfaces utilizing speckle effect. *Journal of Physics E - Scientific Instruments*, 3(3):214–218, 1970.

J. A. Leendertz and J. N. Butters. Image-shearing speckle-pattern interferometer for measuring bending moments. *Journal of Physics E - Scientific Instruments*, 6(11): 1107–1110, 1973.

R. Legarda-Saenz, T. Bothe, and W. P. Juptner. Accurate procedure for the calibration of a structured light system. *Optical Engineering*, 43(2):464–471, 2004.

E. N. Leith and J. Upatniek. Reconstructed wavefronts and communication theory. *Journal of the Optical Society of America*, 52(10):1123–1130, 1962.

R. K. Lenz and R. Y. Tsai. Techniques for calibration of the scale factor and image center for high accuracy 3D machine vision metrology. *IEEE Trans. Pattern Anal. Mach. Intell.*, 10(5):713–720, 1988.

F. K. Ligtenberg. The Moiré method: a new experimental method for the determination of moments in small slab models. In *Proceedings of the Society for Experimental Stress Analysis*, volume 12, pages 83–98, 1954.

J. Liu, H. Furuhashi, A. Torii, N. Hayashi, J. Yamada, Y. Uchida, R. Sharma, A. K. Kanjilal, and V. T. Chitnis. Precision position control systems using Moiré signals. In *IECON Proceedings*, volume 2, pages 968–972, 1995.

H. Lopes. *Desenvolvimento de técnicas interferométricas, contínuas e pulsadas, aplicadas à análise do dano em estruturas compósitas*. PhD thesis, Faculty of Engineering, University of Porto, Porto, Portugal, 2008.

B. D. Lucas and T. Kanade. An iterative image registration technique with an application to stereo vision. In *7th International Joint Conference on Artificial Intelligence*, Proc. IJCAI, pages 674–679, Vancouver, BC, 1981.

A. Macovski, S. D. Ramsey, and L. F. Schaefer. Time-lapse interferometry and contouring using television systems. *Applied Optics*, 10(12):2722–2727, 1971.

W. W. Macy. Two-dimensional fringe-pattern analysis. *Applied Optics*, 22(23):3898–3901, 1983.

S. G. Mallat. *A wavelet tour of signal processing*. Academic Press, San Diego, 2nd edition, 1999.

J. S. Massa, G. S. Buller, A. C. Walker, S. Cova, M. Umasuthan, and A. M. Wallace. Time-of-flight optical ranging system based on time-correlated single-photon counting. *Applied Optics*, 37(31):7298–7304, 1998.

N. A. Massie, R. D. Nelson, and S. Holly. High-performance real-time heterodyne interferometry. *Applied Optics*, 18(11):1797–1803, 1979.

S. R. McNeill, M. A. Sutton, Z. Miao, and J. Ma. Measurement of surface profile using digital image correlation. *Experimental Mechanics*, 371(1):13–20, 1997.

D. M. Meadows, W. O. Johnson, and J. B. Allen. Generation of surface contours by Moiré patterns. *Applied Optics*, 9(4):942–947, 1970.

T. Melen. *Geometrical modelling and calibration of video cameras for underwater navigation*. PhD thesis, Norges Tekniske Hugskole, Trodheim, Norway, 1994.

L. Mertz. Real-time fringe-pattern analysis. *Applied Optics*, 22(10):1535–1539, 1983.

J. Millerd, N. Brock, J. Hayes, B. Kimbrough, M. Novak, M. North-Morris, and J. C. Wyant. Modern approaches in phase measuring metrology (invited paper). In *Optical Measurement Systems for Industrial Inspection IV*, Proc. SPIE, pages 14–22, 2005.

R. D. Mohr and P. Brand. Accuracy in image measure. In *Videometrics III*, Proc. SPIE, pages 218–228, Boston, MA, 1994.

F. Mokhtarian and A. Mackworth. Scale-based description and recognition of planar curves and two-dimensional objects. *IEEE Trans. Pattern Anal. Mach. Intell.*, 8(1): 34–43, 1986.

J. Monteiro, M. Vaz, F. Q. Melo, and J. F. S. Gomes. Use of interferometric techniques for measuring the displacement field in the plane of a part-through crack existing in a plate. *Journal of Pressure Vessels and Piping*, (78):253–259, 2001.

A. J. Moore and F. Mendoza-Santoyo. Phase demodulation in the space domain without a fringe carrier. *Optics and Lasers in Engineering*, 23(5):319–330, 1995.

H. Moravec. *Obstacle avoidance and navigation in the real world by a seeing robot rover*. PhD thesis, Computer Science Department, Stanford University, Stanford, CA, 1980.

C. J. Morgan. Least-squares estimation in phase-measurement interferometry. *Optics Letters*, 7(8):368–370, 1982.

W. Nadeborn, P. Andra, and W. Osten. A robust procedure for absolute phase measurement. *Optics and Lasers in Engineering*, 24(2-3):245–260, 1996.

Y. Nishijima and G. Oster. Moiré patterns: their application to refractive index and refractive index gradient measurements. *Journal of the Optical Society of America*, 54 (1):1–5, 1964.

M. B. North-Morris, J. VanDelden, and J. C. Wyant. Phase-shifting birefringent scatterplate interferometer. *Applied Optics*, 41(4):668–677, 2002.

A. V. Oppenheim and J. S. Lim. The importance of phase in signals. *Proceedings of the IEEE*, 69(5):529–541, 1981.

W. Osten and W. Jüptner. Digital processing of fringe patterns in optical metrology. In P. K. Rastogi, editor, *Optical Measurement Techniques and Applications*, chapter 3. Artech-House, Norwood, MA, 1997.

J. Pagès, J. Salvi, R. García, and C. Matabosch. Overview of coded light projection techniques for automatic 3D profiling. In *IEEE International Conference on Robotics and Automation*, pages 133–138, 2003.

A. Papoulis. New algorithm in spectral analysis and band-limited extrapolation. *IEEE Transactions on Circuits and Systems*, 22(9):735–742, 1975.

H. M. Pedersen, O. J. Løkberg, and B. M. Forre. Holographic vibration measurement using a TV speckle interferometer with silicon target vidicon. *Optics Communications*, 12(2):421–426, 1974.

G. Pedrini, B. Pfister, and H. Tiziani. Double-pulse electronic speckle interferometry. *Journal of Modern Optics*, 40(1):89–96, 1993.

W. H. Peters and W. S. Ranson. Digital image techniques in experimental stress analysis. *Optical Engineering*, 21(3):427–431, 1982.

M. Pieraccini, G. Guidi, and C. Atzeni. 3D digitizing of cultural heritage. *Journal of Cultural Heritage*, 2:63–70, 2001.

M. Pirga and M. Kujawinska. Two directional spatial-carrier phase-shifting method for analysis of crossed and closed fringe patterns. *Optical Engineering*, 34(8):2459–2466, 1995.

C. Y. Poon, M. Kujawinska, and C. Ruiz. Spatial-carrier phase-shifting method of fringe analysis for Moiré interferometry. *Journal of Strain Analysis for Engineering Design*, 28(2):79–88, 1993.

J. L. Posdamer and M. D. Altschuler. Surface measurement by space-encoded projected beam systems. *Computer Graphics and Image Processing*, 18(1):1–17, 1982.

D. Post. Moiré interferometry. In A. Kobayashi, editor, *Handbook on Experimental Mechanics*, chapter 7. Prentice-Hall, Englewood Cliffs, NJ, 1987.

K. M. Qian, S. H. Soon, and A. Asundi. A simple phase unwrapping approach based on filtering by windowed Fourier transform. *Optics and Laser Technology*, 37(6): 458–462, 2005.

B. A. Rajoub, D. R. Burton, and M. J. Lalor. A new phase-to-height model for measuring object shape using collimated projections of structured light. *Journal of Optics A - Pure and Applied Optics*, 7(6):S368–S375, 2005.

P. K. Rastogi. Principles of holographic interferometry and speckle metrology. In P. K. Rastogi, editor, *Photomechanics*, volume 77 of *Topics in Applied Physics*, chapter 4. Springer, Berlin, 2000.

P. K. Rastogi. Displacement and deformation measurements. In R. S. Sirohi, editor, *Speckle Metrology*, chapter 2. Marcel Dekker, New York, NY, 1993.

P. K. Rastogi. Techniques to measure displacements, derivatives and surface shapes. extension to comparative holography. In P. K. Rastogi, editor, *Holographic interferometry*, volume 68 of *Springer series in optical sciences*, chapter 7. Springer, Berlin, 1994.

P. K. Rastogi. Holographic interferometry. In P. K. Rastogi, editor, *Optical Measurement Techniques and applications*, chapter 5. Artech-House, Norwood, MA, 1997.

C. Rigotti, N. A. Borghese, S. Ferrari, G. Baroni, and G. Ferrigno. Portable and accurate 3D scanner for breast implant design and reconstructive plastic surgery. In K. M. Hanson, editor, *Medical Imaging 1998: Image Processing*, volume 3338 of *Proc. SPIE*, pages 1558–1567, 1998.

D. Ritter, J. Orman, C. Schmidgunst, and R. Graumann. 3D soft tissue imaging with a mobile C-arm. *Computerized Medical Imaging and Graphics*, 31(2):91–102, 2007.

D. W. Robinson. Phase unwrapping methods. In D. W. Robinson and G. T. Reid, editors, *Interferogram Analysis: Digital Fringe Pattern Measurement Techniques*, chapter 6. Institute of Physics, Bristol, 1993.

D. W. Robinson and D. C. Williams. Digital phase stepping speckle interferometry. *Optics Communications*, 57(1):26–30, 1986.

C. Roddier and F. Roddier. Interferogram analysis using Fourier-transform techniques. *Applied Optics*, 26(9):1668–1673, 1987.

R. Rodriguez-Vera, D. Kerr, and F. Mendoza-Santoyo. Electronic speckle contouring. *Journal of the Optical Society of America A - Optics: Image Science and Vision*, 9(11): 2000–2008, 1992.

S. H. Rowe and W. T. Welford. Surface topography of non-optical surfaces by projected interference fringes. *Nature*, 216(5117):786–787, 1967.

H. O. Saldner and J. M. Huntley. Profilometry using temporal phase unwrapping and a spatial light modulator-based fringe projector. *Optical Engineering*, 36(2):610–615, 1997.

P. Sandoz, G. Tribillon, and H. Perrin. High-resolution profilometry by using phase calculation algorithms for spectroscopic analysis of white-light interferograms. *Journal of Modern Optics*, 43(4):701–708, 1996.

G. Sansoni, M. Carocci, S. Lazzari, and R. Rodella. A three-dimensional imaging system for industrial applications with improved flexibility and robustness. *Journal of Optics A - Pure and Applied Optics*, 1(1):83–93, 1999.

F. Santos. *Novos métodos de interferometria de speckle com lasers de impulso*. PhD thesis, Faculty of Engineering, University of Porto, Porto, Portugal, 2008.

F. Santos, M. Vaz, and J. Monteiro. A new set-up for pulsed digital shearography applied to defect detection in composite structures. *Optics and Lasers in Engineering*, 42(2):131–140, 2004.

C. Schmid, R. Mohr, and C. Bauckhage. Evaluation of interest point detectors. *International Journal of Computer Vision*, 37(2):151–172, 2000.

J. Schmit and K. Creath. Extended averaging technique for derivation of error-compensating algorithms in phase-shifting interferometry. *Applied Optics*, 34(19): 3610–3619, 1995.

M. A. Schofield and Y. M. Zhu. Fast phase unwrapping algorithm for interferometric applications. *Optics Letters*, 28(14):1194–1196, 2003.

W. Schreiber and G. Notni. Theory and arrangements of self-calibrating whole-body three-dimensional measurement systems using fringe projection technique. *Optical Engineering*, 39(1):159–169, 2000.

J. Schwider, R. Burow, K. E. Elssner, J. Grzanna, R. Spolaczyk, and K. Merkel. Digital wave-front measuring interferometry - some systematic error sources. *Applied Optics*, 22(21):3421–3432, 1983.

O. Schwomma. Österreichisches patentamt, atentschrift nr. 298830. in German, 1972.

M. Servin and R. Rodriguez-Vera. 2-Dimensional phase-locked loop demodulation of interferograms. *Journal of Modern Optics*, 40(11):2087–2094, 1993.

J. Shi and C. Tomasi. Good features to track. In *IEEE Conference on Computer Vision and Pattern Recognition - CVPR94*, pages 593–600, 1994.

G. Sirat and D. Psaltis. Conoscopic holography. *Optics Letters*, 10(1):4–6, 1985.

R. S. Sirohi. Speckle methods in experimental mechanics. In R. S. Sirohi, editor, *Speckle Metrology*, chapter 3. Marcel Dekker, New York, NY, 1993.

R. Sitnik, M. Kujawinska, and J. Woznicki. Digital fringe projection system for large-volume 360-deg shape measurement. *Optical Engineering*, 41(2):443–449, 2002.

S. Sizgoric and A. A. Gundjian. An optical homodyne technique for measurement of amplitude and phase of sub-angstrom ultrasonic vibrations. *Proceedings of the IEEE*, 57(7):1313–1314, 1969.

M. Sjodahl and P. Synnergren. Measurement of shape by using projected random patterns and temporal digital speckle photography. *Applied Optics*, 38(10):1990–1997, 1999.

W. J. Smith. *Modern optical engineering : the design of optical systems*. McGraw Hill, New York, 3rd edition, 2000.

R. Smythe and R. Moore. Instantaneous phase measuring interferometry. *Optical Engineering*, 23(4):361–364, 1984.

G. E. Sommargren. Optical heterodyne profilometry. *Applied Optics*, 20(4):610–618, 1981.

G. S. Spagnolo, D. Ambrosini, and D. Paoletti. Displacement measurement using the Talbot effect with a Ronchi grating. *Journal of Optics A - Pure and Applied Optics*, 4 (6):S376–S380, 2002.

K. A. Stetson. Theory and applications of electronic holography. In *SEM Conf. Hologram Interferometry and Speckle Metrology*, Proc. SEM, page 204âĂŞ300, 1990.

K. A. Stetson and R. L. Powell. Hologram interferometry. *Journal of the Optical Society of America*, 55(11):1570–1576, 1965.

M. A. Sutton, W. Zhao, S. R. McNeill, H. W. Schreier, and Y. J. Chao. Development and assessment of a single-image fringe projection method for dynamical applications. *Experimental Mechanics*, 41(3):205–217, 2001.

T. Suzuki, O. Sasaki, and T. Maruyama. Phase locked laser diode interferometry for surface profile measurement. *Applied Optics*, 28(20):4407–4410, 1989.

T. Suzuki, O. Sasaki, S. Takayama, and T. Maruyama. Real-time displacement measurement using synchronous detection in a sinusoidal phase modulating interferometer. *Optical Engineering*, 32(5):1033–1037, 1993.

H. Takasaki. Moiré topography. *Applied Optics*, 9(6):1467–1472, 1970.

H. Takasaki. Moiré topography. *Applied Optics*, 12(4):845–850, 1973.

M. Takeda and K. Mutoh. Fourier transform profilometry for the automatic measurement of 3D object shapes. *Applied Optics*, 22(24):3977–3982, 1983.

M. Takeda, H. Ina, and S. Kobayashi. Fourier-transform method of fringe-pattern analysis for computer-based topography and interferometry. *Journal of the Optical Society of America*, 72(1):156–160, 1982.

R. P. Tatam, J. C. Davies, C. H. Buckberry, and J. D. C. Jones. Holographic surface contouring using wavelength modulation of laser-diodes. *Optics and Laser Technology*, 22(5):317–321, 1990.

P. J. Tavares and M. A. Vaz. Orthogonal projection technique for resolution enhancement of the Fourier transform fringe analysis method. *Optics Communications*, 266 (2):465–468, 2006.

P. J. Tavares and M. A. Vaz. Linear calibration procedure for the phase-to-height relationship in phase measurement profilometry. *Optics Communications*, 274(2): 307–314, 2007a.

P. J. Tavares and M. A. Vaz. Accurate subpixel corner detection on planar camera calibration targets. *Optical Engineering*, 46(10):2051–2058, 2007b.

P. J. Tavares, N. Viriato, J. Reis, and M. A. Vaz. Coherent fringe projector for 3D surface profilometry. In W. Osten, editor, *Optical Measurement Systems for Industrial Inspection V*, volume 6616 of *Proc. SPIE*, pages 98–107, 2007.

H. J. Tiziani. Optical measurement of engineering surfaces - scope and trends. In P. K. Rastogi, editor, *Optical Measurement Techniques and Applications*, chapter 2. Artech-House, Norwood, MA, 1997.

D. P. Towers, T. R. Judge, and P. J. Bryanston-Cross. Automatic interferogram analysis techniques applied to quasi-heterodyne holography and espi. *Optics and Lasers in Engineering*, 14(4-5):239–281, 1991.

M. Vaz. *Interferometria laser e métodos híbridos em mecânica experimental*. PhD thesis, Faculty of Engineering, University of Porto, Porto, Portugal, 1995.

M. A. Vaz, F. Q. Melo, J. D. Rodrigues, and J. S. Gomes. Noise and vibration analysis of an automobile engine component. *Machine vibration*, 5(2):63–70, 1996.

C. M. Vest. *Holographic interferometry*. John Wiley and Sons, Inc., New York, 1st edition, 1979.

E. Vikhagen. Nondestructive testing by use of tv holography and deformation phase gradient calculation. *Applied Optics*, 29(1):137–144, 1990.

V. V. Volkov and Y. M. Zhu. Deterministic phase unwrapping in the presence of noise. *Optics Letters*, 28(22):2156–2158, 2003.

V. V. Volkov, Y. Zhu, and M. De Graef. A new symmetrized solution for phase retrieval using the transport of intensity equation. *Micron*, 33(5):411–416, 2002.

A. M. Wallace, G. S. Buller, and A. C. Walker. 3D imaging and ranging by time-correlated single photon counting. *Computing and Control Engineering Journal*, 12 (4):157–168, 2001.

J. Y. Wang. Imaging laser radar - an overview. In *Lasers'86; Proceedings of the Ninth International Conference on Lasers and Applications*, pages 19–29, Orlando, FL, 1987.

G. Q. Wei and S. D. Ma. Implicit and explicit camera calibration: theory and experiments. *IEEE Transactions on Pattern Analysis and Machine Intelligence*, 16(5):469–480, 1994.

D. C. Williams, N. S. Nassar, J. E. Banyard, and M. S. Virdee. Digital phase-step interferometry - a simplified approach. *Optics and Laser Technology*, 23(3):147–150, 1991.

R. G. Willson. *Modeling and calibration of automated zoom lenses*. PhD thesis, Carnegie Mellon University, Pittsburgh, Pennsylvania, 1994.

M. Wojtkowski, V. Srinivasan, J. G. Fujimoto, T. Ko, J. S. Schuman, A. Kowalczyk, and J. S. Duker. Three-dimensional retinal imaging with high-speed ultrahigh-resolution optical coherence tomography. *Ophthalmology*, 112(10):1734–1746, 2005.

K. H. Womack. Interferometric phase measurement using spatial synchronous detection. *Optical Engineering*, 23(4):391–395, 1984.

R. J. Woodham. Photometric-method for determining surface orientation from multiple images. *Optical Engineering*, 19(1):139–144, 1980.

J. C. Wyant. White light interferometry. In H. J. Caulfield, editor, *Holography: A tribute to Yuri Denisyuk and Emmett Leith*, volume 4737 of *Proc. SPIE*, pages 98–107, 2002.

J. C. Wyant. Dynamic interferometry. *Optics and Photonics News*, 14(4):36–41, 2003.

J. Yanez-Mendiola, M. Servin, and D. Malacara-Hernandez. Reduction of the edge effects induced by the boundary of a linear-carrier interferogram. *Journal of Modern Optics*, 48(4):685–693, 2001.

D. Yelin, I. Rizvi, W. M. White, J. T. Motz, T. Hasan, B. E. Bouma, and G. J. Tearney. Three-dimensional miniature endoscopy. *Nature*, 443(7113):765–765, 2006.

M. Young, E. Beeson, J. Davis, S. Rusinkiewicz, and R. Ramamoorthi. Viewpoint-coded structured light. In *Proceedings of the 2007 IEEE Computer Society Conference on Computer Vision and Pattern Recognition (CVPR)*, Proc. IEEE, pages 1–8, 2007.

Z. Zalevsky, Y. Kapellner, I. Eyal, and N. Cohen. Self Q-switching effect in a nd:YVO4/KTP lasing unit. *Optical Engineering*, 45(7):0705061–0705063, 2006.

J. S. Zelenka and J. R. Varner. Multiple-index holographic contouring. *Applied Optics*, 8(7):1431–1434, 1969.

X. L. Zhang, Y. C. Lin, M. R. Zhao, X. B. Niu, and Y. G. Huang. Calibration of a fringe projection profilometry system using virtual phase calibrating model planes. *Journal of Optics A - Pure and Applied Optics*, 7(4):192–197, 2005.

Z. Zhang, D. Zhang, and X. Peng. Performance analysis of a 3D full-field sensor based on fringe projection. *Optics and Lasers in Engineering*, 42(3):341–353, 2004.

W. S. Zhou and X. Y. Su. A direct mapping algorithm for phase-measuring profilometry. *Journal of Modern Optics*, 41(1):89–94, 1994.

B. Zitová and J. Flusser. Image registration methods - a survey. *Image and Vision Computing*, (21):977–1000, 2003.

Appendices

Appendix A

The *Inspect* Program Interface

Current day digital cameras already have the capacity to grab frames and send them directly to a Peripheral Component Interconnect (PCI) bus, but at the time this research took off, frame grabbers were absolutely vital for image acquisition, and even some of the fast processing operations such as FFT's had to be carried out on dedicated processors. The use of a frame grabber was not a choice then, and the decision to buy and use one, implied developing the necessary software tools to support image processing operations.

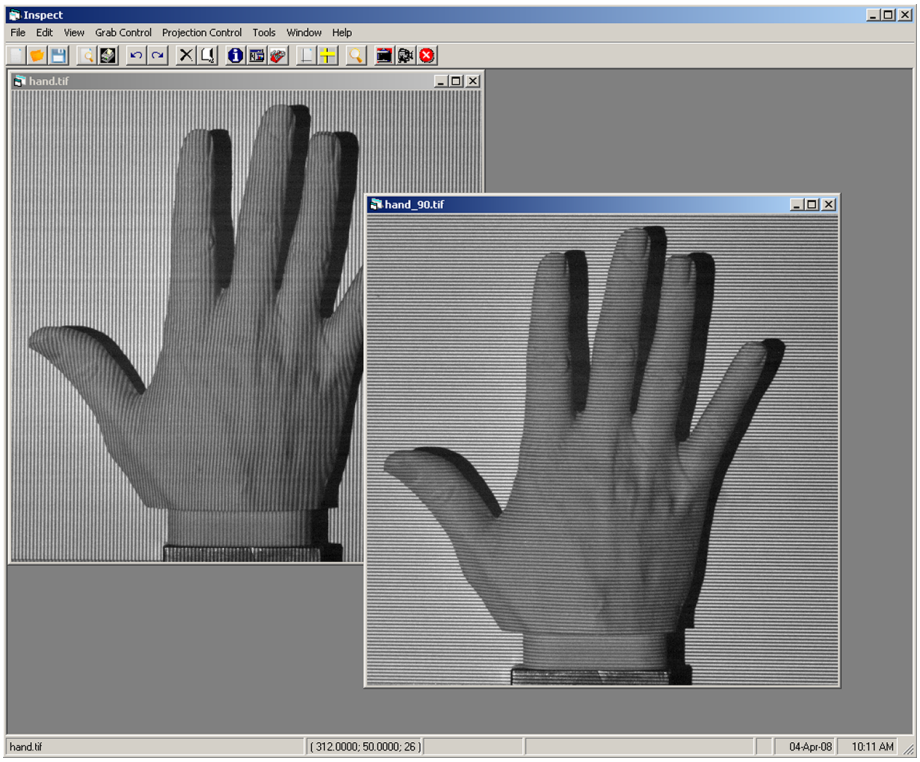

Figure A.1 - *Inspect* main screen.

Having chosen a Matrox frame grabber and the accompanying Matrox Imaging Library that provides most of the processing functions, a software application denominated *Inspect*, built in Visual Basic, has grown steadily throughout this thesis work in LOME. This application, some 50000 programming lines large, provides all the computing capability necessary for the work presented herein, but is also used for other laboratory tasks that require image processing. This application is an open project that will continue to grow as necessity dictates. This appendix describes the Inspect application as it stands today. This will be a menu driven introduction to the available functions, followed by a description of the libraries currently contained in the program.

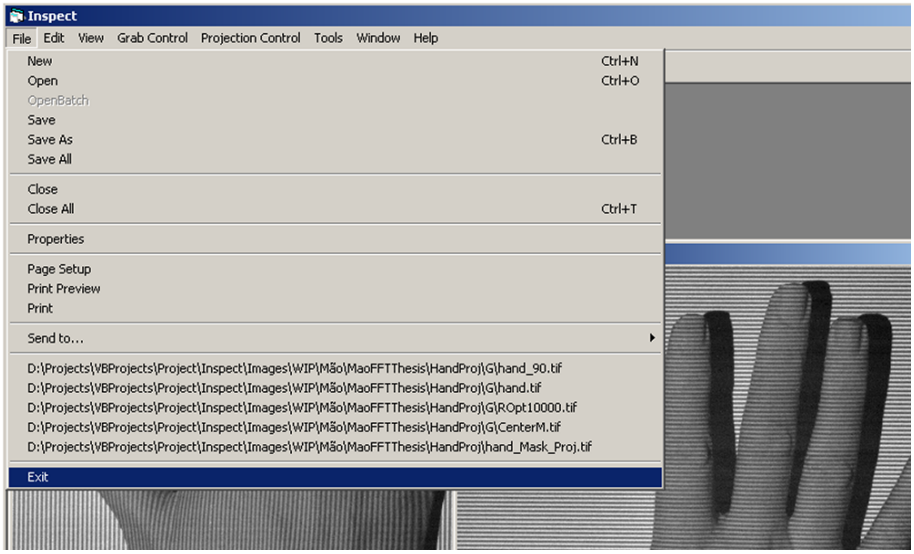

Figure A.2 - *Inspect* File menu.

The program was developed for the Microsoft Windows environment and is currently being used on a Pentium IV personal computer with Windows XP. All the operations are available through menus on top of the main window, although the most common functions can be accessed by a toolbar underneath the main menu, and shortcuts were provided for several of the most widely used. Whenever a function has an associated shortcut, it is presented on the menu, next to the function. Besides, being developed on top of the Microsoft Foundation Class library wrapper class means that several Microsoft Windows *standards* are preserved, such as the commands for opening and closing windows or starting events, copying, cutting and pasting data, etc.

It seemed logical then to follow the conventions with most windows programs, such as having a File menu to group file related operations, an Edit menu for data operations, a View menu for turning the toolbar, status bar and information window on or off as well as some helping objects such as a ruler or data cursors, and a Window menu for arranging the windows on the main screen, stacking them vertically or horizontally, defining zoom values or choosing between normal view or full screen.

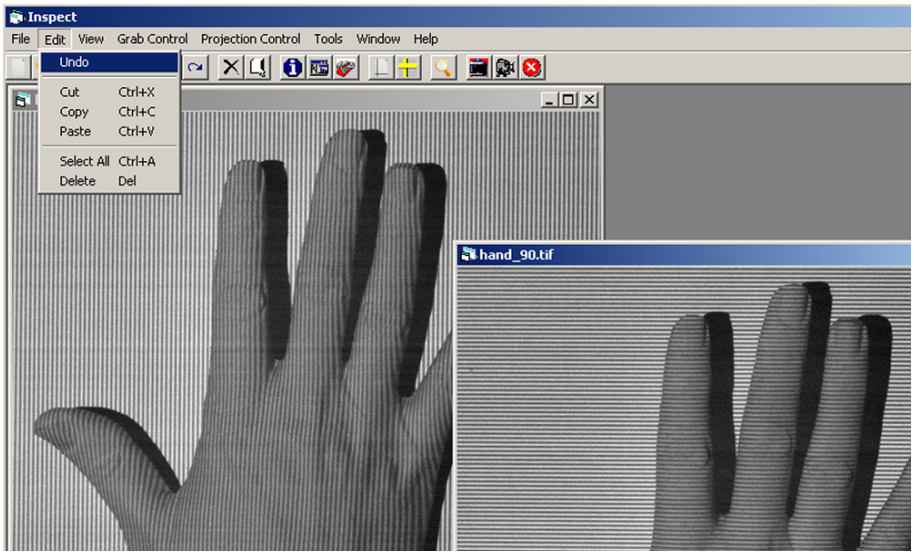

Figure A.3 - *Inspect* Edit menu.

These are common menus to windows users, that don't really need a deeper explanation. The remaining three menus are described next in order.

A.1 Grab control

This is a short menu, where frame grabbing control takes place, whether it is single frame, continuous grabbing or stopping a continuous grabbing. These operations are also available on the toolbar. Grabber setup provides a direct modification of the grabbing parameters, such as digitizer gain or grab window size.

Under this menu, a Focus option activates the MIL Focus procedure and can be setup for motorized objectives.

A.2 Projection control

Under Projection Control, choice and control of the projection device is to be made. As of now, the Coherent Fringe Projector, described in Appendix B, isn't still finished and it hasn't been possible to use any InFocus projector Active-X control, simply because it wasn't made available by the manufacturer. This section isn't thus working. Another capability under Projection Control, which is working, is the real-time analysis of the projected spectrum, in order to understand if there's a large spread in frequencies or, on the contrary, if the projected fringe frequency has appreciable quality. This analysis is provided under Lighting Quality.

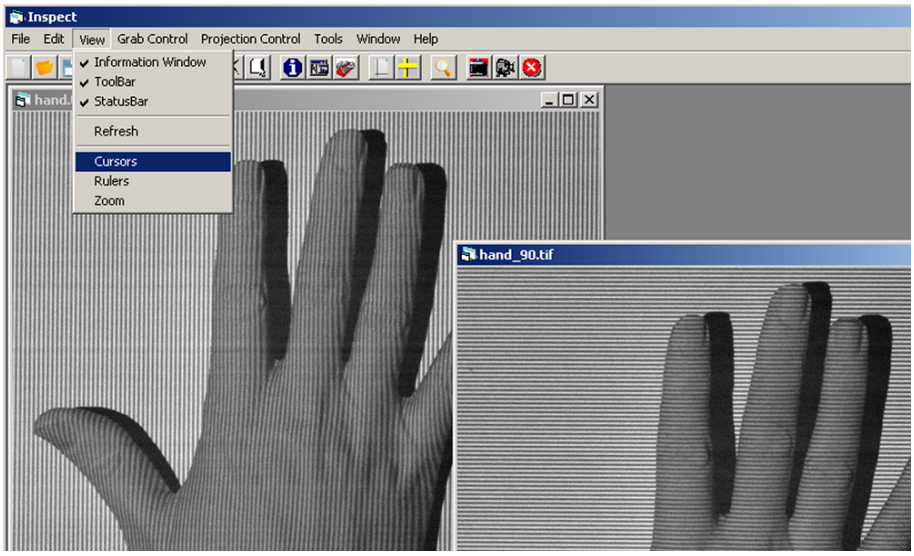

Figure A.4 - *Inspect* View menu.

A.3 Tools

Tools is really the core of the Inspect application. This menu is divided into 5 different sections.

Pre-processing

Pre-processing entails all operations which are performed directly on images. These comprehend:

Arithmetic operations

- Addition;
- Subtraction;
- Multiplication;
- Division.

Special operations

- Average addition:
- Subtraction followed by clipping when there are several images present;
- Histogram equalization, with several algorithms;

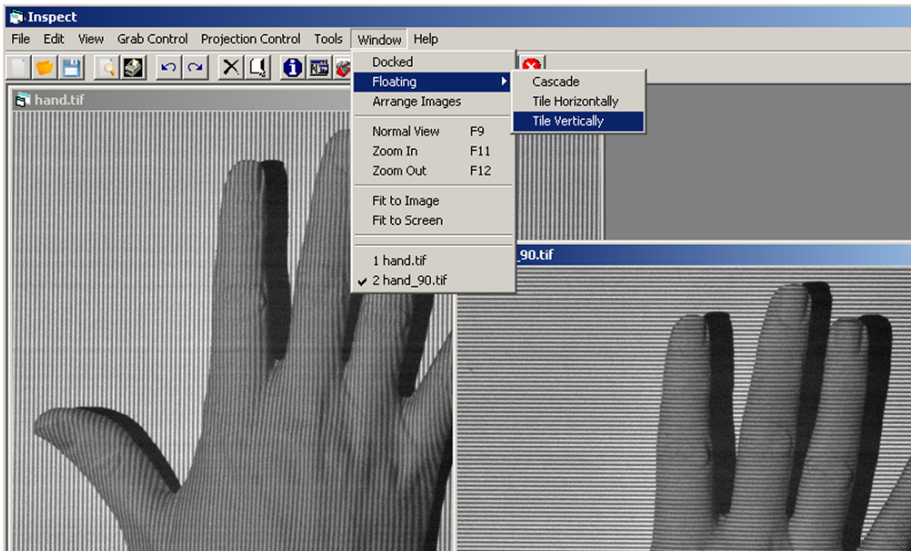

Figure A.5 - *Inspect* Window menu.

- Mask creation, which is able to work by parts, adding each new mask to the previous one;
- Thresholding;
- Negation;
- Absolute value calculation;
- Mirroring.

A bit scroll operation has also been added to the list. Other operations possible under Pre-processing are filtering and edge detection. Several types of filters have been implemented, through convolution with different kernels:

Filtering

- Low-pass;
- High-pass;
- Smoothing;
- Average;
- Median;
- Gaussian;
- Windowed Fourier Transform.

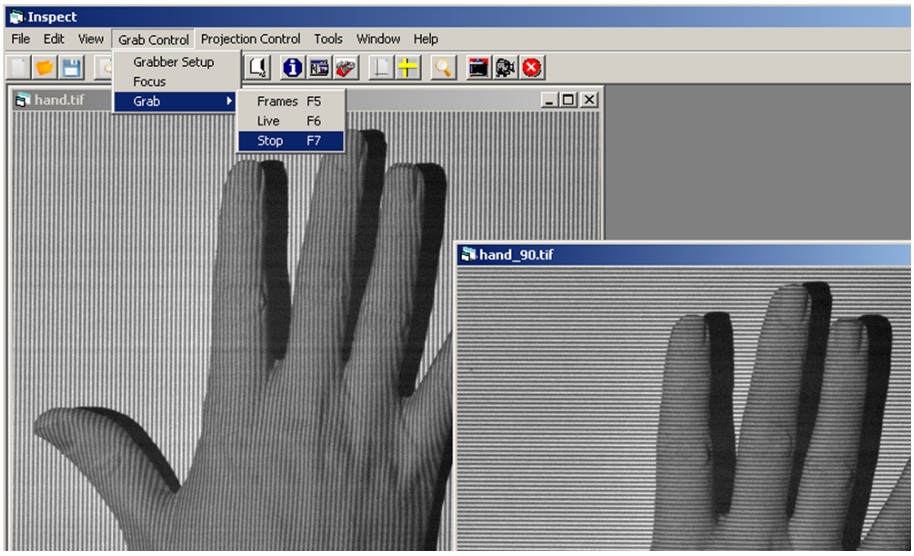

Figure A.6 - *Inspect* Grab Control menu.

The last two filters are in fact more complex than the remaining, and several operations have to be performed, apart from convolutions.

Several edge detection algorithms have been implemented which are also found under Pre-processing:

First-order edge detection algorithms

- Roberts Cross;
- Prewitt;
- Sobel;
- Frei-Chen;
- Canny;
- Compass - Prewitt;
- Compass - Kirsch;
- Compass - Robinson3;
- Compass - Robinson5

Second-order edge detection algorithms

- Laplacian Standard;
- Laplacian Prewitt;

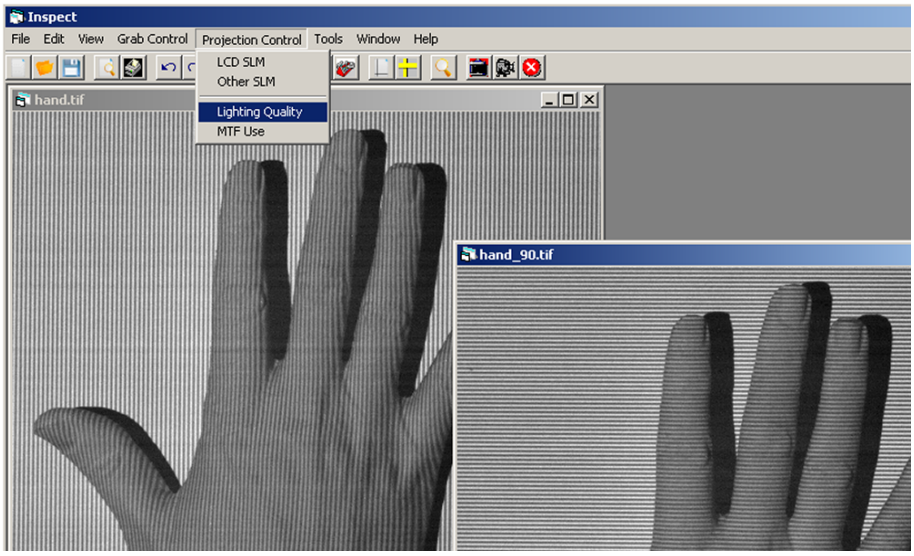

Figure A.7 - *Inspect* Projection Control menu.

- Laplacian Separable;
- Marr-Hildreth.

The following section of the Tools menu is the Calibration section. This section is divided into a subsection with XY camera calibration and zz profilometre calibration, another subsection with MTF and synthetic fringe calculation, and a third subsection for image correction. The envisaged corrections can be distortion, which corrects an image for the amount of lens distortion calculated during camera calibration, or zz correction, which makes a correction to the zz coordinate based on complete camera and profilometre calibration as described in Chapter 4.

The third section of the Tools menu is dedicated to image calculations:

- Fast Fourier Transform and Reverse Transform;
- Hilbert Transforms in xx or yy directions;
- Differentiation in xx or yy directions;
- Image apodization with a $\cos^{\alpha}$ law such as the Hann or the Hamming windows;
- Gerchberg fringe continuation for super-resolution is also selected here.

Phase calculations are also present under this section, such as TPU or the full FTP workflow with FFT, Filter selection, Reverse FFT and Phase calculation.

There's still a fourth section, not working at present, for I/O control such as can be done with shutters or rotation devices.

A final Options sub-menu is available here, where general settings for the application can be selected.

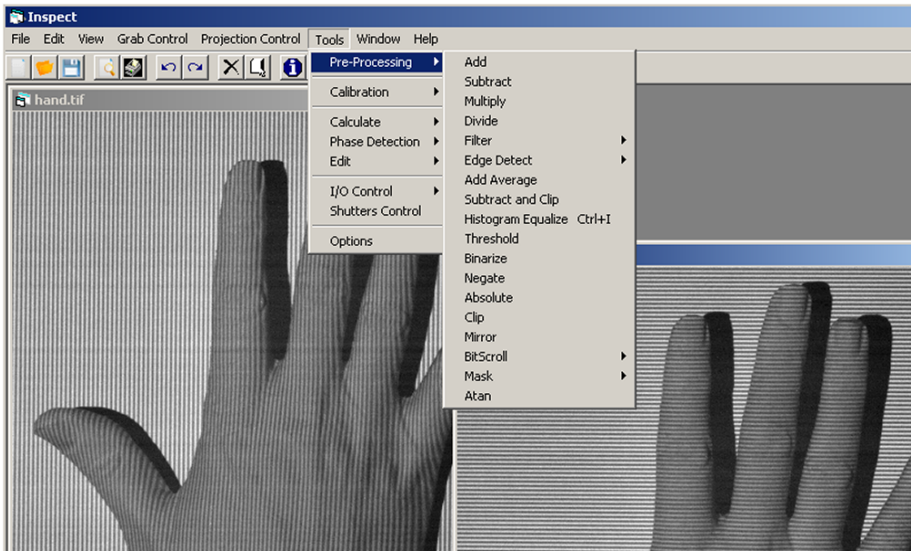

Figure A.8 - *Inspect* Tools - Pre-Processing menu.

The Inspect application is an ongoing project which will keep on being developed in the years to come, as the laboratory sees fit. One major drawback of the choices made during the development of the application is the fact that it is hardly portable because of it's dependency on the MIL library. It is thus regarded as desirable to migrate the application to a platform which does not depend on 3^{rd} party libraries or software. Some public libraries for image processing have been steadily gaining acceptance, which may well become the basis for this vital modification.

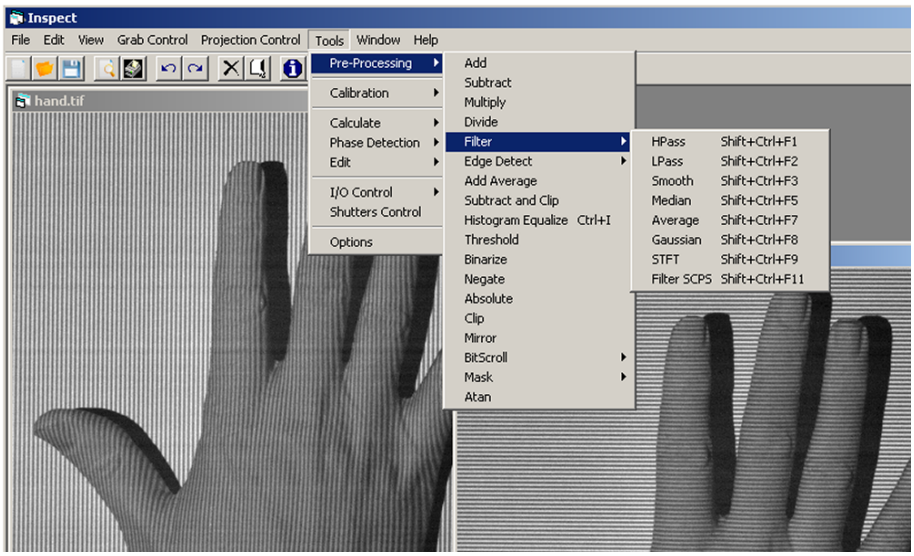

Figure A.9 - *Inspect* Tools - Pre-Processing - Filters menu.

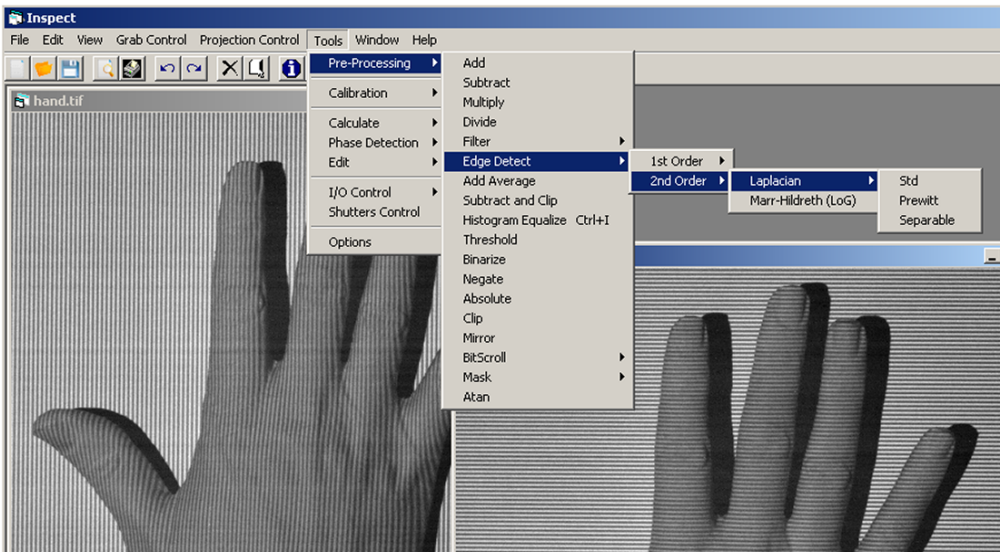

Figure A.10 - *Inspect* Tools - Pre-Processing - Edge Detection - 2^{nd} order menu.

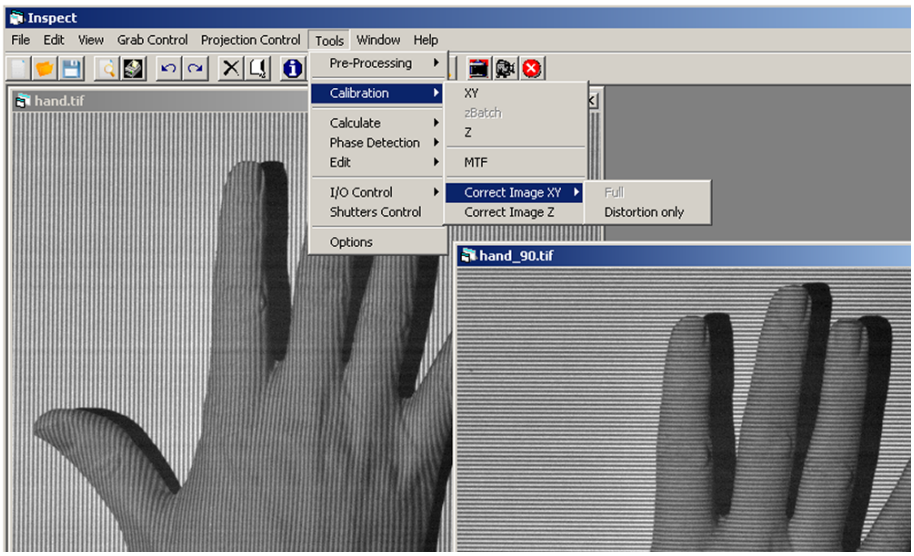

Figure A.11 - *Inspect* Tools - Calibration menu.

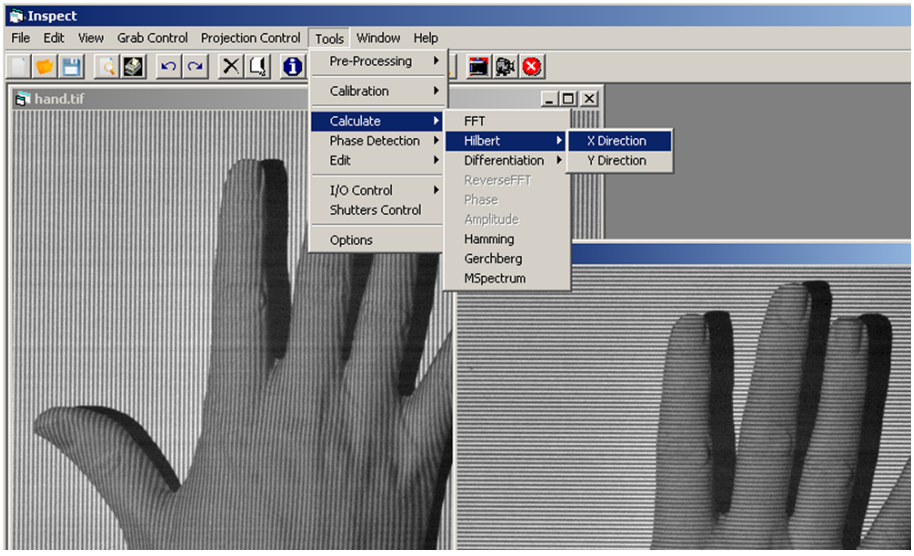

Figure A.12 - *Inspect* Tools - Calculation menu.

Appendix B

The *Coherent Fringe Projector*

The fringe projection system plays a decisive role on the entire phase map acquisition process, significantly impacting both quality and reliability of the final measurements. Moreover, typical phase measurement profilometres can hardly be used outside of laboratory controlled lighting facilities. This appendix describes LOME's project for a coherent fringe projection system which enables outdoor measurements by selectively band pass filtering the projected wavelength.

Fringe projection techniques require high throughput completely addressable fringe projection systems. Originally created with coherent light interferometry, by shedding a sinusoidal fringe pattern that resulted from the superposition of reference and object beams (Creath, 1993), the technique was bound to change with the introduction of spatial light modulators such as video projectors. These systems, either based on LCD or DLP technologies, and currently being used for phase measurement profilometry or digital encoding such as the Gray Code Method (GCM) (Horn and Kiryati, 1999; Sansoni et al., 1999).

Dedicated commercial devices with appreciable resolutions can now be found, most notably the LCP projector by BIAS and Jenoptik (Bothe et al., 2002). Still, most of the developed devices to date, apart from the original interferometers, use incoherent lighting, most likely due to the unavailability of coherent sources with sufficient power. An coherent alternative that has been gaining recognition in industry, is the DLP system from Texas Instruments, which uses monochromatic light emitting diode (LED) illumination (Frankowski and Stenzel, 2007). The advantages of using coherent light are twofold: the first is a dramatic reduction of heat inside the projector case, which otherwise requires special measures to protect both the optics and the electronic components, such as heat deflectors and other protections; the second advantage, which is the most noticeable, is the fact that temporally coherent light can be very efficiently filtered up to a few nm around a central wavelength. This provides the basis for using structured lighting outside of laboratory controlled conditions, and is in fact a sufficient condition for use in broad day light, should the provided laser power be enough. Up until very recently, miniaturized lasers didn't generate enough power to handle these requirements. With the advent of compact laser sources, such as the one used in this work, this possibility becomes real.

The laser source used in this project was originally a 60 mW, 532 nm diode

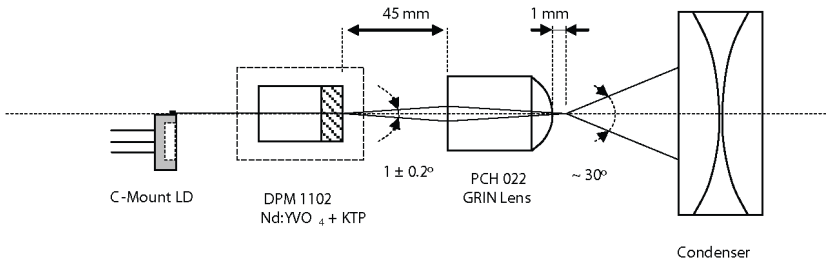

Figure B.1 - Coherent Fringe Projector - laser source and condenser group.

pumped solid state (DPSS) laser source, assembled at LOME. The source was designed with an output beam divergence of 30^o in order to fill the useful area of a 2 inch condenser group at 86 mm distance from the source. It consisted on a 2 W, 808 nm C-Mount diode laser pump, a diode pumped microchip (DPM) laser crystal combining a Nd:YvO4 crystal and a KTP frequency doubler, and a gradient index (GRIN) lens. The DPM1102 module from CASIX is in fact an optically bonded hybrid crystal, which endures much higher powers than previous optically cemented KTP to Nd:YvO4 crystals. According to CASIX, optical bonding is based on diffusion. The crystals are permanently bonded by heating to a high temperature under pressure resulting in a chemical exchange of molecules at the interface. Even so, there seems to be an ongoing discussion about the properties of these DPM modules, as can be seen in (Zalevsky et al., 2006).

In order to achieve alignment of the C-Mount pumping diode and the DPM crystal, an *xyz* micro-positioner was modified to accommodate tilt, as can be seen in Fig. B.2. Accurate positioning is very important due to the fact these laser modules have a rather high sweet spot.

The green, 532 nm, beam has a very small divergence at the KTP output side. In order to fill a 2 inch condenser group at a reasonably small distance, the required beam divergence was calculated at 30^o, which in turn involved using a very short focal distance focusing lens. A PCH022 GRIN lens from CASIX, with a 1mm focal distance, has been used at 45 mm from the KTP exit as shown in Fig. B.1.

The condenser group was calculated having in mind a versatile projection group such as an F-Mount Nikon objective with a typical 46.5 mm back focal distance. Ray tracing the entire optics assembly, from the GRIN lens forward, is shown in Fig. 4. The condenser group comprises two 50 mm diameter plano-convex lenses with an 80 mm focal distance, convex sides apposed, for a better control of spherical aberration.

The Spatial Light Modulator (SLM) used herein was a XGA1 twisted nematic LCD from CRL with a 1024x768 VGA resolution. The entire assembly project can be seen in Fig. B.4. In case a higher resolution is necessary, the LCD can be rapidly exchanged with a Ronchi ruling.

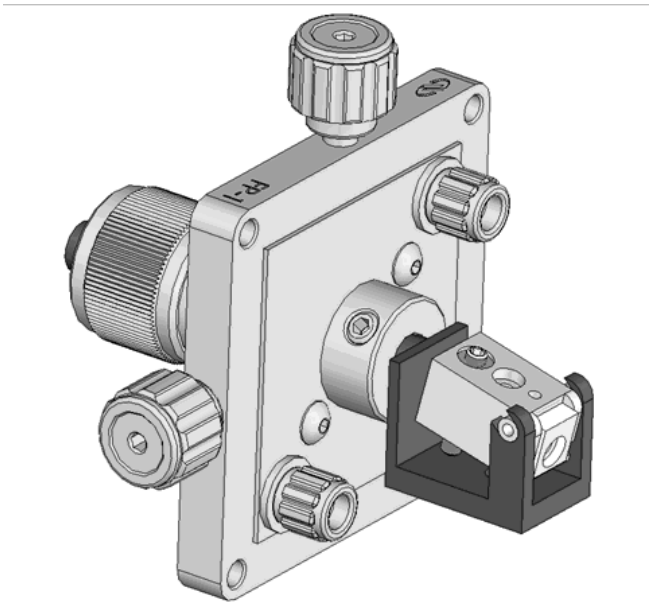

Figure B.2 - Modified XYZ positioner for diode laser alignment.

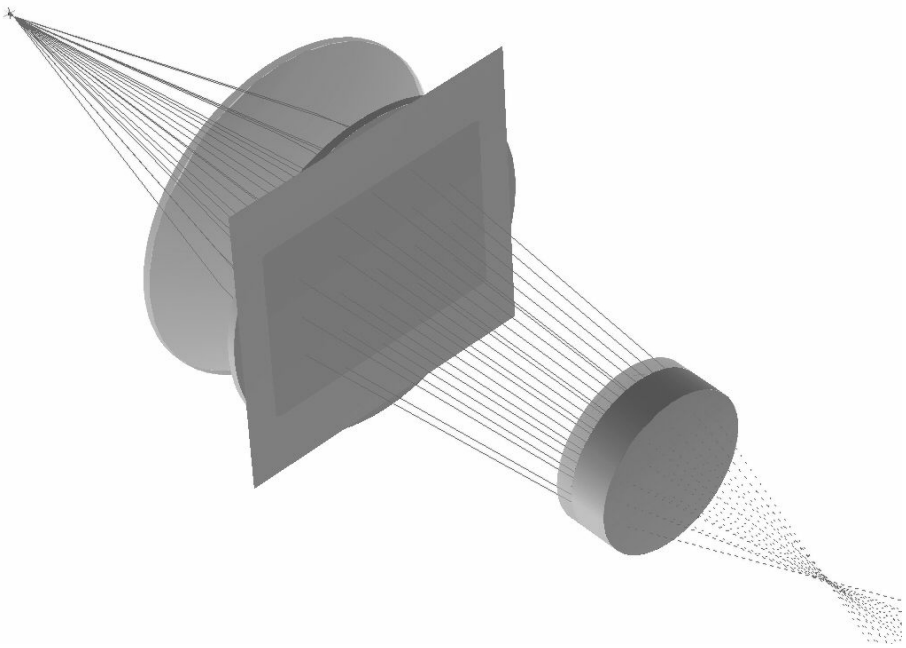

Figure B.3 - Ray tracing the optics assembly.

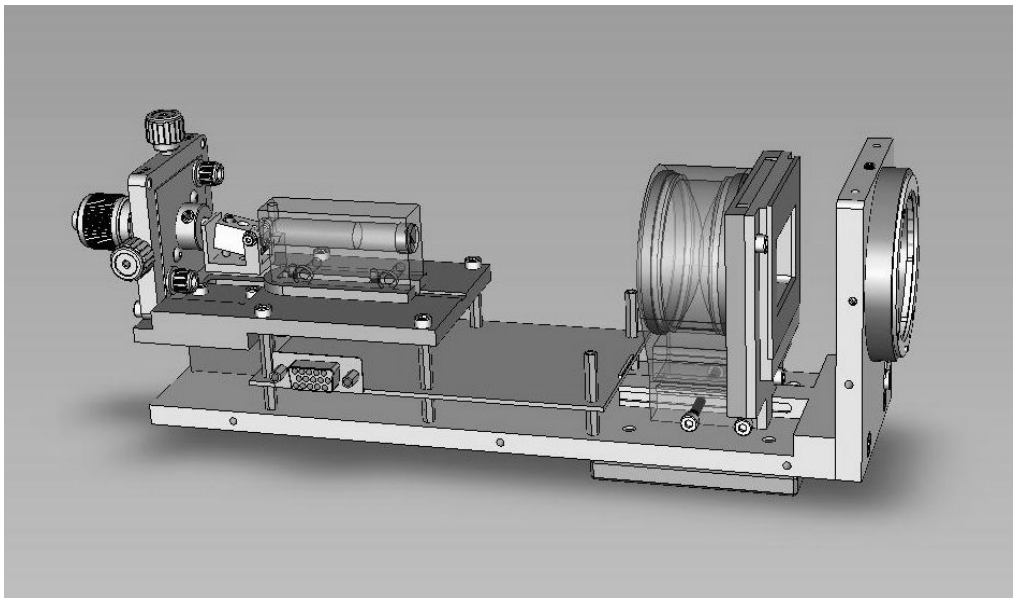

Figure B.4 - Coherent Fringe Projector - complete assembly.

The completed prototype is shown in Fig. B.5. The final footprint of the entire device is 240 x 65 mm, weighting under 800g.

The obtained fringes after correction as reported in § 4.4, can be seen in Fig. B.6 for 16 and 32 fringes accross.

Testing was performed with both Temporal Phase Unwrapping and Fourier Transform Profilometry. The initial results, obtained under normal laboratory illumination, are shown in Figs. B.7 to B.9, and were very encouraging. This projector was presented at SPIE's Optical Metrology 2007 (Tavares et al., 2007).

The project ran into several problems related to coherent noise. The fringes produced by every dust particle or even by the GRIN lens aperture show up in projection. In view of the reduced size of the projector, low pass filtering with a pinhole was not feasible. As such, the option was taken to reduce spatial coherence by time averaging a moving diffuser, with satisfactory results.

After the initial trials with the system reported above, the project underwent a significant modification in order to correct structural debilities and laser limitations. In fact, the laser assembled at LOME had several alignment problems, which imposed too many constraints on the necessary compensation tools that rendered the model difficult to operate. The decision to purchase and incorporate a commercial laser was made, which implied a complete system redesign. At the time of this writing, the new parts have all been received, except for the mechanical support which is still being manufactured. The current completion date forecast is March 2009. The redesigned mechanical construction is shown in Fig. B.10 and the rendered 3D model in Fig. B.11.

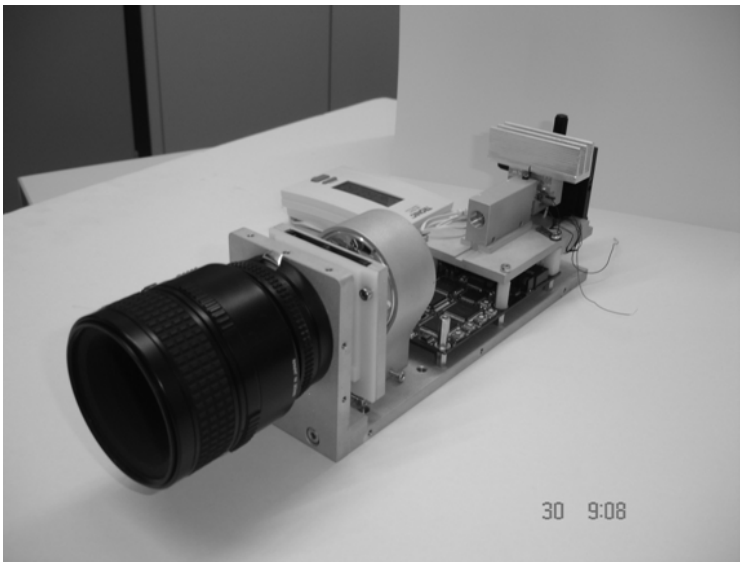

Figure B.5 - Coherent Fringe Projector - completed project.

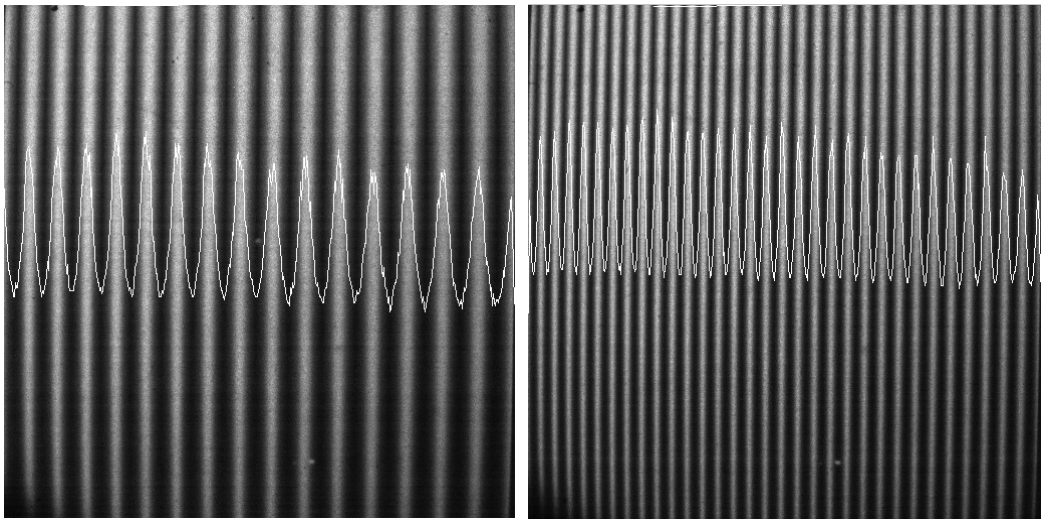

Figure B.6 - Obtained fringes, after correction for the transfer function.

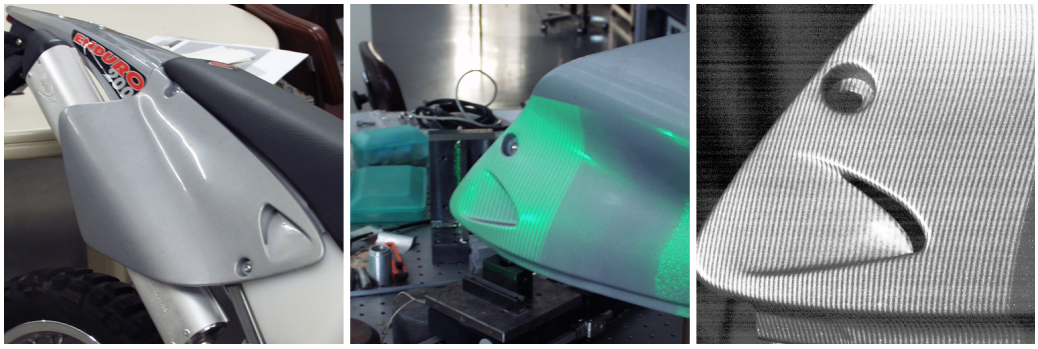

Figure B.7 - Moto side panel shape acquisition with 64 fringes.

Figure B.8 - Phase map obtained with FTP and 3D point cloud.

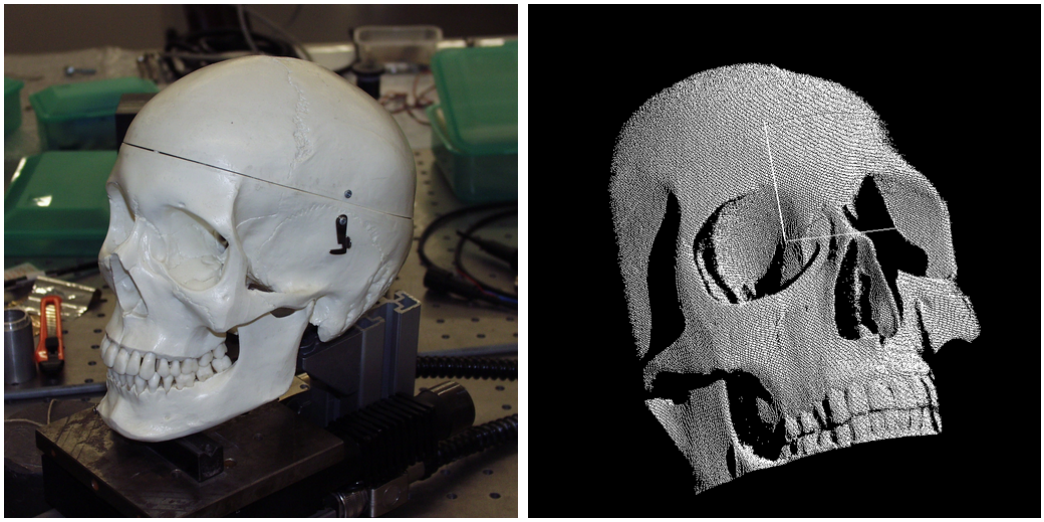

Figure B.9 - 3D point cloud obtained with TPU on a teaching skull model.

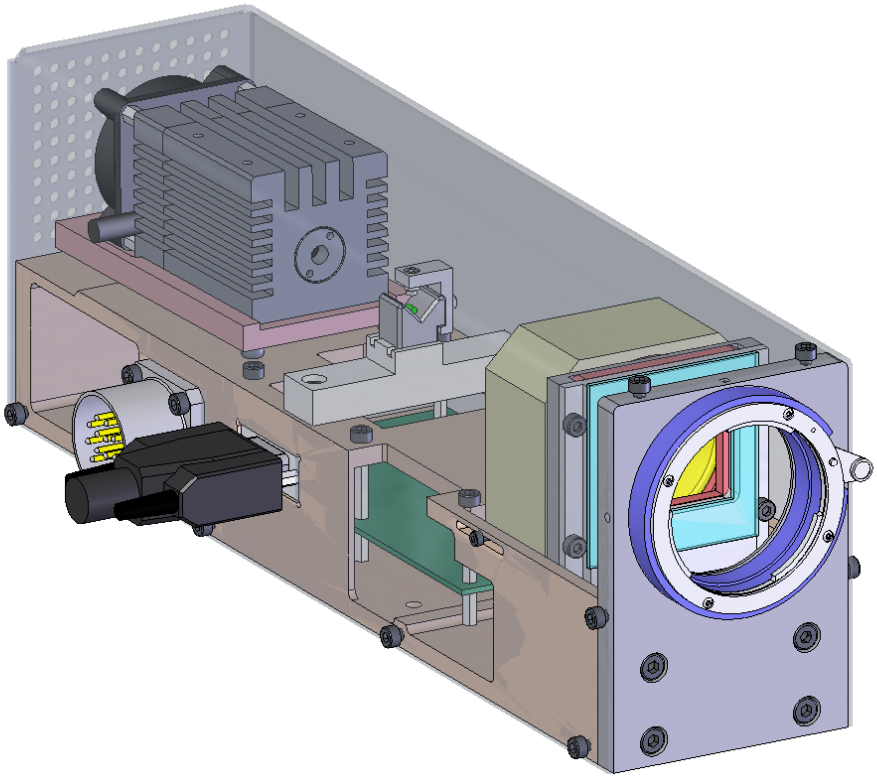

Figure B.10 - The redesigned Coherent Fringe Projector.

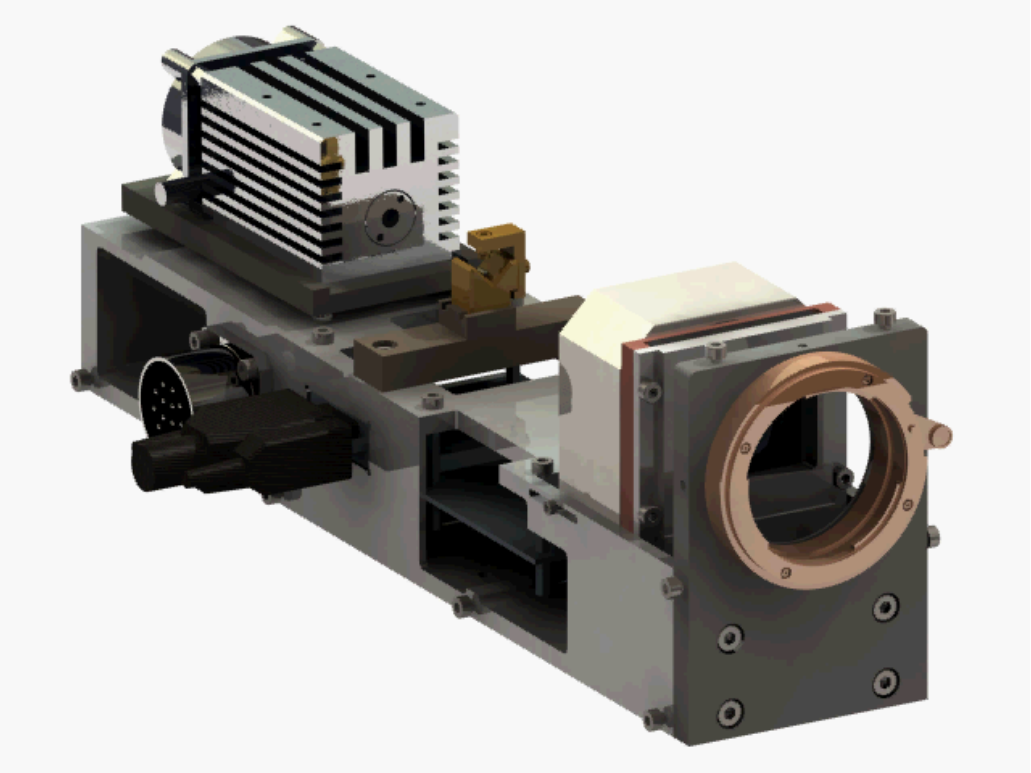

Figure B.11 - Coherent Fringe Projector - rendered 3D model of the final version.

Appendix C

Non-linear intrinsic camera calibration optimization

Most camera calibration procedures rely, at some point, on iterative non-linear optimization. These procedures, simple as they may be, are reasonably fast because the number of control points is usually kept at a minimum. Be that as it may, the calculations involved grow very fast with the number of control parameters. For those people with access to non-linear optimization routines in Fortran, or other calculation dedicated programming language, this may seem a trivial issue, but those who had to code the routines, know just how cumbersome this may rapidly become. This is why the Gradient and Hessian calculations for a complete intrinsic parameters optimization via Levenberg-Marquardt algorithm is left here below.

The parameters to optimize are the focal distance, f, zz translation component, z, radial and tangential distortion coefficients K_1, K_2, P_1 and P_2, as presented in § 4.2, lateral uncertainty factor, s_u, scale factors, d_u and d_v and image centre coordinates, i_0 and j_0. The merit function, χ^2, measures the sum of squared differences between the undistorted coordinates, as calculated from the image data and from the measured object coordinates, back through the camera model. Let

$$u_d = \frac{d_u}{s_u}\,(i - i_0)\,; \qquad v_d = d_v\,(j - j_0) \tag{C.1}$$

represent the corrected coordinates on the image plane,

$$\begin{aligned} u &= u_d\left(1 + K_1 r^2 + K_2 r^4\right) + 2P_1 u_d v_d + P_2\left(r^2 + 2u_d^2\right) \\ v &= v_d\left(1 + K_1 r^2 + K_2 r^4\right) + 2P_2 u_d v_d + P_1\left(r^2 + 2v_d^2\right) \end{aligned} \tag{C.2}$$

represent the uncorrected or undistorted coordinates, as calculated from the projective equations, Eq. 4.5, with

$$r = \sqrt{u_d^2 + v_d^2} \tag{C.3}$$

L_0 and L_1 are just two auxiliary functions to prevent rather large equations,

$$L_0 = 1 + K_1 r^2 + K_2 r^4; \qquad L_1 = K_1 + 2K_2 r^2 \tag{C.4}$$

A and B represent the undistorted image points differences,

$$A = u - f\frac{x}{z}; \qquad B = v - f\frac{y}{z} \tag{C.5}$$

and the merit function is

$$\chi^2 = A^2 + B^2 \tag{C.6}$$

The gradient

$$\beta_k = -\frac{1}{2}\frac{\partial \chi^2}{\partial a_k} \tag{C.7}$$

and Hessian

$$\alpha_{kl} = \frac{1}{2}\frac{\partial^2 \chi^2}{\partial a_k \partial a_l} \tag{C.8}$$

where the a_i are the optimization parameters, are given by,

$$\begin{aligned}
\beta_0 &= -\frac{1}{2}\frac{\partial}{\partial f}\left(\chi^2\right) = -A\frac{\partial}{\partial f}\left(A\right) - B\frac{\partial}{\partial f}\left(B\right) \\
\beta_2 &= -\frac{1}{2}\frac{\partial}{\partial K_1}\left(\chi^2\right) = -A\frac{\partial}{\partial K_1}\left(A\right) - B\frac{\partial}{\partial K_1}\left(B\right) \\
\beta_2 &= -\frac{1}{2}\frac{\partial}{\partial K_1}\left(\chi^2\right) = -A\frac{\partial}{\partial K_1}\left(A\right) - B\frac{\partial}{\partial K_1}\left(B\right) \\
\beta_3 &= -\frac{1}{2}\frac{\partial}{\partial K_2}\left(\chi^2\right) = -A\frac{\partial}{\partial K_2}\left(A\right) - B\frac{\partial}{\partial K_2}\left(B\right) \\
\beta_4 &= -\frac{1}{2}\frac{\partial}{\partial P_1}\left(\chi^2\right) = -A\frac{\partial}{\partial P_1}\left(A\right) - B\frac{\partial}{\partial P_1}\left(B\right) \\
\beta_5 &= -\frac{1}{2}\frac{\partial}{\partial P_2}\left(\chi^2\right) = -A\frac{\partial}{\partial P_2}\left(A\right) - B\frac{\partial}{\partial P_2}\left(B\right) \\
\beta_6 &= -\frac{1}{2}\frac{\partial}{\partial s_u}\left(\chi^2\right) = -A\frac{\partial}{\partial s_u}\left(A\right) - B\frac{\partial}{\partial s_u}\left(B\right) \\
\beta_7 &= -\frac{1}{2}\frac{\partial}{\partial i_0}\left(\chi^2\right) = -A\frac{\partial}{\partial i_0}\left(A\right) - B\frac{\partial}{\partial i_0}\left(B\right) \\
\beta_8 &= -\frac{1}{2}\frac{\partial}{\partial j_0}\left(\chi^2\right) = -A\frac{\partial}{\partial j_0}\left(A\right) - B\frac{\partial}{\partial j_0}\left(B\right)
\end{aligned} \tag{C.9}$$

and

$$
\begin{aligned}
\alpha_{00} &= \frac{1}{2}\frac{\partial^2}{\partial f^2}\left(\chi^2\right) \\
&= \left[\frac{\partial}{\partial f}\left(A\right)\right]^2 + A\frac{\partial^2}{\partial f^2}\left(A\right) + \left[\frac{\partial}{\partial f}\left(B\right)\right]^2 + B\frac{\partial^2}{\partial f^2}\left(B\right) \\
\alpha_{01} &= \frac{1}{2}\frac{\partial^2}{\partial f \partial z}\left(\chi^2\right) \\
&= \frac{\partial}{\partial f}\left(A\right)\frac{\partial}{\partial z}\left(A\right) + A\frac{\partial^2}{\partial f \partial z}\left(A\right) + \frac{\partial}{\partial f}\left(B\right)\frac{\partial}{\partial z}\left(B\right) + B\frac{\partial^2}{\partial f \partial z}\left(B\right) \\
\alpha_{02} &= \frac{1}{2}\frac{\partial^2}{\partial f \partial K_1}\left(\chi^2\right) \\
&= \frac{\partial}{\partial f}\left(A\right)\frac{\partial}{\partial K_1}\left(A\right) + A\frac{\partial^2}{\partial f \partial K_1}\left(A\right) + \frac{\partial}{\partial f}\left(B\right)\frac{\partial}{\partial K_1}\left(B\right) + B\frac{\partial^2}{\partial f \partial K_1}\left(B\right) \\
\alpha_{03} &= \frac{1}{2}\frac{\partial^2}{\partial f \partial K_2}\left(\chi^2\right) \\
&= \frac{\partial}{\partial f}\left(A\right)\frac{\partial}{\partial K_2}\left(A\right) + A\frac{\partial^2}{\partial f \partial K_2}\left(A\right) + \frac{\partial}{\partial f}\left(B\right)\frac{\partial}{\partial K_2}\left(B\right) + B\frac{\partial^2}{\partial f \partial K_2}\left(B\right) \\
\alpha_{04} &= \frac{1}{2}\frac{\partial^2}{\partial f \partial P_1}\left(\chi^2\right) \\
&= \frac{\partial}{\partial f}\left(A\right)\frac{\partial}{\partial P_1}\left(A\right) + A\frac{\partial^2}{\partial f \partial P_1}\left(A\right) + \frac{\partial}{\partial f}\left(B\right)\frac{\partial}{\partial P_1}\left(B\right) + B\frac{\partial^2}{\partial f \partial P_1}\left(B\right) \\
\alpha_{05} &= \frac{1}{2}\frac{\partial^2}{\partial f \partial P_2}\left(\chi^2\right) \\
&= \frac{\partial}{\partial f}\left(A\right)\frac{\partial}{\partial P_2}\left(A\right) + A\frac{\partial^2}{\partial f \partial P_2}\left(A\right) + \frac{\partial}{\partial f}\left(B\right)\frac{\partial}{\partial P_2}\left(B\right) + B\frac{\partial^2}{\partial f \partial P_2}\left(B\right) \\
\alpha_{06} &= \frac{1}{2}\frac{\partial^2}{\partial f \partial s_u}\left(\chi^2\right) \\
&= \frac{\partial}{\partial f}\left(A\right)\frac{\partial}{\partial s_u}\left(A\right) + A\frac{\partial^2}{\partial f \partial s_u}\left(A\right) + \frac{\partial}{\partial f}\left(B\right)\frac{\partial}{\partial s_u}\left(B\right) + B\frac{\partial^2}{\partial f \partial s_u}\left(B\right) \\
\alpha_{07} &= \frac{1}{2}\frac{\partial^2}{\partial f \partial i_0}\left(\chi^2\right) \\
&= \frac{\partial}{\partial f}\left(A\right)\frac{\partial}{\partial i_0}\left(A\right) + A\frac{\partial^2}{\partial f \partial i_0}\left(A\right) + \frac{\partial}{\partial f}\left(B\right)\frac{\partial}{\partial i_0}\left(B\right) + B\frac{\partial^2}{\partial f \partial i_0}\left(B\right) \\
\alpha_{08} &= \frac{1}{2}\frac{\partial^2}{\partial f \partial Cy}\left(\chi^2\right) \\
&= \frac{\partial}{\partial f}\left(A\right)\frac{\partial}{\partial j_0}\left(A\right) + A\frac{\partial^2}{\partial f \partial j_0}\left(A\right) + \frac{\partial}{\partial f}\left(B\right)\frac{\partial}{\partial j_0}\left(B\right) + B\frac{\partial^2}{\partial f \partial j_0}\left(B\right)
\end{aligned}
$$

$$
\begin{aligned}
\alpha_{11} &= \frac{1}{2}\frac{\partial^2}{\partial z^2}\left(\chi^2\right) \\
&= \left[\frac{\partial}{\partial z}\left(A\right)\right]^2 + A\frac{\partial^2}{\partial z^2}\left(A\right) + \left[\frac{\partial}{\partial z}\left(B\right)\right]^2 + B\frac{\partial^2}{\partial z^2}\left(B\right) \\
\alpha_{12} &= \frac{1}{2}\frac{\partial^2}{\partial z \partial K_1}\left(\chi^2\right) \\
&= \frac{\partial}{\partial z}\left(A\right)\frac{\partial}{\partial K_1}\left(A\right) + A\frac{\partial^2}{\partial z \partial K_1}\left(A\right) + \frac{\partial}{\partial z}\left(B\right)\frac{\partial}{\partial K_1}\left(B\right) + B\frac{\partial^2}{\partial z \partial K_1}\left(B\right) \\
\alpha_{13} &= \frac{1}{2}\frac{\partial^2}{\partial z \partial K_2}\left(\chi^2\right) \\
&= \frac{\partial}{\partial z}\left(A\right)\frac{\partial}{\partial K_2}\left(A\right) + A\frac{\partial^2}{\partial z \partial K_2}\left(A\right) + \frac{\partial}{\partial z}\left(B\right)\frac{\partial}{\partial K_2}\left(B\right) + B\frac{\partial^2}{\partial z \partial K_2}\left(B\right) \\
\alpha_{14} &= \frac{1}{2}\frac{\partial^2}{\partial z \partial P_1}\left(\chi^2\right) \\
&= \frac{\partial}{\partial z}\left(A\right)\frac{\partial}{\partial P_1}\left(A\right) + A\frac{\partial^2}{\partial z \partial P_1}\left(A\right) + \frac{\partial}{\partial z}\left(B\right)\frac{\partial}{\partial P_1}\left(B\right) + B\frac{\partial^2}{\partial z \partial P_1}\left(B\right) \\
\alpha_{15} &= \frac{1}{2}\frac{\partial^2}{\partial z \partial P_2}\left(\chi^2\right) \\
&= \frac{\partial}{\partial z}\left(A\right)\frac{\partial}{\partial P_2}\left(A\right) + A\frac{\partial^2}{\partial z \partial P_2}\left(A\right) + \frac{\partial}{\partial z}\left(B\right)\frac{\partial}{\partial P_2}\left(B\right) + B\frac{\partial^2}{\partial z \partial P_2}\left(B\right) \\
\alpha_{16} &= \frac{1}{2}\frac{\partial^2}{\partial z \partial s_u}\left(\chi^2\right) \\
&= \frac{\partial}{\partial z}\left(A\right)\frac{\partial}{\partial s_u}\left(A\right) + A\frac{\partial^2}{\partial z \partial s_u}\left(A\right) + \frac{\partial}{\partial z}\left(B\right)\frac{\partial}{\partial s_u}\left(B\right) + B\frac{\partial^2}{\partial z \partial s_u}\left(B\right) \\
\alpha_{17} &= \frac{1}{2}\frac{\partial^2}{\partial z \partial i_0}\left(\chi^2\right) \\
&= \frac{\partial}{\partial z}\left(A\right)\frac{\partial}{\partial i_0}\left(A\right) + A\frac{\partial^2}{\partial z \partial i_0}\left(A\right) + \frac{\partial}{\partial z}\left(B\right)\frac{\partial}{\partial i_0}\left(B\right) + B\frac{\partial^2}{\partial z \partial i_0}\left(B\right) \\
\alpha_{18} &= \frac{1}{2}\frac{\partial^2}{\partial z \partial j_0}\left(\chi^2\right) \\
&= \frac{\partial}{\partial z}\left(A\right)\frac{\partial}{\partial j_0}\left(A\right) + A\frac{\partial^2}{\partial z \partial j_0}\left(A\right) + \frac{\partial}{\partial z}\left(B\right)\frac{\partial}{\partial j_0}\left(B\right) + B\frac{\partial^2}{\partial z \partial j_0}\left(B\right)
\end{aligned}
$$

$$
\begin{aligned}
\alpha_{22} &= \frac{1}{2}\frac{\partial^2}{\partial K_1^2}\left(\chi^2\right) \\
&= \left[\frac{\partial}{\partial K_1}(A)\right]^2 + A\frac{\partial^2}{\partial K_1^2}(A) + \left[\frac{\partial}{\partial K_1}(B)\right]^2 + B\frac{\partial^2}{\partial K_1^2}(B) \\
\alpha_{23} &= \frac{1}{2}\frac{\partial^2}{\partial K_1 \partial K_2}\left(\chi^2\right) \\
&= \frac{\partial}{\partial K_1}(A)\frac{\partial}{\partial K_2}(A) + A\frac{\partial^2}{\partial K_1 \partial K_2}(A) + \frac{\partial}{\partial K_1}(B)\frac{\partial}{\partial K_2}(B) + B\frac{\partial^2}{\partial K_1 \partial K_2}(B) \\
\alpha_{24} &= \frac{1}{2}\frac{\partial^2}{\partial K_1 \partial P_1}\left(\chi^2\right) \\
&= \frac{\partial}{\partial K_1}(A)\frac{\partial}{\partial P_1}(A) + A\frac{\partial^2}{\partial K_1 \partial P_1}(A) + \frac{\partial}{\partial K_1}(B)\frac{\partial}{\partial P_1}(B) + B\frac{\partial^2}{\partial K_1 \partial P_1}(B) \\
\alpha_{25} &= \frac{1}{2}\frac{\partial^2}{\partial K_1 \partial P_2}\left(\chi^2\right) \\
&= \frac{\partial}{\partial K_1}(A)\frac{\partial}{\partial P_2}(A) + A\frac{\partial^2}{\partial K_1 \partial P_2}(A) + \frac{\partial}{\partial K_1}(B)\frac{\partial}{\partial P_2}(B) + B\frac{\partial^2}{\partial K_1 \partial P_2}(B) \\
\alpha_{26} &= \frac{1}{2}\frac{\partial^2}{\partial K_1 \partial s_z}\left(\chi^2\right) \\
&= \frac{\partial}{\partial K_1}(A)\frac{\partial}{\partial s_u}(A) + A\frac{\partial^2}{\partial K_1 \partial s_u}(A) + \frac{\partial}{\partial K_1}(B)\frac{\partial}{\partial s_u}(B) + B\frac{\partial^2}{\partial K_1 \partial s_u}(B) \\
\alpha_{27} &= \frac{1}{2}\frac{\partial^2}{\partial K_1 \partial C_z}\left(\chi^2\right) \\
&= \frac{\partial}{\partial K_1}(A)\frac{\partial}{\partial i_0}(A) + A\frac{\partial^2}{\partial K_1 \partial i_0}(A) + \frac{\partial}{\partial K_1}(B)\frac{\partial}{\partial i_0}(B) + B\frac{\partial^2}{\partial K_1 \partial i_0}(B) \\
\alpha_{28} &= \frac{1}{2}\frac{\partial^2}{\partial K_1 \partial j_0}\left(\chi^2\right) \\
&= \frac{\partial}{\partial K_1}(A)\frac{\partial}{\partial j_0}(A) + A\frac{\partial^2}{\partial K_1 \partial j_0}(A) + \frac{\partial}{\partial K_1}(B)\frac{\partial}{\partial j_0}(B) + B\frac{\partial^2}{\partial K_1 \partial j_0}(B)
\end{aligned}
$$

$$
\begin{aligned}
\alpha_{33} &= \frac{1}{2}\frac{\partial^2}{\partial K_2^2}\left(\chi^2\right) \\
&= \left[\frac{\partial}{\partial K_2}\left(A\right)\right]^2 + A\frac{\partial^2}{\partial K_2^2}\left(A\right) + \left[\frac{\partial}{\partial K_2}\left(B\right)\right]^2 + B\frac{\partial^2}{\partial K_2^2}\left(B\right) \\
\alpha_{34} &= \frac{1}{2}\frac{\partial^2}{\partial K_2 \partial P_1}\left(\chi^2\right) \\
&= \frac{\partial}{\partial K_2}\left(A\right)\frac{\partial}{\partial P_1}\left(A\right) + A\frac{\partial^2}{\partial K_2 \partial P_1}\left(A\right) + \frac{\partial}{\partial K_2}\left(B\right)\frac{\partial}{\partial P_1}\left(B\right) + B\frac{\partial^2}{\partial K_2 \partial P_1}\left(B\right) \\
\alpha_{35} &= \frac{1}{2}\frac{\partial^2}{\partial K_2 \partial P_2}\left(\chi^2\right) \\
&= \frac{\partial}{\partial K_2}\left(A\right)\frac{\partial}{\partial P_2}\left(A\right) + A\frac{\partial^2}{\partial K_2 \partial P_2}\left(A\right) + \frac{\partial}{\partial K_2}\left(B\right)\frac{\partial}{\partial P_2}\left(B\right) + B\frac{\partial^2}{\partial K_2 \partial P_2}\left(B\right) \\
\alpha_{36} &= \frac{1}{2}\frac{\partial^2}{\partial K_2 \partial s_u}\left(\chi^2\right) \\
&= \frac{\partial}{\partial K_2}\left(A\right)\frac{\partial}{\partial s_u}\left(A\right) + A\frac{\partial^2}{\partial K_2 \partial s_u}\left(A\right) + \frac{\partial}{\partial K_2}\left(B\right)\frac{\partial}{\partial s_u}\left(B\right) + B\frac{\partial^2}{\partial K_2 \partial s_u}\left(B\right) \\
\alpha_{37} &= \frac{1}{2}\frac{\partial^2}{\partial K_2 \partial i_0}\left(\chi^2\right) \\
&= \frac{\partial}{\partial K_2}\left(A\right)\frac{\partial}{\partial i_0}\left(A\right) + A\frac{\partial^2}{\partial K_2 \partial i_0}\left(A\right) + \frac{\partial}{\partial K_2}\left(B\right)\frac{\partial}{\partial i_0}\left(B\right) + B\frac{\partial^2}{\partial K_2 \partial i_0}\left(B\right) \\
\alpha_{38} &= \frac{1}{2}\frac{\partial^2}{\partial K_2 \partial j_0}\left(\chi^2\right) \\
&= \frac{\partial}{\partial K_2}\left(A\right)\frac{\partial}{\partial j_0}\left(A\right) + A\frac{\partial^2}{\partial K_2 \partial j_0}\left(A\right) + \frac{\partial}{\partial K_2}\left(B\right)\frac{\partial}{\partial j_0}\left(B\right) + B\frac{\partial^2}{\partial K_2 \partial j_0}\left(B\right)
\end{aligned}
$$

$$
\begin{aligned}
\alpha_{44} &= \frac{1}{2}\frac{\partial^2}{\partial P_1^2}\left(\chi^2\right) \\
&= \left[\frac{\partial}{\partial P_1}\left(A\right)\right]^2 + A\frac{\partial^2}{\partial P_1^2}\left(A\right) + \left[\frac{\partial}{\partial P_1}\left(B\right)\right]^2 + B\frac{\partial^2}{\partial P_1^2}\left(B\right) \\
\alpha_{45} &= \frac{1}{2}\frac{\partial^2}{\partial P_1 \partial P_2}\left(\chi^2\right) \\
&= \frac{\partial}{\partial P_1}\left(A\right)\frac{\partial}{\partial P_2}\left(A\right) + A\frac{\partial^2}{\partial P_1 \partial P_2}\left(A\right) + \frac{\partial}{\partial P_1}\left(B\right)\frac{\partial}{\partial P_2}\left(B\right) + B\frac{\partial^2}{\partial P_1 \partial P_2}\left(B\right) \\
\alpha_{46} &= \frac{1}{2}\frac{\partial^2}{\partial P_1 \partial s_u}\left(\chi^2\right) \\
&= \frac{\partial}{\partial P_1}\left(A\right)\frac{\partial}{\partial s_u}\left(A\right) + A\frac{\partial^2}{\partial P_1 \partial s_u}\left(A\right) + \frac{\partial}{\partial P_1}\left(B\right)\frac{\partial}{\partial s_u}\left(B\right) + B\frac{\partial^2}{\partial P_1 \partial s_u}\left(B\right) \\
\alpha_{47} &= \frac{1}{2}\frac{\partial^2}{\partial P_1 \partial i_0}\left(\chi^2\right) \\
&= \frac{\partial}{\partial P_1}\left(A\right)\frac{\partial}{\partial i_0}\left(A\right) + A\frac{\partial^2}{\partial P_1 \partial i_0}\left(A\right) + \frac{\partial}{\partial P_1}\left(B\right)\frac{\partial}{\partial i_0}\left(B\right) + B\frac{\partial^2}{\partial P_1 \partial i_0}\left(B\right) \\
\alpha_{48} &= \frac{1}{2}\frac{\partial^2}{\partial P_1 \partial j_0}\left(\chi^2\right) \\
&= \frac{\partial}{\partial P_1}\left(A\right)\frac{\partial}{\partial j_0}\left(A\right) + A\frac{\partial^2}{\partial P_1 \partial j_0}\left(A\right) + \frac{\partial}{\partial P_1}\left(B\right)\frac{\partial}{\partial j_0}\left(B\right) + B\frac{\partial^2}{\partial P_1 \partial j_0}\left(B\right)
\end{aligned}
$$

$$
\begin{aligned}
\alpha_{55} &= \frac{1}{2}\frac{\partial^2}{\partial P_2^2}\left(\chi^2\right) \\
&= \left[\frac{\partial}{\partial P_2}\left(A\right)\right]^2 + A\frac{\partial^2}{\partial P_2^2}\left(A\right) + \left[\frac{\partial}{\partial P_2}\left(B\right)\right]^2 + B\frac{\partial^2}{\partial P_2^2}\left(B\right) \\
\alpha_{56} &= \frac{1}{2}\frac{\partial^2}{\partial P_2 \partial s_u}\left(\chi^2\right) \\
&= \frac{\partial}{\partial P_2}\left(A\right)\frac{\partial}{\partial s_u}\left(A\right) + A\frac{\partial^2}{\partial P_2 \partial s_u}\left(A\right) + \frac{\partial}{\partial P_2}\left(B\right)\frac{\partial}{\partial s_u}\left(B\right) + B\frac{\partial^2}{\partial P_2 \partial s_u}\left(B\right) \\
\alpha_{57} &= \frac{1}{2}\frac{\partial^2}{\partial P_2 \partial i_0}\left(\chi^2\right) \\
&= \frac{\partial}{\partial P_2}\left(A\right)\frac{\partial}{\partial i_0}\left(A\right) + A\frac{\partial^2}{\partial P_2 \partial i_0}\left(A\right) + \frac{\partial}{\partial P_2}\left(B\right)\frac{\partial}{\partial i_0}\left(B\right) + B\frac{\partial^2}{\partial P_2 \partial i_0}\left(B\right) \\
\alpha_{58} &= \frac{1}{2}\frac{\partial^2}{\partial P_2 \partial j_0}\left(\chi^2\right) \\
&= \frac{\partial}{\partial P_2}\left(A\right)\frac{\partial}{\partial j_0}\left(A\right) + A\frac{\partial^2}{\partial P_2 \partial j_0}\left(A\right) + \frac{\partial}{\partial P_2}\left(B\right)\frac{\partial}{\partial j_0}\left(B\right) + B\frac{\partial^2}{\partial P_2 \partial j_0}\left(B\right)
\end{aligned}
$$

$$
\begin{aligned}
\alpha_{66} &= \frac{1}{2}\frac{\partial^2}{\partial s_u^2}\left(\chi^2\right) \\
&= \left[\frac{\partial}{\partial s_u}\left(A\right)\right]^2 + A\frac{\partial^2}{\partial s_u^2}\left(A\right) + \left[\frac{\partial}{\partial s_u}\left(B\right)\right]^2 + B\frac{\partial^2}{\partial s_u^2}\left(B\right) \\
\alpha_{67} &= \frac{1}{2}\frac{\partial^2}{\partial s_u \partial i_0}\left(\chi^2\right) \\
&= \frac{\partial}{\partial s_u}\left(A\right)\frac{\partial}{\partial i_0}\left(A\right) + A\frac{\partial^2}{\partial s_u \partial i_0}\left(A\right) + \frac{\partial}{\partial s_u}\left(B\right)\frac{\partial}{\partial i_0}\left(B\right) + B\frac{\partial^2}{\partial s_u \partial i_0}\left(B\right) \\
\alpha_{68} &= \frac{1}{2}\frac{\partial^2}{\partial s_u \partial j_0}\left(\chi^2\right) \\
&= \frac{\partial}{\partial s_u}\left(A\right)\frac{\partial}{\partial j_0}\left(A\right) + A\frac{\partial^2}{\partial s_u \partial j_0}\left(A\right) + \frac{\partial}{\partial s_u}\left(B\right)\frac{\partial}{\partial j_0}\left(B\right) + B\frac{\partial^2}{\partial s_u \partial j_0}\left(B\right)
\end{aligned}
$$

$$
\begin{aligned}
\alpha_{77} &= \frac{1}{2}\frac{\partial^2}{\partial i_0^2}\left(\chi^2\right) \\
&= \left[\frac{\partial}{\partial i_0}\left(A\right)\right]^2 + A\frac{\partial^2}{\partial i_0^2}\left(A\right) + \left[\frac{\partial}{\partial i_0}\left(B\right)\right]^2 + B\frac{\partial^2}{\partial i_0^2}\left(B\right) \\
\alpha_{78} &= \frac{1}{2}\frac{\partial^2}{\partial i_0 \partial j_0}\left(\chi^2\right) \\
&= \frac{\partial}{\partial i_0}\left(A\right)\frac{\partial}{\partial j_0}\left(A\right) + A\frac{\partial^2}{\partial i_0 \partial j_0}\left(A\right) + \frac{\partial}{\partial i_0}\left(B\right)\frac{\partial}{\partial j_0}\left(B\right) + B\frac{\partial^2}{\partial i_0 \partial j_0}\left(B\right)
\end{aligned}
$$

$$
\begin{aligned}
\alpha_{88} &= \frac{1}{2}\frac{\partial^2}{\partial j_o^2}\left(\chi^2\right) \\
&= \left[\frac{\partial}{\partial j_0}\left(A\right)\right]^2 + A\frac{\partial^2}{\partial j_o^2}\left(A\right) + \left[\frac{\partial}{\partial j_0}\left(B\right)\right]^2 + B\frac{\partial^2}{\partial j_o^2}\left(B\right)
\end{aligned} \tag{C.10}
$$

with partial derivatives,

$$\frac{\partial^2}{\partial f^2}(A) = 0$$
$$\frac{\partial^2}{\partial f^2}(B) = 0$$
$$\frac{\partial^2}{\partial f \partial z}(A) = x/z^2$$
$$\frac{\partial^2}{\partial f \partial z}(B) = y/z^2$$
$$\frac{\partial^2}{\partial f \partial K_1}(A) = 0$$
$$\frac{\partial^2}{\partial f \partial K_1}(B) = 0$$
$$\frac{\partial^2}{\partial f \partial K_2}(A) = 0$$
$$\frac{\partial^2}{\partial f \partial K_2}(B) = 0$$
$$\frac{\partial^2}{\partial f \partial P_1}(A) = 0$$
$$\frac{\partial^2}{\partial f \partial P_1}(B) = 0$$
$$\frac{\partial^2}{\partial f \partial P_2}(A) = 0$$
$$\frac{\partial^2}{\partial f \partial P_2}(B) = 0$$
$$\frac{\partial^2}{\partial f \partial s_u}(A) = 0$$
$$\frac{\partial^2}{\partial f \partial s_u}(B) = 0$$
$$\frac{\partial^2}{\partial f \partial i_0}(A) = 0$$
$$\frac{\partial^2}{\partial f \partial i_0}(B) = 0$$
$$\frac{\partial^2}{\partial f \partial j_0}(A) = 0$$
$$\frac{\partial^2}{\partial f \partial j_0}(B) = 0$$

$$\frac{\partial^2}{\partial z^2}(A) = -2fx/z^3$$
$$\frac{\partial^2}{\partial z^2}(B) = -2fy/z^3$$
$$\frac{\partial^2}{\partial z \partial K_1}(A) = 0$$
$$\frac{\partial^2}{\partial z \partial K_1}(B) = 0$$
$$\frac{\partial^2}{\partial z \partial K_2}(A) = 0$$
$$\frac{\partial^2}{\partial z \partial K_2}(B) = 0$$
$$\frac{\partial^2}{\partial z \partial P_1}(A) = 0$$
$$\frac{\partial^2}{\partial z \partial P_1}(B) = 0$$
$$\frac{\partial^2}{\partial z \partial P_2}(A) = 0$$
$$\frac{\partial^2}{\partial z \partial P_2}(B) = 0$$
$$\frac{\partial^2}{\partial z \partial s_u}(A) = 0$$
$$\frac{\partial^2}{\partial z \partial s_u}(B) = 0$$
$$\frac{\partial^2}{\partial z \partial i_0}(A) = 0$$
$$\frac{\partial^2}{\partial z \partial i_0}(B) = 0$$
$$\frac{\partial^2}{\partial z \partial j_0}(A) = 0$$
$$\frac{\partial^2}{\partial z \partial j_0}(B) = 0$$

$$\frac{\partial^2}{\partial K_1^2}(A) = 0$$
$$\frac{\partial^2}{\partial K_1^2}(B) = 0$$
$$\frac{\partial^2}{\partial K_1 \partial K_2}(A) = 0$$
$$\frac{\partial^2}{\partial K_1 \partial K_2}(B) = 0$$
$$\frac{\partial^2}{\partial K_1 \partial P_1}(A) = 0$$
$$\frac{\partial^2}{\partial K_1 \partial P_1}(B) = 0$$
$$\frac{\partial^2}{\partial K_1 \partial P_2}(A) = 0$$
$$\frac{\partial^2}{\partial K_1 \partial P_2}(B) = 0$$
$$\frac{\partial^2}{\partial K_1 \partial s_u}(A) = -u_d(r^2 + 2u_d^2)/s_u$$
$$\frac{\partial^2}{\partial K_1 \partial s_u}(B) = -2v_d u_d^2/s_u$$
$$\frac{\partial^2}{\partial K_1 \partial i_0}(A) = -d_u(r^2 + 2u_d^2)/s_u$$
$$\frac{\partial^2}{\partial K_1 \partial i_0}(B) = -2d_u v_d u_d/s_u$$
$$\frac{\partial^2}{\partial K_1 \partial j_0}(A) = -2d_v v_d u_d$$
$$\frac{\partial^2}{\partial K_1 \partial j_0}(B) = -d_v(r^2 + 2v_d^2)$$

$$\frac{\partial^2}{\partial K_2^2}(A) = 0$$
$$\frac{\partial^2}{\partial K_2^2}(B) = 0$$
$$\frac{\partial^2}{\partial K_2 \partial P_1}(A) = 0$$
$$\frac{\partial^2}{\partial K_2 \partial P_1}(B) = 0$$
$$\frac{\partial^2}{\partial K_2 \partial P_2}(A) = 0$$
$$\frac{\partial^2}{\partial K_2 \partial P_2}(B) = 0$$
$$\frac{\partial^2}{\partial K_2 \partial s_u}(A) = -u_d(r^4 + 4u_d^2 r^2)/s_u$$
$$\frac{\partial^2}{\partial K_2 \partial s_u}(B) = -4v_d u_d^2 r^2/s_u$$
$$\frac{\partial^2}{\partial K_2 \partial i_0}(A) = -d_u(r^4 + 4u_d^2 r^2)/s_u$$
$$\frac{\partial^2}{\partial K_2 \partial i_0}(B) = -4d_u v_d u_d r^2/s_u$$
$$\frac{\partial^2}{\partial K_2 \partial j_0}(A) = -4d_v v_d u_d r^2$$
$$\frac{\partial^2}{\partial K_2 \partial j_0}(B) = -d_v(r^4 + 4v_d^2 r^2)$$

$$\frac{\partial^2}{\partial P_1^2}(A) = 0$$
$$\frac{\partial^2}{\partial P_1^2}(B) = 0$$
$$\frac{\partial^2}{\partial P_1 \partial P_2}(A) = 0$$
$$\frac{\partial^2}{\partial P_1 \partial P_2}(B) = 0$$
$$\frac{\partial^2}{\partial P_1 \partial s_u}(A) = -2u_d v_d/s_u$$
$$\frac{\partial^2}{\partial P_1 \partial s_u}(B) = -2u_d^2/s_u$$
$$\frac{\partial^2}{\partial P_1 \partial i_0}(A) = -2d_u v_d/s_u$$
$$\frac{\partial^2}{\partial P_1 \partial i_0}(B) = -2d_u u_d/s_u$$
$$\frac{\partial^2}{\partial P_1 \partial j_0}(A) = -2d_v u_d$$
$$\frac{\partial^2}{\partial P_1 \partial j_0}(B) = -6d_v v_d$$

$$
\begin{aligned}
&\frac{\partial^2}{\partial P_2^2}(A) = 0 && \frac{\partial^2}{\partial s_u^2}(A) = (2L_0u_d + 10L_1u_d^3 + 8K_2u_d^5 + 4P_1u_dv_d + 18P_2u_d^2)/s_u^2\\
&\frac{\partial^2}{\partial P_2^2}(B) = 0 && \frac{\partial^2}{\partial s_u^2}(B) = (6L_1v_du_d^2 + 8K_2v_du_d^4 + 4P_2u_dv_d + 6P_1u_d^2)/s_u^2\\
&\frac{\partial^2}{\partial P_2\partial s_u}(A) = -6u_d^2/s_u && \frac{\partial^2}{\partial s_u\partial i_0}(A) = d_u(L_0 + 8L_1u_d^2 + 8K_2u_d^4 + 2P_1v_d + 12P_2u_d)/s_u^2\\
&\frac{\partial^2}{\partial P_2\partial s_u}(B) = -2v_du_d/s_u && \frac{\partial^2}{\partial s_u\partial i_0}(B) = d_u(4L_1v_du_d + 8K_2v_du_d^3 + 2P_2v_d + 4P_1u_d)/s_u^2\\
&\frac{\partial^2}{\partial P_2\partial i_0}(A) = -6d_uu_d/s_u && \frac{\partial^2}{\partial s_u\partial j_0}(A) = d_v(2L_1v_du_d + 8K_2v_du_d^3 + 2P_1u_d)/s_u\\
&\frac{\partial^2}{\partial P_2\partial i_0}(B) = -2d_uv_d/s_u && \frac{\partial^2}{\partial s_u\partial j_0}(B) = d_v(2L_1u_d^2 + 8K_2v_d^2u_d^2 + 2P_2u_d)/s_u\\
&\frac{\partial^2}{\partial P_2\partial j_0}(A) = -2d_vv_d &&\\
&\frac{\partial^2}{\partial P_2\partial j_0}(B) = -2d_vu_d &&
\end{aligned}
$$

$$
\begin{aligned}
&\frac{\partial^2}{\partial i_0^2}(A) = d_u^2(6L_1u_d + 8K_2u_d^3 + 6P_2)/s_u^2 && \frac{\partial^2}{\partial j_o^2}(A) = d_v^2(2L_1u_d + 8K_2u_dv_d^2 + 2P_2)\\
&\frac{\partial^2}{\partial i_0^2}(B) = d_u^2(2L_1v_d + 8K_2u_d^2 + 2P_1)/s_u^2 && \frac{\partial^2}{\partial j_o^2}(B) = d_v^2(6L_1v_d + 8K_2v_d^3 + 6P_1)\\
&\frac{\partial^2}{\partial i_0\partial j_0}(A) = d_ud_v(2L_1v_d + 8K_2v_du_d^2 + 2P_1)/s_u &&\\
&\frac{\partial^2}{\partial i_0\partial j_0}(B) = d_ud_v(2L_1u_d + 8K_2u_dv_d^2 + 2P_2)/s_u &&
\end{aligned}
\tag{C.11}
$$

Appendix D

Natural Vibration Modes of Acquired 3D Shapes

The first 24 vibration modes of the turbine blade and 12 vibration modes of the Renault R5 timing belt cover are presented here below uncommented. These results were obtained with a Finite Element Analysis program study of the acquired 3D shapes in LOME.

This page intentionally left blank.

Turbine Blade

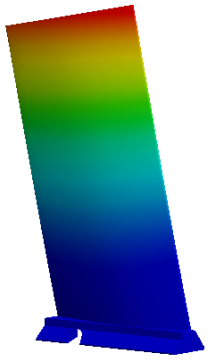

- 1^{st} mode at 460.58 Hz.

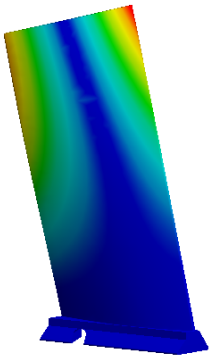

- 2^{nd} mode at 1815.40 Hz.

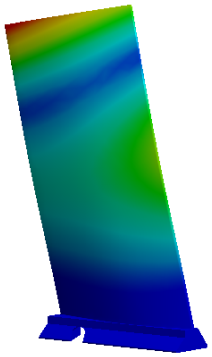

- 3^{rd} mode at 2150 Hz.

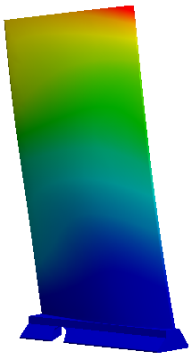

- 4^{th} mode at 4263 Hz.

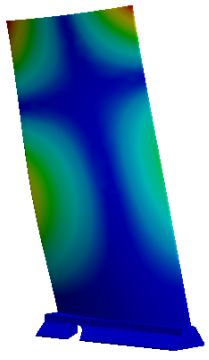

- 5^{th} mode at 4683 Hz.

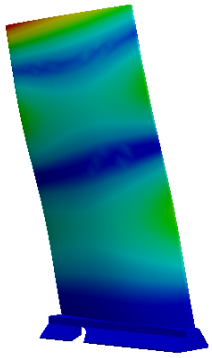

- 6^{th} mode at 5385 Hz.

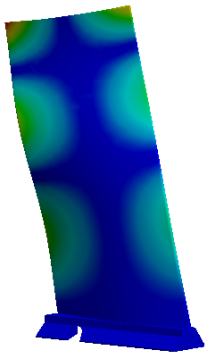

- 7^{th} mode at 8020 Hz.

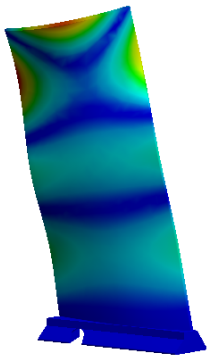

- 8^{th} mode at 9409 Hz.

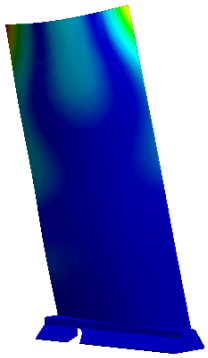

- 9^{th} mode at 10339 Hz.

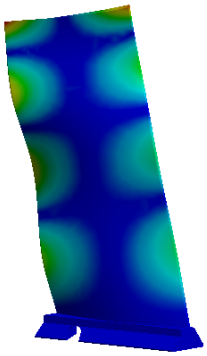

- 10^{th} mode at 12247 Hz.

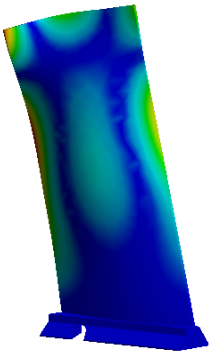

- 11^{th} mode at 14265 Hz.

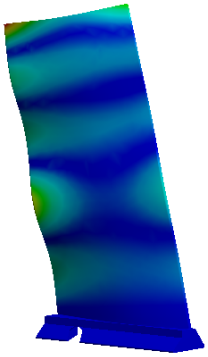

- 12^{th} mode at 15071 Hz.

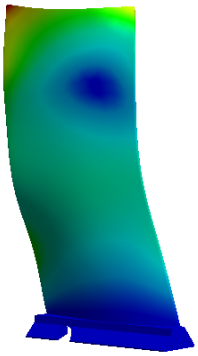

- 13^{th} mode at 16598 Hz.

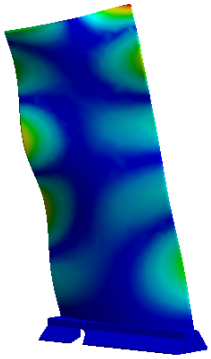

- 14^{th} mode at 17299 Hz.

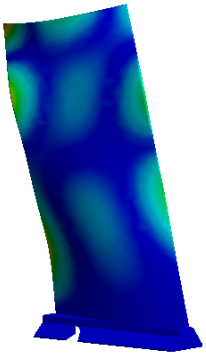

- 15^{th} mode at 17997 Hz.

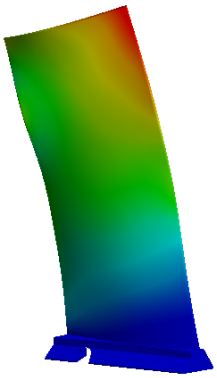

- 16^{th} mode at 18577 Hz.

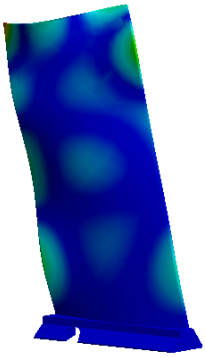

- 17^{th} mode at 21289 Hz.

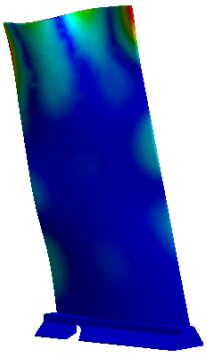

- 18^{th} mode at 22356 Hz.

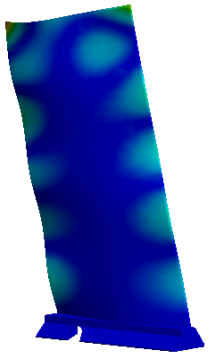

- 19^{th} mode at 23459 Hz.

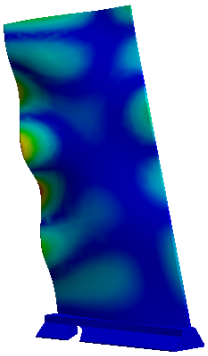

- 20^{th} mode at 24247 Hz.

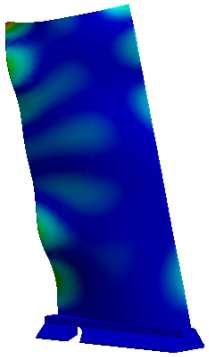

- 21^{st} mode at 28359 Hz.

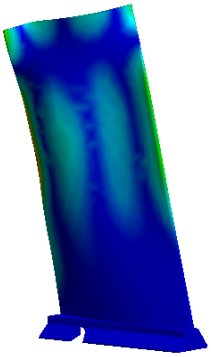

- 22^{nd} mode at 29130 Hz.

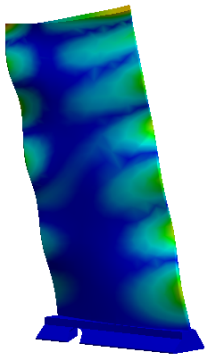

- 23^{rd} mode at 30781 Hz.

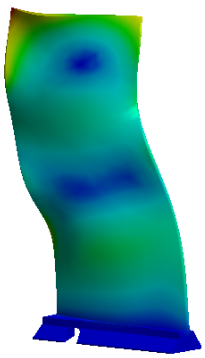

- 24^{th} mode at 31858 Hz.

Timing Belt Cover

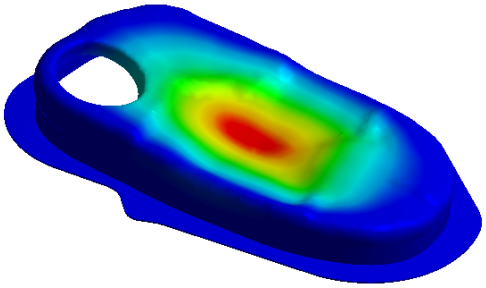

- 1^{st} mode at 677 Hz.

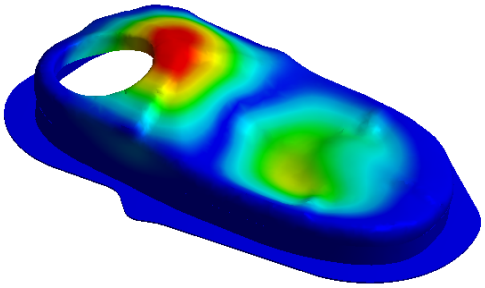

- 2^{nd} mode at 1204 Hz.

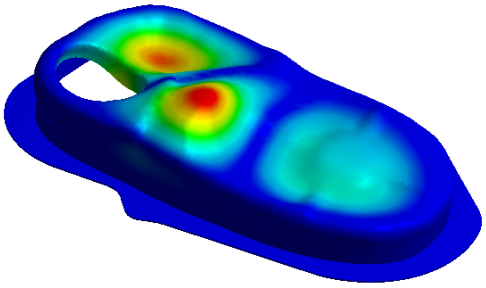

- 3^{rd} mode at 1596 Hz.

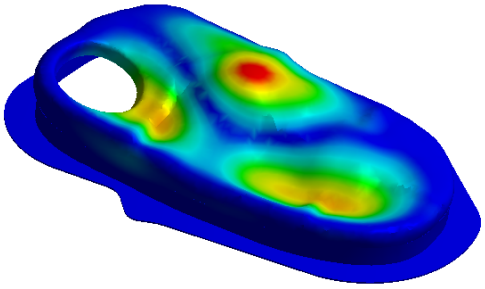

- 4^{th} mode at 1884 Hz.

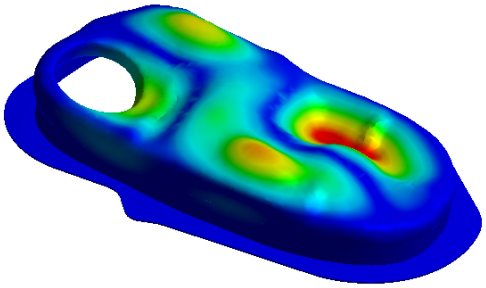

- 5^{th} mode at 2162 Hz.

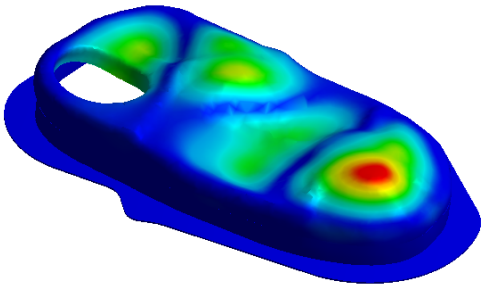

- 6^{th} mode at 2303 Hz.

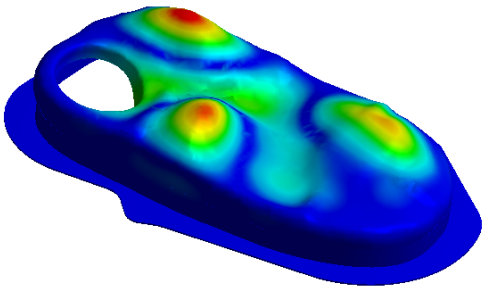

- 7^{th} mode at 2463 Hz.

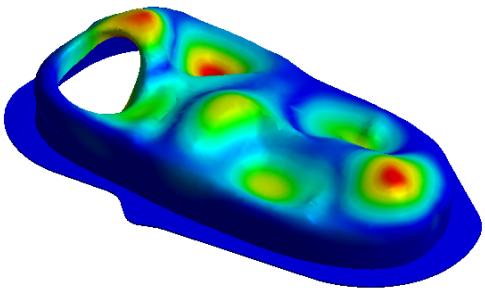

- 8^{th} mode at 2626 Hz.

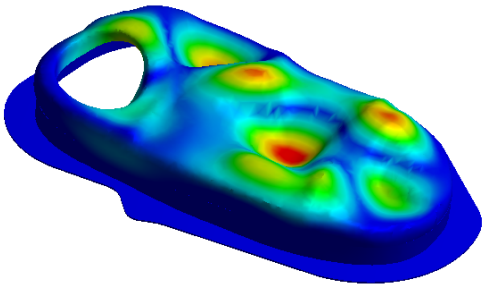

- 9^{th} mode at 2822 Hz.

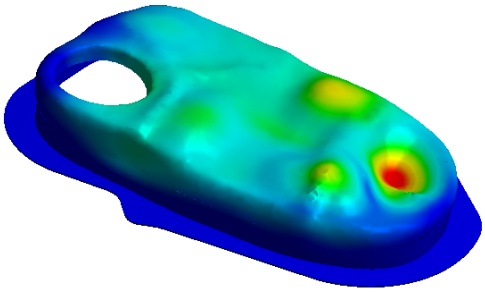

- 10^{th} mode at 2863 Hz.

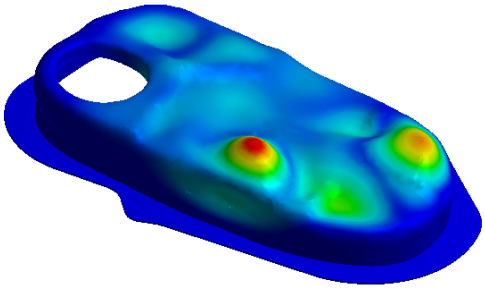

- 11^{th} mode at 3039 Hz.

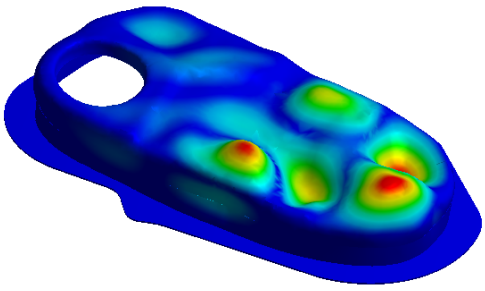

- 12^{th} mode at 3270 Hz.

Appendix E

Publications

The following articles, whether published in scientific journals, presented in a communication or in poster format, represent the most significant publications of the present work.

This page intentionally left blank.

E.1 Orthogonal Projection Technique for Resolution Enhancement of the Fourier Transform Fringe Analysis Method

This page intentionally left blank.

Available online at www.sciencedirect.com
ScienceDirect
Optics Communications 266 (2006) 465–468
OPTICS COMMUNICATIONS
www.elsevier.com/locate/optcom

Orthogonal projection technique for resolution enhancement of the Fourier transform fringe analysis method

Paulo J. Tavares [a,*], Mário A. Vaz [b]

[a] Prudente & Tavares, Technical Consulting, Edifício Península, E# 305, Praça do Bom Sucesso 127, 4150-146 Porto, Portugal
[b] Mechanical Engineering Department, Engineering Faculty, Porto University, Portugal

Received 4 April 2006; received in revised form 3 May 2006; accepted 5 May 2006

Abstract

The spatial resolution of the phase map in the Fourier transform fringe analysis method is determined by the size of the filter's window in frequency domain. This article reports a straightforward technique to improve the method's resolution by a factor of nearly two. The technique requires capturing a second image with a fringe pattern orthogonal to the first one, therefore using the information from both patterns to eliminate the central component in frequency space. The resulting spectrum supports double sized filter windows for removal of the carrier frequency without leaking into adjacent orders. The overall spatial resolution of the method is thus increased. In the following, the Fourier fringe analysis method is briefly reviewed, the new technique is described and analyzed and the experimental results are shown and discussed.

Keywords: Three-dimensional measurement; Shape measurement; Optical metrology; Profilometry; Fringe projection; Structured light

1. Introduction

The Fourier transform fringe analysis method is one of the most successful techniques for fringe pattern analysis. First introduced by Takeda [1] in 1982, the technique was adapted to two-dimensions by Macy [2], although that was essentially a one-dimensional extension of the original work by Takeda. Bone [3], provided a full 2D version in 1986, along with a set of very interesting observations regarding the inherent errors of the technique and some suggestions about how these could be overcome. Several other works have been published throughout the years, as this method remains one of the simplest and more effective methods for shape measurement. Another important reason is its dependence on one frame only, contrary to the phase shift methods that need three frames at the very least. This makes it the only method capable of dealing with dynamic situations where the target object moves and taking three frames becomes prohibitive.

The technique can be simply described as follows: a fringe pattern with a known spatial frequency is projected onto the object under test and a two-dimensional Fourier transform of the resulting image is calculated. The spectrum that results from this fringe projection has two sharp peaks, centered at the carrier fringe frequency. In order to remove this carrier and thus obtain an expression of the phase variation, proportional to the object profile at each image point, a certain amount of frequencies surrounding the carrier are filtered with a suitable window. This window is then moved to the center of the spectrum, and an inverse Fourier transform of those selected frequencies is calculated. This inverse transform holds the phase information which can finally be calculated by the logarithm of a simple inverse tangent calculation.

The method is simple and effective, yet plagued with many error sources. One of the most important is the error that results from the fact that the frequencies spread out to infinity in frequency space, and a too wide filtering window

* Corresponding author. Tel.: +351 22 508 2151; fax: +351 22 508 1584.
E-mail addresses: gmavaz@fe.up.pt (M.A. Vaz), jtavares@fe.up.pt (P.J. Tavares).

0030-4018/$ - see front matter © 2006 Elsevier B.V. All rights reserved.
doi:10.1016/j.optcom.2006.05.020

is bound to include frequencies that belong to adjacent orders. This is a very stringent constraint, in that the filter size is very limited and a number of high frequencies responsible for the image detail can thus be lost. What we propose herein, is a simple technique to eliminate the zero-order in frequency space and widen the filter window size to approximately twice the maximum admissible size without including adjacent orders. The resolution enhancement so obtained is near to double the original's method.

2. Analysis

A sinusoidal fringe pattern projected onto an object, as shown in Fig. 1, is adequately described by

$$g_1(x,y) = a(x,y) + b(x,y)\cos[2\pi f_0 x + \phi(x,y)] \tag{1}$$

where $a(x,y)$ and $b(x,y)$ represent non-uniform distributions of reflectivity on the surface of the object, f_0 is the fundamental frequency of the observed grating image and $\phi(x,y)$ is the phase modulation resulting from the object height distribution.

For convenience of analysis, this fringe pattern can be rewritten as

$$g_1(x,y) = a(x,y) + c(x,y)\exp[2\pi \mathrm{j} f_0 x] + c^*(x,y)\exp[-2\pi \mathrm{j} f_0 x] \tag{2}$$

with the understanding that,

$$c(x,y) = \frac{b(x,y)\exp[\mathrm{j}\phi(x,y)]}{2} \tag{3}$$

and $*$ denotes complex conjugation.

The Fourier transform of the deformed fringe pattern, shown in Fig. 2, is,

$$G_1(u,v) = A(u,v) + C(u - f_0, v) + C^*(u + f_0, v) \tag{4}$$

A second fringe pattern projected over the object, with fringes orthogonal to the first fringe pattern, Fig. 3 can be described by,

$$g_2(x,y) = a(x,y) + c(x,y)\exp[2\pi \mathrm{j} f_0 y] + c^*(x,y)\exp[-2\pi \mathrm{j} f_0 y] \tag{5}$$

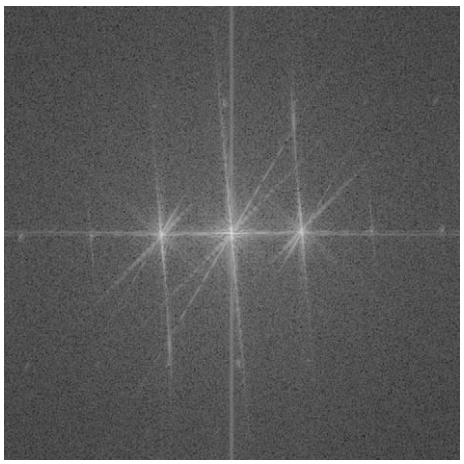

Fig. 2. Object Fourier spectrum.

and its Fourier transform by,

$$G_2(u,v) = A(u,v) + C(u, v - f_0) + C^*(u, v + f_0) \tag{6}$$

The phase, $\phi(x,y)$, which depends only on the object height at each (x,y) point and the structural parameters of the crossed optical axes geometry, remains unchanged, as do $a(x,y)$ and $b(x,y)$ if the contrast and gain of the two fringe patterns is kept constant and the background intensity variation under control. It is clear from Eqs. (4) and (6) and Figs. 2 and 4 that the DC or zero-order component is identical in both spectra.

In order to enforce minimum background intensity variations, and if the problem allows taking more than just one image, several recordings of the deformed fringe pattern can be made and a weighted average calculated, thus eliminating spurious background variations.

An added benefit of the orthogonal projection technique is the total removal of these constraints, for if the two spectra are subtracted, the obtained spectrum is,

$$G_1(u,v) - G_2(u,v) = C(u - f_0, v) - C(u, v - f_0) + C^*(u + f_0, v) - C^*(u, v + f_0) \tag{7}$$

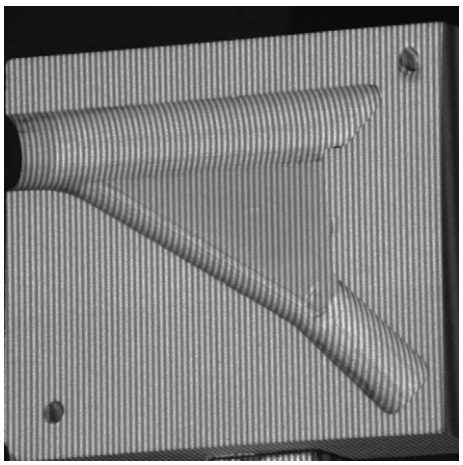

Fig. 1. Projected fringe pattern.

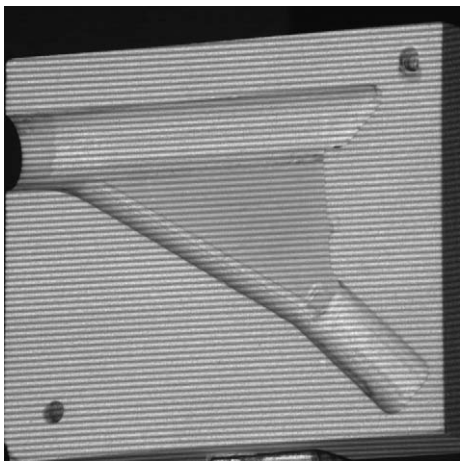

Fig. 3. Orthogonally projected fringe pattern.

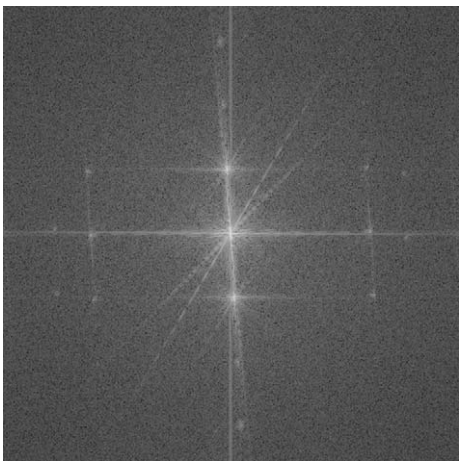

Fig. 4. Object Fourier spectrum – Orthogonal projection.

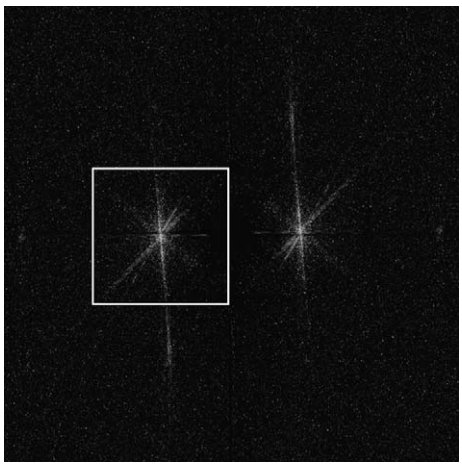

Fig. 5. Clipped spectra after subtraction for removal of carrier frequency.

thus totally eliminating the DC or central component in frequency space. Now the resulting spectrum is digitally manipulated in order to clip the negative going values, i.e., all values below a zero threshold, as seen in Fig. 5,

$$C(u - f_0, v) + C^*(u + f_0, v) \tag{8}$$

Even if there is some variation on the background illumination leading to a different contrast of the second fringe pattern, $b_2(x,y)$, this will be totally eliminated on this clipping operation. Other techniques to improve the method's resolution, such as the "π phase shifting technique" introduced by Su [4], rely on a constant fringe contrast between two consecutive images, which hardly ever occurs.

The usual FTP filtering and centering operations can now be performed on one of the side lobes, say $C(u - f_0, v)$, by first isolating it with a suitable filter window centered at f_0 and then removing the carrier frequency altogether by moving it to the center of the spectrum. The fact there isn't a DC term anymore, allows using a double sized filter window without leaking into the zero order, thus doubling the range of selected frequencies and improving the method's resolution by a factor of two (see Fig. 5).

The resulting spectrum is,

$$G(u, v) = C(u, v) \tag{9}$$

with an inverse Fourier transform equal to

$$g(x, y) = c(x, y) = \frac{b(x, y)\exp[\mathrm{j}\phi(x, y)]}{2} \tag{10}$$

As usual also, the wrapped phase, shown in Fig. 6, is given by,

$$\phi(x, y) = \tan^{-1}\left[\frac{\mathrm{Im}(c(x, y))}{\mathrm{Re}(c(x, y))}\right] \tag{11}$$

3. Results and discussion

The sinusoidal 0.75 fringes/mm pattern used on the previous images was calculated on a PC and projected onto the object using an InFocus LP-70 DLP video projector. The images were captured with an 8 bit ES 1.0 Kodak CCD and a Matrox Genesis frame grabber and stored for processing.

Fig. 6. Obtained phase.

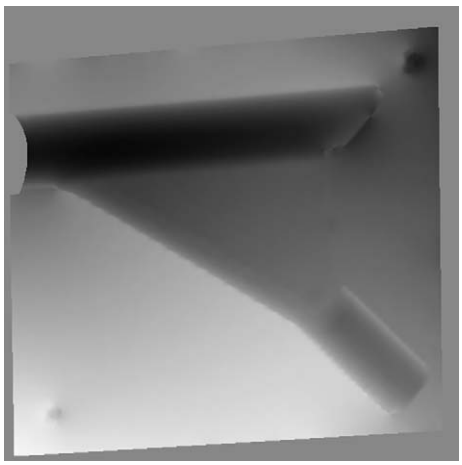

Fig. 7. Unwrapped phase map.

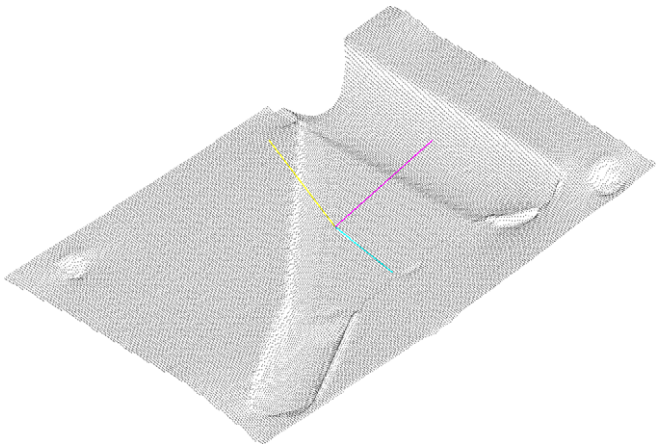

Fig. 8. 3D point cloud.

It is clear from the analysis of the previous images that the advantage of the proposed technique is the use of a much larger window for the removal of the carrier frequency. Theoretically, the filter's window size can be made as big as twice the carrier frequency, f_0, (cf. Fig. 5) before the two remaining terms overlap.

The wrapped phase map, once obtained, can be demodulated using any unwrapping technique, though we found the Volkov [5] deterministic phase unwrapping method to perform well under most circumstances. Figs. 7 and 8 represent the unwrapped phase map and the three dimensions cloud point obtained with the previous object.

4. Conclusions

The Fourier transform profilometry method for 3D surface measurement has become very popular due to the fact that it is inherently simple, standing out as the only method applicable to dynamic situations because it relies on one image only. One of the method's chief restrictions is the limited resolution, due to the well known leakage artifact from the application of FFTs and the constraint it imposes on the carrier removal filter size.

The method presented in this note removes this limitation to a great extent, by eliminating the central DC frequency component in frequency space, thus allowing the filter's size to be twice the carrier frequency.

Acknowledgement

The authors wish to thank INEGI – Instituto Nacional de Engenharia e Gestão Industrial for supporting the current work.

References

[1] M. Takeda, H. Ina, et al., Journal of the Optical Society of America 72 (1) (1982) 156.
[2] W.W. Macy, Applied Optics 22 (23) (1983) 3898.
[3] D.J. Bone, H.A. Bachor, et al., Applied Optics 25 (10) (1986) 1653.
[4] X.Y. Su, W.J. Chen, Optics and Lasers in Engineering 35 (5) (2001) 263.
[5] V.V. Volkov, Y.M. Zhu, Optics Letters 28 (22) (2003) 2156.

E.2 Coherent Fringe Projector for 3d Surface Profilometry - Optical Metrology. München 2006

This page intentionally left blank.

COHERENT FRINGE PROJECTOR FOR 3D SURFACE PROFILOMETRY

Paulo Tavares member SPIE, Nuno Viriato, Jorge Reis, and Mário Vaz member SPIE,
LOME – Optics and Experimental Mechanics Laboratory
Engineering Faculty. Porto University
Rua Dr. Roberto Frias SN, 4200 - 465, Porto, Portugal
jtavares@fe.up.pt, nviriato@fe.up.pt, jmreis@fe.up.pt, gmavaz@fe.up.pt

ABSTRACT: Active image processing full field methods for 3D contactless profilometry are amongst the current methods of choice for obtaining point clouds from object surfaces. The fringe projection system plays a decisive role on the entire process, significantly impacting both quality and reliability of the final measurements. Moreover, most every phase measurement profilometer can only be used under laboratory controlled lighting environments. This note describes the ongoing LOME project for a coherent fringe projection system which will enable outdoor measurements by selectively band pass filtering the projected wavelength.

Keywords: three-dimensional measurement; shape measurement; optical metrology; profilometry; fringe projection; structured light

INTRODUCTION

A vast number of optical 3D measuring techniques have been developed in recent years [1]. Amongst them, the full field active techniques that rely on structured lighting stand out from the rest by their robustness and flexibility. The use of projected square or sinusoidal fringes for phase recovery and shape measurement is thus a well established technique [2]. Basically, it consists on projecting a fringe field over a surface and measuring the deformations produced by the surface topology on the projected fringes. The fringe pattern's phase varies across the image, relative to the original pattern, as a function of the surface topology, which can then be determined as soon as the phase variation is calculated.

These techniques require a high throughput completely addressable fringe projection system. Originally created with coherent light interferometry, by shedding a sinusoidal fringe pattern that resulted from the superposition of reference and object beams [2], the technique was soon to be found awkward with the introduction of fully addressable spatial light modulators such as video projectors. These are either based on Liquid Cristal Displays (LCD) or Digital Light Processing (DLP) technologies and are currently being used for Phase Measurement Profilometry, be it Phase Shift (PSM) or Fourier Transform Profilometry (FTP) [3], or digital encoding such as the Gray Code Method (GCM) [4, 5].

Dedicated commercial devices with appreciable resolutions can now be found, most notably the LCP projector by BIAS and Jenoptik [6].

Still, and to the authors knowledge, all the developed devices to date, apart from the original interferometers, use incoherent lighting, most likely due to the unavailability of coherent sources with sufficient power. The advantages of using coherent light are twofold: the first is a dramatic reduction of heat inside the projector case, which otherwise requires special measures to protect both the optics and the electronic components, such as heat deflectors and other protections; the second advantage, which is the most noticeable, is the fact that temporally coherent light can be filtered with a very high efficiency up to a few nm around a central wavelength. This provides the basis for using structured lighting outside of laboratory controlled conditions and is in fact the sufficient condition for use in broad day light, should the laser power be enough. Up until very recently, miniaturized lasers didn't generate enough power to handle these requirements. With the advent of compact laser sources, such as the one used in this work, this possibility becomes real.

DESIGN

The laser source used in this work is a 60 mW, 532 nm DPSS laser source which was developed for this project. The source was designed with an output beam divergence of 30º in order to fill the useful area of a 2 inch condenser group at 86 mm. It consists on a 2 W, 808 nm C-Mount diode laser pump, a Diode Pumped Microchip (DPM) laser crystal combining a Nd:YvO_4 crystal and a KTP frequency doubler, and a GRIN lens. The DPM1102 module from CASIX is in fact an optically bonded hybrid crystal, which endures much higher powers than previous optically cemented KTP to Nd:YvO_4 crystals. According to CASIX, optical bonding is based on diffusion. The crystals are permanently bonded by heating to a high temperature under pressure resulting in a chemical exchange of molecules at the interface. Even so, there seems to be an ongoing discussion about the properties of these DPM modules, as can be seen in [7].

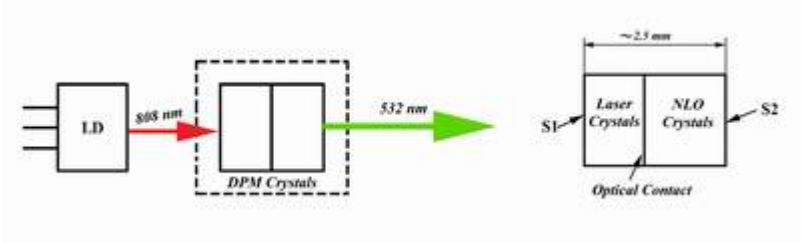

Fig. 1 - High power DPM laser modules

In order to achieve alignment of the C-Mount pumping diode and the DPM crystal, an XYZ micropositioner was modified to accommodate tilt, as can be seen in Fig. 2. Accurate positioning is very important due to the fact these laser modules have a rather high sweet spot.

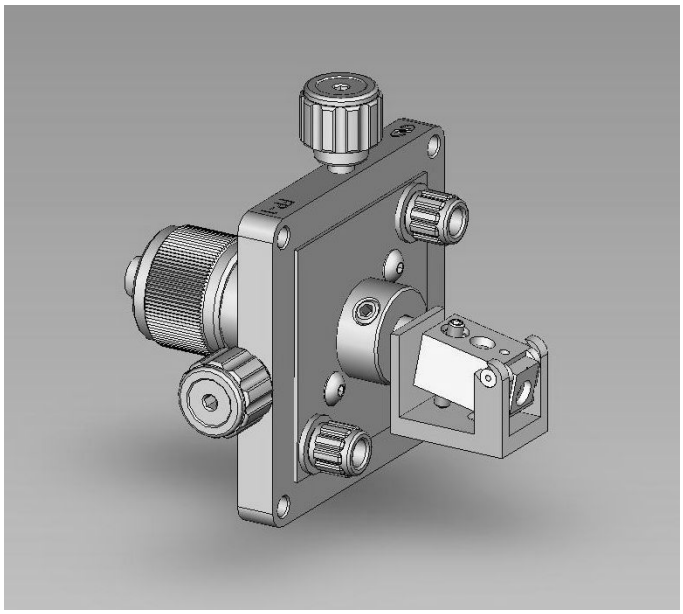

Fig. 2 – C-Mount laser diode positioning

The green, 532 nm, beam has a very small divergence at the KTP output side. In order to fill a 2 inch condenser group at a reasonably small distance, the required beam divergence was calculated at 30º, which in turn involved using a very short focal distance focusing lens. We have used a PCH022 GRIN lens from CASIX with a 1mm focal distance at 45 mm from the KTP exit as shown in Fig. 3.

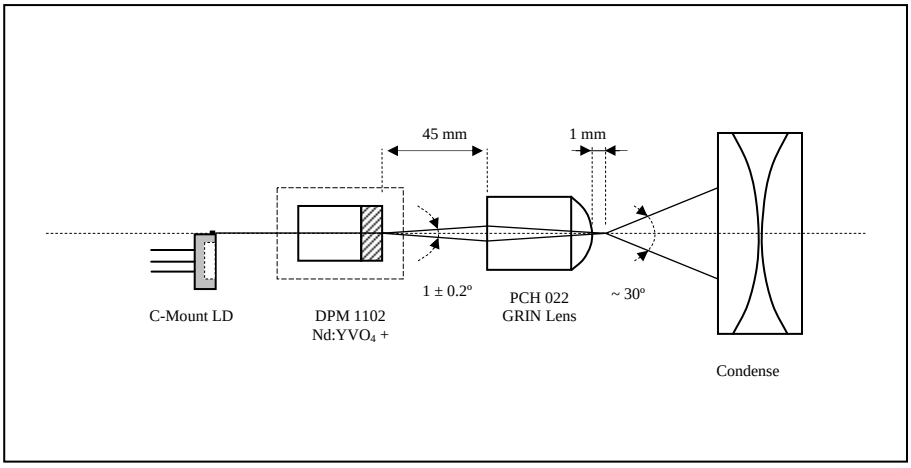

Fig. 3 – Beam forming schematics

The condenser group was calculated having in mind a versatile projection group such as an F-Mount Nikon objective with a typical 46.5 mm back focal distance. Ray tracing the entire optics assembly, from the GRIN lens forward, is shown in Fig. 4. The condenser group comprises two 50 mm diameter plano-convex lenses with an 80 mm focal distance, convex sides apposed, for a better control of spherical aberration.

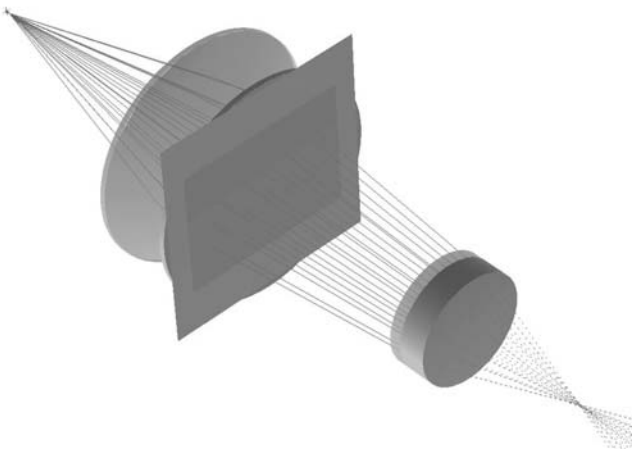

Fig. 4 – Ray tracing study of the condenser and projection groups.

The Spatial Light Modulator (SLM) used herein was a XGA1 twisted nematic LCD from CRL with a 1024x768 VGA resolution. The entire assembly project can be seen in Fig. 5 and an exploded view of the laser stage in Fig. 6. In case a higher resolution is necessary, the LCD can be rapidly exchanged with a Ronchi ruling.

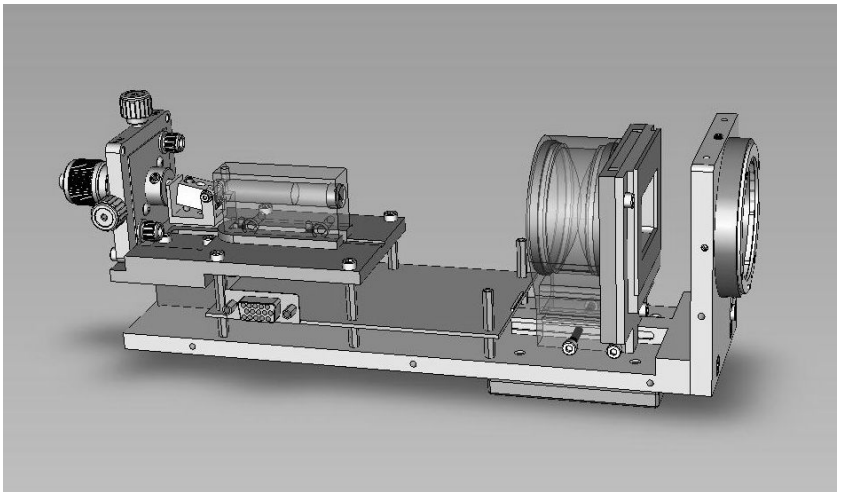

Fig. 5 – Complete assembly

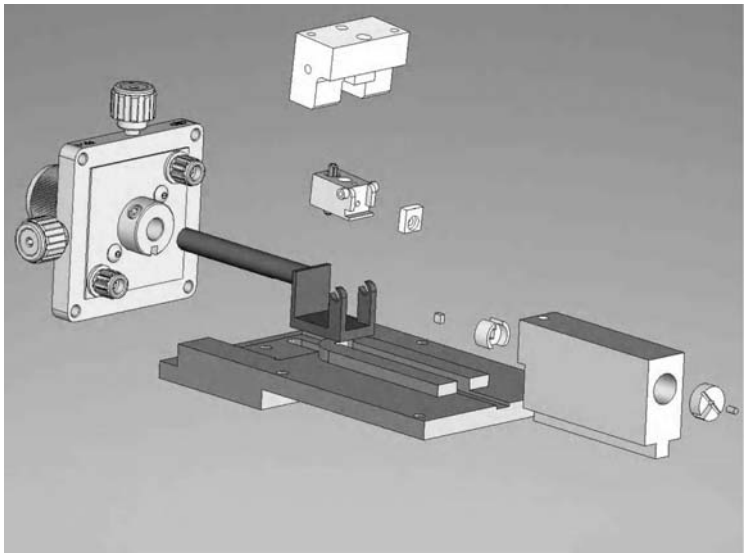

Fig. 6 – Exploded view of the laser assembly

The real model is shown in Figs. 7 and 8. The final footprint of the entire device is 240 x 65 mm, weighting under 800g.

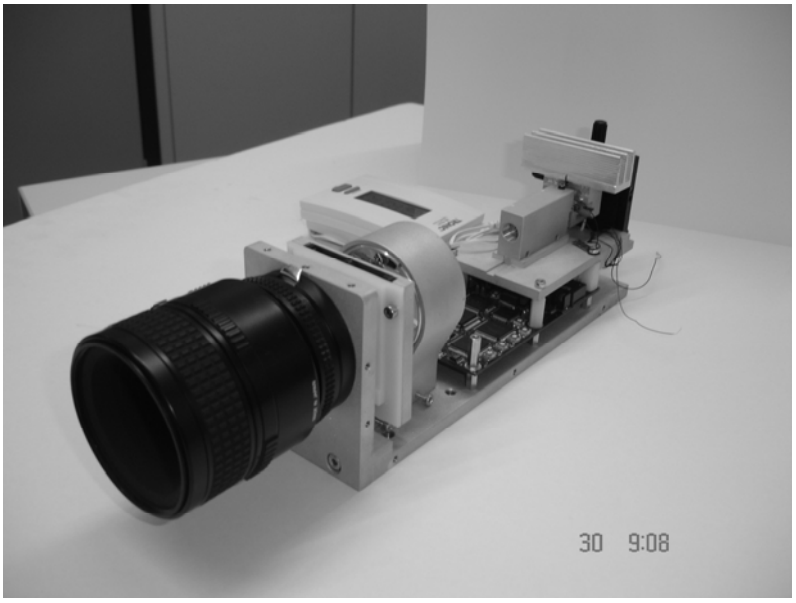

Fig. 7 – The Coherent Fringe Projector

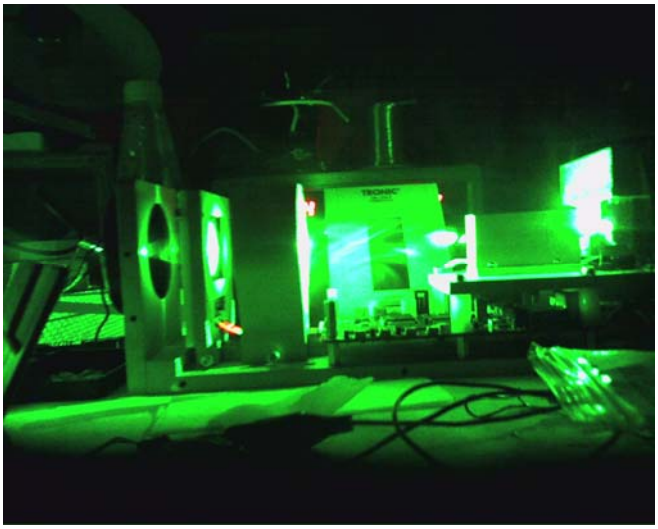

Fig. 8 – The Coherent Fringe Projector in operation

TESTING

Testing was performed with both Temporal Phase Unwrapping, which is basically a Phase-Shift method, and Fourier Transform Profilometry. The object was the same on both experiments – a plaster model which can be seen in the Fig. 9 partially covered by a 256 fringes pattern.

Fig. 9 – Plaster model used in testing with projected fringe for FTP

Calibration of the profilometer was done as described in [8]. This is a two step calibration method wherefore the camera is first XY calibrated and the extrinsic and intrinsic parameters optimized.

The calibration matrices for two different viewing angles of the calibration rig are calculated, as is the phase variation across a plan at these two angles. Phase-to-height is then established from this information.

We have run into several problems related to coherent noise. The fringes produced by every dust particle or even by the GRIN lens aperture show up in projection. In view of the reduced size of the projector, low pass filtering with a pinhole was not feasible. We have opted to destroy spatial coherence by time averaging a speckle translucent film with very satisfactory results. Other problems related to structural stability of the entire device should be corrected in future versions.

Phase Shift

An unwrapped phase map and a shaded mesh of the area in Fig. 9 can be seen in Figs 10 and 11.

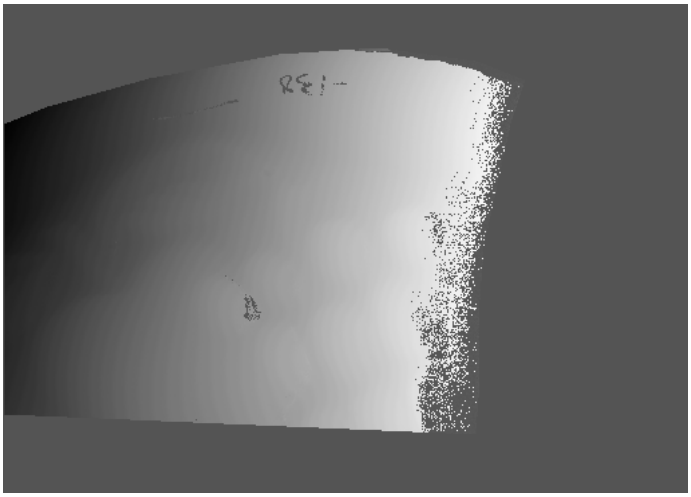

Fig. 10 – Plaster model phase map

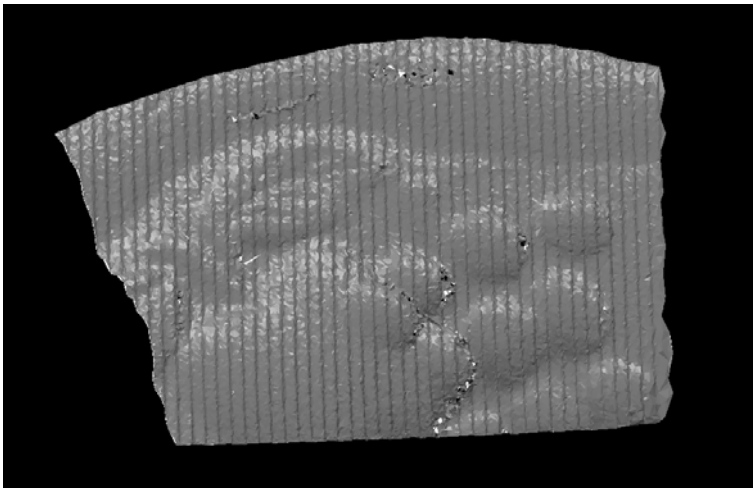

Fig. 11 – 3D Shaded mesh

An over modulation due to a mismatch between the white and the black fringes is apparent in the final 3D mesh.

Fourier Transform

We have used the image in Fig 9. The phase map, both wrapped and unwrapped can be seen in figs 12 and 13, clearly demonstrating the potential of the device.

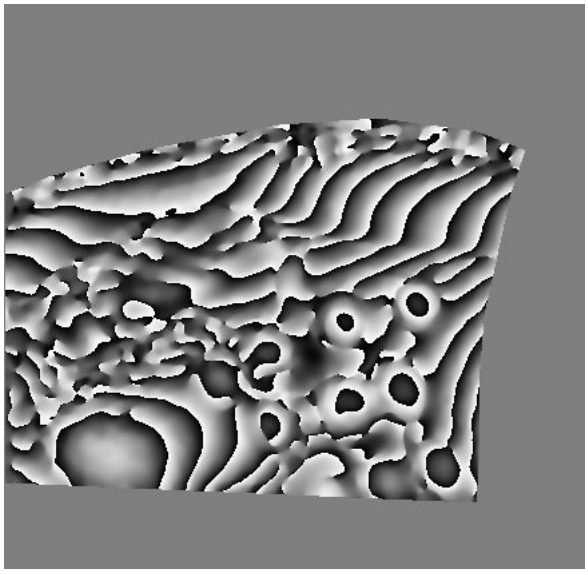

Fig. 12 – Wrapped phase map from FTP

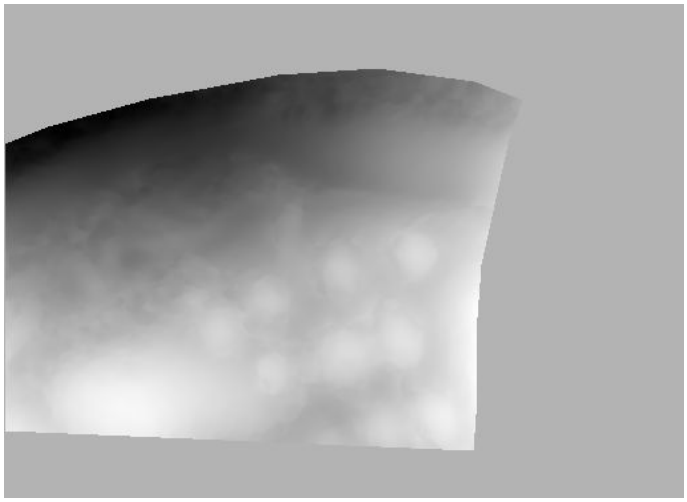

Fig. 13 – Unwrapped phase map from Fig. 12

CONCLUSIONS

Active image processing techniques for 3D shape measurement rely heavily on the quality of the fringe projecting system. An innovative compact design for such a system using a coherent light source was projected and assembled in LOME, and its preliminary version was presented here.

The device will enable the use of phase measurement techniques by fringe projection outside of laboratory controlled lighting. Several problems remain to be solved as project is yet to be completed.

ACKNOWLEDGMENT

This work is being carried out in LOME at DEMEGI and is fully supported by *Instituto Nacional de Engenharia e Gestão Industrial*.

REFERENCES

[1] Chen, F.; Brown, G.; Song, M. (2000): "Overview of three-dimensional shape measurement using optical methods", *Opt. Engineering*, **39**, 10

[2] Creath, K. (1993): "Temporal phase measurement methods", in "*Digital Fringe Pattern Measurement Techniques* eds. D. W. Robinson and G. T. Reid (Bristol: Institute of Physics Publishing), pp 94–140

[3] Takeda, M., H. Ina, et al. (1982): "Fourier-Transform Method of Fringe-Pattern Analysis for Computer-Based Topography and Interferometry." *JOSA* **72**, 1

[4] Horn, E. and Kiryati, N., (1997): "Toward optimal structured light patterns", *Proceedings of the 3-D DIM 1997 International Conference on Recent Advances of 3D Digital Imaging and Modeling*

[5] Sansoni G.; Carocci M.; Lazzari S.; Rodella R., (1998): "A three-dimensional imaging system for industrial applications with improved flexibility and robustness", *Journal of Optics A: Pure and Applied Optics* **1**, 1
[6] Bothe, T.; Osten, W.; Gesierich, A.; Jüptner, W., (2002):"Compact 3D-Camera", *Proc. SPIE* Vol. 4778, , pp. 48-59
[7] Zalevsky, Z. et al (2006): "Self Q-switching effect in a Nd:YVO4/KTP lasing unit", *Opt. Engineering* **45**, 7
[8] Tavares, P. and Vaz, M., (2006): "Orthogonal projection technique for resolution enhancement of the Fourier transform fringe analysis method", *Optics Communications* **266**, 2

E.3 Full Field 3D Profilometry With the Volkov Phase Unwrapping Method - Photo Mechanics 2006, Clermont-Ferrand

This page intentionally left blank.

LOME – Laboratory of Optics and Experimental Mechanics
www.fe.up.pt/~inegi/lome

Full Field 3D Profilometry with the Volkov Phase Unwrapping Method

Tavares, Paulo and Vaz, Mário
LOME - DEMEGI, Faculdade de Engenharia da Universidade do Porto

Phase is a physical parameter bound by $\pm\pi$, whereas object height can exceed π many times over. Unwrapping is the process of calculating a continuous phase by adding $\pm 2\pi$ at every phase transition:

$$\phi(\mathbf{r}) = \phi_w(\mathbf{r}) + 2\pi n(\mathbf{r})$$

The method proposed by Volkov [5] and implemented on our prototype, determines the unwrapped phase exactly by expressing it as a function of the gradient components and finding those components from the wrapped phase map.



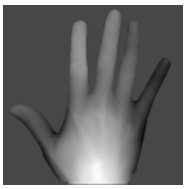

PRINCIPLE

$$\exp(i\phi(\mathbf{r})) = \exp(i\phi_w(\mathbf{r}) + 2\pi i n(\mathbf{r})) = \exp(i\phi_w(\mathbf{r}))$$ (trivial)

$$\nabla(\phi(\mathbf{r})) = 2\pi i \mathcal{F}^{-1}[\mathcal{F}\phi(\mathbf{r})\mathbf{q}]$$ (differentiation theorem for Fourier transforms)

$$\phi(\mathbf{r}) = Re\left\{\frac{1}{2\pi i}\mathcal{F}^{-1}\left[\frac{\mathcal{F}\left(\frac{\partial\phi(\mathbf{r})}{\partial x}\right)q_x + \mathcal{F}\left(\frac{\partial\phi(\mathbf{r})}{\partial y}\right)q_y}{q_x^{\,2} + q_y^{\,2}}\right]\right\}$$ with,

$$\nabla\phi(\mathbf{r}) = Re\left\{\frac{\nabla\left(e^{i\phi(\mathbf{r})}\right)}{ie^{i\phi(\mathbf{r})}}\right\} = \cos\phi_w(\mathbf{r})\nabla(sen\phi_w(\mathbf{r})) - sen\phi_w(\mathbf{r})\nabla(\cos\phi_w(\mathbf{r}))$$

CONCLUSIONS

This result is exact, up to a constant. The method is full-frame and phase at each image pixel is calculated independently from phase at any other point, which means the method is inherently robust to scene discontinuities. The calculation takes approximately 20 s on a Pentium IV computer but can be made much faster with dedicated processing and software optimization.

The use of this technique with Fourier Transform Profilometry, which is a single frame technique, enables a multitude of 3D applications such as dynamic 3D surface reconstruction or surface generation for numerical simulations in structural deformation or damage detection.

SOME RESULTS







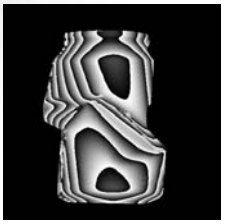

REFERENCES

- Chen, F.; Brown, G.; Song, M. (2000): Overview of three-dimensional shape measurement using optical methods, *Optics Engineering,* **39**, 10
- Saldner, H.O.; Huntley, J. M. (1997): Temporal phase unwrapping: application to surface profiling of discontinuous objects, *Appl. Opt.* **26**, 2770
- Takeda, M.; Ina, H.; Kobayashi, S. (1982): Fourier-transform method of fringe-pattern analysis for computer-based topography and interferometry, *J. Opt. Soc. Am.* **72**, 156
- Ghiglia, D.C.; Pritt, M.D.(1998): *Two-Dimensional Phase Unwrapping: Theory, Algorithms, and Software*
- Volkov, V. V.; Zhu, Y. M. (2003): Deterministic phase unwrapping in the presence of noise, *Optics Letters* **28**, 2156

This page intentionally left blank.

E.4 Linear Calibration Procedure for the Phase-to-height Relationship in Fourier Transform Fringe Analysis

This page intentionally left blank.

Available online at www.sciencedirect.com
ScienceDirect
Optics Communications 274 (2007) 307–314
OPTICS COMMUNICATIONS
www.elsevier.com/locate/optcom

Linear calibration procedure for the phase-to-height relationship in phase measurement profilometry

Paulo J. Tavares [a,*], Mário A. Vaz [b]

[a] Prudente & Tavares, Technical Consulting, Edifício Península, E# 305, Praça do Bom Sucesso 127, 4150-146 Porto, Portugal
[b] Mechanical Engineering Department, Engineering Faculty, Porto University, Portugal

Received 17 October 2006; received in revised form 19 December 2006; accepted 21 February 2007

Abstract

Calibration of the relationship between height and phase is of uttermost importance to perform accurate 3D measurements in phase measurement profilometry. This work reports a different approach to this problem by first looking at the analytical expression for this relationship and determining the regime spanned by the fringe analysis method. The conclusions thus ascertained, amply justify confronting the analytical expression with a simple normalization procedure of the experimental data, with a remarkable matching between both results. In light of this, a linear calibration procedure with just one plane is proposed and verified experimentally.

Keywords: Three-dimensional measurement; Shape measurement; Optical metrology; Profilometry; Fringe projection; Structured light

1. Introduction

Accurate non-contact three-dimensional measurements have drastically influenced physical sensing applications in many areas of knowledge, from industrial production to health care, artwork inspection, robot vision and many other engineering or science activities.

Phase measurement profilometry (PMP), be it phase shift [1] or Fourier transform [2–5], is certainly amongst the most successful three-dimensional active vision techniques available today.

These procedures calculate phase shift mappings of surface deformations or profile-to-reference differences and rely, at some point, on the translation of the obtained phase map to either a dislocation or a height measurement. The relation between phase and height has thus been the subject of a large number of works over the years, due to its impact on the overall method's accuracy. Both analytical [3,6–9] and empirical [10–14] approaches were reported to present days, although an explicit comparison of both trends has not yet been published, to the authors knowledge.

Analytical methods, simple to apply as they may be, rely on a precise determination of the camera and projector locations and do not explicitly account for the distortions of both projection and imaging optics. The latter can become a major issue, in those cases where the aberrations are either unidentified or known to severely impact the final result. The former argument can also be decisive to final accuracy, when even the smallest change between projector and camera positions can result in erroneous measurements.

On the other hand, most of the phase-to-depth empirical calibration methods proposed to date interpolate the results from a set of reference plane dislocations, for each of which a phase map has been calculated. The accuracy of this procedure depends on the precision of the travelling stage that carries the reference plane and is fairly awkward to manoeuvre outside of laboratory installations.

The work depicted herein takes a different view of this issue by looking at the analytical phase-to-depth expression and determining the region of interest along that curve.

* Corresponding author. Tel.: +351 22 508 2151; fax: +351 22 508 1584.
E-mail addresses: jtavares@fe.up.pt (P.J. Tavares), gmavaz@fe.up.pt (M.A. Vaz).

0030-4018/$ - see front matter © 2007 Elsevier B.V. All rights reserved.
doi:10.1016/j.optcom.2007.02.038

The choice of a linear calibration procedure is then strongly supported by the evidence that, for the most part of the plausible working regime, this relation is indeed a linear one. The striking match of the experimental and the analytical results is but another confirmation of these findings, which ultimately led to devising a single image calibration procedure, described and analyzed at the end of the note.

2. Analytical phase-to-depth relation

Fig. 1 depicts a typical optical crossed axis phase measurement profilometry setup. A fringe pattern with a known spatial frequency is projected onto the object under test by projector P and the image is captured at camera C. E_p and E_c refer to the nodal points of the projection and imaging systems, respectively. The projection and imaging systems optical axis cross at point O on a reference plane R_0. L_0 is the distance from the camera – projector plane to the reference plane, d is the distance between centers of projection, θ is the angle between projector and camera and s represents the intersection of E_pB with the object surface.

E_tD represents a telecentric projection through s, adequately described by

$$g_T(x,y) = a(x,y) + b(x,y)\cos[2\pi f_0 x] \tag{1}$$

where $a(x,y)$ and $b(x,y)$ represent non-uniform distributions of reflectivity on the surface of the object and f_0 is the fundamental frequency of the observed grating image.

In the non-telecentric case, the pattern on the reference plane can then be described by

$$g_0(x,y) = a(x,y) + b(x,y)\cos[2\pi f_0 x + \phi_0(x)] \tag{2}$$

with

$$\phi_0(x) = 2\pi f_0 \overline{BD} \tag{3}$$

When the object is in place, the ray from E_p that strikes the reference plane at B is seen from the camera as coming from A and the phase expression for $h(x,y) \neq 0$ is therefore

$$\phi(x,y) = 2\pi f_0 \overline{AD} \tag{4}$$

The fringe pattern on the object surface is expressed by

$$g_s(x,y) = a(x,y) + b(x,y)\cos[2\pi f_0 x + \phi(x,y)] \tag{5}$$

and the phase difference between reference plane and object surface is then

$$\Delta\phi(x,y) = 2\pi f_0(\overline{AD} - \overline{BD}) = 2\pi f_0 \overline{AB} \tag{6}$$

As shown in [3], this phase difference is completely recovered as

$$\Delta\phi(x,y) = \mathrm{Im}\{\log[G_s(u,v)G_0^*(u,v)]\} \tag{7}$$

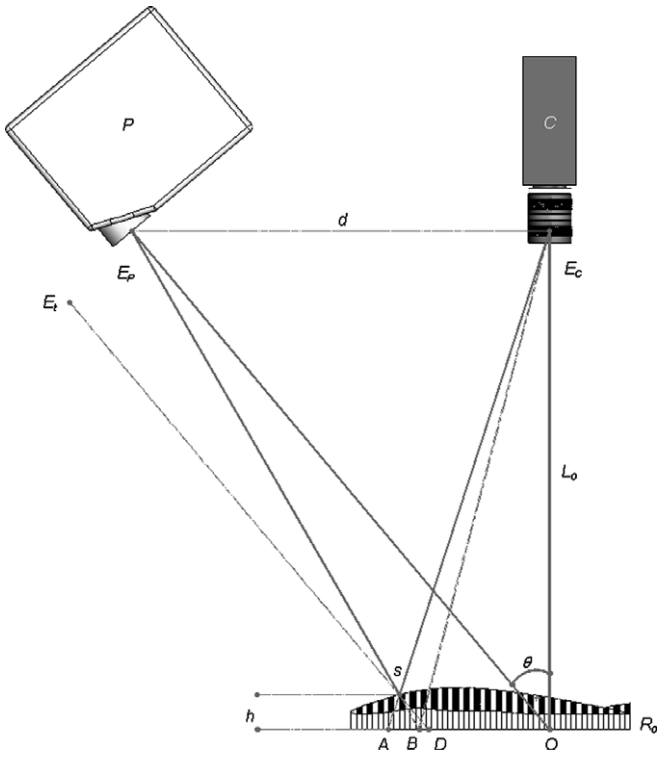

Fig. 1. Fourier transform profilometry crossed axis setup.

where $G(u,v)$ are the Fourier Transforms of the fringe patterns and $*$ denotes complex conjugation.

In order to establish a relation between phase and height one uses the fact triangles E_psE_c and AsB are similar

$$AB = \frac{dh}{L_0 - h} \tag{8}$$

so

$$\Delta\phi(x,y) = 2\pi f_0 AB \Rightarrow h(x,y) = \frac{L_0\Delta\phi(x,y)}{\Delta\phi(x,y) + 2\pi f_0 d} \tag{9}$$

A thorough analysis in [9] indicates $h(x,y)$ is in fact a function of the lateral coordinate x and the angle between projector and camera θ as

$$h(x,y) = \frac{L_0}{\dfrac{2\pi L_0^2 d\cos\theta}{P_0\Delta\phi(x,y)(L_0 + x\cos\theta\sin\theta)^2} - \dfrac{d\cos\theta\sin\theta}{L_0 + x\cos\theta\sin\theta} + 1} \tag{10}$$

with

$$P_0 = \frac{1}{f_0} = \frac{P}{\cos\theta} \tag{11}$$

P being the projected grating period.

Now, an analysis of either expression for $h(x,y)$ will reveal they are not that much different for a plausible application regime. Reversing the last function for $h(x,y)$ above gives

$$\Delta\phi = \frac{2h\pi L_0^2 d\cos\theta}{P_0(h(dL_0\cos\theta\sin\theta + dx\cos^2\theta\sin^2\theta - L_0^2) + L_0^3 + (L_0 - h)x\cos\theta\sin\theta(2L_0 + x\cos\theta\sin\theta))} \tag{12}$$

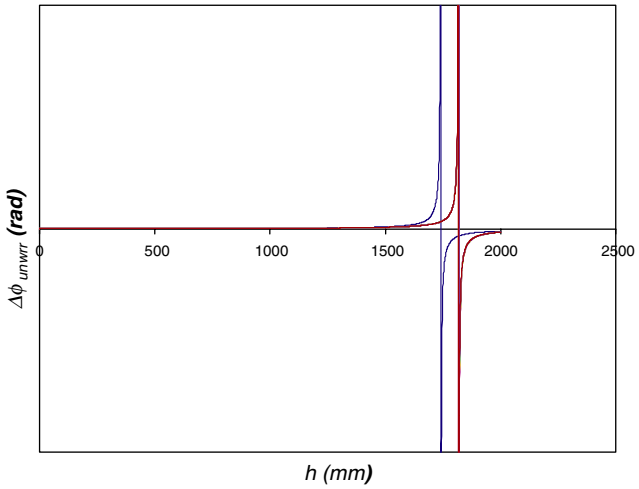

Fig. 2. The plot of $\Delta\phi_{\mathrm{unwr}}(x,y)$ (rad) with varying $h(x,y)$ (mm).

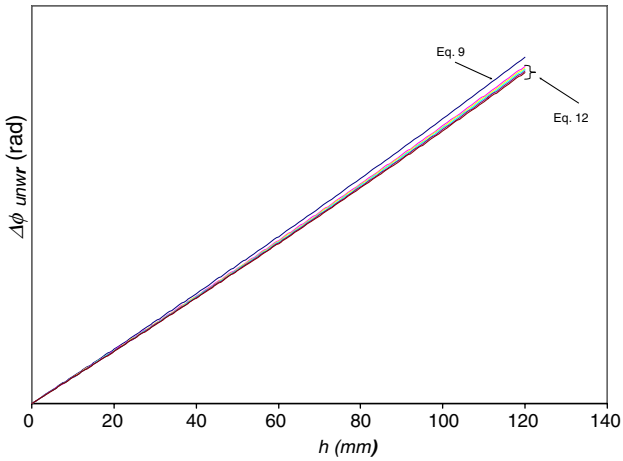

Fig. 3. The plot of $\Delta\phi_{\mathrm{unwr}}(x,y)$ with varying $h(x,y)$ – detail for 0 . . . 120 mm.

This issue has also been reviewed in Zhou and Su [13] and Guo et al. [14] and an expression for non-coplanar projection and camera systems was proposed in [13].

Fig. 2 shows a comparison of the expressions for $\Delta\phi(x,y)$ in Eqs. (9) and (12), taken as functions of $h(x,y)$. Several plots of Eq. (12) corresponding to different values of x ranging from 0 to 100 mm are present, even though any of these would suffice to describe the function correctly.

This plot was done for $L_0 = 1740$ mm, $d = 370$ mm, $f_0 = 0.6$ fringes/mm and a field size of 160 mm. The plots are nearly identical except for the region around camera location. The expression in [3] has a discontinuity at the camera location, $h = L_0$, whereas the phase expression in Eq. (12) has an offset for $x = 0$ given by

$$\frac{L_0^2}{L_0 - d\cos\theta\sin\theta} - L_0 \tag{13}$$

Either way, the highly non-linear discontinuity regions occur near or past the camera location and are totally out of reach for ordinary phase measuring profilometry techniques, because of both depth of focus and the steepness limit of data acquisition. Even with the improved data range described in [7], the maximum observable height for the 160 mm plane would be approximately 78 mm. If one compares the region of 0 to 100 mm for instance the plots are very similar – cf. Fig. 3.

Moreover, the analytical plots are strikingly linear at these regimes. The correlation coefficient for h in Eq. (9) and the first 120 mm is $R^2 = 0.9997$ on this plot.

3. Experimental phase-to-depth relation

Experimental methods are based on the assumption the relation between height and phase for every point of the calibration volume can be described by an expression of the following type [13] or [14]:

$$\frac{1}{h(x,y)} = \zeta(x,y) + \eta(x,y)\frac{1}{\Delta\phi(x,y)} \tag{14}$$

The estimation of coefficients $\zeta(x,y)$ and $\eta(x,y)$ then proceeds by sampling the calibration volume at regular intervals and calculating phase maps for a reference plane in each position, as illustrated in Fig. 4. For every (x,y) position there will be several phase values corresponding to the number of chosen height positions. The coefficients can then be calculated by linear interpolation [12,13], least squares [14], or higher order polynomial fitting [11].

We have conducted experiments with a Micro-Controle TL78 linear positioning system with 0.1 μm resolution at 100 positions separated by 1 mm. We used a Kodak Megaplus ES 1.0 8 bit CCD and an InFocus LP70 video projector.

The wrapped phase maps, once obtained, can be demodulated using any unwrapping technique, though we found the Volkov and Zhu [18] deterministic phase unwrapping method to perform well under most circumstances.

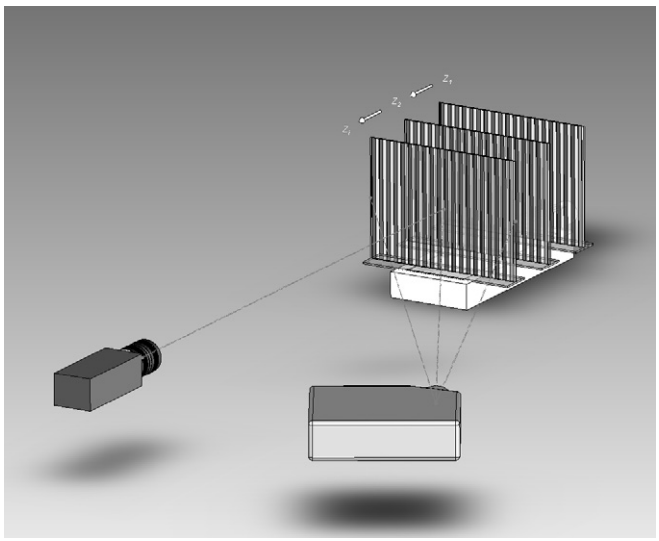

Fig. 4. Experimental setup for traditional calibration of phase-to-height.

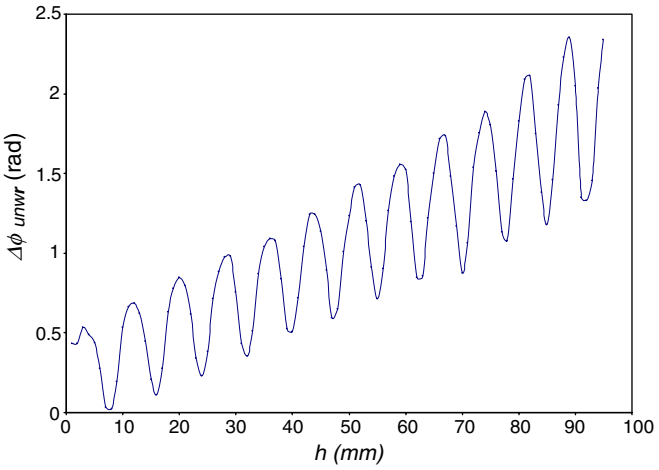

Fig. 5. Phase values at point (50,255) for the 100, 1 mm reference plane z shifts.

The camera was calibrated by a standard pinhole projection method with radial and tangential distortion fourth order correction and full non-linear optimization of both the extrinsic and intrinsic calibration parameters, as can be found in [16] or [17]. One relevant point about the implementation of this sort of camera calibration is the separation of intrinsic from extrinsic calibration. Once the camera intrinsic parameters have been calculated, the view can be changed at will and only the extrinsic ones, i.e., position relative to the object, have to be recalculated by direct linear transformation (DLT), as long as the camera objective settings are not changed.

Fig. 5 shows the plot of the phase values obtained for one particular (i,j) image point as the reference plane was moved forward by 100, 1 mm steps.

The field size was approximately 160 mm, L_0 was 1857 mm and d was 370 mm. There were 97 fringes across the field of view so the spatial frequency f_0 was 0.606 fr/mm. The fringe period P_0 was 1.649 mm and the dislocation of the fringe pattern over the image, $z * \tan(\theta) = 0.199$ so one complete fringe period elapsed every 8.277 mm of forward z movement of the reference plane. This effect is also evident from Fig. 5 and has been reported in [15].

To normalize the previous phase results, one has to add 2π to the phase values every 8.277 mm. The final result is plotted in Fig. 6 along with the theoretical values predicted for that range in Eqs. (9) and (12).

As such, one can safely calibrate the phase-to-height relation with either a linear or a least squares calibration procedure. Higher order polynomial interpolation will not improve the method significantly.

4. Experiments with one calibration plane

In view of the fact a linear calibration procedure is satisfactory for the plausible working depth regime; we have devised a simple, yet effective, phase-to-height calibration procedure. Although the procedure described herein requires *a priori* accurate camera calibration and the possibility to calibrate for rigid body motion within the depth of field, it has the advantage of requiring just one phase map of an inclined reference plane and can thus accelerate the complete process of calibrating phase-to-height.

A necessary step for camera calibration is the acquisition of the image location of a set of points, traditionally on some sort of calibration pattern. The result from extrinsic camera calibration is a set of data describing a rigid body transformation. Basically it transforms the World Coordinate System (X_w, Y_w, Z_w) (WCS1) into a Camera Coordinate System (X_c, Y_c, Z_c) (CCS) as depicted in Fig. 7. If we now rotate the calibration plane to a new position and recalibrate the camera, we will obtain a new transformation, this time from (X_{w2}, Y_{w2}, Z_{w2}) to (X_c, Y_c, Z_c) (WCS2).

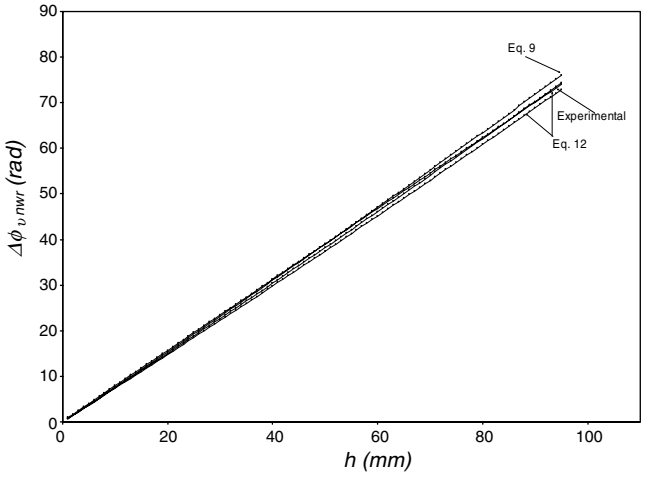

Fig. 6. Normalized phase values at point (50,255) vs. theoretical values for Eqs. (9) and (12).

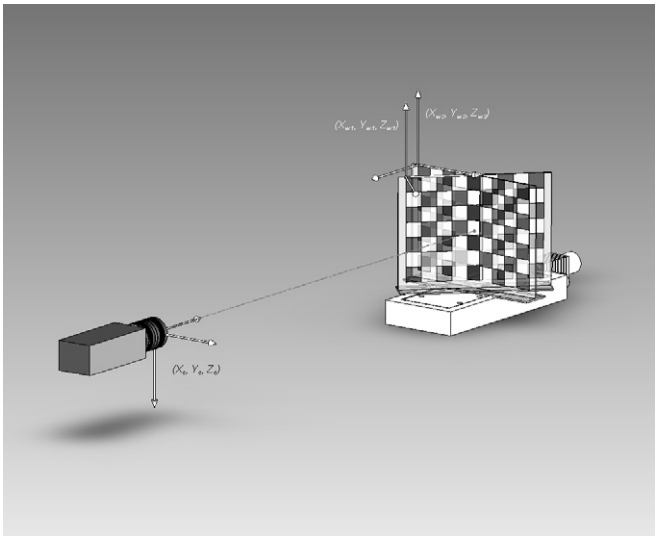

Fig. 7. One frame phase-to-height calibration procedure – coordinate systems.

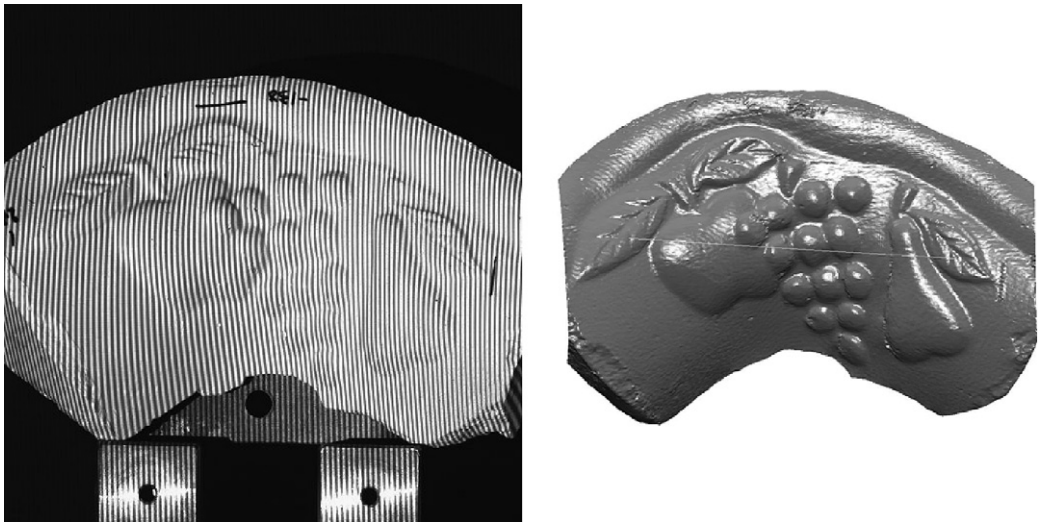

Fig. 8. Plaster mold used in testing and tessellated model after profilometry completion.

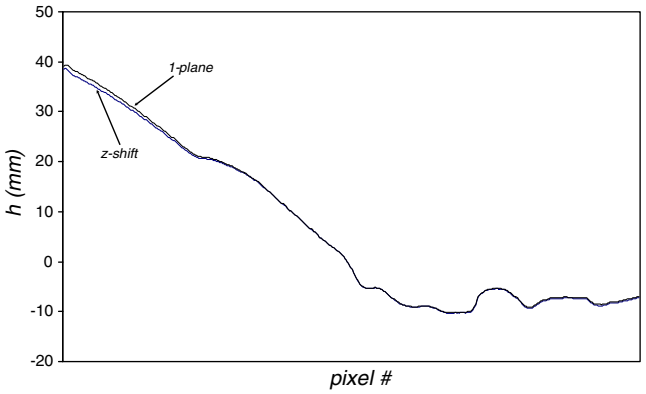

Fig. 9. Profile height on line# 255 of the plaster's model 3D point cloud.

We describe the transformations on projective space with homogeneous coordinates, so the complete transformation, consisting of one rotation followed by one translation is reduced to just one operation:

$$[\mathrm{Tr}] = [R] * [T]: \quad [R] = \begin{bmatrix} R_{00} & R_{01} & R_{02} & 0 \\ R_{10} & R_{11} & R_{12} & 0 \\ R_{20} & R_{21} & R_{22} & 0 \\ 0 & 0 & 0 & 1 \end{bmatrix}$$
$$[\mathrm{Tr}] = \begin{bmatrix} R_{00} & R_{01} & R_{02} & R_{00}T_x + R_{01}T_y + R_{02}T_z \\ R_{10} & R_{11} & R_{12} & R_{10}T_x + R_{11}T_y + R_{12}T_z \\ R_{20} & R_{21} & R_{22} & R_{20}T_x + R_{21}T_y + R_{22}T_z \\ 0 & 0 & 0 & 1 \end{bmatrix} \tag{15}$$

If $[\mathrm{Tr}_1]$ describes the transformation from WCS1 to CCS and $[\mathrm{Tr}_2]$ the transformation from WCS2 to CCS, the transformation we seek, describing points of WCS2 in WCS1, will be given by

$$\begin{bmatrix} X_{w1i} \\ Y_{w1i} \\ Z_{w1i} \\ 1 \end{bmatrix} = [\mathrm{Tr}] * \begin{bmatrix} X_{w2i} \\ Y_{w2i} \\ Z_{w2i} \\ 1 \end{bmatrix} = [\mathrm{Tr}_1]^{-1} * [\mathrm{Tr}_2] * \begin{bmatrix} X_{w2i} \\ Y_{w2i} \\ Z_{w2i} \\ 1 \end{bmatrix} \tag{16}$$

The transformation above calculates the position of the rotated calibration points on WCS1.

A phase map is calculated on each position and subtracted to obtain a phase difference map between both positions. If we define $z = 0$ on WCS1, we will have a set of points with different z_i coordinates, to each of which we have a corresponding phase difference, $\Delta\phi_i(x, y)$. A simple least squares fitting of z_i coordinates to phase differences will result in a couple of global coefficients ε and λ such that

$$z(x, y) = \varepsilon + \lambda\Delta\phi(x, y) \tag{17}$$

5. Results and discussion

We have tested this procedure against a least squares z-shift described in [14] on a plaster mold shown in Fig. 8.

This part, though most of its relief is quite simple to handle, has both a very steep border and a high surface curvature. The part is 70 mm thick and 55 mm high. The lateral dimension recovered was 160 mm. We calibrated the z-shift phase-to-height relation using the full 100, 1 mm shift reference plans mentioned earlier and the proposed technique with the reference plane at 0° and 42°.

The final surface was compared against a high resolution 3D model of the part made by contact profiling. The differences, both in height and in XY coordinates, between the 3D models seem to indicate very small errors, between 0.01 and 0.1 mm, though the exact positioning of the measurement markers on the 3D models may not be as accurate.

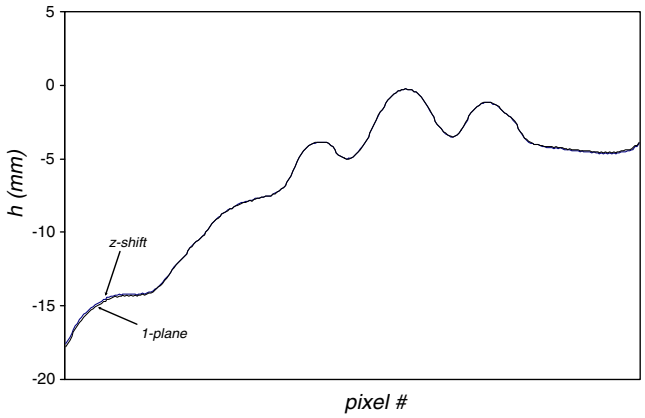

Fig. 10. Column# 255 on the 3D point cloud of the plaster model.

A profile of line and column 255 on the 3D point cloud recovered through both the least squares z-shift and our own procedure can be seen in Figs. 9 and 10. Small deviations between both models can be observed at the beginning and end of the lines, which we think may be attributed to the camera calibration method employed.

The largest measured error between both profiles was approximately 2%.

We have further studied the influence of the calibration plane rotation angle on the results. This can be a major issue in case the rotation angle is such that the increase in frequency of the fringe pattern prevents the fundamental frequency peak from falling inside the carrier elimination filter window in Fourier space. We illustrate this problem in Fig. 11, by showing the frequency shift observed from 0° to 20° and 42° in our experience.

Referring to Fig. 12, let p be the projected fringe period when the projector makes angle θ with the camera, p_0 the period on reference plane R_0 and p_1 on plane R_1, which has been rotated by angle α,

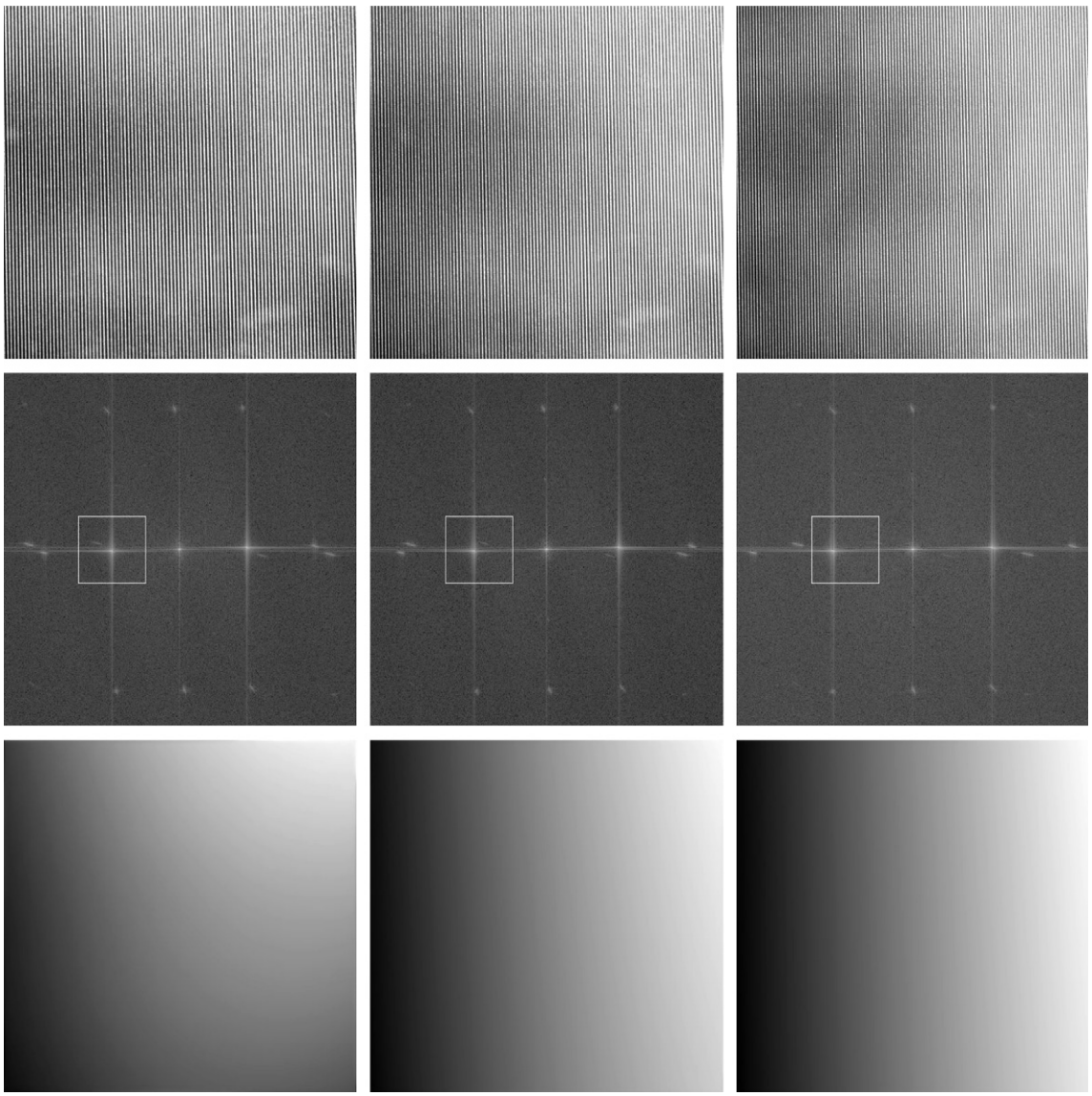

Fig. 11. The effect of increasing rotation angle on Fourier spectra at 0°, 20° and 42°.

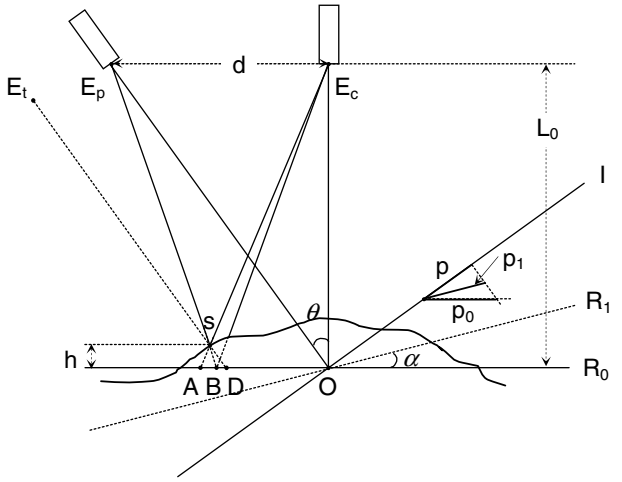

Fig. 12. Dependency of fringe frequency on rotation angle.

$$p_1 \cos(\theta - \alpha) = p = p_0 \cos(\theta) \tag{18}$$

so

$$f_1 = f_0 \frac{\cos(\theta - \alpha)}{\cos(\theta)} \tag{19}$$

On the other hand, the usable window size in Fourier domain depends on the projected frequency. In order to prevent energy leakage between the fundamental frequency and the central DC component, the window size is set at a maximum equal to the fundamental frequency itself, f_0. In case the fundamental frequency is greater than 2/3 of the maximum discernible frequency, $f_{\max}$, the window size will have to shorten to twice $f_{\max} - f_0$, and the frequency on the tilted plane, f_1, will have to stay within

$$f_1 < f_0 + (f_{\max} - f_0) = f_{\max} \tag{20}$$

which is always possible. But if f_0 is kept below $2/3 f_{\max}$, f_1 will have to remain below $3/2 f_0$, or $2 f_0$ at the most, in case the technique described in [19] is used.

Inspection of the function $\cos(\theta - \alpha)/\cos(\theta)$ for values of α ranging from 0° to 50° as a function of θ, shown in Fig. 13, indicates the condition $f_1/f_0 < 3/2$, will be valid

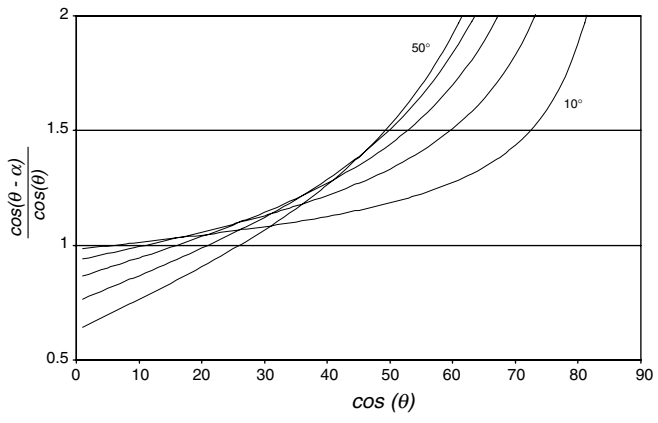

Fig. 13. Dependency of fringe frequency ratio on rotation angle.

for as long as θ is kept under 48° and the reference plane inclination below 50°.

In practical experiments, this constraint is hardly stringent, either because the steepness sensitivity of the method depends on θ not being too large [3 or 7] or because a reference plane inclination too large is prohibitive for successful camera calibration.

6. Conclusions

Phase measurement profilometry methods are amongst the most popular non-contact 3D surface measurement techniques. These are active image processing methods which thus need calibration of the instrument-object interfering mechanism. With PMP methods this requirement translates into a calibration of the relation between phase and object height, which is traditionally obtained by shifting a reference plane perpendicularly to the camera, obtaining phase maps at each shifting step and relating phase-to-height by fitting some sort of function to the calculated phase maps. This is an awkward and lengthy process, which has to be performed in controlled conditions and adequate equipment inside a laboratory.

The method we propose herein, though it requires accurate camera calibration, reduces this process to the acquisition of just one further phase map of the reference plane at an inclined position. Camera calibration data combined with the obtained phase maps provides sufficient information to completely describe the relation between phase and height. We show this is feasible and simple and the results seem to be sufficiently accurate for most tasks.

Acknowledgments

The authors whish to thank INEGI – Instituto Nacional de Engenharia e Gestão Industrial – for supporting the current work.

References

[1] K. Creath, Temporal phase measurement methods, in: D.W. Robinson, G. Reid (Eds.), Interferogram Analysis: Digital Fringe Pattern Measurement, Institute of Physics Publishing, Bristol, Philadelphia, 1993, p. 94 (Chapter 4).
[2] M. Kujawinska, J. Wojciak, Optics and Lasers in Engineering 14 (4–5) (1991) 325.
[3] M. Takeda, K. Mutoh, Applied Optics 22 (24) (1983) 3977.
[4] W. Macy, Applied Optics 22 (23) (1983) 3898.
[5] D. Bone, H. Bachor, et al., Applied Optics 25 (10) (1986) 1653.
[6] B.A. Rajoub, D.R. Burton, et al., Journal of Optics A – Pure and Applied Optics 7 (6) (2005) S368.
[7] X. Su, W. Chen, Optics and Lasers in Engineering 35 (5) (2001) 263.
[8] X. Su et al., Optics and Lasers in Engineering 36 (1) (2001) 49.
[9] Z. Zhang, D. Zhang, et al., Optics and Lasers in Engineering 42 (3) (2004) 341.
[10] R. Legarda-Saenz, T. Bothe, et al., Optical Engineering 43 (2) (2004) 464.
[11] R. Sitnik, M. Kujawinska, et al., Optical Engineering 41 (2) (2002) 443.

[12] X. Zhang, Y. Lin, et al., Journal of Optics A – Pure and Applied Optics 7 (4) (2005) 192.
[13] W. Zhou, X. Su, Journal of Modern Optics 41 (1) (1994) 89.
[14] H. Guo, H. He, et al., Optical Engineering 44 (3) (2005).
[15] A. Asundi, C.S. Chan, Optics and Lasers in Engineering 21 (1–2) (1994) 31.
[16] J. Heikkilä, Accurate camera calibration and feature based 3-D reconstruction from monocular image sequences, Ph.D. thesis, Department of Electrical Engineering, University of Oulu, Oulu, Finland, 1987.
[17] G. Wilson, Modeling and calibration of automated zoom lenses, PhD thesis, The Robotics Institute, Carnegie Mellon University, Pittsburg, Pennsylvania, USA, 1994 (Chapter 5).
[18] V.V. Volkov, Y.M. Zhu, Optics Letters 28 (22) (2003) 2156.
[19] P. Tavares, M. Vaz, Optics Communications 266 (2) (2006) 465.

E.5 Accurate Subpixel Corner Detection on Planar Camera Calibration Targets

This page intentionally left blank.

Optical Engineering 46(10), 107205 (October 2007)

Accurate subpixel corner detection on planar camera calibration targets

Paulo J. da Silva Tavares, MEMBER SPIE
Prudente and Tavares Technical Consulting
Edifício Península, Esc. - 305
Praça do Bom Sucesso 127-131
4150-146 Porto, Portugal
E-mail: jtavares@fe.up.pt

Mário A. Vaz, MEMBER SPIE
Porto University
Mechanical Engineering Department
Engineering Faculty
Rua Dr Roberto Frias SN
Porto, NA 4200-465
Portugal

Abstract. Feature detectors have long been one of the touchstones of image processing. Most vision tasks are entirely dependent on the accurate determination of fiducial marks on images, which ultimately led to a quest for methods able to detect feature locations with high resolution. We report the development of an intensity-based subpixel corner detector based on the two-dimensional (2-D) Hilbert transform. Extensive testing of both accuracy and precision with live images finds the method adequate for subpixel detection at better than 10^{-1} pixel accuracy. The subpixel corner detectors and the evaluation proposals to date are briefly reviewed, and the proposed method is described. The results are shown and discussed.
[DOI: 10.1117/1.2790926]

Subject terms: edge and feature detection; tracking; camera calibration; computer vision.

Paper 060976R received Dec. 20, 2006; revised manuscript received Apr. 27, 2007; accepted for publication May 11, 2007; published online Oct. 3, 2007.

1 Introduction

Feature detection and tracking is of utmost importance to several disciplines related to computer vision and image-based metrology tasks, whenever high-precision measurements are sought. Whether performing camera calibration, detecting deformations, or otherwise using images to measure physical quantities, the need to accurately locate specified features within an image is frequently unavoidable. Subpixel target location has been used in areas such as star or satellite tracking, mask alignment in semiconductor fabrication, and other scientific or industrial processes. In machine vision, all subsequent image processing tasks rely heavily on the quality and reliability of the data processed in this initial step. Numerous works have been published on the subject, and several methods have been tried to date. Excellent accounts of these are given in Shortis et al.,[1] West and Clarke,[2] and Schmid et al.[3]

The proliferation of point registration techniques in recent years led to a growing difficulty in deciding, on each occasion, which method is best for the task at hand. The fact that most of these methods are developed for specific tasks naturally implies the absence of a universal evaluation method capable of determining the performance of a specific technique in face of every challenging application. Still, some effort in this direction has been observed recently, as seen in Schmid et al.[3] and Heath et al.,[4] although a general agreement on the most important evaluation parameters is yet to be reached.

As proposed in Schmid et al.,[3] one can separate the point detector techniques into three broad categories, namely, contour-based, intensity-based, and parametric-modeling methods. Contour methods rely on the extraction of a contour around the interest point and a search along that contour of maximal inflection or curvature points.[5,6] Intensity methods stipulate a measure of interest point detection from the image gray values.[7–10] Last, parametric model methods fit an intensity model to the original image by varying a certain number of the model's parameters, usually through an optimization process.[11,12]

Clearly, one advantage of working with intensity methods is the access to a region of interest where the exact point is located, instead of a determined pixel location. One solution to accurate corner detection then lies on using peak detection techniques conjugated with a method that produces a sharp peak on each location. We have chosen to use the two-dimensional (2-D) Hilbert transform for the specific application of planar camera calibration target corner location with the Kohlmann method,[12] as this seems par-

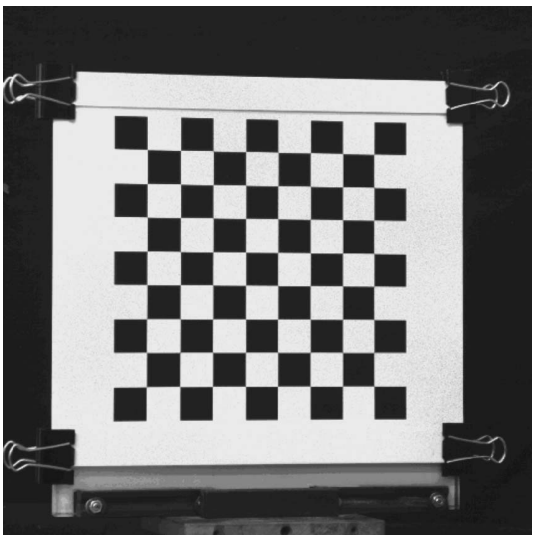

Fig. 1 Camera calibration pattern.

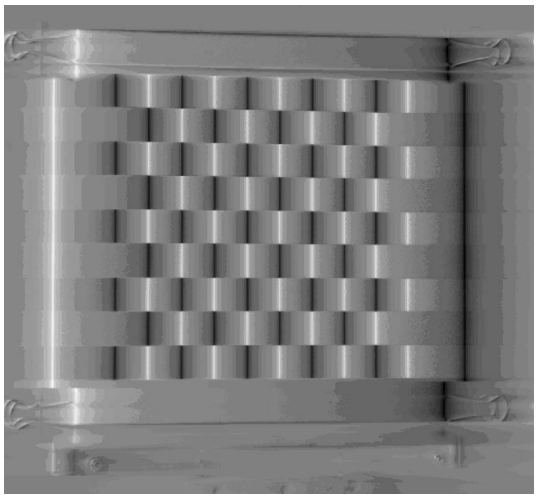

Fig. 2 Hilbert transform along *xx*.

ticularly well suited to the task, producing a sharp peak on each corner. Any other method that produces peaks around the corner locations can be used instead, although this one has produced reliable and stable results with accuracy comparable to the best parametric models in the literature.

2 The 2-D Hilbert Transform

The Hilbert transform has been used for a long time in communications theory and frequency analysis, where it provides a practical means of isolating the frequency components of a given function. Its application to corner detection is thoroughly described in Refs. 12 and 13 and briefly presented here. A successful extension of one-dimensional (1-D) to 2-D analytical signals based on the Hilbert tansform is described in Ref. 14.

Let $s(t_1,t_2)$ be a real integrable function. Its Fourier transform is given by

$$S(\omega_1,\omega_2)=\int_{-\infty}^{+\infty}\int_{-\infty}^{+\infty}s(t_1,t_2)\exp(-j\omega_1 t_1)\times\exp(-j\omega_2 t_2)\,\mathrm{d}t_1\,\mathrm{d}t_2, \quad (1)$$

and its Hilbert transform by

$$\hat{s}(t_1,t_2)=\frac{1}{\pi^2}p.v.\int_{-\infty}^{+\infty}\int_{-\infty}^{+\infty}\frac{s(\tau_1,\tau_2)}{(t_1-\tau_1)(t_2-\tau_2)}\,\mathrm{d}\tau_1\,\mathrm{d}\tau_2 = \frac{1}{\pi^2 t_1 t_2}*s(t_1,t_2), \quad (2)$$

where *p.v.* refers to the principal value of the integral, and $*$ is the convolution operator. Now the Fourier transform of $1/(\pi^2 t_1 t_2)$ is

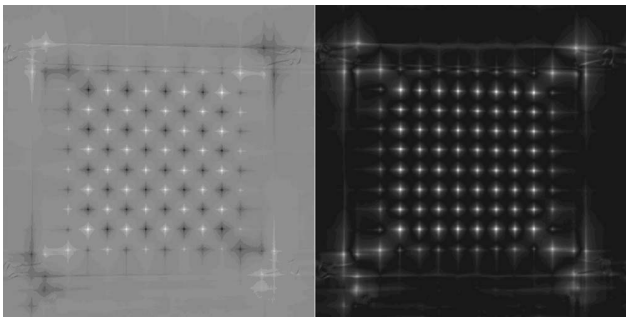

Fig. 3 Hilbert transform along *xx* and *yy* and its absolute value.

$$F\left(\frac{1}{\pi^2 t_1 t_2}\right)=-j[1-2H(-\omega_1)]-j[1-2H(-\omega_2)] = -\operatorname{sgn}(\omega_1)\operatorname{sgn}(\omega_2), \quad (3)$$

where $H(x)$ is the Heaviside step function, and $\operatorname{sgn}(x)$ is the signum function:

$$H(x)=\begin{cases}0 & \text{for } x<0\\ \frac{1}{2} & \text{for } x=0\\ 1 & \text{for } x>0\end{cases};\quad \operatorname{sgn}(x)=\begin{cases}-1 & \text{for } x<0\\ 0 & \text{for } x=0\\ -1 & \text{for } x>0\end{cases}. \quad (4)$$

By the convolution theorem, the Fourier transform of the Hilbert transform of $s(t_1,t_2)$ relates to the Fourier transform of $s(t_1,t_2)$ by

$$\hat{S}(t_1,t_2)\equiv F[\hat{s}(t_1,t_2)]=-\operatorname{sgn}(\omega_1)\operatorname{sgn}(\omega_2)F[s(t_1,t_2)] \equiv -\operatorname{sgn}(\omega_1)\operatorname{sgn}(\omega_2)S(\omega_1,\omega_2). \quad (5)$$

If the calibration pattern is composed of squares, such as the one in Fig. 1, the Hilbert transform can be thought of as a separable function in a 2-D space. When applied along direction *xx*, it detects the edges in that direction, as shown in Fig. 2.

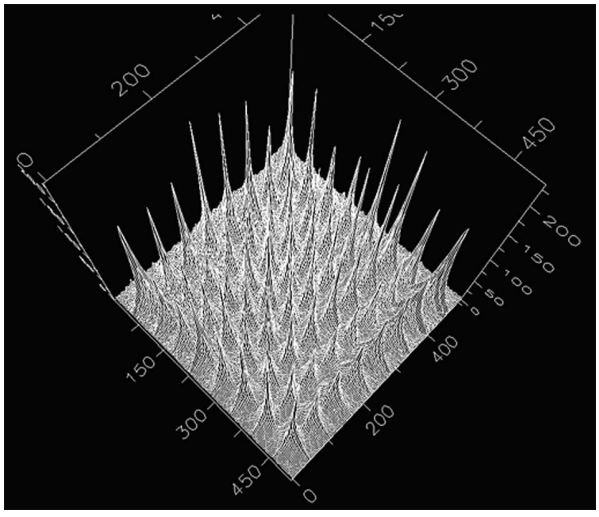

Fig. 4 The Hilbert transform absolute value intensity profile.

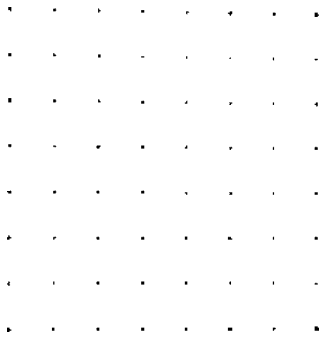

Fig. 5 Regions of interest around each corner location.

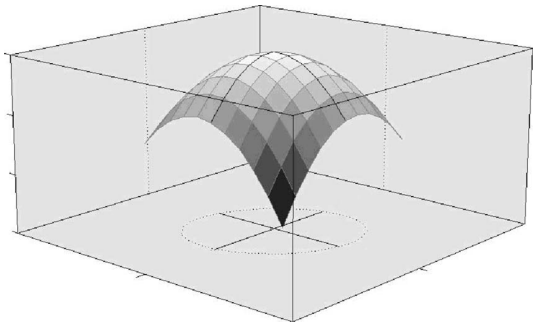

Fig. 6 Ridge peak detection.

If it is now applied along the *yy* direction to the result of the first transformation, it will detect the edges along the new direction, i.e., the corners of the given squares. This is the basis of this method, where the absolute values are retained after calculating the transforms; see Figs. 3 and 4.

Regions of interest are established around each peak through a simple yet effective method. A Gaussian filter is first applied to the Hilbert transform, reducing most of the unwanted peaks. The resulting image is then binarized to retain just the central, stronger peak regions (Fig. 5).

Last, a peak detection algorithm is applied to the regions of interest in the original peaks image, centered at the intensity maxima of subregions around each binary region, to find exact subpixel locations of the respective corner. Two peak detection methods were compared in this study: centroiding and ridge detection by paraboloid fitting.

3 Centroiding

Centroiding is a common method in image processing.[1,2] The technique uses the full region of interest to calculate the intensity centroid as follows:

$$\bar{x} = \frac{\sum_i \sum_j i \cdot I_{i,j}^2}{\sum_i \sum_j I_{i,j}^2}, \quad \bar{y} = \frac{\sum_i \sum_j j \cdot I_{i,j}^2}{\sum_i \sum_j I_{i,j}^2}. \tag{6}$$

The centroid can be simple, squared as in Eq. (6), or higher orders, although the results do not seem to change much between second and higher orders.

4 Ridge Detection by Paraboloid Fitting

Centroiding was further compared against a ridge peak location intersection in perpendicular directions. This is a less common technique in image processing, although it has been used before, in Refs. 15 and 16, in different contexts and consists of locally bidimensional fitting of the image obtained in each region of interest and determining the location of the first derivatives maxima ridges on *xx* and *yy*. The intersection of the ridge projections is a fair approximation to the peak location.

The technique, illustrated in Fig. 6, can be described as

Table 1 Maximum and average standard deviations of corner locations.

	Centroid Detection Technique				Ridge Detection Technique			
Image Set	Average StDev on *xx* (pixel)	Max StDev on *xx* (pixel)	Average StDev on *yy* (pixel)	Max StDev on *yy* (pixel)	Average StDev on *xx* (pixel)	Max StDev on *xx* (pixel)	Average StDev on *yy* (pixel)	Max StDev on *yy* (pixel)
A0	0.0055	0.0079	0.0075	0.0097	0.0100	0.0703	0.0099	0.0138
A10	0.0064	0.0090	0.0071	0.0094	0.0075	0.0113	0.0100	0.0566
A20	0.0041	0.0058	0.0070	0.0332	0.0058	0.0080	0.0132	0.0169
B0	0.0086	0.0112	0.0092	0.0128	0.0088	0.0123	0.0128	0.0172
B10	0.0063	0.0080	0.0079	0.0105	0.0073	0.0102	0.0114	0.0430
B20	0.0057	0.0074	0.0109	0.0490	0.0053	0.0074	0.0085	0.0560
C0	0.0086	0.0865	0.0105	0.0135	0.0098	0.0673	0.0066	0.0085
C10	0.0061	0.0078	0.0079	0.0099	0.0073	0.0108	0.0086	0.0110
C20	0.0035	0.0049	0.0111	0.0439	0.0049	0.0068	0.0066	0.0087

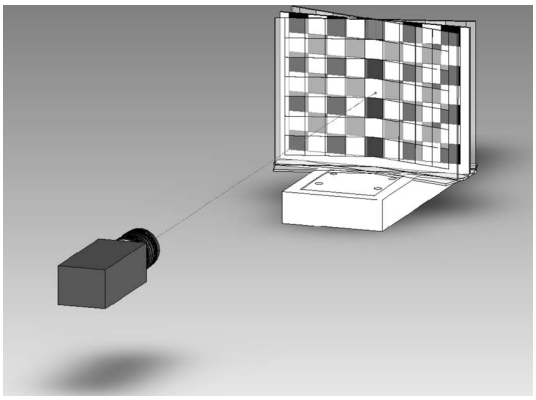

Fig. 7 Image acquisition setup for cross ratio analysis—A, B, and C positions.

follows. Let $I(x,y)$ represent the image at point (x,y). A bidimensional paraboloid fitting to the image can be represented by

$$I(x,y) = a + bx + cy + dx^2 + ey^2 + fxy. \tag{7}$$

A least-squares solution is readily found by singular value decomposition. The first derivatives of $I(x,y)$ are equaled to zero and the ridges location thus determined. The ridges intersection is the approximate location of the intensity peak:

$$\begin{cases} 2dx_{\max} + fy_{\max} + b = 0 \\ fx_{\max} + 2ey_{\max} + c = 0 \end{cases} \Leftrightarrow \begin{cases} x_{\max} = \dfrac{fc - 2be}{4de - f^2} \\ y_{\max} = \dfrac{bf - 2dc}{4de - f^2} \end{cases}. \tag{8}$$

5 Evaluation

A multitude of evaluation methods for feature detectors are found in the literature.[3] Due to the specific nature of the task at hand, i.e., detecting corners on a planar calibration target, methods that need to rely on human intervention such as ground truth verification or visual inspection were avoided due to being highly subjective. The analysis focused instead on methods to ascertain accuracy and precision, verifying the results' repeatability and examining some cross ratios. Verification through a specific task was also envisaged. To that end, a 3-D reconstruction of the detected corners was projected back through the calibration matrix obtained with the corners previously found, and the resulting 3-D locations compared to the given world coordinates of the corners.

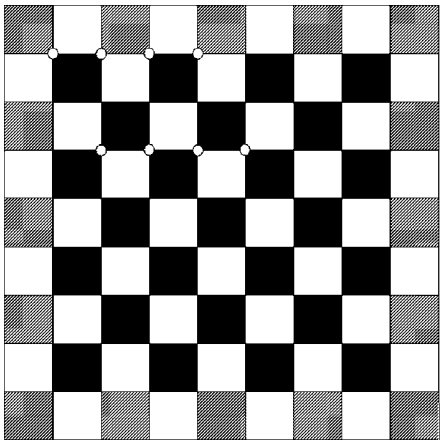

Fig. 8 Studied cross ratio configurations—examples of set #1 and set #2 (horizontal).

Table 2 Alignment evaluation.

		Centroid Detection Technique		Ridge Detection Technique	
Image Set	Line	Average (pixels)	Standard deviation	Average (pixels)	Standard deviation
A0	Vertical	0.0874	0.0540	0.0979	0.0619
	Horizontal	0.0885	0.0552	0.0988	0.0607
A10	Vertical	0.0953	0.0567	0.1034	0.0609
	Horizontal	0.0959	0.0490	0.1045	0.0524
A20	Vertical	0.0757	0.0609	0.0794	0.0630
	Horizontal	0.0901	0.0536	0.0987	0.0567
B0	Vertical	0.0801	0.0569	0.0893	0.0638
	Horizontal	0.0892	0.0590	0.0996	0.0647
B10	Vertical	0.0989	0.0575	0.1060	0.0602
	Horizontal	0.0973	0.0595	0.1065	0.0643
B20	Vertical	0.0712	0.0549	0.0766	0.0593
	Horizontal	0.0921	0.0556	0.1030	0.0589
C0	Vertical	0.0821	0.0587	0.0905	0.0615
	Horizontal	0.0914	0.0534	0.1030	0.0637
C10	Vertical	0.0956	0.0535	0.1033	0.0568
	Horizontal	0.0872	0.0466	0.0951	0.0514
C20	Vertical	0.0859	0.0617	0.0917	0.0643
	Horizontal	0.0926	0.0546	0.1023	0.0593

Live images were preferred over the traditional synthetic pictures in this study. There is no substitute for real images, however complete the noise addition considerations may be. This decision confers additional credibility to the final results, at the expense of making the whole exercise considerably harder, due to the innumerable noise sources in image capturing, even under laboratory conditions.

We used a pattern such as the one in Fig. 1. A traditional camera calibration checkers pattern was preferred over simple squares, simply because this method benefits from the peak reinforcement on the corners that result from link-

Table 3 Reconstruction accuracy.

	Centroid Detection Technique			Ridge Detection Technique		
Image Set	Average (mm)	Standard deviation	Accuracy	Average (mm)	Standard deviation	Accuracy
A0	0.09024564	0.04624801	0.00045123	0.09339381	0.04767054	0.00046697
A10	0.06555464	0.0316727	0.00032777	0.07149049	0.0343057	0.00035745
A20	0.07574253	0.03886055	0.00037871	0.07648046	0.03938635	0.0003824
B0	0.08901933	0.04979285	0.0004451	0.09264058	0.05086036	0.0004632
B10	0.06877196	0.0327247	0.00034386	0.07399058	0.03579606	0.00036995
B20	0.0896462	0.04324937	0.00044823	0.09450143	0.04560876	0.00047251
C0	0.08932197	0.04743729	0.00044661	0.07640904	0.04055834	0.00038205
C10	0.07417592	0.03652406	0.00037088	0.07666427	0.03468278	0.00038332
C20	0.09145519	0.04325582	0.00045728	0.0992616	0.04751126	0.00049631

ing squares. This fact was used to retain just the central peaks, by use of a suitable threshold. The images were acquired with a Kodak Megaplus ES 1.0 camera and a Matrox Genesis frame grabber. The calculations were performed on a Pentium IV, 3.2-GHz computer.

As noted in Mohr,[11] the usefulness of a feature detector for calibration purposes becomes apparent only when it has been proven effective in different images and depths, due to the necessity of having a valid calibration throughout a certain volume region. As such, we performed all measurements on images acquired at three different angles, 0 and ±15 deg from the camera optical axis, and three different depths, 0, 10, and 20 mm along that axis. From here on, these images will be referred to as A0, A10, A20, B0, B10, B20, C0, C10, and C20. The target setup is depicted in Fig. 7, illustrating the A, B, and C positions. The number of captured images for each position was 100 for both peak detection techniques, on a total of 1800 acquired images.

5.1 *Precision*

Precision was evaluated by performing 10 consecutive detections on the 64 central corners. Fluctuations of the camera image can be perceived by the difference in subpixel positions of some of the corners, typically 3 to 4 among the 64. These corners can readily be identified as outliers because the standard deviation of their position lies between two to three orders of magnitude greater than the remaining ones. At the 95th percentile, however, with 60/64 points available and plenty of room for camera calibration, the maximum standard deviation stands below 0.09 pixel on *xx* and 0.06 pixel on *yy*, and the average standard deviations even lower, at 0.010 pixel on *xx* and 0.013 pixel on *yy*, as can be seen on Table 1.

5.2 *Alignment*

Alignment was tested by least-squares fitting of vertical and horizontal lines to the corners and calculating the individual distance of each corner to these lines. The average distances and the standard deviations, shown on Table 2, illustrate the subpixel detection capability of the method.

5.3 *3-D Reconstruction*

In order to observe the 3-D reconstruction accuracy, camera calibration was performed with the acquired corner locations. The locations were projected back through the camera calibration matrix to determine the world coordinates of the observed corners. The distance between these coordinates and the initially given world coordinates was then calculated for each corner. Camera calibration was done in two steps. A modified Tsai's algorithm with nonlinear optimization was used to find the intrinsic camera parameters. Tsai's algorithm is basically a perspective projection calibration with nonlinear optimization of the focal distance and the optical axis translation coordinate, which uses a radial alignment constraint to determine part of the calibration parameters. The modification consists of making full use of the calibration data in both the *xx* and the *yy* directions of the error function at the optimization step, instead of just the *yy* data, as proposed by Tsai.[17] The external parameters, i.e., rotation and translation, were calculated at each image position by a standard direct linear transformation algorithm.

The average distances between the given and reprojected corner locations are given in Table 3, as well as the standard deviations and the ratios of these distances to the image scene, which was approximately 200 mm. These ratios are reasonable estimates of the 3-D reconstruction accuracy. The worst case is still better than 1/2000th the scene size. This result was somehow expected, in view of the high stability of the nonlinear optimization algorithm used in camera calibration.

Table 4 Data bias and accuracy.

				Centroid Detection Technique				Ridge Detection Technique			
Image Set	Direction	Data Set	No. of CRs	Avg. CR (pixels)	StDev (pixels)	λ (mm)	Accuracy σ	Avg. CR (pixels)	StDev (pixels)	λ (mm)	Accuracy σ
A0	Horizontal	1	24	3.981	0.023	20.034	0.053	3.979	0.026	20.037	0.060
		2	24	4.021	0.025	21.740	0.058	4.023	0.028	19.935	0.064
	Vertical	1	16	3.998	0.019	20.004	0.043	3.996	0.021	20.008	0.049
		2	16	3.999	0.019	19.994	0.044	4.001	0.021	19.988	0.047
A10	Horizontal	1	24	3.984	0.013	20.039	0.029	3.984	0.013	20.039	0.030
		2	24	4.019	0.015	19.959	0.035	4.020	0.016	19.956	0.038
	Vertical	1	16	3.996	0.010	20.005	0.022	3.994	0.010	20.008	0.022
		2	16	4.003	0.007	19.976	0.016	4.005	0.007	19.971	0.016
A20	Horizontal	1	24	3.980	0.022	20.051	0.049	3.978	0.022	20.055	0.051
		2	24	4.023	0.021	19.946	0.047	4.024	0.021	19.944	0.048
	Vertical	1	16	3.999	0.020	20.004	0.046	3.999	0.022	20.007	0.050
		2	16	4.001	0.018	19.989	0.042	4.001	0.020	19.989	0.045
B0	Horizontal	1	24	3.977	0.021	20.040	0.047	3.976	0.023	20.045	0.053
		2	24	4.029	0.022	19.922	0.052	4.031	0.025	19.919	0.057
	Vertical	1	16	4.000	0.019	20.000	0.043	3.998	0.021	20.004	0.048
		2	16	3.999	0.017	19.994	0.038	4.000	0.019	19.992	0.043
B10	Horizontal	1	24	3.982	0.021	20.046	0.049	3.981	0.024	20.051	0.054
		2	24	4.021	0.025	19.957	0.057	4.021	0.027	19.958	0.061
	Vertical	1	16	3.996	0.022	20.009	0.050	3.995	0.024	20.014	0.055
		2	16	4.003	0.019	19.984	0.044	4.004	0.021	19.982	0.048
B20	Horizontal	1	24	3.981	0.022	20.055	0.049	3.980	0.024	20.055	0.054
		2	24	4.023	0.026	19.960	0.060	4.023	0.028	19.957	0.065
	Vertical	1	16	4.001	0.019	20.000	0.044	4.000	0.021	20.001	0.049
		2	16	3.997	0.019	19.999	0.044	3.997	0.021	19.999	0.049
C0	Horizontal	1	24	3.984	0.021	20.038	0.048	3.980	0.022	20.041	0.049
		2	24	4.020	0.023	19.958	0.054	4.024	0.023	19.943	0.053
	Vertical	1	16	3.994	0.018	20.014	0.040	4.000	0.022	20.001	0.050
		2	16	4.006	0.018	19.979	0.041	3.999	0.020	19.996	0.046
C10	Horizontal	1	24	3.986	0.027	20.037	0.062	3.986	0.030	20.039	0.068
		2	24	4.017	0.026	19.971	0.059	4.018	0.028	19.971	0.065
	Vertical	1	16	3.997	0.027	19.996	0.062	3.994	0.031	20.004	0.070
		2	16	4.004	0.027	19.975	0.062	4.006	0.030	19.970	0.070

Table 4 (*Continued.*)

				Centroid Detection Technique				Ridge Detection Technique			
Image Set	Direction	Data Set	No. of CRs	Avg. CR (pixels)	StDev (pixels)	λ (mm)	Accuracy σ	Avg. CR (pixels)	StDev (pixels)	λ (mm)	Accuracy σ
C20	Horizontal	1	24	3.986	0.025	20.034	0.056	3.986	0.027	20.036	0.062
		2	24	4.017	0.026	19.965	0.060	4.018	0.029	19.964	0.066
	Vertical	1	16	3.996	0.021	20.014	0.047	3.994	0.023	20.017	0.052
		2	16	4.007	0.018	19.981	0.041	4.009	0.020	19.974	0.046

5.4 *Cross Ratio Inspection*

The cross ratio of four aligned points in an image is a basic invariant of projective geometry,[18] i.e., it remains constant under a perspective transformation. The cross ratio can be expressed as:

$$K(a,b,c,d) = \frac{\left(\frac{a-c}{a-d}\right)}{\left(\frac{b-c}{b-d}\right)}, \tag{9}$$

where a, b, c, and d are the coordinates of four aligned points. One can easily check that $K(0,3,2,1)=4$, which is the theoretical cross ratio used here.

The methodology used by Mohr[11] has been followed closely to show that the cross ratios are unbiased measures with a normal distribution and, having established that result, to find a measure of the standard deviation of the corners extraction.

6 Bias

The nonexistence of a bias on the detected corners is established by showing that the averages and standard deviations of two different configurations of cross ratios, namely, the one with four aligned points on two consecutive squares and another with the points on three consecutive squares, here designated as set #1 and set #2 as depicted in Fig. 8, are very similar. We have checked both the horizontal and the vertical cross ratios on both sets for completeness, on a total of 80 cross ratios for each image.

The results, shown in Table 4, clearly indicate the inexistence of a bias among the cross ratios.

7 Accuracy

Having established that the data is unbiased, it can be shown[11] that, for the cross ratios of four consecutive points with the configuration of the theoretical cross ratio $K(0,3,2,1)=4$, the standard deviation of the feature detection is given by

$$\sigma = \sigma_k \frac{\lambda}{\sqrt{80}}, \tag{10}$$

where σ_k is the standard deviation of cross ratio K, and λ is the average distance between two consecutive data points. This distance, calculated with the points re-projected through the calibration matrix, is very stable, which enables us to take the mean of the reconstructed distances to calculate λ, approximately 20 mm in our case. Table 4 shows these distances along with the standard deviations σ. We can observe that the accuracy is always better than 1/10th of a pixel. There is no significant difference between accuracies calculated with centroiding or ridge detection.

8 Conclusions

Traditional corner location methods cannot reach precisions below 1 pixel. In order to obtain accuracies beyond the pixel resolution with intensity-based techniques, it seems plausible to start with a method that yields intensity peaks at each corner location and detects that location through a centroiding or a ridge intersection technique. We have studied the application of both techniques coupled with a corner transformation based on the 2-D Hilbert transform. The study was performed on a reasonable number of live images, for robustness assertion.

We have observed a redundancy between both localization techniques employed on all evaluation parameters, which further strengthens the feasibility of the method. Although there is no standardized evaluation procedure in the literature, the task we envisage with this method is accurate camera calibration, and all evaluations returned reasonable results to this end, with precision under 1/2000 of the scene size and accuracy better than 1/10 pixel

Acknowledgments

The authors want to thank INEGI—Instituto Nacional de Engenharia e Gestão Industrial—for supporting the current work.

References

1. M. R. Shortis, T. A. Clarke, and T. Short, "A comparison of some techniques for the sub-pixel location of discrete target images," in *Videometrics III*, S. F. El-Hakim, Ed., Boston, *Proc. SPIE* **2350**, 239–250 (1994).
2. G. A. W. West and T. A. Clarke, "A survey and examination of sub-pixel measurement techniques," in *ISPRS Int. Conf. on Close Range Photogrammetry and Machine Vision*, A. Gruen and E. P. Baltsavias, Eds., *Proc. SPIE* **1395**, 456–463 (1990).
3. C. Schmid, R. Mohr, and C. Bauckage, "Evaluation of interest point detectors," *Int. J. Comput. Vis.* **37**(2), 151–172 (2000).
4. M. D. Heath, S. Sarkar, T. Sanocki, and K. W. Bowyer, "A robust visual method for assessing the relative performance of edge-detection algorithms," *IEEE Trans. Pattern Anal. Mach. Intell.* **19**(12), 1338–1359 (1997).

5. H. Asada and M. Brady, "The curvature primal sketch," *IEEE Trans. Pattern Anal. Mach. Intell.* **8**(1), 2–14. (1986).
6. F. Mokhtarian and A. Mackworth, "Scale-based description and recognition of planar curves and two-dimensional shapes," *IEEE Trans. Pattern Anal. Mach. Intell.* **8**(1), 34–43. (1986).
7. C. Harris and M. Stephens, "A combined corner and edge detector," in *Proc. 4th Alvey Vision Conf., Manchester, August 1988*, 189–192 (1988).
8. B. D. Lucas and T. Kanade, "*Proc. 7th Intl. Joint Conf. on Artificial Intelligence (IJCAI '81)*," pp. 674–679 (1981).
9. H. Moravec, "Object avoidance and navigation in the real world by a seeing robot rover," Tech. Report CMU-RI-TR-3, Carnegie-Mellon University, Robotics Institute (1980).
10. R. Deriche and G. Giraudon, "Accurate corner detection: An analytical study," in *Proc. 3rd Int. Conf. on Computer Vision*, pp. 66–70, IEEE Comput. Soc. Press, Los Alamitos, CA (1990).
11. R. Mohr and P. Brand, "Accuracy in image measure," in *Videometrics III*, S. F. El-Hakim, Ed., Boston, *Proc. SPIE* **2350**, 218–228 (1994).
12. K. Kohlmann, "Corner detection in natural images based on the 2-D Hilbert transform," *Signal Process.* **48**, 225–234 (1996).
13. H. Stark, "An extension of the Hilbert transform product theorem," *Proc. IEEE* **59**(9), 1359–1360 (1971).
14. T. Bülow and G. Sommer, "A novel approach to the 2-D analytic signal," in *Computer Analysis of Images and Patterns—CAIP'99*, F. Solina and A. Leonardis Eds., Ljubljana, Slovenia, pp. 25–32 (1999).
15. P. H. S. Torr, "A structure and motion toolkit in matlab: Interactive adventures in S and M," Microsoft Research Technical Report MSR-TR-2002–56 (2002).
16. D. Chen and G. Zhang, "A new sub-pixel detector for x-corners in camera calibration targets," *13th Intl. Conf. in Central Europe on Computer Graphics, Visualization, and Computer Vision (WSCG 2005)*, Plzen-Bory, Czech Republic, Jan. 31– Feb. 4, 2005, pp. 97–100 (2005).
17. R. Y. Tsai, "A versatile camera calibration technique for high-accuracy 3D machine vision metrology using off-the-shelf TV cameras and lenses," *IEEE Trans. Rob. Autom.* **RA–3**(4), 323–344 (1987).
18. G. Semple and G. T. Kneebone, *Algebraic Projective Geometry*, Oxford University Press, Amen House, London (1963).

Paulo J. da Silva Tavares is currently a doctoral student at LOME—the Optics and Experimental Mechanics Laboratory of the Mechanical Engineering and Industrial Management Department of the Engineering Faculty of the University of Porto, Portugal. He graduated in physics and obtained an MsC in lasers and optoelectronics from the Sciences Faculty at the University of Porto. He was at Texas Instruments, Portugal, for 10 years, working in failure analysis. He is a cofounder and manager of Prudente & Tavares Technical Consulting, an optics and engineering systems consulting company in Porto. He is a member of SPIE and serves at the Iberia Chapter, which he helped found. He is currently involved in active image processing for 3-D shape measurement. His research interests include optical metrology, machine vision, optical instrument design, strain and stress measurement, and applied computation for image analysis such as neural systems and wavelets.

Mário A. Vaz is an associate professor in the Mechanical Engineering and Industrial Management Department of the Faculty of Engineering of the University of Porto. He received his PhD in mechanical engineering from the University of Porto in 1997. He is a member of SPIE. His main research interests are lasers, optical interferometry, and image techniques applied to experimental mechanics. He is currently director of the Optics and Experimental Mechanics Laboratory of the Institute of Mechanical Engineering and Industrial Management (INEGI).

E.6 A Simple Technique for Correcting Image Distortion in Fringe Projection Methods - Photo Mechanics 2008, Loughborough

This page intentionally left blank.

inegi Institute of Mechanical Engineering and Industrial Management

LOME – Laboratory of Optics and Experimental Mechanics
www.fe.up.pt/~inegi/lome

A Simple Technique for Correcting Image Distortion in Fringe Projection Methods

Paulo J. S. Tavares and Mário A. P. Vaz
Mechanical Engineering Department, University of Porto
Rua Dr. Roberto Frias, SN, 4200 – 465 Porto, Portugal
jtavares@fe.up.pt gmavaz@fe.up.pt

Imaging distortion artefacts in full-field fringe projection systems, due to the system's inability to reproduce the ideal sinusoidal patterns projected onto the object are particularly stringent with multi-frequency methods such as Temporal Phase Unwrapping (TPU), because inadequate fringe width results in wrong or incomplete fringe superposition, necessary to the phase-shift algorithm. A less visible effect, but one which can still degrade final image quality, is the contrast degradation imposed by the system's impulse response width.

There are several causes to image degradation, such as the reduced contrast ratio of Digital Light Processors (DLP) or Liquid Crystal Displays (LCD) used as light modulators.
A simple solution to this problem is suggested by the OTF analysis, and has been successfully applied to the TPU method in our lab. We seek the periodic function which has to be projected so the final image is a near perfect sinusoid.

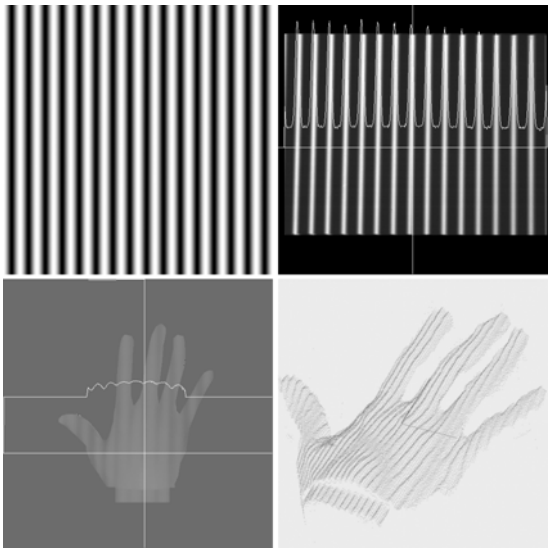

Distortion of an ideal sinusoid and the corresponding imaging artefacts.

PRINCIPLE

Calculate the complex OTF for the projection and imaging system:

$$I_i(x,y) = I_o(x,y) \otimes IR(x,y) = \int_{-\infty}^{+\infty}\int_{-\infty}^{+\infty} I_o(u,v)\cdot IR(x-u,y-v)dudv \Rightarrow F(I_i(x,y)) = F(I_o(x,y))\cdot OTF(u,v)$$

where Ii is the image intensity, Io is the object intensity, IR is the system's impulse response and is the convolution operator.
For each ideal sinusoid pattern, there must be some artificially distorted image which, when sent to the projector and imaged through the system, will result in a perfect sinusoid,

$$I_{ideal}(x,y) = I_?(x,y) \otimes IR(x,y) \Rightarrow F(I_?(x,y)) = \frac{F(I_o(x,y))}{OTF(u,v)} \Rightarrow I_?(x,y) = F^{-1}\left\{\frac{F(I_o(x,y))}{OTF(u,v)}\right\}$$

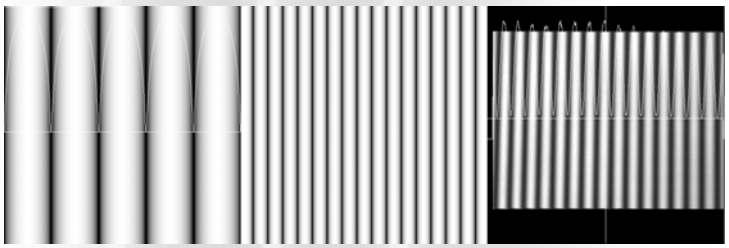

Artificially created .patterns with 5 and 16 fringes to obtain sinusoidal fringes when sent through the imaging system and the observed result from the 16 fringe pattern.

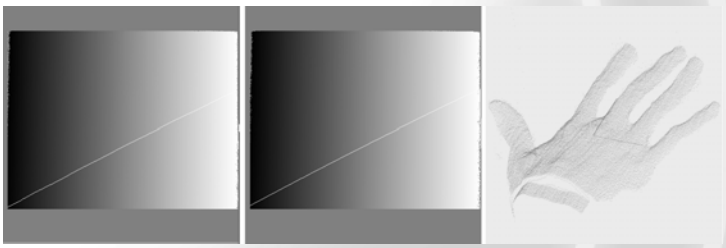

A reference plane captured with 5 and 16 fringes; the previous surface captured with 16 fringes. The improvement is readily observed.

CONCLUSIONS

The performance of imaging and projection systems can seriously hinder the quality of full-field fringe projection methods for 3D surface acquisition or displacement measurements. A solution to the poor contrast ratio exhibited by these systems was proposed and tested with satisfactory results.

REFERENCES

1. Smith, W. J. (2000) Modern optical engineering : the design of optical systems, McGraw Hill, New York
2. Guenther, R. (1990) Modern Optics, John Wiley & Sons, New York
3. Saldner, H.O. and Huntley, J.M. (1997) Temporal phase unwrapping: application to surface profiling of discontinuous objects. Appl. Opt 36, 2770 – 2775
4. Saldner, H.O. and Huntley, J.M. (1997) Profilometry by temporal phase unwrapping and spatial light modulator-based fringe projector, Opt. Eng. 36, 610 – 615
5. Huntley, J.M. and Saldner, H. O. (1997) Shape measurement by temporal phase unwrapping: comparison of unwrapping algorithms. Meas. Sci. Technol. 8, 986–992.